



HAL
open science

Ultrasonic characterization of the bone-implant interface

Yoann Hériveaux

► **To cite this version:**

Yoann Hériveaux. Ultrasonic characterization of the bone-implant interface. Biomechanics [physics.med-ph]. Université Paris-Est, 2020. English. NNT : 2020PESC0064 . tel-03547665

HAL Id: tel-03547665

<https://theses.hal.science/tel-03547665>

Submitted on 28 Jan 2022

HAL is a multi-disciplinary open access archive for the deposit and dissemination of scientific research documents, whether they are published or not. The documents may come from teaching and research institutions in France or abroad, or from public or private research centers.

L'archive ouverte pluridisciplinaire **HAL**, est destinée au dépôt et à la diffusion de documents scientifiques de niveau recherche, publiés ou non, émanant des établissements d'enseignement et de recherche français ou étrangers, des laboratoires publics ou privés.

UNIVERSITÉ PARIS EST CRÉTEIL

École doctorale SIE : Sciences, Ingénierie et Environnement

Laboratoire MSME : Modélisation et Simulation Multi-Échelle

Thesis submitted for the grade of Doctor of Philosophy

Major: Biomechanics

Ultrasonic characterization of the bone-implant interface

by

Yoann HÉRIVEAUX

supervised by Guillaume HAIAT and Vu-Hieu NGUYEN

defended on March 3, 2020

in front of the following board of examiners :

M. Guillaume HAIAT	PhD Supervisor
Directeur de recherche (CNRS - Université Paris-Est)	
M. Vu-Hieu NGUYEN	PhD Supervisor
Maitre de conférences (Université Paris-Est)	
Mme. Sabine BENSAMOUN	President of the Jury & Rapporteur
Directrice de recherche (CNRS - UTC)	
M. Daniel RITTEL	Rapporteur
Professor (Technion, Haifa)	
M. Jordi CABALLÉ SERRANO	Examiner
Associate professor (UIC Barcelona)	
M. Sylvain CHATILLON	Examiner
Ingénieur de recherche (CEA)	
M. Vincenzo CARBONE	Invited Member
Product Manager for InSilicoTrials Technologies	
Mme. Keren SHEMTOV-YONA	Invited Member
Private practice (Technion, Haifa)	

Acknowledgments

First, I would like to express my sincere gratitude to my supervisor Guillaume Haiat for giving me the opportunity to complete this PhD thesis, which has been a very interesting and rewarding experience. I really appreciated his continuous support and encouragement. Moreover, I thank him for his availability and listening. His advice guided me during these three years, and he gave me the resources to work in the best conditions.

I would also like to express my sincere gratitude to my co-supervisor Vu-Hieu Nguyen. He always took the time to answer my questions, which I truly appreciated. His advice and knowledge were a great help for the simulation works realized during this PhD thesis.

Besides my two supervisors, I would like to thank the other members of the jury who have done me the honor of evaluating my work: Mrs. Sabine Bensamoun and M. Daniel Rittel as rapporteurs; M. Jordi Caballé Serrano, M. Vincenzo Carbone, M. Sylvain Chatillon and Mrs. Keren Shemtov-Yona as examiners and as invited members.

Thanks also to all the members of the MSME laboratory for creating a positive environment to work in and for always being nice with me. It was a real pleasure to meet you all during this journey.

Thanks to Manon for her kindness. I really appreciated her presence in the lab during these three years. Thanks to Olivier for all the discussions we had together. I missed the ants and the capoeira demonstrations during this last year ! Thanks (or should I say Mamnoon?) to the badminton team : Ali, Nicolas, Sophie and Anne-Sophie, for the intensive evening sessions. Thanks to Ilaria for her support during the "Dublin adventure", to Madge for her enthusiasm and for the time we spent together at the association, to Yunsang for being a super ambassador of Korean culture, to Katharina for her very helpful feedback on my thesis, and to Romain, who knew absolutely everything in the lab. Thanks also to all the other PhD students and labmates I met during these 3 years: Antoine, Ivan, Alexis, Hugues, Fakhraddin, Léo, Florian, Bao.

I would also like to thank Hung-Son and Yasmin for their valuable help and for their sympathy, as well as Isabelle for her communicative zest for life. I must thank Didier too for his very useful advice and experience. And thanks to all those who I didn't get the opportunity to work with, but still had the occasion to talk with: Matthieu, Vittorio, Thibault, Giuseppe, Gilles, Alexandre, Salah...

Acknowledgments

I'm grateful to Bertrand Audoin and Christine Biateau for giving me the opportunity to use the equipment from their lab at I2M in Talence. I truly appreciated their help and knowledge on how to perform laser-ultrasonic measurements.

My sincere thanks also goes to Pr. Biwa for welcoming me in his laboratory at Kyoto University during one month, and for his helpful advice on analytical modeling. I deeply thank Dr. Ye and Dr. Li for their friendly welcome and the good times we had.

Last but not least, I would like to thank my family, who is so important to me. Thanks to my parents and to my siblings Alexis and Rachel, Aline and Thomas, Laetitia and Sylvain, Damien and Sandrine for their love and their support. And of course, thanks to my nephews and nieces Mélisse, Philippine, Gabriel, Héloïse, Inès, Olivia and Mão for being always there to play with me during holidays and week-ends !

Contents

Acknowledgments	iii
Contents	vii
Acronyms and abbreviations	xiii
Introduction	1
I General context	3
Chapter 1. The bone-implant interface	5
1.1 The multiscale structure of bone	6
1.1.1 Bone tissue	6
1.1.2 Bone remodeling	7
1.2 Endosseous implants	8
1.2.1 Titanium alloy as implant material	8
1.2.2 Geometry of dental implants	8
1.2.3 Surface roughness	9
1.3 Osseointegration and implant stability	10
1.3.1 Osseointegration	10
1.3.2 Implant stability	10
1.3.3 Peri-implant healing	11
1.3.4 Factors influencing implant stability	12
1.4 Stability assessment methods	13
1.4.1 Empirical methods	13
1.4.2 Maximal insertion torque	14
1.4.3 X-ray and Magnetic Resonance Imaging	14
1.4.4 Impact methods	15
1.4.5 Resonance Frequency Analysis	16
1.4.6 Summary of the main methods to assess dental implant stability	18
Chapter 2. Ultrasonic techniques for the bone-implant interface	19
2.1 Characterization of the bone-dental implant interface with quantitative ultrasound	20
2.1.1 Evolution of periprosthetic bone properties during healing	20
2.1.2 Influence of healing time on the ultrasonic response of the BII	21
2.1.3 <i>In vitro</i> estimation of dental implant stability using QUS	21
2.1.4 Simulation of ultrasonic wave propagation in dental implants	25
2.1.5 <i>In vivo</i> estimation of dental implant stability using QUS	28
2.1.6 Alternative use of ultrasound to assess implant stability	30

2.1.7	Perspectives	31
2.2	Stimulation of the bone-implant interface with low intensity pulsed ultrasound	31
2.2.1	Configuration used by Exogen [©]	31
2.2.2	Mechanisms of action of LIPUS on bone remodeling	32
2.2.3	<i>In vivo</i> studies	33
 II In vitro evaluation of the ultrasonic response of the bone-implant interface		37
 Chapter 3. Elastography of the bone-implant interface		39
3.1	Introduction	40
3.2	Material and methods	40
3.2.1	Bone samples and implant	40
3.2.2	Compression device	41
3.2.3	Ultrasonic measurements	41
3.2.4	Analysis of the compressive stress and strain applied to bone samples	42
3.2.5	Bone constitutive behavior	43
3.2.6	Data analysis of ultrasonic measurements	43
3.3	Results	45
3.3.1	Neo-hookean behavior of bone	45
3.3.2	Ultrasonic response of the bone-implant interface	46
3.3.3	Relation between mechanical and ultrasonic measurements	49
3.4	Discussion	49
3.4.1	Originality and comparison with literature	49
3.4.2	Physical interpretation of results	50
3.4.3	Limitations	51
3.5	Conclusion	52
 III Modeling of the reflection of an ultrasonic wave on a rough bone-implant interface		55
 Chapter 4. Sinusoidal description of the bone-implant interface		57
4.1	Introduction	58
4.2	Material and methods	58
4.2.1	Description of the problem	58
4.2.2	Parametric study	60
4.2.3	Governing equations	61
4.2.4	Finite element simulation	62
4.2.5	Signal processing	62
4.2.6	Analytical modeling of a planar BII	63
4.2.7	3D modeling of the bone-implant interface	63
4.3	Results	64
4.3.1	Validation of the numerical model	64
4.3.2	Influence of the roughness period L	66

4.3.3	Influence of the soft tissue thickness W	66
4.3.4	Influence of the bone properties	68
4.3.5	Influence of the frequency	68
4.4	Discussion	70
4.4.1	Originality and comparison with literature	70
4.4.2	Comparison between 2-D and 3-D models	71
4.4.3	Physical interpretation of the results in the microscopic case	72
4.4.4	Physical interpretation of the results in the macroscopic case	72
4.4.5	Variations of bone material properties	75
4.4.6	Frequency variations	75
4.4.7	Sinusoidal approximation of the implant roughness	76
4.4.8	Limitations	77
Chapter 5. Tackling real implant surface roughness		79
5.1	Introduction	80
5.2	Material and methods	80
5.2.1	Description of the problem	80
5.2.2	Construction of the bone-implant interface	80
5.2.3	Determination of the optimal equivalent sinusoidal profile	82
5.3	Results	83
5.3.1	Influence of roughness on the ultrasonic response	83
5.3.2	Effect of low-pass filtering the surface profile	84
5.3.3	Optimal equivalent sinusoidal profile	87
5.4	Discussion	89
5.4.1	Originality and comparison with literature	89
5.4.2	Influence of the roughness	91
5.4.3	Equivalence of the sinusoidal profile	91
Chapter 6. Analytical modeling of the bone-implant interface		93
6.1	Introduction	94
6.2	Material and methods	95
6.2.1	Numerical model	95
6.2.2	Analytical model	96
6.2.3	Reflection and transmission coefficients	98
6.3	Results	99
6.3.1	Stiffness K_c due to the bone-implant contact	99
6.3.2	Stiffness K_{st} due to the presence of a soft tissue layer	100
6.3.3	Total stiffness of the interface K	101
6.3.4	Comparison between analytical and numerical reflection and transmission coefficients	101
6.4	Discussion	104
6.4.1	Originality and comparison with the literature	104
6.4.2	Error between analytical and numerical results	105
6.4.3	Contributions of K_c and K_{st}	106
6.4.4	Limitations	106
6.5	Conclusion	106

IV Applications of ultrasonic methods to dental implant stability estimation	109
Chapter 7. Experimental and numerical study of the ultrasonic propagation in a dental implant	111
7.1 Introduction	112
7.2 Material and Methods	112
7.2.1 Dental implant	112
7.2.2 Ultrasonic device	113
7.2.3 Laser-ultrasonics measurements	114
7.2.4 Numerical modeling and simulation	114
7.3 Results	115
7.3.1 Reproducibility of the measurements	115
7.3.2 Measurements of displacements along the threading	115
7.3.3 Numerical validation	117
7.4 Discussion	119
7.4.1 Propagation of a guided wave in a dental implant	119
7.4.2 Influence of the frequency of the excitation signal	120
7.4.3 Amplitude of displacements and transmitted energy	121
7.4.4 Limitations	121
7.5 Conclusion	122
Chapter 8. Comparison of resonance frequency analysis and quantitative ultrasound methods to assess bone-implant contact	123
8.1 Introduction	124
8.2 Material and Methods	124
8.2.1 Animals	124
8.2.2 Surgical procedure	124
8.2.3 Resonance frequency analysis	125
8.2.4 Quantitative ultrasound device	125
8.2.5 Histology	127
8.3 Results	127
8.3.1 Sample analysis and BIC estimation	127
8.3.2 Resonance frequency analysis	128
8.3.3 Ultrasonic measurements	129
8.4 Discussion	131
8.4.1 Originality of the study	131
8.4.2 Evolution of ISQ, UI and BIC values with healing time	131
8.4.3 Correlation between ISQ and BIC values	131
8.4.4 Correlation between UI and BIC values	132
8.4.5 Comparison between RFA and QUS techniques	132
8.4.6 Limitations	133
8.5 Conclusion	133
Conclusion	135
Bibliography	138

List of personal publications	163
Résumé substantiel	165

Acronyms and abbreviations

- AC : Acetabular Cup
- AE : Acoustic Emission
- ANOVA : ANalysis Of VAriance
- BIC : Bone-Implant Contact
- BII : Bone-Implant Interface
- DEXA : Dual Energy X-ray Absorptiometry
- FAS : First Arriving Signal
- FDA : Food and Drug Administration
- FEM : Finite Element Model
- FFT : Fast Fourier Transform
- ISQ : Implant Stability Quotient
- LIPUS : Low Intensity Pulsed UltraSound
- PCF : Pound-force per Cubic Foot
- PTV : PerioTest Value
- QUS : Quantitative UltraSound
- RF : Radio-Frequency
- RFA : Resonance Frequency Analysis
- SR- μ CT : Synchrotron Radiation Micro Computed Tomography
- UI : Ultrasonic Indicator

Introduction

The general context of the present work is to assess the potentiality of quantitative ultrasound (QUS) to characterize the biomechanical evolution of tissues surrounding an implant. Titanium implants are routinely used in clinical procedures in various fields, such as orthopedic, maxillofacial or dental surgeries. However, implant failures still occur and may have dramatic consequences. The phenomena leading to implant failures remain poorly understood because of the complexity of bone tissue, which is in constant remodeling. These remodeling processes involve the coupling of biological, chemical and mechanical phenomena, and allow bone tissue to adapt its structure to the mechanical stresses it undergoes. In particular, following surgical interventions of endosseous implants, bone tissue will progressively grow in intimate contact with the implant, which process is known as osseointegration.

An important cause of implant failures is related to the lack of standardization of surgical procedures, since many surgeons are still using empirical methods to determine implant stability. Therefore, the development of quantitative methods is required. Interestingly, QUS has emerged as a promising technique to retrieve information on the biomechanical properties of the bone-implant interface (BII), whose evolution determines the implant long term success. QUS has the advantage to be non-invasive, non-radiating and relatively cheap. Moreover, recent work have shown the potentiality of low intensity pulsed ultrasound (LIPUS) to stimulate implant osseointegration. However, phenomena determining the interaction between an ultrasonic wave and the BII remain unclear. Therefore, a better understanding of the aforementioned phenomena could help improving the performances of QUS techniques to estimate implant stability, which is the aim of the present work. This manuscript contains four parts organized as follows.

Part I describes various elements related to the general context of this work. Bone tissue is briefly introduced from a biomechanical perspective. The concepts of implant stability and osseointegration are presented, as well as the factors involved in these processes. The techniques used to evaluate the implant stability are described and discussed. A review of the studies investigating the use of QUS to characterize the BII and of LIPUS to stimulate bone growth at the BII is also provided.

Part II presents an *in vitro* study investigating the effects of the mechanical stresses applied to the BII on its ultrasonic response. An acousto-mechanical device was conceived to compress 18 trabecular bovine bone samples onto coin-shaped implants and to measure the ultrasonic response of the BII during compression. The reflection coefficient of the

BII was shown to decrease as a function of the compressive stress during the elastic compression of the trabecular bone samples and during the collapse of the trabecular network. The sensitivity of the ultrasonic response of the BII to compressive stresses confirmed the potential of QUS to estimate implant primary stability.

Part III is dedicated to the modeling of the reflection of an ultrasonic wave at the BII. The aim is to investigate the sensitivity of the ultrasonic response to osseointegration processes and to the microscopic and macroscopic properties of the BII, in particular to the implant surface roughness. The reflection coefficient of the BII was modeled for different frequencies using two-dimensional and three-dimensional finite element models. In a first study, the implant surface roughness was modeled by a sinusoidal function with varying amplitude and spatial frequency, which can approximate the implant surface roughness, but gives an accurate modeling of macroscopic roughness such as dental implant threading. In a second study, actual implants surface roughness measured by profilometry were introduced in the numerical model. Finally, an analytical model of the ultrasonic propagation at the BII was developed. The approach presented in this part provides a better understanding of the ultrasonic response of the BII, and may be used in future numerical simulations that will consider the macro-geometry of the implant.

Part IV proposes to apply the use of QUS to the specific case of dental implants. First, the ultrasonic propagation in a dental implant was investigated by combining experimental and numerical approaches. Laser interferometric techniques were employed to measure the amplitude of the displacements generated in a dental implant by an ultrasonic excitation. First arriving signal and spectral analysis evidenced the propagation of a guided wave mode along the implant axis, which was confirmed by the numerical results. Second, an *in vivo* study was performed in order to compare the performance of QUS and of Resonance Frequency Analysis (RFA) to estimate implant stability in a rabbit model. Both methods were compared with results obtained via histological analysis, and QUS were shown to have a better sensitivity to changes of bone quantity and quality during the process of osseointegration.

Part I

General context

Chapter 1. The bone-implant interface

Contents

1.1	The multiscale structure of bone	6
1.1.1	Bone tissue	6
1.1.2	Bone remodeling	7
1.2	Endosseous implants	8
1.2.1	Titanium alloy as implant material	8
1.2.2	Geometry of dental implants	8
1.2.3	Surface roughness	9
1.3	Osseointegration and implant stability	10
1.3.1	Osseointegration	10
1.3.2	Implant stability	10
1.3.3	Peri-implant healing	11
1.3.4	Factors influencing implant stability	12
1.4	Stability assessment methods	13
1.4.1	Empirical methods	13
1.4.2	Maximal insertion torque	14
1.4.3	X-ray and Magnetic Resonance Imaging	14
1.4.4	Impact methods	15
1.4.5	Resonance Frequency Analysis	16
1.4.6	Summary of the main methods to assess dental implant stability . .	18

In this chapter, aspects about bone tissue and implant surgery are presented. In particular, notions of osseointegration and implant stability are introduced. In the last section, current methods to assess implant stability are briefly described.

1.1 The multiscale structure of bone

Bones are the main constituents of the human skeleton, whose functions include the support and movement of the body, the protection of organs, the production of blood cells and the storage of mineral constituents such as calcium and phosphate [38]. Bones have many different shapes, sizes and have a complex 3D geometry. From a biomechanical point of view, bone is a multiscale composite and heterogeneous medium [236] with anisotropic and viscoelastic properties [50]. Moreover, bone properties are in constant evolution through remodeling processes, and may vary depending on the observation scale.

1.1.1 Bone tissue

Bone composition

Like cartilage and other connective tissues, bone is composed of an extracellular matrix and cells [160]. The extracellular matrix is responsible for the different functions of bone previously presented. It is composed of a mineral and an organic phase. The organic phase represents 35% of the total mass of the matrix, is essentially constituted of collagen fibers (95%) and provides elasticity to the bone tissue. The mineral phase is composed of 85% of calcium phosphate crystals and 10% of calcium carbonate crystals, that are fixed among collagen fibers. It provides rigidity to the bone tissue. Bone is composed of two different types of bone tissue, namely cortical and trabecular bone.

Cortical bone

Cortical bone contributes about 80% of the total skeletal mass within the body and forms the hard cortex of most bones. It has a porosity comprised between 3% and 15%, which is mostly due to bone vascularization [49, 50]. The main architecture of cortical bone is represented in Fig. 1.1. It consists of multiple microscopic cylinders, called osteons or haversian systems, orientated along the bone axis. Each osteon is composed of dozens of concentric parallel bone lamellae. Osteons are centered around haversian canals through which blood vessels run. Haversian canals are connected with each other, with the medullary cavity and with the periosteum by transverse canals, called Volkmann's canals. The periosteum is a fibrous layer present at the surface of long and flat bones which insures exchanges between bone tissue and the environment.

Trabecular bone

Trabecular (also called spongy or cancellous) bone contributes about 20% of the total skeletal mass within the body and is mostly present at the distal parts of long bones and inside flat bones. It has a higher porosity (around 85%) than cortical bone and presents a wider specific surface. It is constituted by a three-dimensional network of

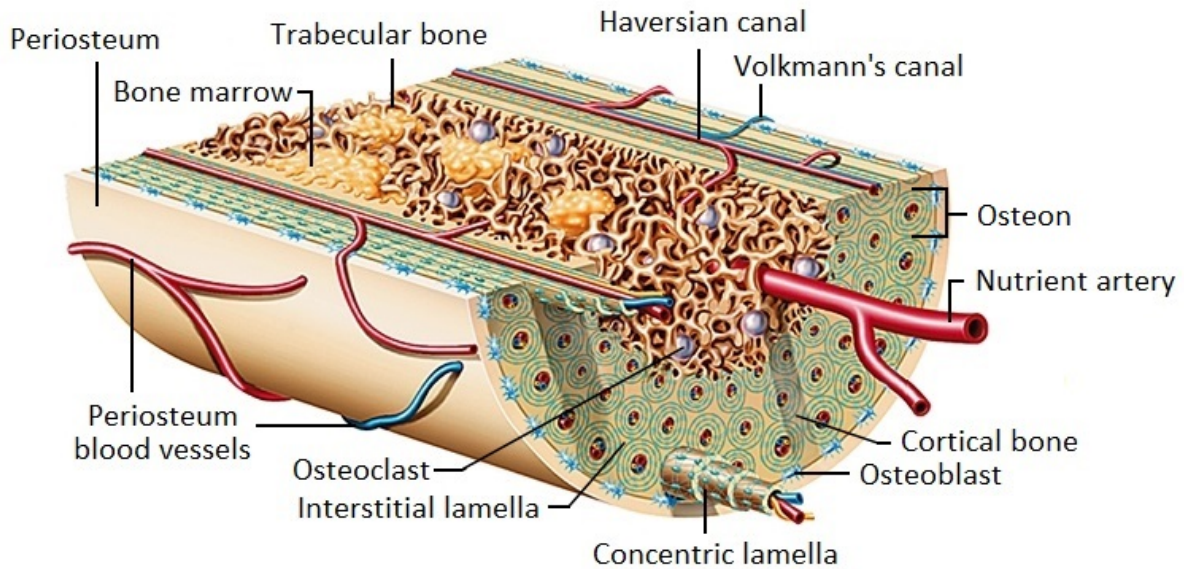


Figure 1.1 – Schematic microstructure of cortical and trabecular bone (adapted from Larousse encyclopedia) [133]

trabeculae embedded in a medium composed of bone marrow and blood. The orientation of trabeculae is determined by the mechanical loading that the bone tissue undergoes.

1.1.2 Bone remodeling

Bone tissues undergo continuous remodeling through resorption and osteogenesis, and around 10% of the human skeleton is renewed each year. Remodeling processes control the reshaping and replacement of bone following injuries like fracture, but also microcracks which occur during normal activity due to mechanical cyclic loading. Bone remodeling also occurs following the insertion of an endosseous implant, with bone tissue progressively growing in intimate contact with the implant. This process corresponds to osseointegration, which will be detailed in Section 1.3.

Bone resorption is due to the activity of osteoclasts. Once activated, osteoclasts secrete acid and collagenase, which leads to the erosion of the bone matrix, and thus to the break down of bone tissue. Bone osteogenesis is insured by osteoblasts. Osteoblasts produce collagen lamellae, which constitute the organic matrix of bone, as well as hydroxyapatite, that is deposited into the organic matrix and forms a dense mineralized tissue. Once trapped in the bone matrix, osteoblasts reduce their activity and become osteocytes, which are the most commonly found cells in bone tissue, and contribute to the routine turnover of bone matrix.

The bone remodeling process is composed of 5 phases [123, 150] that may take several months:

- **Quiescence:** An idle state, where osteoclast activity is inhibited by osteocytes.
- **Activation:** Activation of osteoclasts due to biochemical signals generated by the programmed cell death (*i.e.* the apoptosis) of osteocytes around the trauma site.

- **Resorption:** Removal of bone matrix by osteoclasts. Resorption is terminated by the apoptosis of osteoclasts, ensuring that no excess resorption occur.
- **Reversal:** Replacement of osteoclasts by cells of an osteoblastic lineage that will smooth the resorbed areas by removing unmineralized collagen matrix. Then, a non-collagenous mineralized matrix called "cement line" is deposited to enhance osteoblasts adherence.
- **Formation:** New bone osteogenesis due to osteoblasts activity, as previously described. At the end of the bone formation process, osteoblasts synthesize growth factors regulating their own metabolism [232].

1.2 Endosseous implants

An endosseous implant is inserted within the bone structure in order to replace a joint function or a missing tooth. The correct design of endosseous implants is determinant in order to avoid rejection by surrounding tissues and to promote osseointegration. The choice of an adequate material is particularly important since it will interact directly with bone tissue. Moreover, implant geometry and surface roughness may affect the stress distribution around the implant, and therefore play an important role in the healing process. The present section will especially focus on titanium alloys and on dental implants since they correspond to configurations of interest in the present work.

1.2.1 Titanium alloy as implant material

Titanium alloys are light, strong and biocompatible materials, which is why they are widely used for implants conception [246, 292]. In particular, titanium-based materials rely on the spontaneous formation of a thin (around 300 to 600 nm of thickness [294]), adherent, protective titanium oxide film to get an excellent resistance to corrosion. Moreover, titanium alloys are also used for their mechanical properties, with relatively low elastic modulus and mass density. For orthopedic applications, an excessive difference between bone and implant mechanical properties could cause non-homogeneous stress transfers between the implant and the surrounding tissues, leading to stress shielding [194, 259]. However, a recent study showed that this concern may not apply to dental implants [125].

Among all titanium alloys, Ti-6Al-4V (grade 5) is the most widely used for hard tissue replacement. It is composed of 90% titanium, 6% aluminum and 4% vanadium [116], and has improved mechanical properties compared to pure titanium.

1.2.2 Geometry of dental implants

As represented in Figure 1.2a, a dental implant is an artificial root inserted into the jaw that acts as a support to a prosthesis in order to replace a missing tooth [9, 33]. The implant is hollow and has an internal thread serving as a receptacle for the prosthetic abutment on which the dental prosthesis is fixed (see Figure 1.2b). The depth and spacing of the threading may vary, depending on the design of the implant.

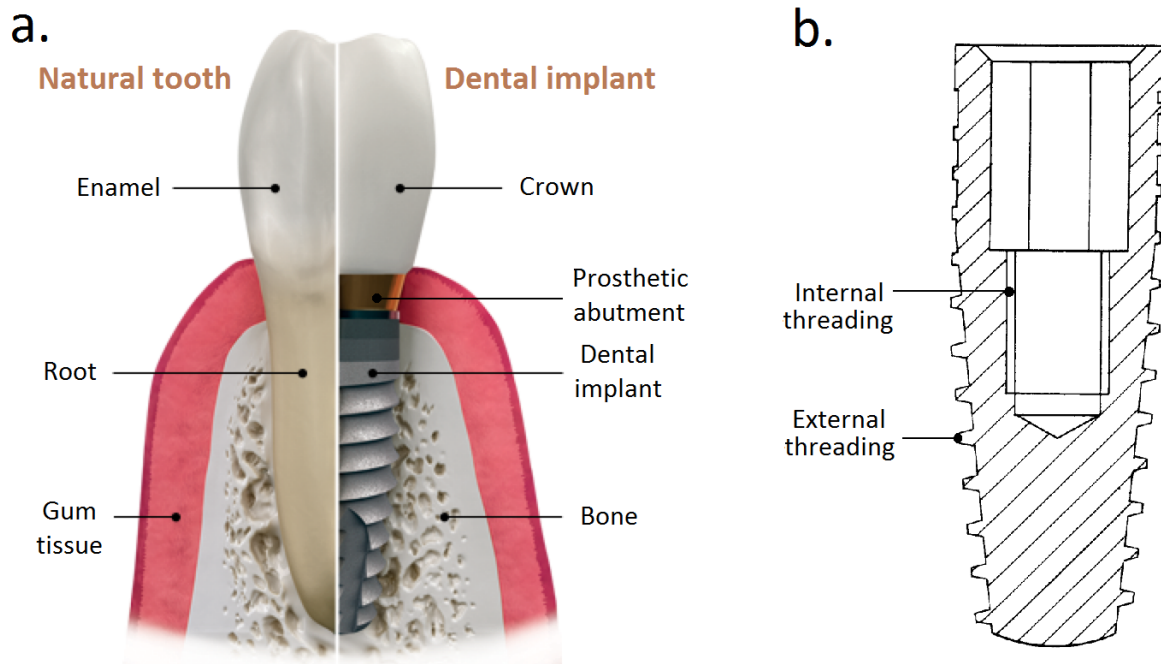


Figure 1.2 – (a) Schematic illustrations of a natural tooth and of a dental implant. (b) Technical drawing of a dental implant - Figure adapted from Patent EP0895757 (1999).

The American Academy of Implant Dentistry states that more than 500,000 dental implants are placed every year in the United States, and this number is expected to increase over the coming years [10]. Therefore, an increasing number of industries are now producing and commercializing dental implants with many different designs. For instance, dental implants may feature holes, be cylindrical or conical, and their end parts may be flat, round or sharp. The geometric properties of the implant play an important role in its stability [122, 205, 226] and in the enhancement of osseointegration [198, 200]. However, industrial design of dental implants is often based on an aggressive copycat strategy, so that implant manufacturers tend to copy the existing designs of their competitors rather than using scientific approaches [32].

For example, using longer dental implants may improve the primary stability of the implant [176, 187] and allow a better distribution of mechanical stresses at the BII, thus promoting osseointegration. However, shorter dental implants necessitate to remove less bone than longer ones, so that a compromise has to be found when considering the length of dental implants. The control of chewing forces is the predominant factor in the loss of osseointegration of implants inserted into a healthy bone, since overloads may damage the consolidating BII. The number, orientation, distribution and possible fastening of implants inserted in the dental arch are other parameters that may increase the resistance of the BII and preserve osseointegration.

1.2.3 Surface roughness

Surface roughness also influences the primary stability of the implant [134] and the osseointegration process [218]. Implants surfaces are mostly treated by acid etching and / or by sand-blasting [257] to improve their osteoconductivity and thus promote bone heal-

ing [139, 199]. In particular, a rougher surface induces a better tolerance of newly-formed bone to micromotion [31] and leads to an increase of the bone-implant contact (BIC) [114], so that the implant has a better anchorage within the bone. Calcium phosphate coatings were also shown enhance osseointegration [135]. However, implant asperities may promote bacterial contamination, and uncontrolled surface roughening may accelerate fatigue fracture of implants [251, 252].

1.3 Osseointegration and implant stability

Remodeling and healing processes are stimulated by the insertion of an implant in bone tissue, leading to its progressive integration: this process is known as osseointegration. Clinical long term success of implant surgery is directly related to this process of osseointegration and to the stability conditions of the implant.

1.3.1 Osseointegration

The process of osseointegration was first evidenced in the 1950s by Per-Ingvar Brånemark (University of Göteborg, Sweden) [29, 30]. In 1981, Albrektsson et al. [7] clarified the notion of osseointegration by defining it as "a direct contact between living bone and implant" at a microscopic level, without intervening fibrous tissue. More generally, osseointegration also characterizes the process leading to the connection between bone tissue and the implant. Osseointegration ultimately allows the implant mechanical stability within surrounding tissues. It is a key factor of implant success [124] since osseointegration failure may lead to the implant aseptic loosening, which is one of the major causes of surgical failure [217].

1.3.2 Implant stability

Implant stability plays a critical role for successful osseointegration, but is difficult to assess because of the complexity and heterogeneity of bone tissue [80, 290]. It may be defined as the capacity of the implant to withstand usual mechanical loading [168], without excessive alteration of the mechanical properties of the surrounding bone tissue. Two kinds of implant stability should be distinguished: the primary stability and the secondary stability.

Primary stability

Primary (or initial) stability corresponds to the implant stability just after surgery. It is strongly related to (i) the quality of bone tissue around the implantation site [234], (ii) the geometry and design of the implant [176, 205] and (iii) the surgical procedure [204, 221], which will be further detailed in Section 1.3.4. Considering these parameters, the implant insertion may be simulated prior to the surgical act to maximize the success of implantation in a patient-specific manner [57]. In particular, an excessive insertion torque may cause significant residual stresses and lead to bone necrosis or to an insufficient blood irrigation that may cause the formation of fibrous tissue [256]. However, excessive micromotion of the implant after surgery due to poor bone quality or inadequate drilling may disrupt the healing process and cause aseptic loosening [13, 34, 217, 261]. Thus, a

maximum micromotion threshold of around 150 μm [217] is recommended. Therefore, long term success of implants is conditioned by their primary stability [145, 162].

Secondary stability

Secondary (or long-term) stability is defined as the implant stability after the healing period. It corresponds to the initial stability of the implant reinforced by new bone formation and maturation due to the remodeling process. Therefore, the secondary stability of an implant directly depends on its primary stability, especially since peri-implant healing is also highly affected by primary stability.

1.3.3 Peri-implant healing

In order to achieve surgical success, it is necessary to understand the mechanisms occurring during the healing process of tissues surrounding the implant. The correct preparation of the implantation site is especially determinant for peri-implant healing because (i) it allows for primary stability, and (ii) it causes bleeding that leads to formation of a haematoma [131].

Contact osteogenesis

Following the implant site preparation, the bone tissue at the interface is surrounded by medullary tissue and by a haematoma containing bone chips generated by the drilling procedure [244, 245]. Within a few seconds after the implantation, platelets start to aggregate around the implant [120] and progressively create a clot. Formation of a stable clot provides both the mechanical and biochemical components required for osteoconduction [131], which is defined as the recruitment and migration of osteogenic cells at the BII [6]. The clot then converts into a three-dimensional collagen matrix. Concurrently, the presence of a haematoma engenders an inflammatory response, with the expression of signaling molecules promoting bone growth [88]. Within 24 hours after the implantation, mesenchymal cells starts migrating from the preliminary matrix of the clot towards the implant surface [170] and differentiates into cells from the osteoblastic lineage, leading to the formation of a fibrous film at the surface of the implant [220]. This process is known as contact osteogenesis. In the case of an unstable implant, this film tends to grow thicker due to an excessive bone formation compared to bone resorption [288].

Distance osteogenesis

In addition to contact osteogenesis, bone growth may also occur from the cut surface of the bone toward the implant, which is called distance osteogenesis [52]. In this case, new bone is deposited on the outer surface of the cut bone by osteoblasts, similarly to what occurs during bone remodeling (see Section 1.1.2). The space between the bone and the implant is thus progressively filled by newly formed immature bone tissue.

Late stage healing

Following contact and distance osteogenesis, fibrous bone tissue is present at the BII. At the late stage of peri-implant healing, these fibrous bone tissue will progressively

mineralize into mature bone tissue through the remodeling process (see Section 1.1.2). Remodeling is enhanced surrounding the implant during up to six months after surgery [32], and occurs first within the host bone and then within the fibrous tissue between the bone and the implant. At the end of successful peri-implant healing, no fibrous tissue should be present at the BII since it should have been entirely converted into mineralized bone tissue. Bone surrounding the implant also adapts its structure to the stress it undergoes [231]. A controlled stress level may enhance osteogenesis, while excessive stresses may damage the interface and cause bone resorption [290].

1.3.4 Factors influencing implant stability

Different factors may influence implant osseointegration and stability, and are therefore determinant for the implant success. The following subsection will present the major ones.

Surgical procedure

Bacterial contamination of the operation site during surgery is an important cause of implant failure. Therefore, it is crucial to work under sterile conditions to minimize infection risks. Contamination may be both direct (*e.g.* due to manipulation errors or patient germs) or indirect (due to air dust contaminants).

More generally, the surgical protocol and operative procedures need to be strictly respected. In particular, drilling is required during the preparation of the implantation site and may cause tissue warming. Bone necrosis has been reported when temperature increases by more than around 10°C during more than one minute [69]. In order to avoid this situation, the implantation site may be cooled with physiological serum when appropriate.

The choice of the surgical procedure also influences the osseointegration process. For example, two techniques are currently used in dental implantology. The first one consists in burying the dental implant entirely. In that case, a cover screw is first placed on the head of the dental implant to avoid bone growth inside the implant. Gum tissue is then closed and sutured to "bury" the implant. After a period of healing, a second surgery is performed to finally screw the prosthetic abutment in the dental implant (see Fig 1.2) and enable gum tissue healing. The second technique consists in placing the dental implant and the prosthetic abutment during a single surgery, so that both bone and gum tissues heal simultaneously. The latter method is more comfortable for the patient, but induces a higher mechanical stimulation of the implant due to its immediate loading, which may damage the BII [83]. The choice of the healing duration before loading an implant is determinant for its long-term success. An early loading may enhance osseointegration through mechanical stimulation [33, 169], but also damage the consolidating BII [2, 31]. Meanwhile, shortening the implant loading time has become a challenge in recent implant developments to (i) diminish the time of social disfigurement and (ii) avoid tissue loss. Both primary stability of the implant [68] and bone quality at the implantation site [82] should be considered when choosing when to load an implant.

Bone properties around the implant site

Bone quality and quantity around the implant site are important factors in the osseointegration process. Bone microarchitectural properties and density depend on the

anatomical site location and function [87] in addition to patients specific factors such as age, sex, pathology or medical treatment. For example, in the case of dental implants, cortical bone tissue usually has a higher density in the mandible than in the maxillary [71]. Therefore, mandibular implantation sites have a higher implant success rate than maxillary sites. Similarly, the density of mandibular trabecular bone is heterogeneous, which leads to a better osseointegration in anterior sites than in posterior sites [174].

Different techniques have been developed to assess patient bone quality. First, based on its proprioception, the surgeon may estimate the bone quality of the patient depending on the strength necessary to drill and insert the implant. The torque required to drill the hole at the implantation site can also be recorded and is correlated with bone density [77, 78]. Second, dual energy X-ray absorptiometry (DEXA), based on the attenuation of X-ray of different energies in bone tissue, is mostly used for osteoporosis diagnosis but has also been successfully tested to assess bone mineral density in jawbone [54]. Third, bone mechanical properties may be assessed based on the ultrasonic speed of propagation and attenuation in bone [5, 129, 286]. Last, histology and image analysis enable to distinguish pre-existing mature from newly formed bone tissue and to estimate bone mineral density and micro-architectural properties [43, 240, 280]. However, histomorphometry cannot be used clinically since it is a destructive method that requires to collect a bone sample at the implantation site.

Implant properties

As discussed in Section 1.2, the implant properties such as its material, geometry and surface roughness may influence osseointegration process. In particular, the implant material may either be bioinert, bioactive or bioresorbable, which will highly affects its interaction with the surrounding tissues. Moreover, implant geometry is a main determinant for the stress distribution around the implant.

1.4 Stability assessment methods

Implant stability and osseointegration are complex phenomena influenced by numerous factors (see Section 1.3). Assessing implant stability can help the surgeon to adapt the clinical strategy in a patient-specific manner in order to avoid implant failure. The clinical strategy corresponds to "the plan that the surgeon develops in order to anticipate and avoid all the technical pitfalls and danger points" inherent to the implant placement [99]. Immediately after the surgery, determining the implant primary stability is required to verify that it is sufficient to allow osseointegration. If the loading is not immediate, it may also help the surgeon to choose when the implant can be loaded, especially for dental implants. In that case, secondary stability has to be checked just before loading the implant to ensure that the osseointegration is sufficient. Finally, during the healing period, assessing the implant stability constitutes a decision support system that helps the surgeon to predict potential implant failures and to adapt the surgical strategy.

1.4.1 Empirical methods

Most surgeons currently use empirical methods to determine the primary stability of an implant based on their perceptions [269]. It is often based on the cutting resistance

and seating torque of the implant during insertion, since the sensation of an abrupt stop may be felt when the implant is correctly seated and thus stable [260]. Another technique consists in slightly hitting the implant and listening to the sound it produces: a crystal sound corresponds to a correct stability while a dull sound suggests poor stability. Palpation and patient sensations may also help the surgeon in his diagnosis [248]. The perception of an experienced surgeon is of course important; however, empirical methods lack of standardization and do not give enough precision about the properties of the BII.

1.4.2 Maximal insertion torque

The measurement of the maximal insertion torque of an implant screwed into bone tissue has been used to determine its primary stability [112, 206]. It is a simple method that only requires a surgical motor or a dynamometric key to perform the measure. Primary stability tends to increase with the value of the maximal insertion torque [270]. Depending on the implant type and geometry, critical values of insertion torque, that guarantee sufficient primary stability for immediate loading of implants, have been determined [100, 204]. However, conflicting results have been reported on the correlation between maximal insertion torque and primary stability [196]. Moreover, this technique may not be used for secondary stability assessment.

A possible way to assess secondary stability is the reverse torque test [14, 231]. During that test, a low reverse torque is applied to the implant. If there is a rotation of the implant, it indicates that the secondary stability is not achieved. However, studies showed that the stress generated by the reverse torque may be responsible for failures [258].

1.4.3 X-ray and Magnetic Resonance Imaging

Imaging techniques are sometimes used to assess implant stability [28, 45, 76, 191]. They allow to observe the evolution of cortical bone thickness during healing [64], which is a determinant of implant success [8]. However, imaging techniques have several limitations. First, most of them only provide a 2-D image of a 3-D structure, which is not sufficient to retrieve information on the bone mechanical properties nor on the bond strength at the BII. Second, neither X-ray nor magnetic resonance imaging can provide a high resolution of the BII because of artifacts due to scattering of X-rays in presence of metal [250] in the first case and due to their own magnetic field disturbance [86, 96] in the second case. Therefore, changes in the bone mineral density cannot be detected until 40% of demineralization has occurred [291], and fibrous tissue development can only be identified at an advanced stage.

Nonetheless, artifacts may be reduced through the use of synchrotron radiation. In particular, synchrotron radiation microtomography (SR- μ CT) constitutes an interesting imaging method in order to retrieve information on implant osseointegration. SR- μ CT may provide a 3-D reconstruction of the bone-implant structure with a spatial resolution of a few micrometers and with a high signal-to-noise-ratio [188, 189]. A recent study showed that it was possible to measure BIC values with SR- μ CT [190]. However, SR- μ CT could not be considered as more effective than histology due to a large variability of the measured BIC values. Moreover, important limitations of SR- μ CT lie in the necessity to handle enormous amounts of data, and in the difficulty to apply this technique clinically.

1.4.4 Impact methods

Impact methods allow to quantify the stability of an implant by analyzing the response of the BII to a defined impact load. Based on this concept, a device called Periotest[®] was introduced by Schulte et al. [243] for applications to dental implantology and was commercialized in 1986. The Periotest[®] device is constituted by a mobile metallic rod placed in a handpiece (see Figure 1.3) and which displacement is driven by an electromagnetic force. The test consists in impacting the healing screw with the metallic rod 16 times with a frequency of 4 Hz and a force of 5N. An accelerometer positioned at the end of the rod records its deceleration, and calculates the mean contact time between the rod and the implant. An indicator called Periotest Value (PTV) is derived from this value. A low PTV indicates the presence of a solid structure surrounding the implant, which corresponds to a good stability [273].

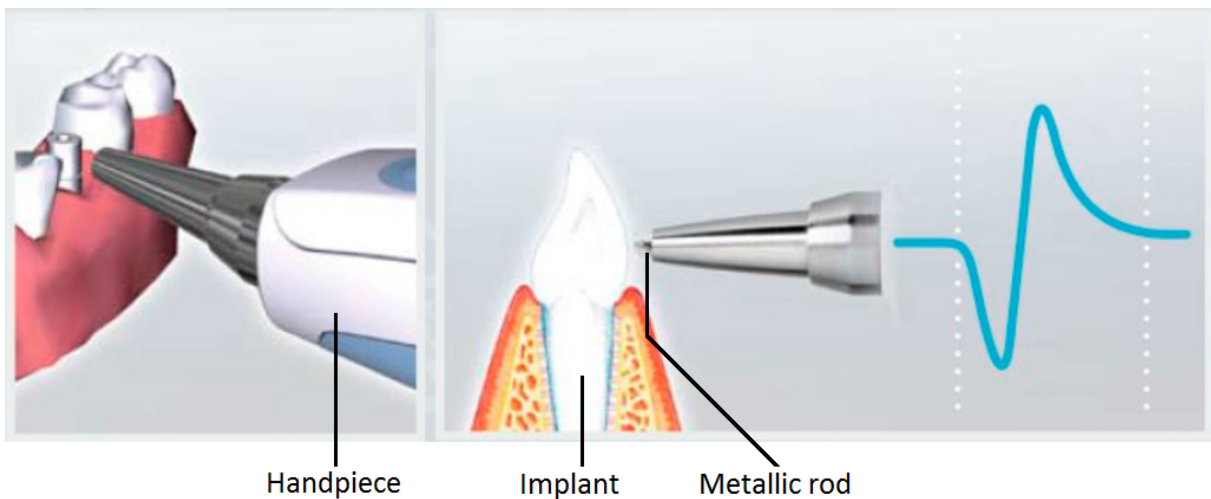


Figure 1.3 – Principle of measurement of implant stability with the Periotest[®] device - Figure adapted from a Periotest[®] advertisement [161].

In vitro and *in vivo* studies showed a good correlation between the PTV and the bone quantity surrounding the implant [118, 196]. Moreover, the PTV was shown to decrease during healing due to an increase of bone density surrounding the implant [11, 167, 268, 274]. However, no correlation was found between the PTV and the BIC values [40, 167, 196]. Therefore, Periotest[®] is not sensitive to BII properties, which are determinant for the implant stability. Other limitations have also been highlighted, such as a strong dependence to handpiece angulation and more generally to measurement conditions [162, 165, 268], which lead to a low reproducibility of the method.

Impact methods may also be used for orthopedic applications. An approach based on the analyses of the impact between a hammer and the ancillary to assess acetabular cup (AC) primary stability was recently developed. The contact duration was shown to be correlated to the AC implant insertion [156]. Following this preliminary study, an indicator based on the impact momentum was designed to reflect implant stability [171]. An instrumented hammer [173, 266, 267] was developed to predict the AC implant stability and was successfully tested in a cadaveric study [172]. However, research on this device is still ongoing and it has not yet been clinically validated.

1.4.5 Resonance Frequency Analysis

Resonance Frequency Analysis (RFA) consists in applying vibrations to the implant at different frequencies and recording the amplitude of the generated displacements in order to determine the first resonance frequency of the BII, which corresponds to a bending mode. This technique has been mostly applied to the dental field, and a device called the Osstell[®] (Göteborg, Sweden) is currently commercialized to estimate dental implant stability.

Figure 1.4 summarizes the principle of measurement of this device [272]. A transducer consisting of a metallic rod (called "SmartPeg") is first screwed on the dental implant. It is then excited without contact by the magnetic field emitted by a handpiece (see Fig. 1.4b). The first resonance frequency of the system is determined, and converted to derive a standardized stability indicator called the ISQ (Implant Stability Quotient), with values ranging from 0 to 100. Stable implants lead to high ISQ values. ISQ values have been shown to increase with healing time [163, 164], and were successfully correlated with primary stability when measured directly after implant placement [111, 224]. Moreover, different studies showed that RFA was sensitive to the implant anchorage depth into bone [164], to the marginal bone level [79], to the cortical bone thickness [164, 166, 196, 247] and to the stiffness of the BII [70, 210]. This technique has the advantage to be non-invasive for the BII.

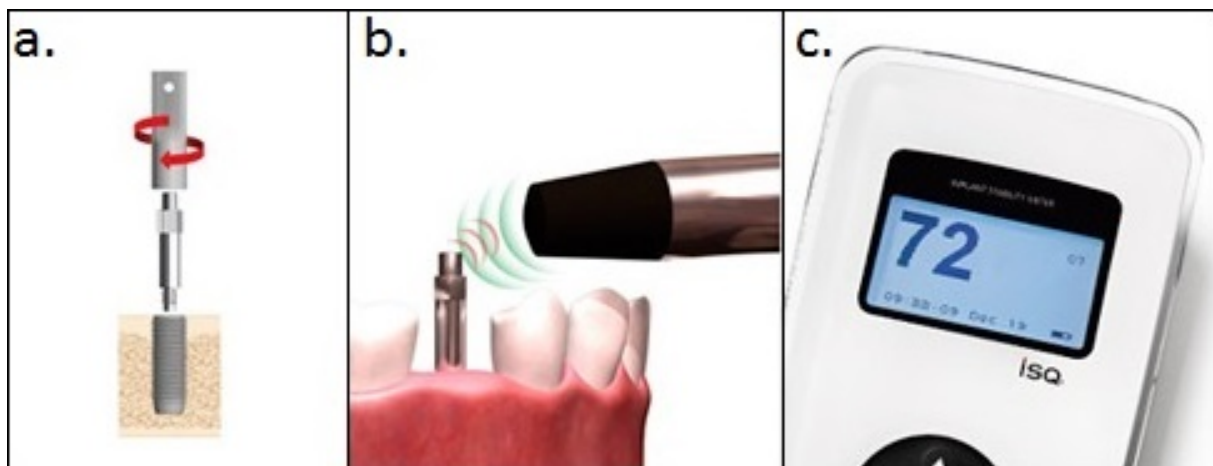


Figure 1.4 – Principle of measurement of implant stability with the Osstell[®] device : (a) the SmartPeg is attached to the implant. (b) The SmartPeg is stimulated magnetically with the handpiece. (c) The ISQ value reflects the degree of stability - Figure adapted from Osstell[®] website [203]

However, ISQ values are dependent on the anatomic implantation site [17, 18, 24, 204] and on the geometry of the implant [186]. Moreover, ISQ is related to the resonance frequency of the bone-implant system, which depends on properties of the entire host bone that vibrates when excited mechanically [227]. RFA is thus sensitive to the properties of tissues surrounding the implant at the organ scale [12], while osseointegration phenomena are known to occur at a distance lower than around 200 μm from the BII [110, 147]. Therefore, the sensitivity of RFA to properties of bone directly in contact with the implant is not sufficient to accurately assess the implant stability [227, 283], and particularly since only the first bending mode is considered [227]. The correlation between ISQ and BIC

values is also weakly understood [51, 113, 130, 178, 240, 247]. Finally, the fixation and orientation of the transducer were shown to significantly influence ISQ measurements [35, 211, 283, 284, 285].

1.4.6 Summary of the main methods to assess dental implant stability

Figure 1.5 lists the advantages and drawbacks of the main methods to assess dental implant stability, which were described in Section 1.4. In particular, Fig. 1.5 indicates whether it is possible or not to assess primary and secondary stability and to retrieve information on the BII with each method.

Method		Primary stability assessment	Secondary stability assessment	Bone-Implant interface characterization	Simplicity, Practicability	Reliability, Reproducibility
Technique	Type of device					
Proprioception	-	✓	✓	✗	✓	✗
Insertion Torque	Torque Wrench	✓	✗	✗	✓	✗
X-ray Imaging	Galileos Comfort Plus®	✓	✓	✗	✗	✗ Artifacts
Percussion Test	Periotest®	✓	✓	✗	✓	✗ Sensible to striking height + to handpiece angulation
Resonance Frequency Analysis	Osstell®	✓	✓	✗	✓	✗/✓ Controversial, sensible to the direction of measurements
Quantitative Ultrasound	<i>In development</i>	✓	✓	✓	✓	✓

Figure 1.5 – Advantages and drawbacks of the main methods to assess dental implant stability

Chapter 2. Ultrasonic techniques for the bone-implant interface

Contents

2.1	Characterization of the bone-dental implant interface with quantitative ultrasound	20
2.1.1	Evolution of periprosthetic bone properties during healing	20
2.1.2	Influence of healing time on the ultrasonic response of the BII	21
2.1.3	<i>In vitro</i> estimation of dental implant stability using QUS	21
2.1.4	Simulation of ultrasonic wave propagation in dental implants	25
2.1.5	<i>In vivo</i> estimation of dental implant stability using QUS	28
2.1.6	Alternative use of ultrasound to assess implant stability	30
2.1.7	Perspectives	31
2.2	Stimulation of the bone-implant interface with low intensity pulsed ultrasound	31
2.2.1	Configuration used by Exogen [©]	31
2.2.2	Mechanisms of action of LIPUS on bone remodeling	32
2.2.3	<i>In vivo</i> studies	33

Chapter 1 evidenced the importance to assess implant stability in order to ensure the surgical success of implants. However, none of the methods described in Section 1.4 have a sufficient sensitivity to the properties of bone tissue in direct contact with the implant. On the contrary, the ultrasonic propagation within an endosseous implant is directly depending on the boundary conditions constituted by the biomechanical properties of the BII. Therefore, QUS methods constitute an attractive alternative to assess implant stability. Moreover, QUS methods are relatively cheap, non-invasive and non-ionizing [157], so that they are adapted to capture information on living tissues for clinical applications. In particular, the possibility to perform ultrasonography on dental implants was recently proved [41]. Therefore, the present chapter will investigate the use of QUS to assess implant stability and will focus on the case of dental implants. Finally, low-intensity pulsed ultrasound (LIPUS) were also shown to be able to stimulate bone remodeling, which will be briefly introduced in the second section of this chapter.

2.1 Characterization of the bone-dental implant interface with quantitative ultrasound

This section reviews various types of work including *in silico*, *in vitro* and *in vivo* studies dealing with QUS approaches to assess dental implant stability. First, the evolution of periprosthetic bone properties during healing and its influence on the ultrasonic response of the BII will be described. Second, the validation of a QUS device will be considered *in vitro*, then numerically, and eventually *in vivo*. Finally, perspectives of clinical applications will be detailed. The review presented in this section was published in a book chapter [106].

2.1.1 Evolution of periprosthetic bone properties during healing

Implant stability is highly dependent on the biomechanical properties of bone tissue at a distance lower than around 200 μm from the implant surface [75, 110, 147]. Different experimental approaches may be used to retrieve quantitative information on newly formed bone properties at the scale of a few micrometers around the implant. Table 2.1 summarizes the biomechanical properties of newly formed bone tissue obtained in a rabbit model by coupling histology with nanoindentation [275, 276, 279] and micro Brillouin scattering [154, 279]:

Nanoindentation is widely used to measure the apparent Young's modulus of different materials at the microscopic scale [295], while micro Brillouin scattering technique uses the photo acoustic interaction between a laser beam and a sample to measure the speed of sound of bone with a resolution of a few micrometers. Thanks to these methods, it was established that newly formed bone tissue has lower Young's modulus and ultrasonic velocities compared to mature bone tissue, which is due to a lower mineral content. Coupling nanoindentation with micro Brillouin analysis also allows to derive the relative variation of mass density between newly formed and mature bone tissues. The evolution of bone biomechanical properties during healing ultimately leads to a decrease of the gap of acoustical properties at the BII.

2.1. Characterization of the bone-dental implant interface with quantitative ultrasound

Table 2.1 – Mean values and standard deviation of the apparent Young’s modulus measured by nanoindentation and of the ultrasound velocity measured with micro Brillouin scattering in newly formed (NB) and mature (MB) bone tissue of New Zealand White Rabbits. Data from Vayron et al. [276, 279].

Healing time	7 weeks		14 weeks	
	NB	MB	NB	MB
Young’s Modulus (GPa)	15.85(± 1.55)	20.46(± 2.75)	17.82(± 2.10)	20.69(± 2.41)
Ultrasound velocity ($m.s^{-1}$)	4966(± 145)	5305(± 36)	5030(± 80)	5360(± 10)
Mass density*	$0.878\rho_{7w}$	ρ_{7w}	$0.978\rho_{13w}$	ρ_{13w}

* Only a relative variation of the bone mass density was obtained.

2.1.2 Influence of healing time on the ultrasonic response of the BII

Mathieu et al. [155] investigated the effect of bone healing on the ultrasound response of the BII in the case of coin-shaped implants placed on rabbit tibiae, in cortical bone tissue. The ultrasound response of the BII was measured *in vitro* at 15 MHz after seven and thirteen weeks of healing time. The BIC was measured by histomorphometry and the degree of mineralization of bone was estimated qualitatively by histological staining. A significant decrease of the amplitude of the echo of the BII as a function of healing time was obtained, which was explained by (i) the increase of the BIC ratio as a function of healing time from 27% to 69% and (ii) the increase of mineralization of newly formed bone tissue, which modifies its Young’s modulus and its ultrasound velocity (see Table 2.1). This study demonstrated the sensitivity of QUS to osseointegration phenomena.

2.1.3 *In vitro* estimation of dental implant stability using QUS

The use of QUS to assess dental implant biomechanical stability was first suggested by de Almeida et al. [53], who measured the variations of the 1 MHz response of a screw inserted in an aluminium block. Based on this pioneer work, dental implants have been used as an ultrasound wave guide in order to assess their stability, using a QUS device that was validated *in vitro* [152, 277, 278, 284] and *in vivo* [280, 283].

The principle of this QUS device is to place an ultrasonic transducer with a central frequency of 10 MHz in contact with the top surface of a dental implant inserted in bone, as represented in Fig. 2.1. The ultrasonic probe is linked to an analyzer, and a transient recorder records the radiofrequency (rf) signal from the analyzer with a sampling frequency equal to 100 MHz. An indicator I is then derived from the RF signals by computing its Hilbert’s envelope to get a simple score representing the average amplitude of the measured signal. The precise definition of I may depend on the considered study so that the values obtained for different studies could not be compared. Note that a multifractal analysis was also performed to retrieve information from the inner structure of the RF signal [239].

The amplitude of the RF signals depends on the biomechanical properties of the media in the vicinity of the BII. The acoustical impedance gap is lower when the implant is surrounded by bone than by fluids (blood, water or air), and the energy leakage of the

ultrasonic wave out of the implant is therefore more important. Moreover, the evolution of the bone mechanical properties described in Table 2.1 also influences the ultrasonic propagation at the BII [276]. Consequently, I is sensitive to the mechanical properties of the BII, and its evolution is representative of the dental implant stability.

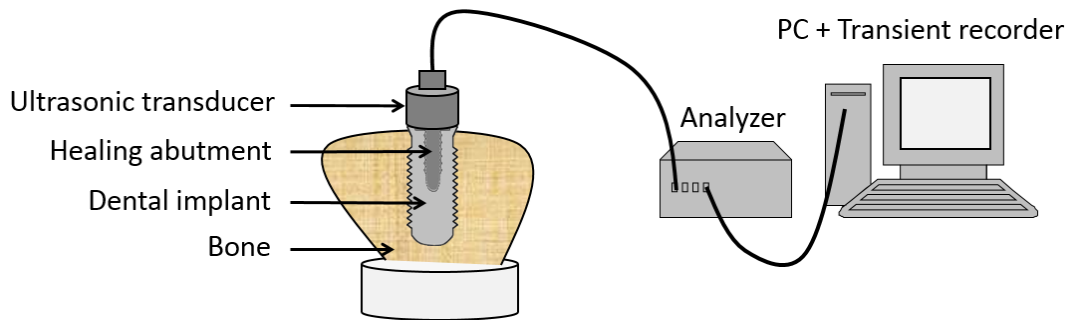


Figure 2.1 – Ultrasonic device including the implant, the transducer and the dedicated electronics.

Preliminary study with titanium cylinders

An *in vitro* experimental preliminary study was first carried out with prototype titanium cylinder shaped implants in Mathieu et al. [152]. The aim of this study was to propose an *in vitro* methodology to identify the amount of bone surrounding titanium cylinders, paving the way for the assessment of implant stability by QUS techniques. Identical implants were inserted into rabbit distal femurs with four different geometric configurations represented in Fig. 2.2, each configuration corresponding to a given amount of bone in contact with the implants. All implants were placed in defects created in bone tissue with the same depth (6 mm). However, the diameter of the defect changed (from 4 to 4.8 mm) at a different depth depending on the configuration. All samples were then analyzed using the QUS device. The obtained RF signals exhibited an approximately periodic repetition of echoes recorded on the upper surface of the implant. Moreover, the amplitudes of the echoes decreased faster as a function of time when the amount of bone in contact with the implant increases, and the value of the indicator I was correlated to the amount of bone in contact with the implant.

In biomaterials

A second *in vitro* study [277] was performed using real dental implants placed in a tricalcium silicate-based cement (TSBC) called Biodentine (Septodont, Saint-Maur-des-Fossés, France) [126, 127], which is used as bone substitute biomaterial for dental implant surgery in the case of edentulous patients with poor bone quality. The use of synthetic biomaterials avoids to perform invasive surgical procedures of autogenous bone grafts (*i.e.* grafts taken from and received by the same individual) while preventing the higher risks of rejection and infection of allografts (*i.e.* grafts from another donor) [119].

Vayron et al. [277] studied the evolution of the ultrasonic response of an implant embedded in TSBC and subjected to fatigue stresses. Six titanium dental implants were embedded in Biodentine. Cyclic lateral stresses were then applied to the implants during

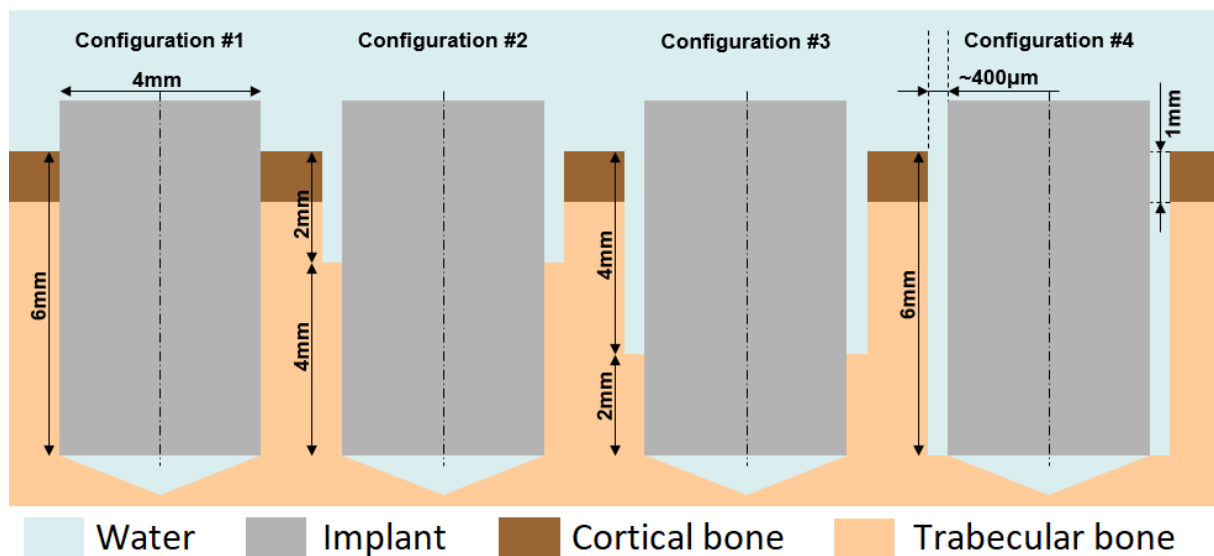


Figure 2.2 – Schematic illustrations of the four drilling configurations used to mimic different configurations of primary stability. Figure adapted from Mathieu et al. [152]

24 hours via a custom-made mechanical device, and the stability of the implant was regularly evaluated with the QUS device. A significant increase of I was obtained as a function of fatigue time for all implants, which is due to the progressive debonding of the Biodentine-implant interface, leading to a higher acoustic energy recorded at the upper surface of the implant.

In bone-mimicking materials

The use of bone-mimicking phantoms made of polyurethane foams allows working under standardized and reproducible conditions. Therefore, it has recently been used to compare the performances of QUS and RFA methods [284]. Bone test blocks composed of rigid polyurethane foam (Orthobones; 3B Scientific, Hamburg, Germany) with different values of bone density and of cortical thickness (1 and 2 mm) were used to perform this study. Cortical bone was modeled by the material type #40 PCF (pound-force per cubic foot) with a mass density equal to 0.64 g/cm³. Trabecular bone was modeled by three different material types (# 10, # 20, and # 30 PCF) with mass density values respectively equal to 0.16, 0.32, and 0.48 g/cm³. Conical cavities were created in the blocks with surgical drills, and implants were then screwed into these cavities.

Four different parameters affecting the implant stability were considered in the study, namely (i) trabecular bone density, (ii) cortical bone thickness, (iii) final drill diameter and (iv) implant insertion depth. The RFA response of the implant was measured in ISQ units using the Osstell[®] device (see Section 1.4.5). The ultrasonic response of the implant was measured with the indicator I , corresponding to the average amplitude of the signal between 10 and 120 μ s. Figure 2.3 shows the variation of the values of the ISQ and of I as a function of the different input parameters.

The results shown in Fig. 2.3 indicate that the values of ISQ (respectively I) increase (respectively decrease) as a function of trabecular density, cortical thickness and the screwing of the implant. However, ANOVA and Tukey-Kramer tests indicate significant difference for the values of I obtained for all the tested trabecular densities and cortical

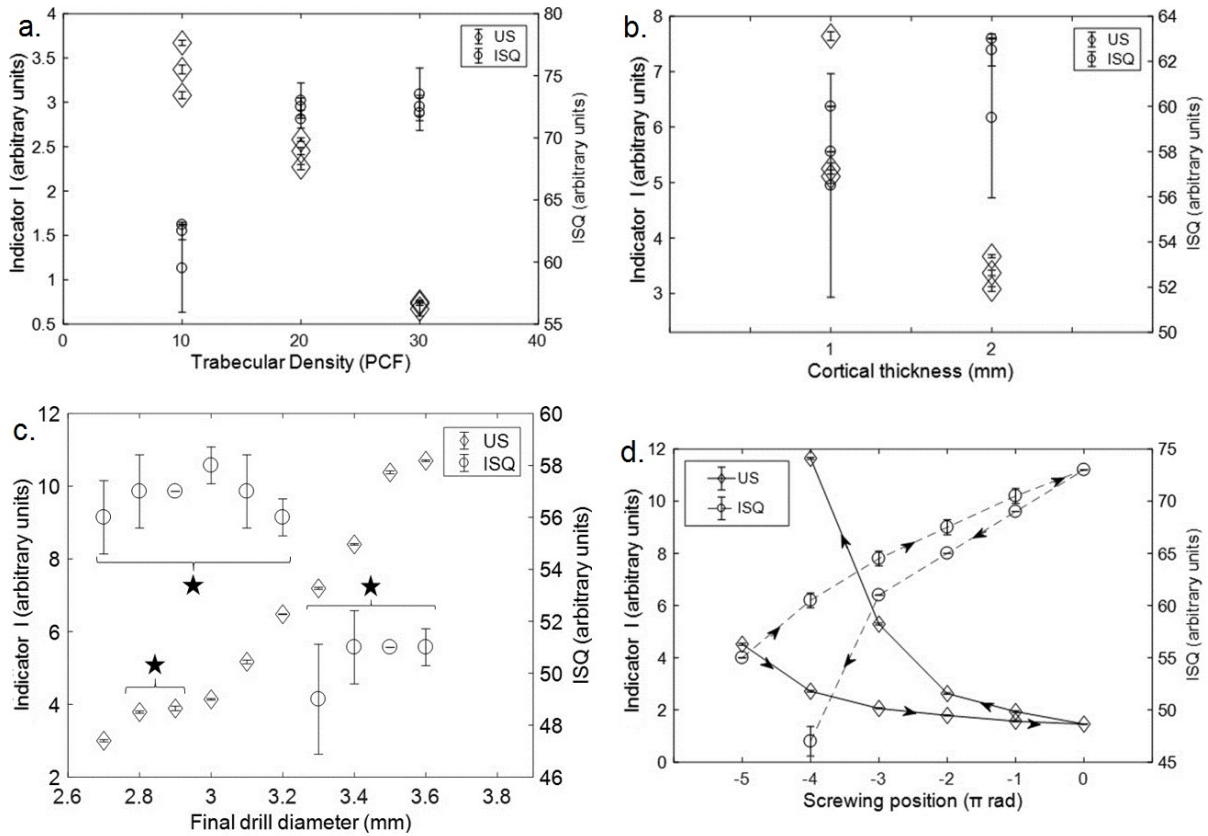


Figure 2.3 – Variations of the values of the ISQ and of the indicator I for implants inserted in bone mimicking phantoms with different values of (a) trabecular density (# 10, # 20, and # 30 PCF), (b) cortical thickness (1 or 2 mm), (c) final drill diameter and (d) screwing of the implant. Three implants are considered per test block for (a) and (b). The stars indicate the results that are statistically similar for (c). The error bars correspond to the reproducibility of each measurement. Figure adapted from Vayron et al. [284]

thickness, which was not the case for the ISQ values (see Fig. 2.3a and 2.3b). When the final drill diameter varies, values of I were significantly different for all considered configurations except for two (see Fig. 2.3c), while the ISQ values were similar for all final drill diameters lower than 3.2 mm and higher than 3.3 mm. Moreover, Table 2.2 shows that the errors produced by the RFA technique on the estimation of the different parameters was between 4 and 8 times higher compared to that produced by the QUS device. Therefore, QUS has a better sensitivity to changes of the parameters related to the implant stability and thus a higher potentiality to assess correctly the dental implant stability than the RFA technique.

Table 2.2 – Estimation error of each parameter in Vayron et al. [284].

Indicator (technique)	Trabecular density	Cortical thickness	Insertion depth
ISQ (RFA)	2.73 PCF	0.31 mm	0.16 mm
I (QUS)	0.6 PCF	0.04 mm	0.04 mm

In bone tissue

An *in vitro* validation of the QUS device has been carried out with implants inserted into bone tissue [280] to establish the dependence of I on the amount of bone in contact with the implant. Ten identical implants were fully inserted in cylindrical cavities (3.5 mm diameter and 13 mm deep) created in the proximal part of bovine humeri. After recording the ultrasonic response of the implant, it was unscrewed by 2π rad in order to reduce the surface area of the implant in contact with bone tissue. The procedure of unscrewing the implant and recording its ultrasonic response was then repeated until the implant was detached from bone tissue. Figure 2.4 compares results obtained experimentally in Vayron et al. [280] with numerical data [282] and shows that the value of the indicator I significantly increases as a function of the number of rotations when the implant is unscrewed. Therefore, despite the more complex wave propagation occurring within the implant than in the preliminary study with titanium cylinders [152], the ultrasonic response is shown to be still sensitive to the implant environment.

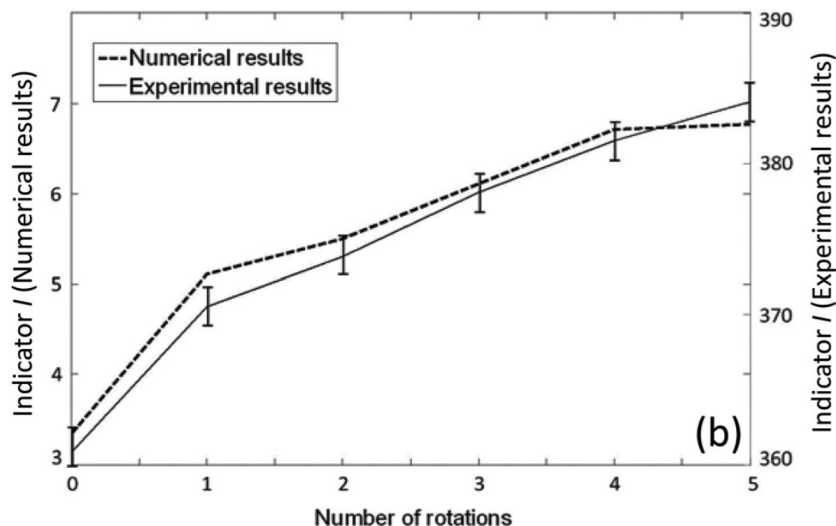


Figure 2.4 – Variation of the simulated and experimental values of I as a function of the number of unscrewing rotations of the dental implant in bone tissue. Figure adapted from Vayron et al. [282].

2.1.4 Simulation of ultrasonic wave propagation in dental implants

The development of acoustical modeling and of the associated numerical simulation is mandatory in order to understand the interaction between an ultrasonic wave and the bone-implant system because it allows to improve the performances of the device. Moreover, using acoustical modeling is the only solution in order to discriminate the effects of the different bone parameters (such as bone structure, geometry and material properties) on the ultrasonic response of the implant, which is impossible to achieve *in vivo* because all parameters vary in parallel. In the studies described in the following, the ultrasonic source was modeled by a broadband longitudinal velocity pulse centered at 10 MHz in the direction normal to the implant surface. Note that all media were assumed

to have homogeneous, elastic and isotropic mechanical properties, and that the values of ultrasound velocity and density of all media were taken from Haiat et al. [94], Njeh et al. [195], Pattijn et al. [210, 211].

2-D model

A 2-D numerical study of the ultrasonic propagation in cylinder-shaped titanium implants was first performed in Mathieu et al. [153] using SIMSONIC, a 2-D finite-difference time-domain (FDTD) algorithm. The geometry considered in this study was identical as the one described in section 2.1.3 (see Fig. 2.2). A good qualitative agreement with experimental results was obtained. However, for numerical simulations, a faster decay of the amplitude of the ultrasonic response was observed, and contributions due to mode conversions were lower, which may be related to the 2-D approximation made on the study. Therefore, 3-D modeling is necessary to derive a more precise description of the interaction between the ultrasonic wave and the bone-implant system.

3-D model

Vayron et al. [281] considered the same configuration as the one considered in Mathieu et al. [153] (see Fig. 2.2) but using a 3-D axisymmetric finite element model (FEM) in COMSOL Multiphysics (Stockholm, Sweden). Figure 2.5 shows a comparison between the relative evolution of the ultrasonic indicator I obtained experimentally [152], numerically by 2-D FDTD simulation, and with the 3-D FEM. The indicator I is shown to increase when bone quantity around the implant increases for all models. However, there remains some discrepancy between data obtained numerically and experimentally, which may be explained by possible experimental errors on the geometry of the configuration as well as on material properties. Nonetheless, the results obtained with the 3-D model are closer to experimental results than the ones obtained with the 2-D model, which is due to a more realistic description of the problem, especially regarding boundary conditions.

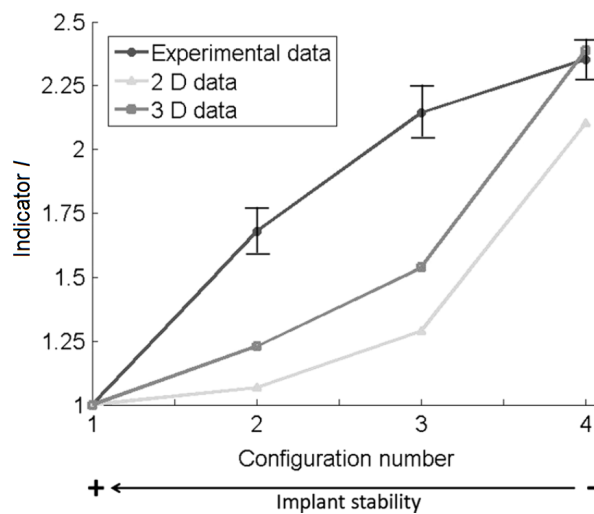


Figure 2.5 – Variation of the normalized value of the ultrasonic indicator as a function of the configuration number corresponding to the amount of bone in contact with the implant (see Fig. 2.2) for results obtained experimentally, with 2-D FDTD simulations and with the 3-D finite element model. Figure adapted from Vayron et al. [281].

2.1. Characterization of the bone-dental implant interface with quantitative ultrasound

The evolution of the indicator I as a function of the healing time was also simulated by progressively modifying the mechanical properties of bone tissue around the dental implant considering experimental values measured in Table 2.1. The indicator I was shown to significantly decrease as a function of healing time and therefore to be sensitive to bone quality.

In order to derive a more realistic description of the implant structure, another 3-D axisymmetric study was performed in Vayron et al. [282] considering actual geometries of dental implants, as shown in Fig. 2.6. The effects of changes of three different parameters on the ultrasonic response of the implant were assessed, namely (i) introducing fibrous tissue in Ω_L (see Fig. 2.6) and progressively reducing the depth of this fibrous layer, (ii) unscrewing the implant and (iii) modifying the peri-implant bone mechanical properties from $\pm 20\%$.

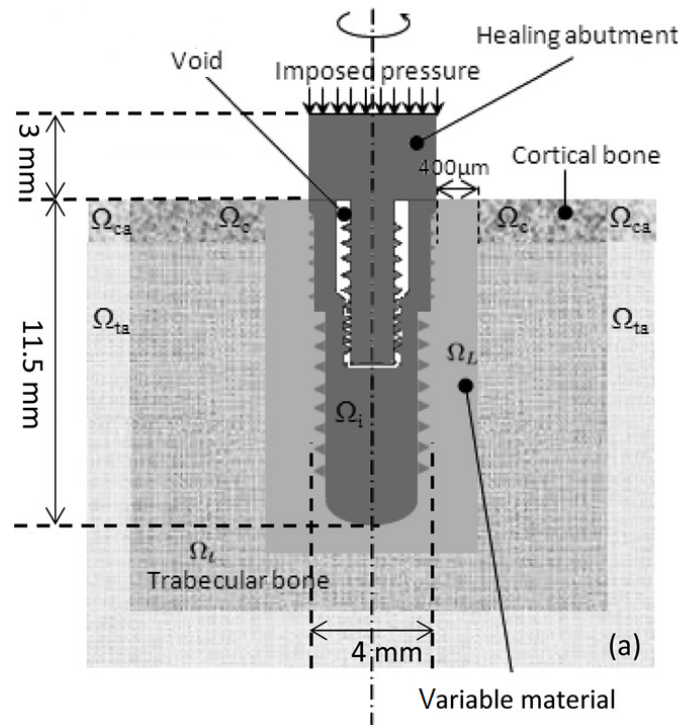


Figure 2.6 – Cross-sectional view of the 3-D axisymmetric geometrical configuration used in Vayron et al. [282]. Ω_L corresponds to the region where the material properties are varied. Ω_i , Ω_c , and Ω_t denote the implant, the cortical bone and the trabecular bone, respectively. Ω_{ca} and Ω_{ta} correspond to absorbing layers associated to trabecular bone and cortical bone, respectively. The white parts inside the implant are filled with a void. Figure adapted from Vayron et al. [282].

Figure 2.4 shows that I increases as a function of the number of rotations when unscrewing the implant, which is in good agreement with experimental results [280]. Increasing longitudinal wave velocity and mass density of bone tissue around the implant also leads to a decrease of the values of I . These results may be explained by the decrease of the gap of material properties between bone tissue and the implant, which leads to a lower gap of acoustic impedance between bone and the implant and therefore, to a higher transmission coefficient at the bone-implant interface. 2-D results presented in Chapter 4 further confirm these assumptions.

Recently, a last 3-D axisymmetric study was performed considering a real implant geometry [58]. However, a more realistic description of the osseointegration process was considered compared to Vayron et al. [282], with the introduction of a parameter ξ representing a combined variation of the Young's modulus, the Poisson's ratio and of the mass density of the tissue surrounding the implant. Moreover, the influence of the thickness W of the layer where osseointegration occurs was introduced, which is an important parameter for the implant success that will be further considered in Chapters 4, 5 and 6. An important difference (around 150–200%) in the indicator values was obtained between an implant inserted in fully healed or in fully deteriorated bone, which further confirmed the sensitivity of QUS to peri-implant bone healing.

As a conclusion, in all the aforementioned numerical simulations, the indicator I was shown to decrease as a function of the implant stability.

2.1.5 *In vivo* estimation of dental implant stability using QUS

An initial *in vivo* validation of the QUS device was performed in Vayron et al. [280] using a rabbit model. Twenty-one dental implants were inserted in the femur of eleven New Zealand white rabbits. Two (respectively three and six) rabbits were sacrificed after 2 weeks (respectively 6 and 11 weeks) of healing time. The QUS device was used to measure the ultrasonic response of the implant directly after implantation and just before the sacrifice of the animals. Each measurement was reproduced 10 times to assess their reproducibility. The BIC was also determined by histological analyses.

Figure 2.7 shows that the RF signals obtained on the day of the implantation have a higher amplitude than signals obtained after 11 weeks of healing time. A significant decrease of the ultrasonic indicator was obtained between the initial and the final measurements for all but one (respectively for all) implants after 6 (respectively 11) weeks of healing time, whereas no global tendency could be assessed after 2 weeks of healing time. Moreover, the indicator I had significantly different values for samples obtained after 2, 6 and 13 weeks of healing, which validates the use of QUS to assess dental implant stability.

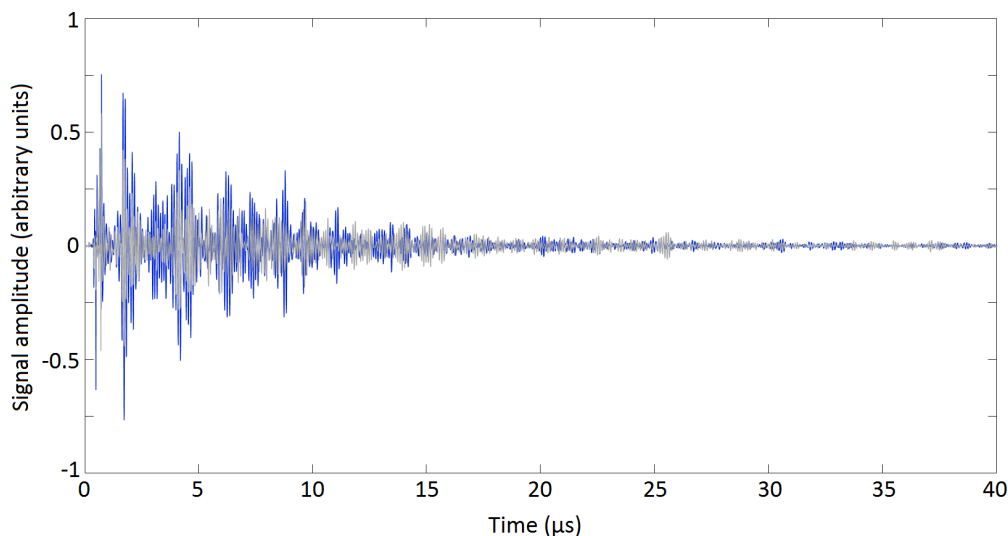


Figure 2.7 – Time gated RF signals obtained on the day of the implantation (blue line) and after 11 weeks of healing time (gray line). Figure adapted from Vayron et al. [280].

Figure 2.8 shows the variation of the indicator I as function of the BIC ratio for 13 implants. A significant but limited correlation was obtained between I and the BIC, which may be explained by (i) the low number of analyzed samples, (ii) the measurement of the BIC ratio in a given plane rather than in 3-D and (iii) the dependence of the implant ultrasonic response on the mechanical properties of bone tissue in contact with the implant, which are not described by the BIC ratio.

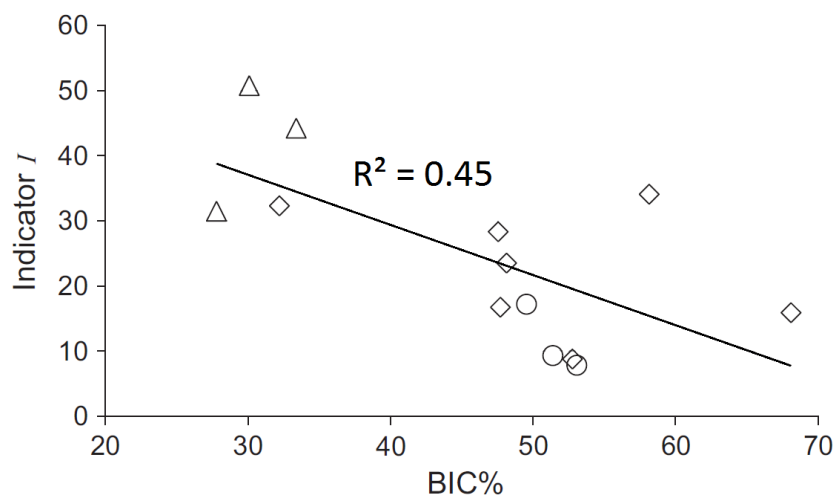


Figure 2.8 – Variation of the indicator I as a function of the BIC ratio. The triangles (respectively the circles and the squares) represent the samples with 2 (respectively 6 and 11) weeks of healing time. Figure adapted from Vayron et al. [280].

Recently, a second *in vivo* study was performed with sheep [283] in order to compare the performance of the RFA and of QUS techniques to retrieve dental implant stability. Compared to Vayron et al. [280], the study considered (i) a larger number of samples, (ii) a bigger animal model inducing bone properties closer to those of human tissue, (iii) the comparison with the RFA technique and (iv) a controlled torque of insertion (3.5 N.cm) when screwing the ultrasonic probe on the implant, which allowed a better reproducibility compared to the manual positioning performed in the former study.

Eighty-one dental implants were inserted in the iliac crests of eleven sheep. QUS and RFA measurements were performed after healing times of 5, 7, and 15 weeks. The RFA response was measured in ISQ as described in subsection 2.1.3. The ultrasonic indicator I that was used in previous studies was modified in order to obtain an ultrasonic indicator $UI = 100 - 10 \times I$ having values comprised from 1 to 100 and increasing when bone quality and quantity increase around the implant.

Figure 2.9 shows the variations of UI and of ISQ as a function of healing time for 2 given implants. ISQ measurements were performed in two perpendicular directions, denoted 0° and 90° . The values obtained in the 0° direction (respectively in the 90° direction) were denoted $ISQ0$ (respectively $ISQ90$). ANOVA showed that UI significantly increased from 0 to 5 healing weeks and from 0 to 7 healing weeks for 97% of implants. However, variations of UI between 5 and 15 healing weeks were implant dependent and UI decreased as a function of healing time for several implants. This result may be explained by the fact that implants were not loaded mechanically in the iliac crest, which is likely to lead to bone tissue resorption around the implants [142]. Results obtained by the RFA technique were shown not to depend on healing time, with significant variations of the

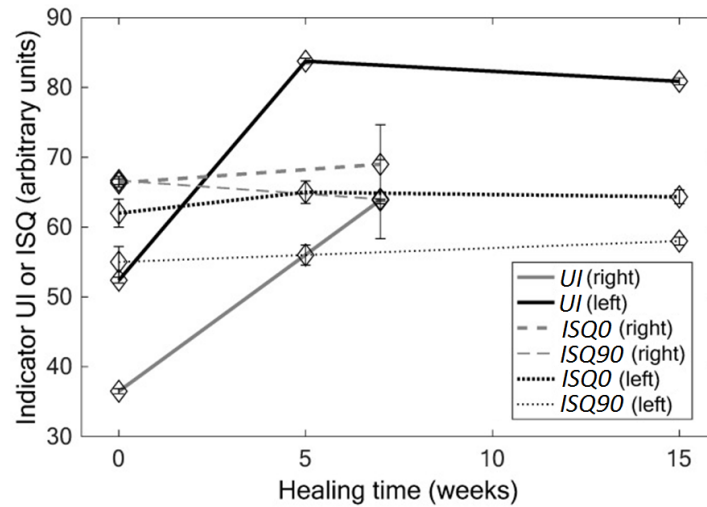


Figure 2.9 – Results obtained for implant #2 right and left of the sheep #3 for the different healing times for *UI*, *ISQ0* and *ISQ90* values. Error bars show the reproducibility of the measurements. Figure adapted from Vayron et al. [283].

ISQ values for only 18% of the implants. Moreover, the error on the estimation of the healing time when analyzing the results obtained with QUS was around 10 times lower than that made when using RFA, which may be explained by a better reproducibility of measurements. The conclusion of the study is that QUS allows to determine the evolution of dental implant stability with a better accuracy than RFA.

2.1.6 Alternative use of ultrasound to assess implant stability

Sections 2.1.3, 2.1.4 and 2.1.5 reviewed studies using a QUS device to assess the acoustical reflection at the BII in order to retrieve information on dental implant stability. While it represents the main field of investigation to assess implant stability with QUS in the literature [23], a few alternative methods have also been proposed.

In particular, the transmission of acoustic emission (AE) from an intra-oral source to a sensor mounted on the patient’s face have been investigated to monitor dental implant stability [201, 202]. An *ex vivo* bovine study confirmed the potentiality of AE to retrieve information on implant primary stability [201]. Moreover, different parameters affecting AE and especially the degree of hydration of bone were assessed [202]. However, no *in vivo* validation of this method has been performed yet.

Different studies [228, 229, 230] also showed the potential of non-linear ultrasound techniques, which are already used in other fields such as geophysics or non-destructive testing, to retrieve information on implant stability. Non-linear ultrasonic responses were shown to have a greater sensitivity than linear responses to contact quality at a threaded interface [228]. Based on this preliminary study, the non-linear characteristics of the interface between a dental implant and a bone phantom were studied [230]. Two approaches were carried out, namely (i) the termed pulse inversion procedure, which consists in successively sending two ultrasonic pulses of inverse polarity to the interface and summing their responses, and (ii) the scaling subtraction method, which consists of successively sending two pulses of different amplitudes to the interface and computing their difference. Both approaches enabled to retrieve information on the non-linearity of the interface be-

tween the implant and the bone phantom, which were then successfully related to the implant stability. A third study allowed to determine the most promising nonlinear parameters for the assessment of implant stability [229]. However, these approaches were only validated *in vitro*.

2.1.7 Perspectives

The studies summarized in this section have shown the potential of QUS techniques to retrieve information on the BII and pave the way for the development of an ultrasonic device that could be used clinically to estimate dental implant stability. Comparisons with the RFA technique highlight the better sensitivity and precision of QUS. However, it remains difficult to precisely define implant stability [92, 157]. Moreover, clinical studies are now needed in order to define a target value for the ultrasonic indicator above which an implant is considered to be stable enough to be loaded.

2.2 Stimulation of the bone-implant interface with low intensity pulsed ultrasound

Section 2.1 summarized the state of the art regarding the ultrasonic characterization of implant stability. However, surgeons are often helpless when secondary stability could not be achieved due to osseointegration failures. Therefore, this section investigates a second possible application of ultrasound techniques to the BII, which is the stimulation of implant osseointegration by LIPUS.

LIPUS started to be considered in order to promote soft tissue healing in the 1950s [148]. However, the ultrasonic stimulation of bone growth was only evidenced in 1983 by Duarte [59], which showed that a 15 minutes per day exposure of the wound site to LIPUS could enhance bone remodeling on a rabbit model. Many studies then demonstrated the potential of LIPUS to accelerate bone healing [47, 149], more specifically in the case of fractures taking longer than expected to heal (delayed unions or non-unions) [136, 181, 233]. In 1994, the Food and Drug Administration (FDA) approved the use of LIPUS in clinical applications. A LIPUS stimulation device (Exogen[©], Bioventus, Durham, NC, USA) was subsequently introduced in the market, and was shown to improve the total recovery time of patients with non-union fractures by 38% [97]. However, the efficiency of LIPUS stimulation is still controversial. A recent clinical review [242] concluded that no effect of LIPUS stimulation on bone growth could be demonstrated. Moreover, precise mechanisms of action of LIPUS stimulation are still poorly understood. Therefore, a better understanding of the interaction between ultrasound and bone could help to improve LIPUS stimulation techniques.

2.2.1 Configuration used by Exogen[©]

In order to stimulate bone growth, an ultrasonic probe is placed on the skin of the patient at the location of the bone defect (see Fig. 2.10), so that the transducer emits an ultrasonic wave in the direction of the healing site. Important parameters of the LIPUS include frequency, intensity, duty cycle and pulse duration, which were respectively fixed to 30 mW.cm⁻², 1.5 MHz, 20% and 1 ms in the case of the Exogen[©] device. Therefore,

most studies in the literature used these parameters, while only a few ones investigated their influence on the stimulation of bone growth (see Table 2.3). Bioventus recommends a treatment duration of 20 min per day.



Figure 2.10 – Use of the Exogen 4000+[©] device to stimulate tibia fracture repair (Source: Bioventus Global).

2.2.2 Mechanisms of action of LIPUS on bone remodeling

Even if hypotheses have been made on how LIPUS influences bone remodeling [47, 95, 207] and more specifically implant osseointegration [55, 141], precise mechanisms of action are still unclear. Thermal and mechanical mechanisms could both have an impact on osseointegration:

Thermal effects

The ultrasonic propagation at the BII induce a temperature increase due to viscous damping. Even if this temperature increase was shown to be well below 1°C for standard LIPUS intensities [42, 59], it may be sufficient to affect thermo-sensitive enzyme activities. Welgus et al. [289] demonstrated that minimal heating effects may activate metalloproteinase, which plays a major role in bone matrix remodeling. However, recent studies enhanced that mechanical effects probably play a predominant role in the stimulation of bone remodeling [55, 207].

Mechanical effects

A possible effect of LIPUS on bone remodeling is related to micromotions induced by the ultrasonic wave, which may produce mechanical stimulation. LIPUS may in particular produce strain gradients, which are known to be correlated to periosteal bone formation [89]. The oscillatory strains generated by LIPUS at high frequencies compared to physiological strains are likely to affect the mechanotransduction processes [207], which

correspond to a physical stimulus switched by cells into chemical activities to trigger downstream signaling. However, the precise pathways affected by LIPUS stimulation are still to be investigated.

Acoustic streaming, which corresponds to a small scale eddying of fluids near a vibrating structure such as cell membranes and the surface of stable cavitation gas bubble [62], is also generated by LIPUS. This process has been shown to affect diffusion rates and membrane permeability, which may result in an increase in micromechanical blood pressure and therefore to an acceleration of fracture healing [225].

However, the research on how LIPUS may affect bone remodeling is still ongoing [19, 95]. Numerical modeling and simulation of the interaction between an ultrasonic wave and the bone-implant interface could help clarifying these mechanisms and optimize LIPUS stimulation devices.

2.2.3 *In vivo* studies

Most research on bone growth stimulation by LIPUS was performed in the cases of bone fracture and of distraction osteogenesis, a process mostly used in reconstructive surgery and to repair skeletal deformities. However, a few studies investigated the use of LIPUS to stimulate implant osseointegration. A literature search with keywords "LIPUS", "stimulation", and "osseointegration" was performed, and Table 2.3 exhaustively lists the *in vivo* studies found on the LIPUS stimulation of osseointegration.

Porous cylindrical implants

The LIPUS stimulation of osseointegration was first investigated on porous cylindrical implants in four different studies [115, 144, 262, 263]. Lin et al. [144] considered bioglass cylinders on a rabbit model, and investigated to what extent LIPUS could enhance bioglass degradation and bone growth around the implant. To do so, implants were inserted in both the right and left femoral condyles of rabbits, and only one leg received LIPUS treatment for each rabbit. Rabbits were regularly sacrificed between 1 and 8 weeks after the implant surgery. Histology was then performed to estimate the percentages of bioglass and of newly formed bone tissue around the implant for the different healing times. Bone growth in the porous structure of the implant and bioglass degradation were found to be significantly higher for healing times superior to 3 weeks when considering LIPUS stimulated implants. Tanzer et al. [262, 263] performed similar studies on a dog model with titanium porous cylindrical implants, and showed an increase of bone growth by respectively 18% and 119% in these two studies when the implants were stimulated with LIPUS. The significantly more important increase of bone growth in the latter study may be due to the higher LIPUS intensity considered (respectively of 30 and 250 $\text{mW}\cdot\text{cm}^{-2}$, see Table 2.3). Iwai et al. [115] investigated the use of LIPUS stimulation on rabbits in the case of hydroxyapatite cylinders. Microtomography, histological analysis and compression tests were performed on samples with and without LIPUS stimulation. The results showed that LIPUS stimulation induced (i) a significant increase in the volume of mineralized tissue after 3 weeks of healing, especially in depth of the implant, (ii) a higher number of osteoblast cells inside the implant and (iii) a non significantly higher strength of the implant.

Dental and orthodontic implants

Following preliminary studies on cylindrical implants, the use of LIPUS stimulation was then tested in animal models with dental [109, 146, 184, 271] and orthodontic implants [81, 175]. Microtomography, histology analyses, torque tests and ISQ measurements (see Section 1.4.5) were performed in order to evaluate the implant stability and the quantity of newly formed bone tissue around the implant. Results have been contrasted, some studies showing no significant effect of the action of LIPUS [271] and others promising results with similar parameters [146, 293]. Ruppert et al. [235] also underlined that for the rat model, the effect of LIPUS stimulation was maximal after 4 weeks of healing, whereas no effect of LIPUS stimulation could be evidenced after 8 weeks of healing, which may be explained since LIPUS aims at accelerating the process of osseointegration. Therefore, it takes longer for the control group to achieve total healing, but once achieved, the final situation of the implant is the same whether it has been stimulated or not.

Parametric studies with different intensities, duty cycles, frequencies and treatment times have also been performed [109, 184] (see Table 2.3). Nakanishi et al. [184] concluded that stimulation with a low intensity (40 mW.cm^{-2}) and a frequency of 3 MHz was the most efficient. Hsu et al. [109] demonstrated that 20%-pulsed LIPUS waves were more efficient than continuous waves, and that intensities of 50 and 150 mW.cm^{-2} led to a faster osseointegration than an intensity of 300 mW.cm^{-2} . These two studies are in qualitative agreement concerning the influence of intensity, since they both concluded that a lower intensity should be favored. However, this conclusion is conflicting with the one from Tanzer et al. [263]. Moreover, these studies only tested a maximum of five different parameter configurations, and results may depend on the animal model tested. Therefore they could not be extended to clinical issues.

Clinical studies

As of September 2019, Abdulhameed et al. [1] constitutes the only clinical study investigating the use of LIPUS on the stimulation of implant osseointegration. More specifically, the study focused on the effect of LIPUS stimulation on marginal bone loss and on implant osseointegration, which were evaluated based on cone beam computed tomography image analysis, torque wrench and RFA techniques (see Section 1.4.5). The study comprised 22 patients, divided into a control group ($n = 11$) and a LIPUS stimulated group ($n = 11$). Six months after the surgery, a marginal bone gain at the buccal plate bone site occurred in the latter group, whereas marginal bone loss was observed for the control group. Moreover, the torque wrench and ISQ values increased for the LIPUS-stimulated group. Therefore, it concluded that LIPUS may be used as treatment modality to save dental implants with questionable primary stability.

Table 2.3 – Main characteristics of the *in vivo* studies performed on the LIPUS stimulation of implant osseointegration.

Article	Implant type	Model	Intensity (mW.cm ⁻²)	Frequency	Duty cycle
Lin et al. [144]	Bioglass cylinder	Rabbit femur	500	1.5 MHz	50%
Tanzer et al. [262]	Titanium cylinder	Dog femur	30	1.5 MHz	20%
Tanzer et al. [263]	Titanium cylinder	Dog cubitus	250	1.5 MHz	20%
Iwai et al. [115]	Hydroxyapatite cylinder	Rabbit femur	30	1.5 MHz	20%
Ustun et al. [271]	Dental implant	Rabbit tibia	30	1.5 MHz	20%
Nakanishi et al. [184]	Dental implant	Rabbit femur	40 & 100	1 & 3 MHz	10%
Hsu et al. [109]	Dental implant	Rabbit tibia	50 & 150 & 300	1 MHz	20 & 100%
Liu et al. [146]	Dental implant	Rabbit tibia & femur	40	1.5 MHz	20%
Miura et al. [175]	Orthodontic screw	Rat tibia	30	1.5 MHz	20%
Ganzorig et al. [81]	Orthodontic screw	Rat tibia	30	1.5 MHz	20%
Zhou et al. [293]	Screw	Rat tibia	40	1.5 MHz	20%
Abdulhameed et al. [1]	Dental implant	Human mandible	30	1.5 MHz	20%
Ruppert et al. [235]	Screw	Rat femur	30	1.5 MHz	20%

Part II

**In vitro evaluation of the ultrasonic
response of the bone-implant interface**

Chapter 3. Elastography of the bone-implant interface

Contents

3.1	Introduction	40
3.2	Material and methods	40
3.2.1	Bone samples and implant	40
3.2.2	Compression device	41
3.2.3	Ultrasonic measurements	41
3.2.4	Analysis of the compressive stress and strain applied to bone samples	42
3.2.5	Bone constitutive behavior	43
3.2.6	Data analysis of ultrasonic measurements	43
3.3	Results	45
3.3.1	Neo-hookean behavior of bone	45
3.3.2	Ultrasonic response of the bone-implant interface	46
3.3.3	Relation between mechanical and ultrasonic measurements	49
3.4	Discussion	49
3.4.1	Originality and comparison with literature	49
3.4.2	Physical interpretation of results	50
3.4.3	Limitations	51
3.5	Conclusion	52

3.1 Introduction

Chapter 2 summarized different works related to the characterization and stimulation of the BII using ultrasound techniques. In particular, the effects of healing time on the ultrasonic response of the BII have been extensively studied. However, the sensitivity of QUS to the loading conditions at the BII is still unknown. The stress distribution around the implant during and after surgery is an important determinant for the implant success [84]. As discussed in Chapter 1, osseointegration phenomena are stimulated by “low level” stresses applied to the BII [33], while excessive level of stresses may damage the consolidating BII and lead to implant failure. Nevertheless, the loading conditions at the BII remain difficult to be assessed experimentally. None of the techniques described in Section 1.4 can so far be used to retrieve information on the stresses applied to the BII.

An interesting approach to assess the level of stress at the BII consists in employing FEM. For example, stress and strain fields have been predicted around the BII in the context of dental [15, 238] and orthopedic implants applications [180]. The results showed that stresses in the range of 0-10 MPa could be obtained at the BII, depending on the physiological boundary conditions. However, despite the progresses realized in computational analyses, it remains difficult to assess the loading conditions at the BII in a patient specific manner due to the complexity of the implant geometry and of the bone material properties.

Interestingly, magnetic resonance elastography [287] and ultrasound elastography [192, 253] have been extensively used to characterize the stiffness of soft tissues. The principle of elastography is the following [140]. A stimulus is imposed onto the target tissue, and its deformations, which can be static or dynamic, are monitored using imaging methods (either magnetic resonance or ultrasound techniques). Based on an inverse analysis, it is then possible to retrieve the mechanical properties of the target soft tissue, which can provide information for the diagnosis of certain diseases such as cancer, inflammation and fibrosis. Information on the loading conditions of an implant and therefore on its primary stability could also potentially be retrieved by elastography. However, such techniques have currently never been applied to the BII.

The aim of the present work is to determine whether a QUS technique may be used to assess the effect of compressive stresses on the ultrasonic response of the BII. To do so, trabecular bovine bone samples were progressively compressed onto coin-shaped implants. The ultrasonic response of the BII was measured throughout the compression stage in order to retrieve the reflection coefficient of the compressed BII.

The work presented in this chapter was published in *Scientific Reports* [103].

3.2 Material and methods

3.2.1 Bone samples and implant

Eighteen trabecular bone samples were cut from three bovine femoral heads. Each cubic sample had dimensions of around 14 x 14 x 14 mm that were measured with a digital caliper. Each sample was also weighed and its apparent density ρ was determined. A mirror-polished Ti-Al6-V4 titanium alloy coin-shaped implant (20 mm diameter and 5 mm thickness) was used throughout the study.

3.2.2 Compression device

Figure 3.1a shows a schematic description of the device used to compress the bone sample onto the implant surface and to measure the stress applied to the BII. The device was composed of the coin-shaped implant, the bone sample, an elastomer cylinder made of polyurethane and a force sensor stacked inside a rigid cylindrical frame. The elastomer cylinder (35 cm long and 30 cm diameter at rest) acted as an elastic spring aiming at applying forces to the bone sample and to the BII. The force sensor measured the force F applied to the elastomer, which allowed to deduce the stress σ at the BII. Friction phenomena between the sensor and the frame were minimized using lubrication. The compression was realized by tightening a screw with a thread pitch of 1.5 mm positioned on the opposite side of the device compared to the implant, allowing to control the displacement at one end of the elastomer.

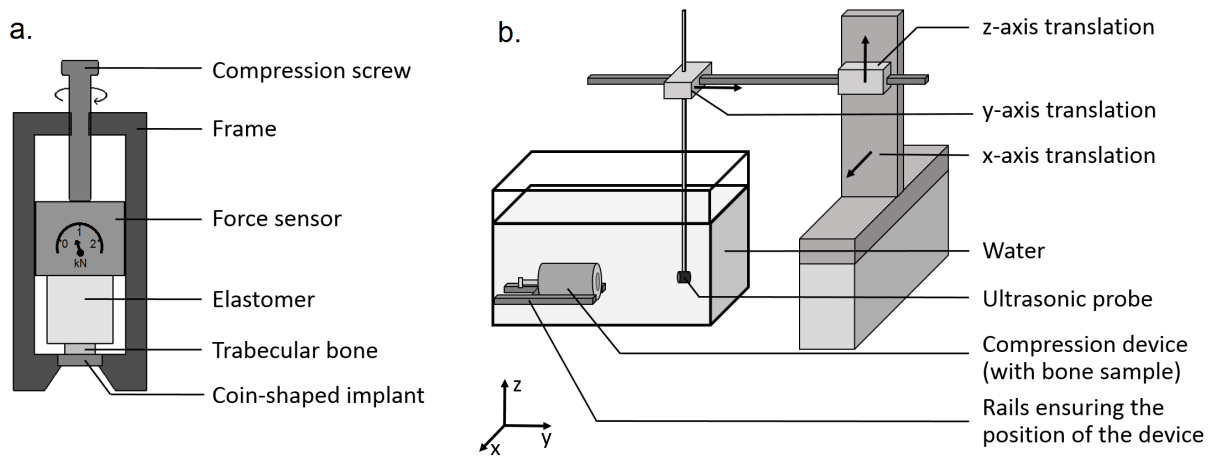


Figure 3.1 – Schematic illustrations of the devices used (a) to compress the bone sample and measure the applied stress and (b) to realize ultrasonic measurements.

3.2.3 Ultrasonic measurements

The ultrasonic probe consists in a broadband focused immersed transducer (CMF-25; Sonaxis, Besançon, France) with a center frequency equal to 15 MHz, a diameter of 6 mm and a focal length of 40 mm, which leads to a beam width at the focus approximately equal to 0.5 mm in water. The transducer acts as an emitter-receiver. The supporting electronics comprises a pulse-receiver amplifier and an A/D conversion card of 100-MHz sampling frequency.

As shown in Fig. 3.1b, the ultrasonic measurements were performed by immersing the device described in Fig. 3.1a in a container filled with water at room temperature. The compression device described in section 3.2.2 was positioned in the container so that (i) the BII was located approximately at the focus of the transducer and (ii) the normal of the implant surface and of the axis of the transducer coincide with the y-direction, with a maximum parallelism error of 1° . The displacement of the probe for 2-D imaging was controlled using two translation stages moving in the x and z directions and fixed to a rigid frame (see Fig. 3.1b). A spatial acquisition square window of 8 x 8 mm centered on the axis of the coin-shaped implant was considered with a displacement step equal

to 1 mm. A total number of 64 radiofrequency signals were recorded for each ultrasonic measurement and i denotes the number of the signal recorded. The reproducibility of the ultrasonic measurements was assessed by repositioning a given bone sample and repeating the procedure six times with the same force (50 N) applied to the BII.

For each bone sample, the first ultrasonic measurement (corresponding to the 2-D scan described above) was performed with a force F equal to 50 N applied to the BII. Then, the compression screw was tightened by 2π rad, which corresponds to a displacement of 1.5 mm, and the ultrasonic measurements were reproduced. The compression screw was tightened by 2π rad six more times in order to realize ultrasonic measurements for six increasing values of the force applied to the BII. Then, the compression screw was tightened by 4π rad and the ultrasonic measurements were reproduced. This process of tightening the compression screw by 4π rad and reproducing the ultrasonic measurements was carried out until the force reached a value of 2 kN. The upper limit equal to 2 kN for the force was considered because it corresponds to a compressive stress σ equal to around 10.2 MPa on the BII, which approximately corresponds to the maximum stress simulated at the BII using FEM [15, 238]. A homogeneous stress distribution at the BII was assumed. A total number of N loading steps (which corresponds to N values of the force F) was considered and $j \in [1, N]$ corresponds to the running number of the loading step.

The force applied to the BII was measured at the beginning and at the end of each ultrasonic measurement (which lasted around 500 seconds) in order to account for effects related to the stress relaxation of the system (see below).

3.2.4 Analysis of the compressive stress and strain applied to bone samples

Due to stress relaxation effects, the compressive stress applied to the BII decreased during the 500 seconds corresponding to the duration of the ultrasonic measurement. The values of the compressive stress applied to the BII obtained at the beginning and at the end of the ultrasonic measurement corresponding to loading step # j were noted $\sigma^+(j)$ and $\sigma^-(j)$ respectively. The average and standard deviation value of $\sigma^+(j)$ and $\sigma^-(j)$ were denoted $\sigma^m(j)$ and $\sigma^{sd}(j)$, respectively. The deformations of the force sensor, of the coin-shaped implant and of the frame were neglected compared to the deformation of the elastomer and of the bone sample, leading to:

$$\epsilon(j) = \frac{\Delta h_T - \Delta h_E}{h_b} \quad (3.1)$$

where $\epsilon(j)$ corresponds to the strain of the bone sample, Δh_T is the displacement imposed by the compression screw (see Fig 3.1a), Δh_E is the variation of length of the elastomer and h_b is the initial length of the bone sample at rest. The error realized on Δh_T was given by the uncertainty on the rotation of the screw, which was of the order of 5° , leading to an error on Δh_T of 0.02 mm. A compression test of the elastomer was carried out without any bone sample and reproduced three times in order to assess its constitutive law. The following linear elastic macroscopic law was found:

$$\Delta h_E = 7.35 \cdot 10^{-6} F \quad (3.2)$$

Uncertainties on Δh_E were directly linked to uncertainties on $\sigma(j)$ since F varies as a function of time between the beginning and the end of the ultrasonic acquisition. The uncertainty on $\epsilon(j)$ was defined as the sum of the contributions of the uncertainties on Δh_T and on Δh_E by the relation:

$$\epsilon^{sd}(j) = \frac{0.02 \cdot 10^{-3} + 7.35 \cdot 10^{-6} S (\sigma^+(j) - \sigma^-(j))}{h_b} \quad (3.3)$$

where S is the surface of the bone sample in contact with the implant.

3.2.5 Bone constitutive behavior

The constitutive law of the trabecular bone samples was considered to be Neo-Hookean, following previous studies [37, 39, 132]. Such behavior consists in three regimes. σ first varies linearly as a function of ϵ , then reaches a nearly constant value, and eventually increases again as a function of ϵ . Here, a linear dependence of σ as a function of ϵ was assumed for this last regime, so that the relation between σ and ϵ could be interpolated by:

$$\tilde{\sigma}(\epsilon) = \begin{cases} \sigma_1 \frac{\epsilon}{\epsilon_i}, & \text{if } \epsilon \leq \epsilon_i \\ \sigma_1, & \text{if } \epsilon_i \leq \epsilon \leq \epsilon_f \\ \sigma_1 + B \cdot (\epsilon - \epsilon_f), & \text{if } \epsilon \geq \epsilon_f \end{cases} \quad (3.4)$$

where ϵ_i and ϵ_f are the strain values delimiting the different regimes, σ_1 is the stress value at the plateau and B is the slope of the curve representing the variation of σ as a function of ϵ during the final regime. Based on the experimental results, a cost function $e_\sigma(B, \sigma_1, \epsilon_i, \epsilon_f)$ was defined in order to assess the difference between the experimental measurements and values given by Eq. 3.4 following:

$$\epsilon_\sigma(B, \sigma_1, \epsilon_i, \epsilon_f) = \sum_{j=1}^N \frac{|\sigma(j) - \tilde{\sigma}(\epsilon(j))|}{N} \quad (3.5)$$

An optimization procedure based on a conjugate gradient method was carried out in order to determine the optimal values of the parameters $(B, \sigma_1, \epsilon_i, \epsilon_f)$ minimizing the cost function e_σ for each bone sample.

3.2.6 Data analysis of ultrasonic measurements

The same signal processing as the one used in Mathieu et al. [155] was applied to the signals obtained using the ultrasonic device. Briefly, the envelope of each radiofrequency (rf) signal was determined by computing the modulus of its Hilbert's transform. For each RF signal $\#i$, three echoes were considered corresponding to the reflection of the ultrasound wave on i) the water-implant interface, ii) the BII and iii) the BII, the implant-water interface and again the BII. The maximum amplitude of the envelope of the echo $\#1$ (respectively of echoes $\#2$ and $\#3$) corresponding to the RF signal $\#i$ and to the loading step $\#j$ was denoted $A_{i,1}(j)$ (respectively $A_{i,2}(j)$ and $A_{i,3}(j)$). The time window was centered on the time of the maximum of the corresponding echo and had a total length equal to the signal duration (0.9 μ s).

The following analysis was carried out for all 18 bone samples. For each loading step # j , the average value of the ratio $R_2(j)$ (respectively $R_3(j)$) of the amplitudes of echo #2 (respectively echo #3) and echo #1 was calculated over the 8 mm x 8 mm window following:

$$R_2(j) = \frac{1}{64} \sum_{j=1}^N \frac{A_{i,2}(j)}{A_{i,1}(j)} \quad (3.6)$$

$$R_3(j) = \frac{1}{64} \sum_{j=1}^N \frac{A_{i,3}(j)}{A_{i,1}(j)} \quad (3.7)$$

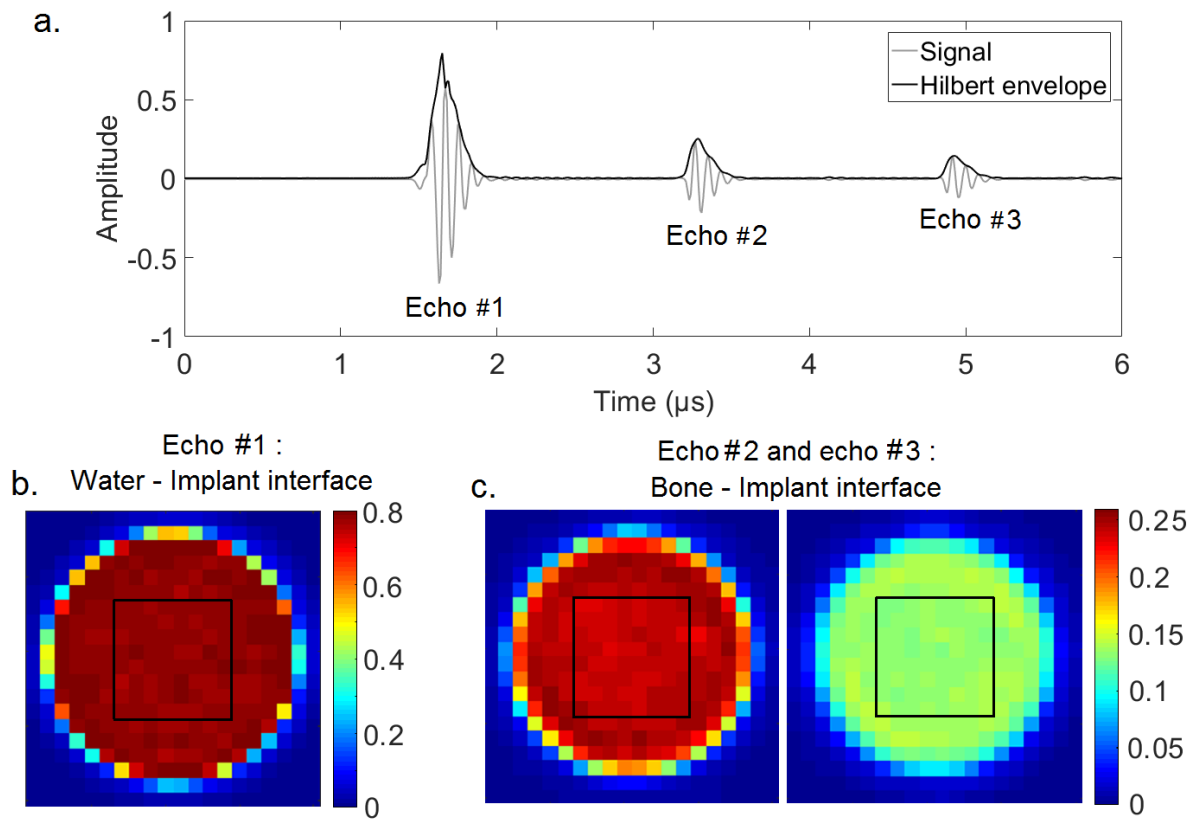


Figure 3.2 – (a) Representation of a radiofrequency signal and of its envelop corresponding to an echo obtained of the coin-shaped implant. Echo #1 (respectively #2) corresponds to the echo of the water-implant interface (respectively the BII). Echo #3 corresponds to the rebound of the ultrasonic wave on the BII, on the implant-water interface and on the BII. (b) 2-D C-scan corresponding to the maximum amplitude of echo #1 in a 20x20 mm spatial window. (c) 2-D C-scans corresponding to the maximum amplitude of echoes #2 and #3 in a 20x20 mm spatial window. The 8x8 mm measurement windows realized to assess R_2 and R_3 are represented by black squares in Fig. 3.2b and 3.2c.

Figure 3.2a shows the three echoes previously described. Figures 3.2b and 3.2c show the 2-D images obtained by plotting the maximum amplitudes $A_{i,1}$, $A_{i,2}$ and $A_{i,3}$ of the RF signals on a 20x20 mm window corresponding to the position of the transducer relatively to the sample in the x-z directions. The chosen window size allows to determine the

position of the coin shaped implant in the plan perpendicular to the transducer axis. However, in the rest of the study, 2-D scans were only performed on 8x8 mm windows centered on the axis of the coin-shaped implant because (i) it allowed to avoid edge effects and (ii) it reduced the time required to obtain each ultrasonic image.

The reproducibility of the ultrasonic measurements was assessed by determining the values obtained for R_k ($k \in 1,2$) for each of the six measurements realized with the same sample with repositioning (see subsection 3.2.3). The reproducibility a_k of the measurement of R_k was defined as the standard deviation obtained for the six corresponding values of R_k . The variation of R_k as a function of σ was interpolated by a continuous function linear by pieces of σ following:

$$\tilde{R}_k(\sigma) = \begin{cases} \lambda_{i,k}\sigma + R_{0,k}, & \text{if } \sigma \leq \sigma_k \\ \lambda_{f,k}(\sigma - \sigma_k) + \lambda_{i,k}\sigma_k + R_{0,k}, & \text{if } \sigma \geq \sigma_k \end{cases} \quad (3.8)$$

where σ_k corresponds to the stress value at which the change of the slope occurs. $\lambda_{i,k}$ (respectively $\lambda_{f,k}$) represents the initial (respectively final) slope of the linear interpolation of $\tilde{R}_k(\sigma)$, and $R_{0,k}$ represents the initial ratio when $\sigma = 0$. Based on the experimental results, a cost function $e_{R,k}(\lambda_{i,k}, \lambda_{f,k}, R_{0,k}, \sigma_k)$ was defined in order to assess the difference between the experimental measurements and values obtained with Eq. 3.8 following:

$$e_{R,k}(\lambda_{i,k}, \lambda_{f,k}, R_{0,k}, \sigma_k) = \sum_{j=1}^N \frac{R_k(j) - \tilde{R}_k(\sigma(j))}{N} \quad (3.9)$$

An optimization procedure based on a conjugate gradient method was carried out in order to determine the optimal values of the parameters $(\lambda_{i,k}, \lambda_{f,k}, R_{0,k}, \sigma_k)$ minimizing the cost function $e_{R,k}$ for each trabecular bone sample.

Eventually, a simple method was derived in order to assess the error made on the estimation of the stress based on the ultrasonic measurement for $\sigma < \sigma_k$. Assuming a linear variation of R_k as a function of σ , the precision on the estimation of the stress $\Delta\sigma_k$ at the BII was defined by the relation:

$$\Delta\sigma_k = a_k \cdot \lambda_{i,k} \quad (3.10)$$

3.3 Results

3.3.1 Neo-hookean behavior of bone

Figure 3.3 shows the variation of $\sigma(\epsilon)$ for bone samples #2 and #15 corresponding to apparent densities of 0.475 g/cm³ and 0.736 g/cm³ respectively. The results illustrate the three regimes of the Neo-Hookean behavior of trabecular bone ($\epsilon < \epsilon_i$, $\epsilon_i < \epsilon < \epsilon_f$ and $\epsilon > \epsilon_f$) described in Section 3.2.5 (see equation 3.4). The errors bars relative to σ and to ϵ correspond to σ^{sd} and ϵ^{sd} , and increase with stress relaxation effects, in particular for $\sigma \geq \sigma_1$.

Table 3.1 shows the average, minimum and maximum values of σ_1 , ϵ_i , ρ and ϵ_f and their standard variations for the 18 bone samples.

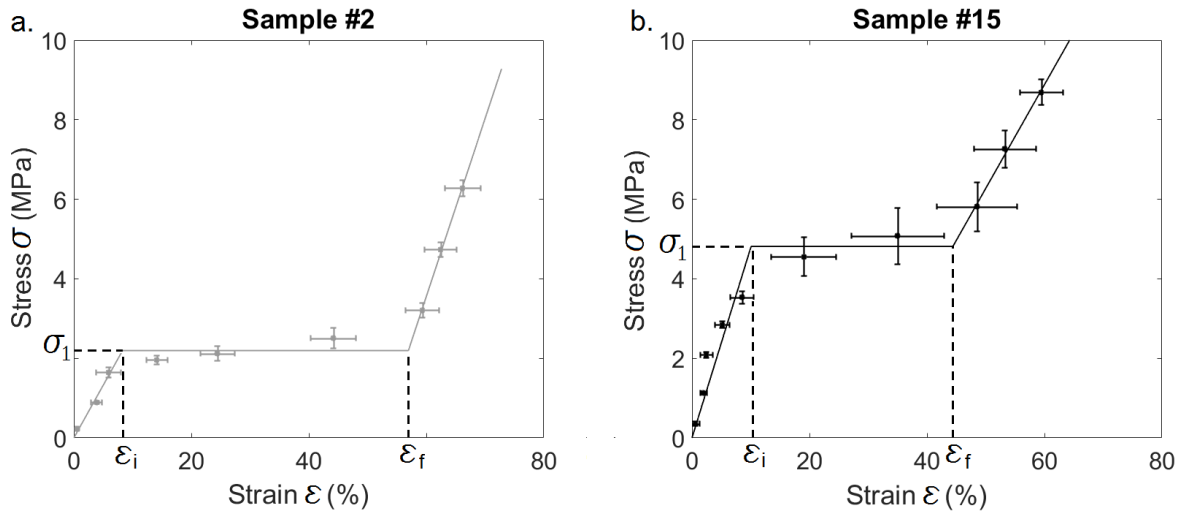


Figure 3.3 – Variation of the stress applied to the bone-implant interface as a function of the strain obtained for bone samples #2 (a) and #15 (b). Parameters σ_1 , ϵ_i and ϵ_f corresponding to the Neo-Hookean behavior of bone tissue are indicated. The solid lines represent the optimal functions $\tilde{\sigma}$ corresponding to each bone sample.

Table 3.1 – Mean, minimum, maximum values and standard variation of parameters σ_1 , ϵ_i and ϵ_f describing the neo-hookean behavior of bone and of the density ρ of samples

Parameter	Mean (\pm SD)	Min	Max
σ_1 (MPa)	4.34(\pm 1.37)	2.19	6.58
ϵ_i	8.8%(\pm 3.1%)	4.6%	17.5%
ϵ_f	46.3%(\pm 14.1%)	18.9%	68.3%
ρ (g.cm ⁻³)	0.661(\pm 0.130)	0.451	0.929

3.3.2 Ultrasonic response of the bone-implant interface

The black (respectively grey) line in Fig. 3.4 shows the variation of R_2 (respectively R_3) as a function of the stress σ applied to the BII for bone samples #2 and #15. The solid lines represent the optimal functions \tilde{R}_2 (respectively \tilde{R}_3) and indicate a change of slope occurring for σ_2 (respectively σ_3). The reproducibility of the ultrasonic measurements was equal to $a_2 = 1.2 \cdot 10^{-3}$ for R_2 and of $a_3 = 8.0 \cdot 10^{-4}$ for R_3 .

Table 3.2 shows the values obtained for the parameters ($\lambda_{i,k}, \lambda_{f,k}, R_{0,k}, \sigma_k$) using the analysis described in subsection 3.2.6 and describing the variation of R_2 and R_3 as a function of σ . For $k \in \{1, 2\}$, the values of $\lambda_{i,k}$ are negative for all bone samples, which indicates that R_2 and R_3 always decrease as a function of σ for $\sigma < \sigma_k$. However, the values of $\lambda_{f,k}$ may be positive or negative depending on the sample, which indicates that no specific behavior was obtained for R_2 and R_3 , which weakly depend on σ for $\sigma > \sigma_k$.

Table 3.2 also shows the results corresponding to the values of $\Delta\sigma_k$. For a given bone sample, $\Delta\sigma_3$ is always lower than $\Delta\sigma_2$, which indicates that considering echo #3 gives a better sensitivity of the ultrasonic response of the BII on variations of stresses compared to considering echo #2. This result may be explained by the fact that echo #3 results

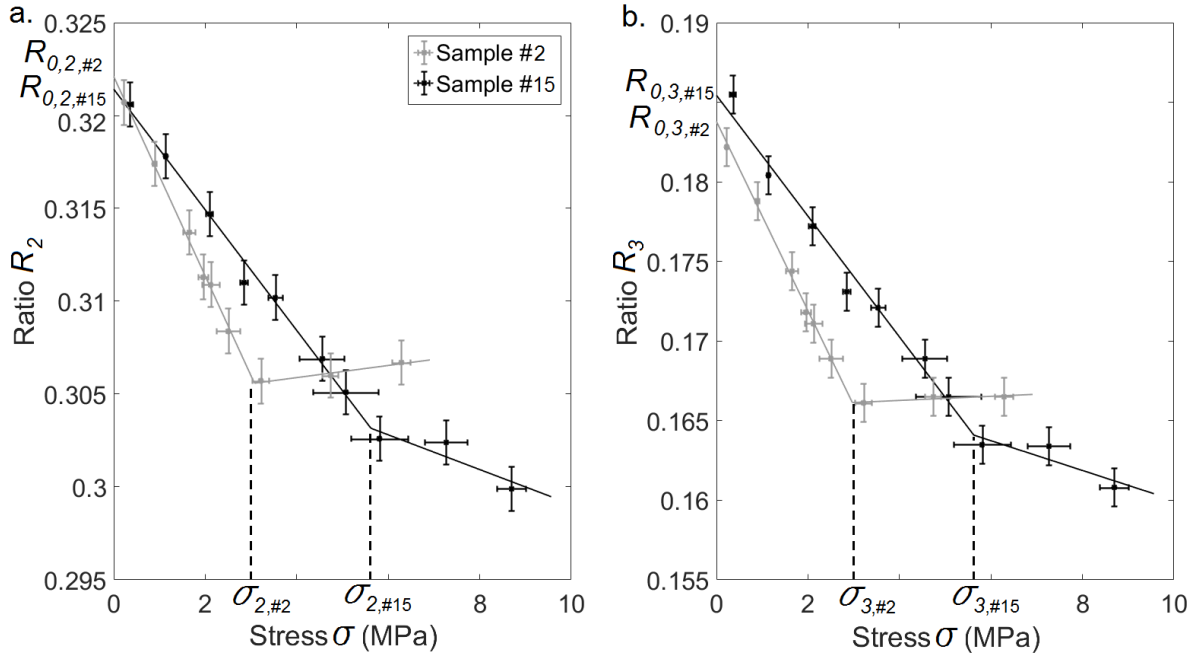


Figure 3.4 – Variation of (a) R_2 and (b) R_3 as a function of the stress σ at the BII for bone samples #2 and #15. Parameters σ_k and $R_{0,k}$ are indicated, subscript # m corresponding to sample # m . Solid lines represent the optimal functions \tilde{R}_2 and \tilde{R}_3 corresponding to each bone sample. $\sigma_{2,\#2}$ and $\sigma_{2,\#15}$ correspond to the values of σ_2 obtained for the samples #2 and 15, respectively. $\sigma_{3,\#2}$ and $\sigma_{3,\#15}$ correspond to the values of σ_3 obtained for the samples #2 and 15, respectively.

Table 3.2 – Mean, minimum and maximum values of the parameters describing the evolution of the ultrasonic ratios.

Parameter	Mean (\pm SD)	Min	Max
$R_{0,2}$	0.323(\pm 0.009)	0.307	0.340
σ_2 (MPa)	5.05(\pm 1.39)	3.05	7.80
$\lambda_{i,2}$ (GPa $^{-1}$)	-4.82(\pm 1.95)	-8.65	-1.24
$\lambda_{f,2}$ (GPa $^{-1}$)	-0.51(\pm 1.29)	-2.35	1.84
$\Delta\sigma_2$ (MPa)	0.633(\pm 0.424)	0.277	1.937
$R_{0,3}$	0.186(\pm 0.009)	0.171	0.203
σ_3 (MPa)	4.90(\pm 1.41)	2.97	7.80
$\lambda_{i,3}$ (GPa $^{-1}$)	-5.46(\pm 1.84)	-9.46	-2.28
$\lambda_{f,3}$ (GPa $^{-1}$)	-0.75(\pm 1.17)	-2.54	1.50
$\Delta\sigma_3$ (MPa)	0.334(\pm 0.141)	0.169	0.701

from two successive reflections of the ultrasonic wave on the BII whereas echo #2 results from a single reflection on the BII.

Figure 3.5a (respectively 3.5b) shows the variation of $\lambda_{i,3}$ as a function of $\lambda_{i,2}$ (respectively $\lambda_{f,3}$ as a function of $\lambda_{f,2}$). The results show that there is a significant correlation

between i) $\lambda_{i,3}$ and $\lambda_{i,2}$ and ii) $\lambda_{f,3}$ and $\lambda_{f,2}$, which indicates that results obtained for echo #2 are consistent with results obtained for echo #3.

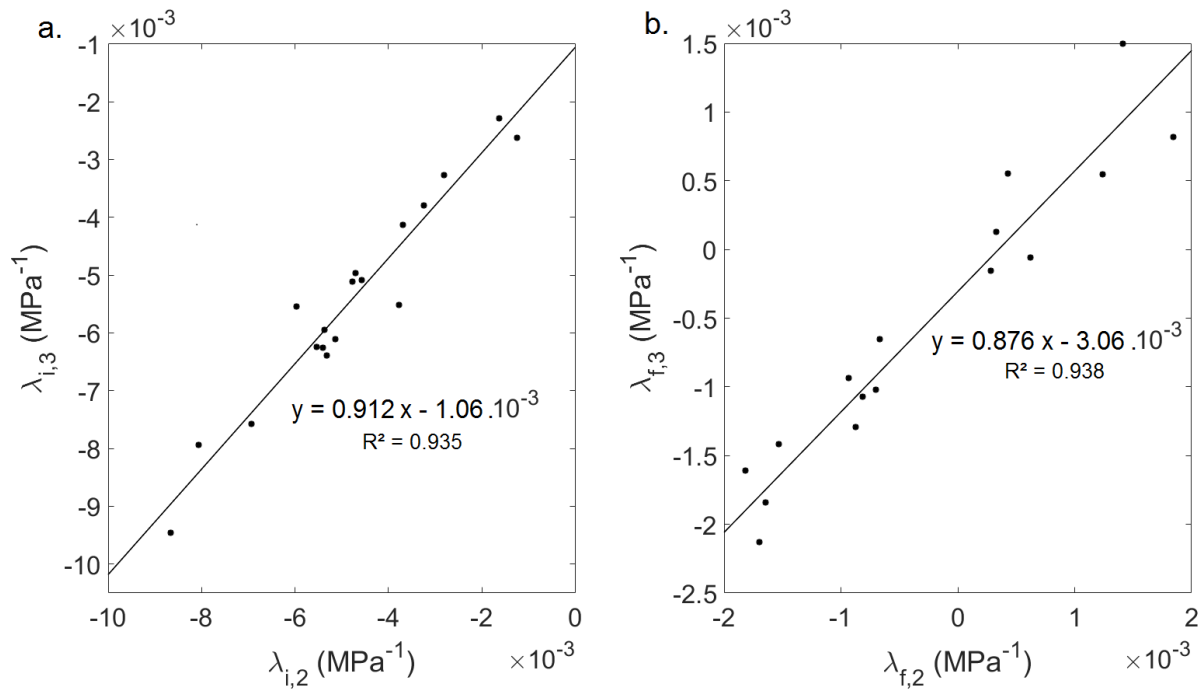


Figure 3.5 – Variations of (a) $\lambda_{i,3}$ as a function of $\lambda_{i,2}$ and (b) $\lambda_{f,3}$ as a function of $\lambda_{f,2}$. The solid lines correspond to linear regression analysis.

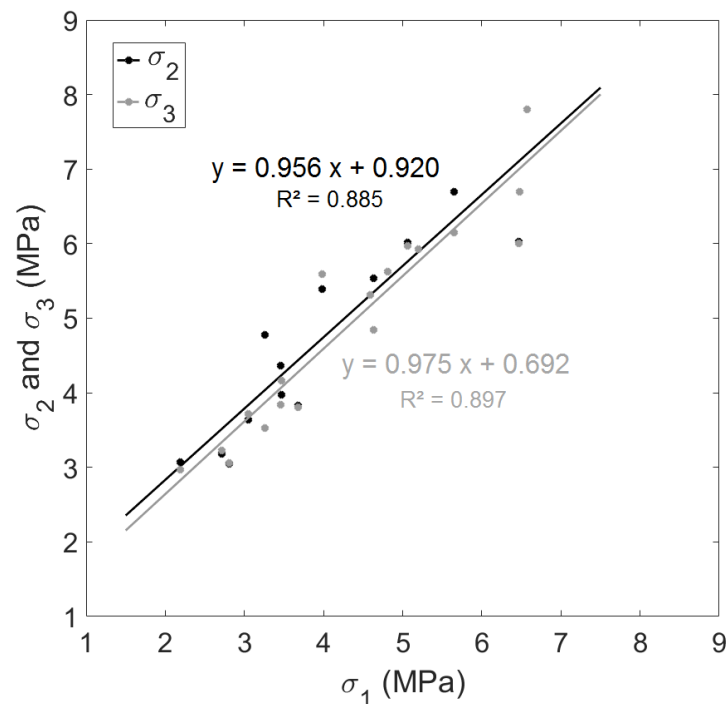


Figure 3.6 – Variation of σ_2 and σ_3 (see Fig. 3.4) as a function of σ_1 (see Fig. 3.3). The solid lines correspond to linear regression analysis.

3.3.3 Relation between mechanical and ultrasonic measurements

Figure 3.6 shows the variation of σ_2 and σ_3 (derived from the ultrasonic measurements, see Eq. 3.8) as a function of σ_1 (derived from the mechanical measurements, see Eq. 3.4). A significant correlation is obtained between σ_1 and σ_2 and between σ_1 and σ_3 , which indicates that the results obtained from ultrasonic measurements are directly related to the mechanical behavior of the BII. Moreover, the results shown in Fig. 3.6 indicate that $\sigma_2 > \sigma_1$ and $\sigma_3 > \sigma_1$ for 17 out of 18 samples.

Figure 3.7 shows the relationship between i) σ_1 , σ_2 and σ_3 and ii) the apparent density ρ of the bone samples. It illustrates that σ_1 , σ_2 and σ_3 tend to increase as a function of ρ .

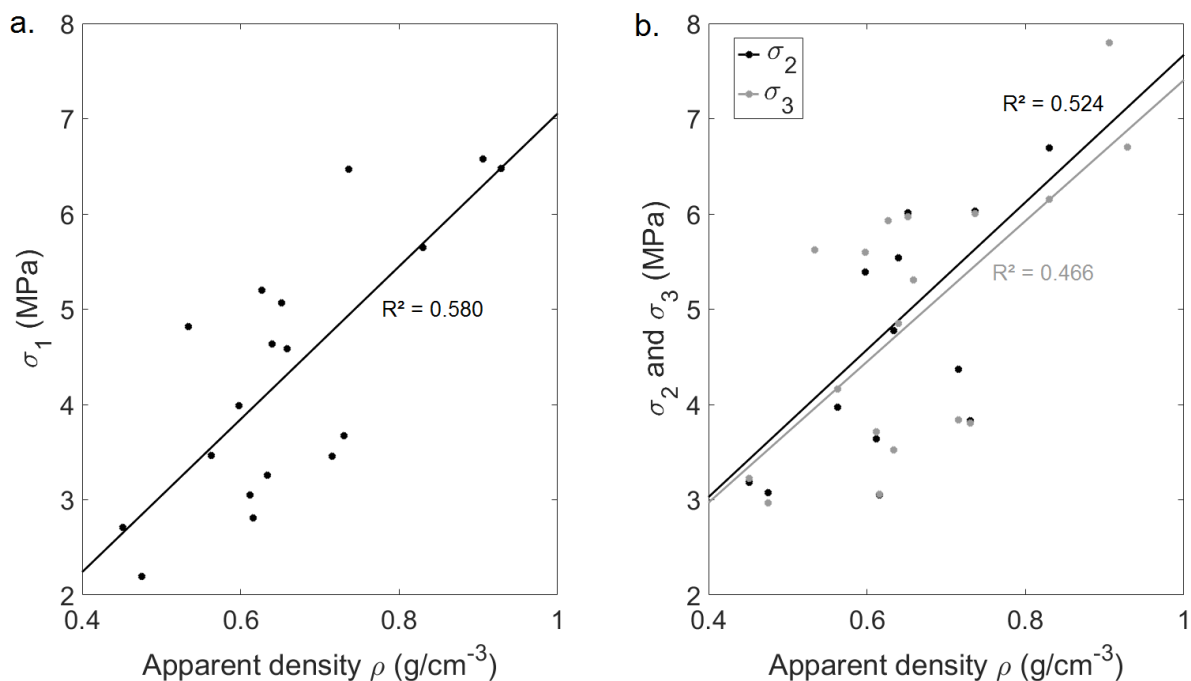


Figure 3.7 – Variation of σ_1 (a) and of σ_2 and σ_3 (b) as a function of the apparent density of the bone samples ρ . The solid lines correspond to linear regression analysis.

3.4 Discussion

3.4.1 Originality and comparison with literature

The originality of the present study is to evidence the dependence of the ultrasonic response of the BII on the compressive stresses applied to this same interface. To do so, a dedicated set up coupling mechanical testing and ultrasound measurements was conceived in order to work under standardized conditions. The results showed a strong elastoacoustic coupling for the behavior of the BII.

Previous studies have shown both numerically [281, 282] and experimentally [276, 280, 283] that the amplitude of the ultrasonic response of the BII decreases as a function of healing time (see Section 2.1). It was explained by a combined effect of the increase of the BIC ratio and of the periprosthetic bone material properties (see Table 2.1), leading to a decrease of the gap of acoustical properties at the BII. These results concerning the effect

of healing time are in agreement with the results obtained herein because an increase of the compressive stresses at the BII is likely to lead to i) an increase of the BIC due to local deformation of bone tissue near the BII and ii) an increase of the bone material properties due to compression. Moreover, in a recent study [284], the amplitude of the ultrasonic response of a dental implant was shown to decrease when the diameter of the hole where the implant was inserted decreased (see Fig. 2.3c), which is also consistent with the results obtained herein under standardized conditions.

The results obtained in the present study could be compared more quantitatively with the experimental results from Mathieu et al. [155] (see Section 2.1.2) focusing on echo #2 of the ultrasonic response of the BII, allowing a comparison with the results found for the variation of R_2 in the present work. Mathieu et al. [155] showed that the reflection coefficient decreased by 7.8% when the BIC increased from around 27% to around 69%, which corresponds to an increase of the BIC equal to 42%. In the present study, bovine trabecular bone had a porosity around 50% [65]. The compression applied by the set up was likely to increase the BIC from around 50% up to a maximum of 100% for very strong compression stresses, and was associated to a decrease of R_2 equal to 7.2% from $\sigma = 0.25$ MPa to $\sigma = \sigma_2$, which is in good agreement with results from Mathieu et al. [155]. Moreover, the precision P on the ultrasonic measurements was equal to 0.011 in Mathieu et al. [155], which is around 10 times higher than the reproducibility obtained in the present study ($a_2 = 1.2 \cdot 10^{-3}$). The significant difference between these 2 values may be explained by the larger diameter of the coin-shaped implants considered herein (20 mm) in comparison to the ones from Mathieu et al. [155] (5 mm), which allowed to take more points of measures for each sample and to avoid edge effects. Moreover, implants from Mathieu et al. [155] were osseointegrated, which implies a higher heterogeneity in the surface conditions at the BII. Therefore, the reflection coefficient was more dependent on the precise position of measures than herein. However, since the complex geometry of real implants may also lead to reproducibility issues, the precision value found in Mathieu et al. [155] might be more representative of real implants.

The results obtained in Table 3.1 indicate that values of σ_1 were comprised between 2.19 MPa and 6.58 MPa, which is in agreement with values found in literature, since typical values of bovine femoral trabecular bone strength when uniaxial stress is applied are comprised between 0.2 MPa and 16 MPa [87, 132].

3.4.2 Physical interpretation of results

Figure 3.6 illustrates that the evolution of the reflection coefficient of the BII as function of the compressive stress is significantly correlated to the mechanical behavior of the bone samples. As shown in Table 3.2, R_2 and R_3 were shown to decrease as a function of σ for $\sigma < \sigma_2$ and for $\sigma < \sigma_3$ respectively, with $\sigma_2 > \sigma_1$ and $\sigma_3 > \sigma_1$ for 94% of bone samples. For $\sigma < \sigma_1$, which corresponds to $\epsilon < \epsilon_i$ (see Fig. 3.3, bone tissue had an elastic behavior, so that the compression led to an elastic deformation of the trabecular network which was pressed onto the implant surface. However, local stresses near the BII may exceed the elastic limit and this compression in the macroscopic elastic regime may lead to an increase of the BIC, explaining the decrease of R_2 and R_3 . Moreover, during the elastic compression ($\sigma < \sigma_1$), the deformation of the trabecular network led to an increasing bone density, which also explains the decrease of R_2 and R_3 because it contributed to a decrease of the gap of acoustical properties at the BII.

Then for $\sigma = \sigma_1$, which corresponds to $\epsilon_i < \epsilon < \epsilon_f$ (see Fig. 3.3), the trabeculae may fracture and the trabecular network progressively collapses [39, 85]. Debris will progressively fill the pores of the trabecular structure, which also results in an increase of the BIC as well as of the apparent bone density of the trabecular sample, leading to a decrease of R_2 and R_3 .

Eventually, for $\sigma > \sigma_1$, which corresponds to $\epsilon > \epsilon_f$ (see Fig. 3.3), the BIC ratio is close to 100% and could not increase anymore because all pores have already been filled. However, the strain increased faster as a function of the stress, so that the bone density and stiffness also increase due to nonlinear effects in bone tissue [85], which contributed to a decrease of R_2 and R_3 . As a consequence, R_2 and R_3 were globally decreasing functions of the stress, and the mean values of $\lambda_{i,k}$ and $\lambda_{f,k}$ were both negative. However, $\lambda_{i,k}$ was always lower than $\lambda_{f,k}$ (see Table 3.2), which indicates that for $\sigma > \sigma_2$ (respectively $\sigma > \sigma_3$), R_2 (respectively R_3) had a lower dependence on σ compared to the elastic regime ($\sigma < \sigma_1$). This last result may be explained by the fact that the increase of the BIC during compression had a higher influence on the ultrasonic response of the BII than the changes of bone mechanical properties.

Figure 3.7a shows that σ_1 increases as a function of the apparent density ρ , which may be explained by the fact that the mechanical strength of the trabecular bone samples increased as a function of density. Note that such result is in good agreement with previous results obtained in the literature [39, 85]. Moreover, Fig. 3.7b shows that σ_2 and σ_3 increased as a function of the apparent density ρ , which may be explained by the fact that σ_2 and σ_3 were positively correlated to σ_1 (see Fig. 3.6).

3.4.3 Limitations

This study has several limitations. First, the error related to the determination of the values of σ can be explained by two phenomena. The first one has been quantified by Table 3.2 and comes from the error made on the ultrasonic measurement for a given sample. The second one arises when different samples are considered and comes from the dispersion of the values of $R_{0,2}$ and $R_{0,3}$ (see Table 3.2), which have standard deviations of $9 \cdot 10^{-3}$. This standard deviation may come from the variability of microstructural properties of the bone directly in contact with the implant, such as porosity or mineral density, which are difficult to estimate. Assuming a linear variation of R_k as a function of σ and given the values of $\lambda_{i,2}$ (respectively of $\lambda_{i,3}$), a decrease of $9 \cdot 10^{-3}$ on the measured value of R_2 (respectively of R_3) would correspond to an increase of the stress applied to the BII of 1.9 MPa (respectively of 1.6 MPa). Therefore, it is difficult to determine the stress applied to the BII directly from the ultrasonic measurements. Second, errors on strain measurements were introduced by stress relaxation effects of bone tissue due to the time necessary to realize the ultrasonic measurements, which should be decreased in future studies. Third, the present study was performed using coin-shaped flat implants in order to work in a standardized environment where the stress distribution is approximately uniform on the BII, which has the advantage of allowing to identify the effect of the compressive stress on the ultrasonic response of the BII.

3.5 Conclusion

This study quantifies the influence of compressive stresses applied to the BII on its ultrasonic response. A significant decrease of the reflection coefficient of the BII as a function of the compressive stress was obtained during the elastic compression of the trabecular bone samples and during the collapse of the trabecular network, with an average slope of -4.82 GPa^{-1} . The results may be explained by an increase of the BIC when trabecular bone is compressed onto the implant as well as by changes of bone material properties. The influence of the compressive stress on the ultrasonic response of the BII is particularly important until a plateau stress corresponding to bone fracture is reached. Future works should focus on studying the effect of the implant surface roughness and on considering clinically used implants since their complex geometry may highly affect the stress distribution. Moreover, the effect of shear stresses should also be investigated.

Part III

Modeling of the reflection of an ultrasonic wave on a rough bone-implant interface

Chapter 4. Sinusoidal description of the bone-implant interface

Contents

4.1	Introduction	58
4.2	Material and methods	58
4.2.1	Description of the problem	58
4.2.2	Parametric study	60
4.2.3	Governing equations	61
4.2.4	Finite element simulation	62
4.2.5	Signal processing	62
4.2.6	Analytical modeling of a planar BII	63
4.2.7	3D modeling of the bone-implant interface	63
4.3	Results	64
4.3.1	Validation of the numerical model	64
4.3.2	Influence of the roughness period L	66
4.3.3	Influence of the soft tissue thickness W	66
4.3.4	Influence of the bone properties	68
4.3.5	Influence of the frequency	68
4.4	Discussion	70
4.4.1	Originality and comparison with literature	70
4.4.2	Comparison between 2-D and 3-D models	71
4.4.3	Physical interpretation of the results in the microscopic case	72
4.4.4	Physical interpretation of the results in the macroscopic case	72
4.4.5	Variations of bone material properties	75
4.4.6	Frequency variations	75
4.4.7	Sinusoidal approximation of the implant roughness	76
4.4.8	Limitations	77

4.1 Introduction

An *in vitro* approach was presented in Chapter 3 to investigate the characterization of the BII with QUS. However, one of the major difficulties when considering the characterization and the stimulation of the BII using ultrasound lies in the possibility to accurately control the different parameters influencing the interaction between an ultrasonic wave and the rough BII. Moreover, these parameters may vary simultaneously. Therefore, acoustical modeling and numerical simulation is the only way to gain further knowledge on the understanding of the interaction between an ultrasonic wave and the BII.

As detailed in Chapter 2 (see subsection 2.1.4), several approaches have been proposed to model the ultrasonic propagation in bone-implant systems. However, all the aforementioned approaches considered a fully bounded BII and did not account for the effect of surface roughness. Osseointegration was considered only through variations of the biomechanical properties of periprosthetic bone tissue and the influence of the BIC ratio could therefore not be taken into account. The main difficulty lies i) in the roughness of the implant surface, ii) in the multiphase description of the periprosthetic bone tissue, iii) in the multiscale nature of the problem and iv) in the time dependence of bone properties.

Different approaches have also been developed to simulate the interaction of an elastic wave with rough interfaces, in particular in the context of geological applications and non-destructive testing [16, 182]. Studies have considered the simplified case of spatially periodic interfaces [73, 74] and of random interface profiles [21, 22, 143, 212] to assess the propagation of an ultrasonic wave at an interface. However, such methods have never been applied in the literature to the BII.

The aim of this chapter is to model the interaction between an ultrasonic wave and the rough BII, which is described by a sinusoidal function. To do so, a 2-D finite element model of time domain transient wave propagation was developed. Different parametric studies were performed considering variations of the roughness parameters of the interface, of the wave frequency and of the properties of the periprosthetic bone tissue, including the presence of a soft tissue layer whose thickness was progressively decreased in order to simulate osseointegration phenomena. Namely, the dependence of the reflection coefficient of an incident plane compression wave emitted from implant domain in a direction perpendicular to the interface was determined as a function of the aforementioned parameters.

The main part of the work presented in this chapter was published in the *Journal of Acoustical Society of America* [101]. The comparison between 2-D and 3-D finite element models developed in Sections 4.2.7, 4.3.1 and 4.4.2 was published in the *JASA Express Letters* [104].

4.2 Material and methods

4.2.1 Description of the problem

Two coupled 2-dimensional half-spaces separated from each other by an irregular interface were considered, which corresponds to an interphase. The first one represents an implant made of titanium alloy (Ti-6Al-4V) and the other one represents cortical bone tissue, as shown in Fig. 4.1a.

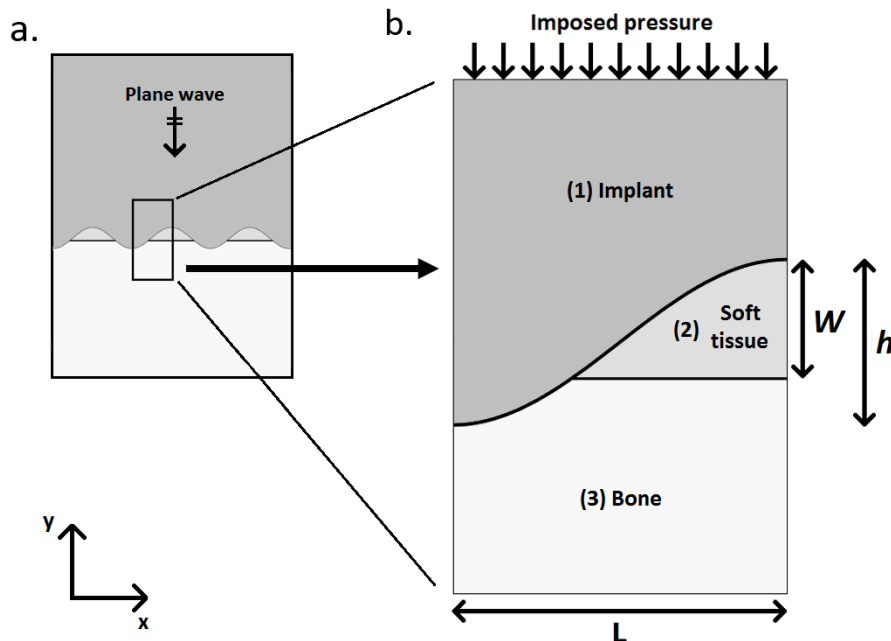


Figure 4.1 – Schematic illustrations of (a) the geometrical configuration of the bone-implant interface considered and (b) the 2-D model used in the numerical simulations.

The implant surface roughness was modeled by a sinusoidal function of amplitude h and half-period L , which corresponds to a simple situation that will be discussed in subsection 4.4.7.

The description of the interface roughness can be considered at two different scales. The first scale, denoted by “microscopic roughness” in what follows, corresponds to variations of the surface roughness amplitude h comprised between 0 and 25 μm , while the second scale, denoted by “macroscopic roughness”, corresponds to variations of h comprised between 100 μm and 1 mm. The microscopic roughness corresponds to implant surface roughness usually obtained by sandblasting and/or acid etching [257] and aims at improving osseointegration [139, 199]. The macroscopic roughness corresponds to the implant geometry, in particular threading, for instance for dental implants or pedicle screws.

Due to the symmetry of the problem, a simplified model described in Fig. 4.1b was introduced. Only a single half-sine period of the interface was considered, which is sufficient to simulate the propagation of the acoustic wave using symmetrical boundary conditions in the interfaces perpendicular to the direction x . The point of origin of the model was defined as the middle of the half-sine. As shown in Fig. 4.1, a soft tissue layer was considered between bone and the implant in order to model non-mineralized fibrous tissue that may be present at the BII in the case of non-osseointegrated implants [98, 177] or just after surgery. The thickness W of the soft tissue layer is likely to decrease when osseointegration processes increase at the implant interface. Figure 4.1 shows a configuration where $W < h$. Note that the case $W > h$, corresponding to non-contact between bone and the implant, was also studied since such situation may occur locally, for example in the case of coin-shaped implants developed in previous studies [155, 276].

The acoustical source is modeled as a broadband ultrasonic pulse with a uniform

pressure $p(t)$ applied at the top surface of the implant domain (see Fig. 4.1b) defined by:

$$p(t) = Ae^{-4(f_c t - 1)^2} \sin(2\pi f_c t) \quad (4.1)$$

where A is an arbitrary constant (all computations are linear) representing the signal amplitude and f_c is its central frequency, which may vary between 1 and 15 MHz according to the situation. The total lengths of the implant and of the bone domain, denoted H_{ti} and H_b respectively were chosen to be able to distinguish the signal reflected from the interface and to avoid any reflection from the boundary of the simulation domain. Namely a value of $H_{ti} = H_b = 7.5$ cm was chosen throughout the study. All media considered in this model were assumed to have homogeneous isotropic mechanical properties. The values used in the present study for the different media are shown in Table 4.1.

Table 4.1 – Material properties used in the numerical simulations.

	C_p (m.s ⁻¹)	C_s (m.s ⁻¹)	ρ (kg.m ⁻³)
Soft tissue	1500	10	1000
Titanium	5810 ^a	3115 ^a	4420 ^a
Cortical bone tissue	4000	1800	1850 ^b

^a : See Pattijn et al. [210, 211]. ^b : See Haiat et al. [94], Njeh et al. [195].

4.2.2 Parametric study

A parametric study was carried out to investigate the dependence of the ultrasound response of the considered system characterized via the reflection coefficient. Variations of the following parameters were taken into account and described below: (1) the interface roughness parameters h and L , (2) the thickness of the soft tissue layer W , (3) the bone properties C_p , C_s and ρ (corresponding to the longitudinal velocity, shear velocity and mass density respectively) and (4) the center frequency f_c of the emitted wave.

Interface properties

Table 4.2 describes the range of variation and the reference value considered for the values of h and L in order to simulate the microscopic and macroscopic roughness. The values obtained for the microscopic roughness were obtained based on [139, 199, 257], while the values obtained for the macroscopic roughness were chosen arbitrarily based on typical dental implant geometry.

Thickness of the soft tissue layer

The thickness W of the layer of fibrous tissue located between bone tissue and the implant surface was assumed to decrease during osseointegration phenomena. In the case of microscopic studies, W was assumed to vary between 0 and 500 μm according to the configuration and to the frequency, while for macroscopic studies, the range of variation of W is $[0; 1.5 h]$. Note that for clarity issues, the results obtained in the macroscopic case were plotted as a function of the ratio W/h . The value $W/h = 0$ corresponds to a

Table 4.2 – Range of variation and reference values of the geometrical parameters used in the numerical simulations.

	Microscopic roughness	Macroscopic roughness
Surface roughness amplitude h:		
Range of variation	[0; 25 μm]	[100 μm ; 1 mm]
Reference value	5 μm	360 μm
Surface roughness half-period L:		
Range of variation	[10; 300 μm]	[50 μm ; 2 mm]
Reference value	50 μm	900 μm
Soft tissue thickness W:		
Range of variation	[0; 500 μm]	[0; 1.5 h]

perfectly bounded interface, while $W/h = 1$ represents the limit above which no contact occurs between bone and the implant.

Bone properties

The periprosthetic bone biomechanical properties are known to vary as a function of healing time (see Section 2.1.1). Therefore, the values of C_p , C_s and ρ were modified in order to assess the effects of osseointegration on the ultrasonic response of the BII. The values of C_p , C_s and ρ were modified by considering an increase and a decrease of 20% compared to their reference values indicated in Table 4.1, similarly to what was done in previous studies [281, 282].

Frequency

The value of the center frequency f_c of the emitted signal was varied between 1 MHz and 15 MHz and the reference value of f_c was set to 10 MHz because it corresponds to the value used in the medical device under development by my research group (see Section 2.1).

4.2.3 Governing equations

As mentioned above, three subdomains were considered with different materials: (1) titanium implant, (2) soft tissues, and (3) cortical bone. The dynamic equations of wave propagation were solved in each subdomain (i) and reads:

$$\rho^{(i)} \mathbf{u}^{(i)} - \text{div}(\boldsymbol{\sigma}^{(i)}) = \mathbf{0} \quad (4.2)$$

where ρ is the mass density, \mathbf{u} is the displacement vector and $\boldsymbol{\sigma}$ is the stress tensor in the subdomain (i). The constitutive relation using Hooke's laws is given by:

$$\boldsymbol{\sigma}^{(i)} = \lambda^{(i)} \text{tr}(\boldsymbol{\epsilon}^{(i)}) \mathbf{I} + 2\mu^{(i)} \boldsymbol{\epsilon}^{(i)} \quad (4.3)$$

where $\boldsymbol{\epsilon}$ is the strain tensor in the subdomain (i) and $(\lambda^{(i)}, \mu^{(i)})$ are the Lamé parameters in the subdomain (i) corresponding to respective values of (ρ, C_p, C_s) listed in Table

4.1. At both interfaces (1) - (2) and (2) - (3), the continuity of displacement and stress fields leads to the following boundary conditions at interface (i-j):

$$\begin{cases} \mathbf{u}^{(i)} = \mathbf{u}^{(j)} \\ \boldsymbol{\sigma}^{(i)}\mathbf{n} = \boldsymbol{\sigma}^{(j)}\mathbf{n} \end{cases} \quad (4.4)$$

where $i, j = 1, 2, 1, 3$ or $2, 3$ and \mathbf{n} is the unitary vector normal to the interface. At the top boundary of the implant domain (see Fig. 4.1b), a uniform pressure $p(t)$ is imposed to model the ultrasound generation from the acoustical source:

$$\boldsymbol{\sigma}^{(1)}\mathbf{n} = -p(t)\mathbf{n} \quad (4.5)$$

At the bottom boundary $y = -H_b$ of the bone domain (see Fig. 4.1b), which is supposed to be sufficiently large so that reflected waves on the bottom boundary of the model may be neglected, a fixed boundary is imposed:

$$\mathbf{u}^{(3)} = \mathbf{0} \quad (4.6)$$

The symmetry conditions also impose that $u_x = 0$ at the lateral surfaces $x = -L/2$ and $x = L/2$.

4.2.4 Finite element simulation

The system of dynamic equations was solved in the time domain using the commercial finite element software COMSOL Multiphysics (Stockholm, Sweden), which had been successfully employed in several studies in the context of bone quantitative ultrasound [91, 93, 183, 281, 282]. The implicit direct time integration generalized- α scheme [46] was used to calculate the transient response of the system.

The elements size was chosen equal to $\lambda_{min}/10$, where $\lambda_{min} = C_{p,min} / f_c$ corresponds to the shortest wavelength in the simulation subdomain and $C_{p,min}$ is the velocity of P-waves in soft tissues. The implant and bone subdomains were meshed by structured quadrangular quadratic elements, and the soft tissue subdomain was meshed with triangular quadratic elements.

The time step was chosen using the stability Courant–Friedrichs–Lewy (CFL) condition $\Delta t \leq \alpha \min(h_e/c)$ where $\alpha = 1/\sqrt{2}$, h_e is the elements size and c is the velocity in the considered subdomain. For simulations presented here, the time step is set at $\Delta t = 4.10^{-3}/f_c$. The duration of the simulations was equal to $1.5 \mu\text{s}$ for $f_c = 10 \text{ MHz}$ and $15 \mu\text{s}$ for $f_c = 1 \text{ MHz}$, respectively.

4.2.5 Signal processing

The reflection coefficient was determined for each simulated configuration. To do so, the signal representing the displacement along the direction of propagation was averaged along an horizontal line located at the top of the titanium implant. Two signals were compared to determine the reflection coefficient r . The first signal corresponds to the averaged simulated incident signal, noted $s_i(t)$. The second signal corresponds to the averaged simulated reflected signal, noted $s_r(t)$. The moduli of the Hilbert's transform of $s_i(t)$ and $s_r(t)$ were computed, and the maximum amplitudes of these envelopes are noted A_i and A_r , respectively. The reflection coefficient in amplitude is determined by:

$$r = A_r/A_i \quad (4.7)$$

4.2.6 Analytical modeling of a planar BII

An analytical model was developed in order to validate the numerical model in the case of a planar BII (*i.e.* with no implant roughness), which corresponds to a 1-D configuration model with respect to x due to the symmetry of the problem. In the analytical model, the time-domain solution was determined in a similar way as what had been done in a previous paper [193]. The wave propagation equations were first transformed into the Laplace domain using the Laplace transform with respect to time. The equations were then solved considering the boundary conditions described in Eqs 4.4 - 4.6. The velocity field obtained was finally transformed back into the time domain by using the inverse Laplace transform. The reflection coefficient was determined by using Hilbert transforms, following the description given in subsection 4.2.5.

4.2.7 3D modeling of the bone-implant interface

A 3D model was developed in order to validate the 2-D approximation made in this study and is represented in Figure 4.2. In the 3D case, the implant surface roughness was modeled by a bi-sinusoidal function $f(x,y)$ of amplitude h and half-period L given by:

$$f(x,y) = \frac{h}{2} \sin\left(\frac{\pi x}{L}\right) \sin\left(\frac{\pi y}{L}\right) \quad (4.8)$$

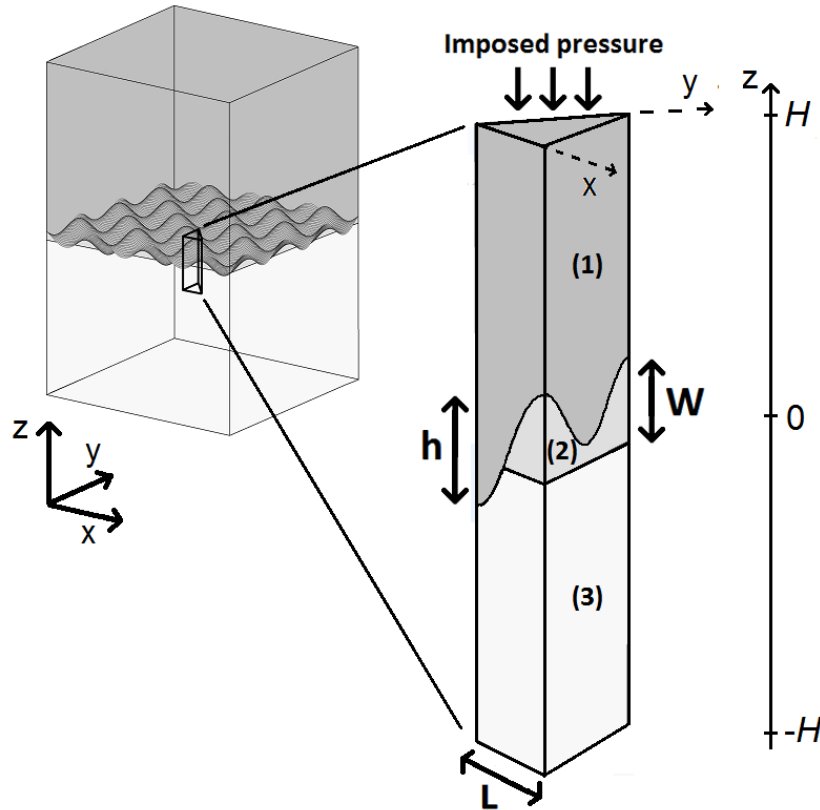


Figure 4.2 – Schematic illustrations of the geometrical configuration of the bone-implant interface and of the 3D model used in numerical simulations.

Due to the symmetry of the problem, 3-D simulations were performed on a triangular prism corresponding to a single half-sine period of the interface, *i.e.* for $x \in [(-L)/2; L/2]$ and $y \in [-L/2; x]$ as represented in Fig. 4.2. Symmetrical boundary conditions were applied to the surfaces parallel to the direction z by imposing zero displacements following the normal direction of the lateral surfaces. Signal processing was realized similarly as for the 2-D model (see subsection 4.2.4), except that signals were obtained by averaging the vertical displacements on a surface perpendicular to the direction of propagation instead of along an horizontal line. Finite element simulation was performed identically as for the 2-D model (see subsection 4.2.5), except that all the domains were meshed with tetrahedral quadratic elements.

The comparison between the reflection coefficients obtained with the 2-D and 3-D models was realized based on the difference of the reflection coefficients computed for a set of parameters composed of 10 values of h , 4 values of L and 14 values of W , which are listed in Table 4.3.

Table 4.3 – Values of the geometrical parameters used in the numerical simulations.

	Values considered
Roughness amplitude h (μm)	{1; 3; 5; 10; 15; 20; 25; 30; 40; 50}
Roughness half-period L (μm)	{50; 70; 80; 90}
Soft tissue thickness W (μm)	{0; 2; 5; 10; 15; 20; 25; 30; 40; 50; 60; 70; 80; 100}

For each combination of surface roughness amplitude h_i ($i \in [1,10]$) and half-period L_j ($j \in [1,4]$), the reflection coefficient $r(i,j,k)$ (resp. $r_{3D}(i,j,k)$) was determined for $W = W_k$, $k \in [1,14]$ with the 2-D model (resp. with the 3-D model). An error function $e(h_i, L_j)$ was defined in order to assess the difference between the ultrasonic response of the 2-D and 3-D models following:

$$e(h_i, L_j) = \sum_{k=1}^{14} \frac{|r(i, j, k) - r_{3D}(i, j, k)|}{14} \quad (4.9)$$

4.3 Results

4.3.1 Validation of the numerical model

Analytical model

Figure 4.3 shows the variation of the reflection coefficient as a function of the soft tissue thickness W for a planar BII for $f_c = 10$ MHz using the numerical and the analytical models described in subsection 4.2.1 and 4.2.6 respectively. The maximum relative error between the analytical and numerical results was equal to 0.24% when the soft tissue thickness varies from 0 to 300 μm and when the frequency varies from 2 MHz to 10 MHz. These results constitute a validation of the numerical model described in section 4.2.

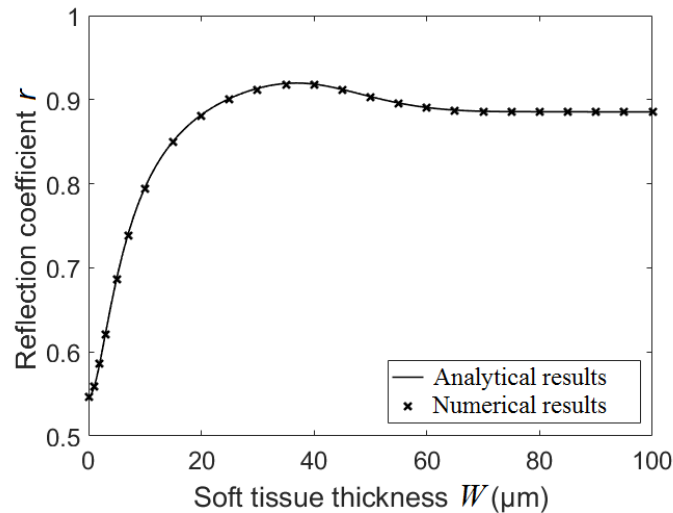


Figure 4.3 – Variation of the reflection coefficient r for $f_c = 10$ MHz as function of the soft tissue thickness W obtained with the analytical (solid line) and numerical models (crosses) in the case of a planar bone-implant interface.

Comparison between 2-D and 3-D models

Figure 4.4 shows the variation of the reflection coefficients r and r_{3D} obtained respectively for the 2-D and the 3-D models as a function of the soft tissue thickness W for different values of h . The dependence of r and r_{3D} with respect to W is qualitatively similar for all values of h . However, the difference between r and r_{3D} increases when h increases.

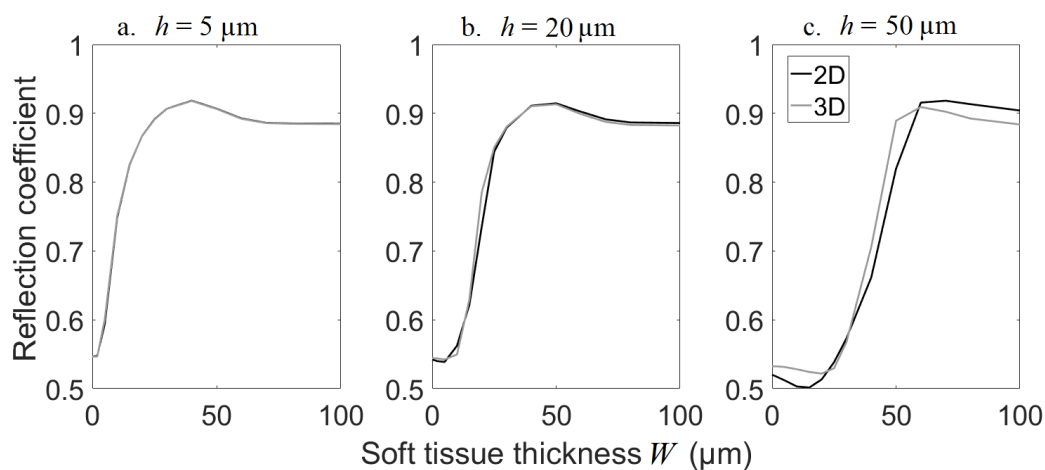


Figure 4.4 – Variation of the reflection coefficients r and r_{3D} of the bone-implant interface as a function of the soft tissue thickness W for roughness parameters $L = 50$ μm and (a) $h = 5$ μm , (b) $h = 20$ μm and (c) $h = 50$ μm .

Figure 4.5 shows the variation of the error function e as a function of h for different values of L . The results further highlight the previous observations since e increases as a function of h for all values of L . Moreover, except for values of h/L relatively close to 1, e increases as a function of L . In all cases, the value of e within the considered

range of geometrical parameters is always lower than 0.03, which corresponds to the case $L = 90 \mu\text{m}$ and $h = 50 \mu\text{m}$ (see Fig. 4.5).

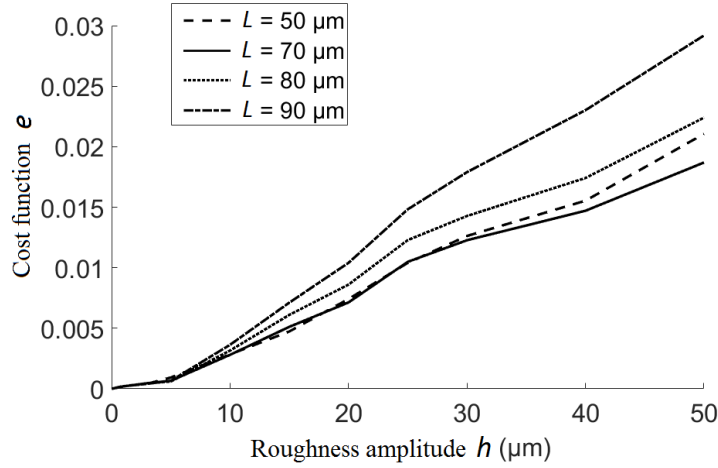


Figure 4.5 – Variation of the error function e as a function of the roughness height h for different values of roughness half-period L .

4.3.2 Influence of the roughness period L

Figure 4.6 shows the variation of the reflection coefficient r for $f_c = 10$ MHz as a function of L and h in the case of an absence of soft tissue at the BII ($W = 0$), which corresponds to a full osseointegration. All bone properties were taken equal to their reference value.

Microscopic roughness

Figure 4.6a shows the variations of r in the microscopic case as a function of L and for different values of h comprised between 0 and $25 \mu\text{m}$. The values of r are shown to slightly decrease as a function of h , while r weakly varies as a function of L .

Macroscopic roughness

Figure 4.6b shows the variation of r in the macroscopic case as a function of L for different values of h comprised between $100 \mu\text{m}$ and 1 mm . When $L \geq 1.5 h$, the reflection coefficient r does not depend on L and its value increases as a function of h . However, when $L \leq h$, the reflection coefficient r oscillates as a function of L , which will be discussed in subsection 4.4.4.

4.3.3 Influence of the soft tissue thickness W

Figure 4.7 shows the variation of the reflection coefficient r for a frequency $f_c = 10$ MHz as a function of W and h for fixed values of L , equal to $50 \mu\text{m}$ (respectively $900 \mu\text{m}$) in the microscopic (respectively macroscopic) case. All bone properties were taken equal to their reference value.

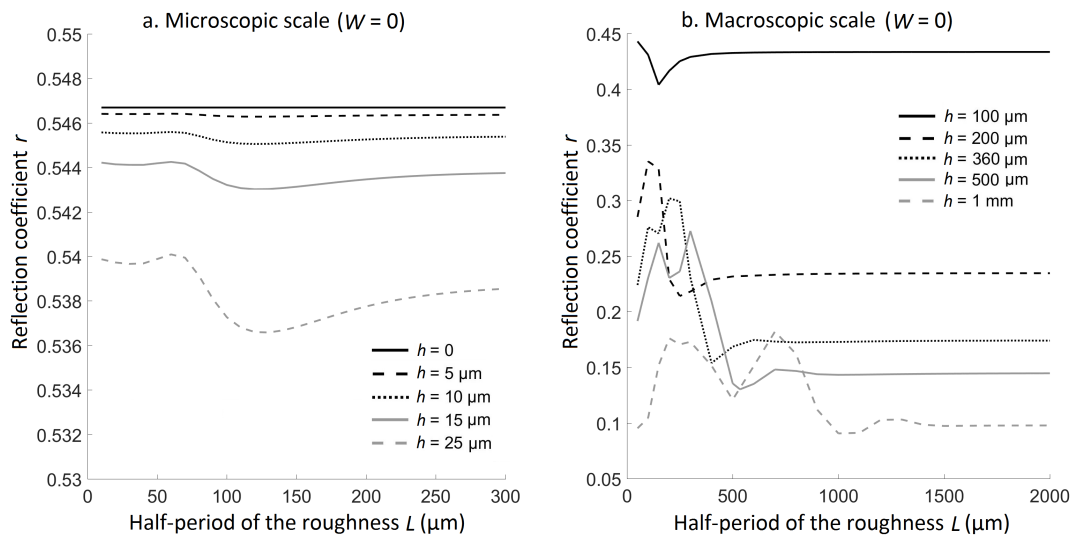


Figure 4.6 – Variation of the reflection coefficient r as function of the roughness parameters h and L for $f_c = 10$ MHz in the microscopic (a) and macroscopic (b) cases.

Microscopic roughness

Figure 4.7a shows the variation of r as a function of the soft tissue thickness W for different values of microscopic roughness amplitudes h , while L was taken equal to 50 μm . The results obtained for the different values of h are qualitatively comparable since r first increases as a function of W from 0.55 to a maximum value equal to 0.92 . Then, r slightly decreases as a function of W and tends towards 0.88 for all values of h . However, the increase of r occurs for smaller values of W when considering lower values of h . Similarly, the maximum value of the reflection coefficient is reached for lower values of W when considering surfaces with lower values of h . Note that the values of the reflection coefficient obtained for $W = 0$ (respectively for $W = 100$ μm) correspond to values obtained for a planar bone-implant interface (respectively soft tissue-implant interface), since the microscopic roughness weakly influences the value of the reflection coefficient, as shown in Fig. 4.6a.

Macroscopic roughness

Figure 4.7b shows the variation of r as a function of the ratio W/h in the case of macroscopic roughness for different values of h , comprised between 100 μm and 1 mm. The reflection coefficient r is shown to increase as a function of W/h for all values of h . More specifically, for $h \leq 500$ μm , r increases as a function of W and then tends towards constant values above $W/h = 1.1$. Note that $W/h = 1$ corresponds to the limit case where there is no more contact between the bone and the implant. Moreover, the values of r obtained for $W/h = 0$ and for $W/h = 1.5$ depend on the surface roughness amplitude h , which is a different situation compared to the results obtained for the microscopic roughness (see Fig. 4.7a). When $h \leq 500$ μm , the reflection coefficient obtained for each value W/h is shown to decrease when h increases. However, the results obtained in the case of $h = 1$ mm are qualitatively different compared to the results obtained for lower values of h . In particular, the reflection coefficient continues to increase when $W/h > 1$,

which will be discussed in section 4.4.4.

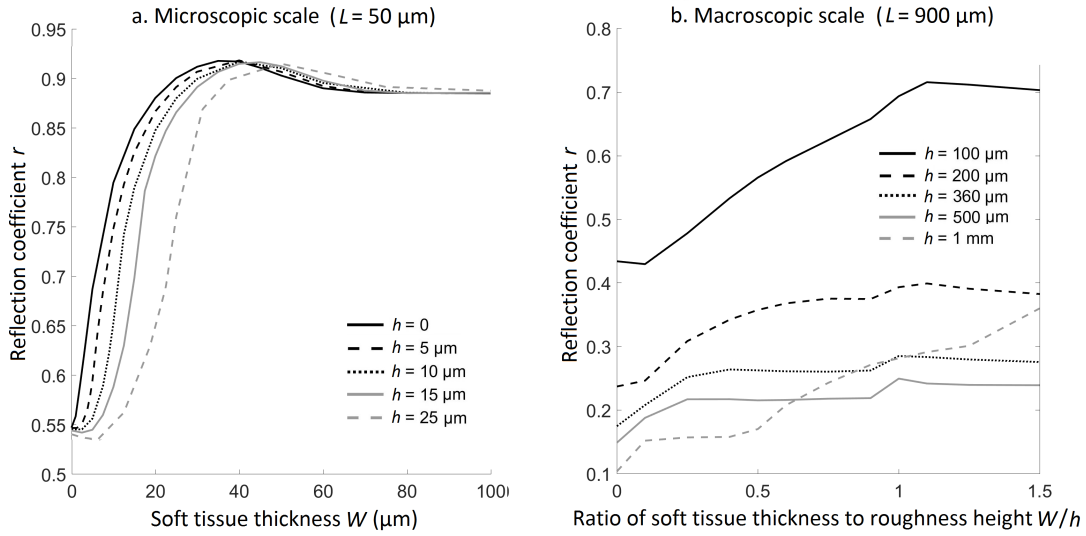


Figure 4.7 – Variation of the reflection coefficient r for $f_c = 10$ MHz and for different values of the roughness amplitude h as function of (a) the soft tissue thickness W in the microscopic case and (b) the ratio of the soft tissue thickness W and of the roughness amplitude h in the macroscopic case.

4.3.4 Influence of the bone properties

Figure 4.8a (respectively 4.8b) shows the relative variation of r when varying the bone properties (C_p , C_s and ρ) compared to their reference values (see Table 4.1) in the case of the microscopic (respectively macroscopic) roughness. The results are shown as a function of the soft tissue thickness W (respectively the ratio W/h) in the case of the microscopic (respectively macroscopic) roughness. Note that a variation of $\pm 20\%$ of C_p leads to almost the same variation of r than a variation of $\pm 20\%$ of ρ . Figure 4.8 shows that r decreases when ρ and C_p increase, while r weakly depends on the transverse wave velocity of bone tissue C_s . Moreover, r depends on C_p and ρ only for $W < 10 \mu\text{m}$ in the microscopic roughness case and for $W/h < 0.25$ in the macroscopic case.

4.3.5 Influence of the frequency

Figure 4.9 shows the variation of the reflection coefficient r for different values of f_c as a function of the product $k \cdot W$ (respectively of W/h) for constant values of $h = 5 \mu\text{m}$ and $L = 50 \mu\text{m}$ (respectively $h = 360 \mu\text{m}$ and $L = 900 \mu\text{m}$) in the microscopic (respectively macroscopic) case, with $k = 2\pi f_c / C_{p,ti}$ representing the wavenumber of the ultrasonic wave in titanium and $C_{p,ti}$ being the velocity of P-waves in the implant. All bone properties were taken equal to their reference value.

Figure 4.9a shows that the results obtained for the different values of f_c in the microscopic case are qualitatively comparable since the slope, the minima and the maxima of the curve representing the variation of r as a function of $k \cdot W$ are the same for all values of f_c . Moreover, two regimes of operation may be distinguished. When $k \cdot W < 1$,

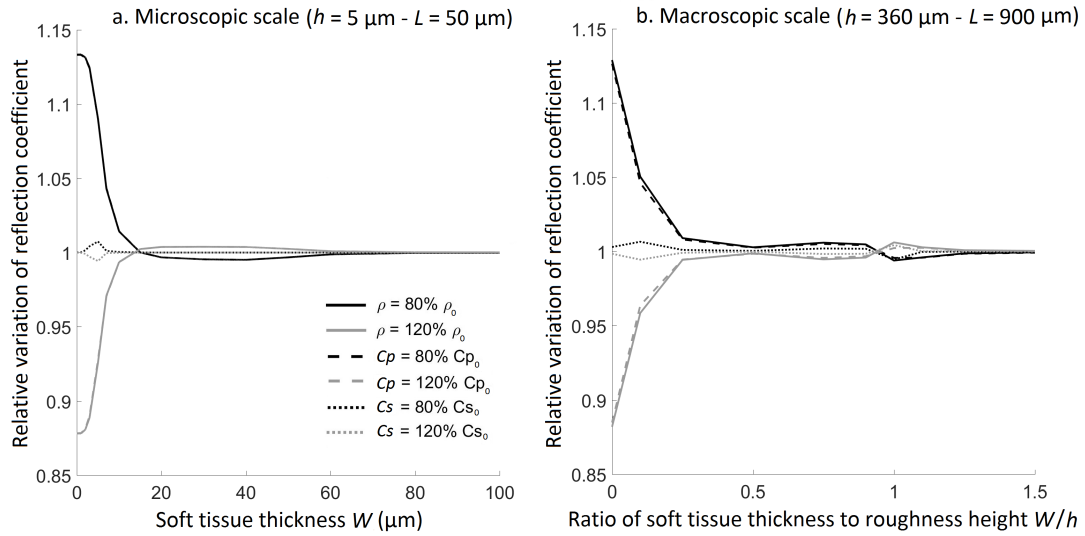


Figure 4.8 – Relative variation of the reflection coefficient r for $f_c = 10$ MHz as function of (a) the soft tissue thickness W in the microscopic case ($h = 5 \mu\text{m}$, $L = 50 \mu\text{m}$) and (b) the ratio of the soft tissue thickness W and of the roughness amplitude h in the macroscopic case ($h = 360 \mu\text{m}$, $L = 900 \mu\text{m}$) corresponding to relative variations of $\pm 20\%$ of the bone properties (C_p , C_s and ρ)

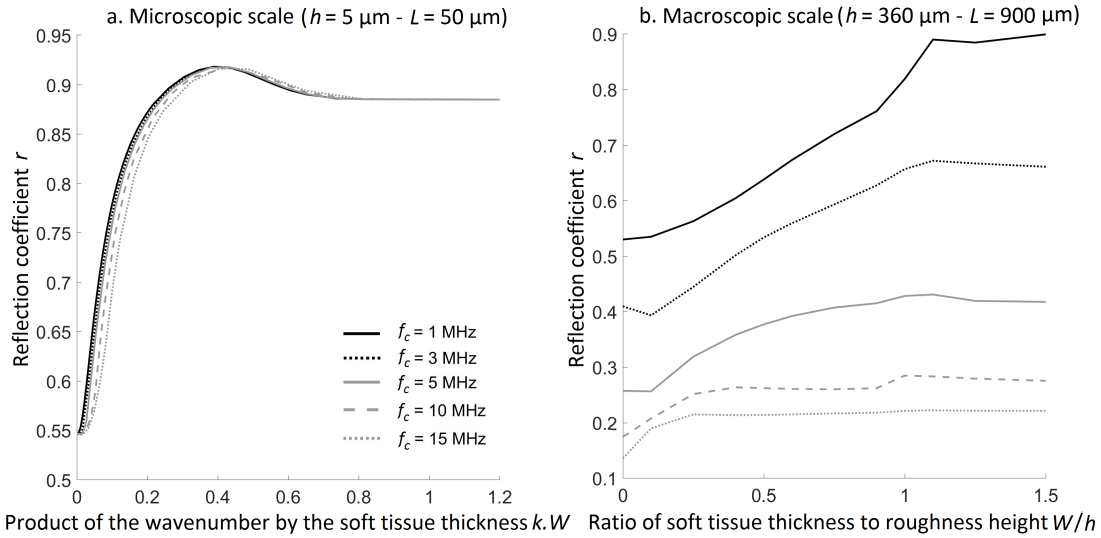


Figure 4.9 – Variation of the reflection coefficient r as function of (a) the product of the wavenumber k by the soft tissue thickness W in the microscopic case ($h = 5 \mu\text{m}$, $L = 50 \mu\text{m}$) and (b) the ratio of the soft tissue thickness W and of the roughness amplitude h in the macroscopic case ($h = 360 \mu\text{m}$, $L = 900 \mu\text{m}$) for different values of f_c .

r increases as a function of $k.W$ from 0.55 to a maximum value equal to 0.92, and then slightly decreases as a function of $k.W$ to tend towards 0.88 for all values of f_c . However, when $k.W \geq 1$, r does not depend on W nor on f_c . These two regimes will be further discussed in section 4.4.6. Figure 4.9b shows that r increases as a function of W/h for all frequencies and then reaches a maximum value that is a decreasing function of the frequency. Moreover, r is a decreasing function of the frequency for each value of W/h .

4.4 Discussion

4.4.1 Originality and comparison with literature

The originality of the present study is to analyze the effect of variations of periprosthetic bone properties and of the implant surface properties on the ultrasonic response of the BII in the cases of microscopic and macroscopic roughness. As illustrated in Fig. 4.6, 4.7 and 4.9, taking into account the surface roughness is important when considering ultrasonic characterization of the BII. The results obtained in Figs. 4.7 and 4.9 show that r is generally an increasing function of the soft tissues thickness, which may be explained by the increase of the gap of acoustical properties when soft tissues are in contact with the implant surface compared to a fully bounded interface. Moreover, as expected, when the value of W becomes sufficiently large so that the echo of the soft-tissue – bone interface does not affect the echo of the BII, the value of r reaches a constant value.

Three experimental studies [155, 280, 283] have evidenced the influence of osseointegration on the ultrasonic response of the BII (see Sections 2.1.2 and 2.1.5). These studies showed a significant decrease of the echographic response obtained at 10 MHz as a function of healing time, which is in qualitative agreement with the results found in the present study indicating that r decreases as a function of the BIC (see Figs. 4.7 and 4.9) and when bone properties increase (see Fig. 4.8).

The quantity measured in Mathieu et al. [155] can be considered as an apparent reflection coefficient of the BII, allowing a comparison with the results found herein. In this previous study, the implants had an average roughness of $R_a = 1.9 \mu\text{m}$, which is close to the case $h = 5 \mu\text{m}$ and $L = 50 \mu\text{m}$ (see Fig. 4.7a). Mathieu et al. [155] found a decrease of the apparent reflection coefficient of 7.8% between 7 and 13 healing time, which corresponds to an increase of the BIC from 27% to 69%. The model considered herein predicts that an increase of the BIC from 27% to 69% should result in a decrease of r by 4%, which is lower than the experimental results. The difference between experimental results and numerical prediction may be explained by the following reasons. First, the present study does not consider the changes of the bone material properties, which are known to occur during healing (see Section 2.1.1) and which induce a concurrent increase of the reflection coefficient as a function of healing time [282]. Second, in the experimental configuration, the ultrasonic wave is not fully planar due to the use of a focused immersed transducer, which has not been considered in the present study. Despite these limitations, a good agreement is obtained between numerical and experimental results.

Other simulation studies have previously investigated the variation of the ultrasonic response of an implant as a function of bone properties (see Section 2.1.4). However, the implant surface was considered as either fully bounded with bone tissue or immersed in water. Vayron et al. [281] considered a cylindrical implant, which corresponds to the case $h = 0$ of the present study (see Fig. 4.7a). The amplitude of the ultrasonic response of the implant was multiplied by 0.50 in Vayron et al. [281] when comparing a non-bonded implant with a fully bonded implant, whereas r is multiplied by 0.63 herein for $h = 0$ when comparing results obtained for $W = 500 \mu\text{m}$ to $W = 0$. The effect of a decrease of 20% of ρ associated with a concomitant decrease of 26% of the bone Young's modulus E was considered in Vayron et al. [281] and led to an increase of 17% of the amplitude of the echographic response. Using the model developed herein, the value of r was predicted to increase by 15.5% for $h = 0$ and $W = 0$ when the values of ρ and E were simultaneously

considered to decrease by respectively 20% and 26%.

Vayron et al. [282] considered dental implants and only the macroscopic roughness was taken into account, with an implant threading corresponding to $h = 285 \mu\text{m}$, which is close to the case $h = 360 \mu\text{m}$ herein presented (see Fig. 4.7b). The amplitude of the ultrasonic response of the implant was multiplied by 0.73 in Vayron et al. [282] when comparing a non-bonded implant with a fully bonded implant, whereas r is multiplied by 0.63 herein for $h = 360 \mu\text{m}$ when comparing results obtained for $W = 500 \mu\text{m}$ and for $W = 0$. The effect of a decrease of 20% of ρ (respectively C_p) was also considered in Vayron et al. [282] and led to an increase of 4.2% (respectively 2.1%) of the amplitude of the echographic response. Using the model developed herein, the value of r was predicted to increase by 12.9% (respectively 12.7%) for $h = 360 \mu\text{m}$ and $W = 0$ when considering a decrease of 20% of ρ (respectively C_p). The differences between the results found in the present study and in Vayron et al. [281, 282] may be explained by the fact that the reflection coefficient is considered herein while the amplitude of the coda resulting from the complex echo of a dental implant was considered in the former studies. However, a relatively good agreement is obtained between the different numerical models.

The results obtained in the present study may also be compared with the experimental results obtained in Chapter 3 for the echo #2 of the ultrasonic response of the BII. In Chapter 3, the compression applied by the set up was likely to increase the BIC from around 50% up to a maximum of 100% for very strong compression stresses (see Section 3.4.1), which corresponded to a decrease of R_2 equal to 7.2% from $\sigma = 0.25 \text{ MPa}$ to $\sigma = \sigma_2$. In the present chapter, the reflection coefficient obtained for implants with a low roughness amplitude equal to $5 \mu\text{m}$ was shown to decrease by 9.3% when the BIC varied from 50% to 100%, which is in quantitative agreement with results obtained in the previous chapter.

4.4.2 Comparison between 2-D and 3-D models

Figures 4.4 and 4.5 show that the difference between r and r_{3D} increases when h increases. When the interface is perfectly smooth ($h = 0$), 2-D and 3-D models lead to the same exact results. Therefore, the difference between the 2-D and 3-D cases increases as a function of h , which may explain the increase of e as a function of h . Although significant, the dependence of e as a function of L is relatively weak. Note that the behavior of e as a function of L is different for low values of L ($L = 50 \mu\text{m}$), which may be explained by the fact that multiple scattering become significant when h/L becomes close to 1 and will be further detailed in subsection 4.4.4.

However, the difference between r and r_{3D} remains below 0.03 for all values of h and L considered. Note that the average experimental precision P corresponding to the determination of the reflection coefficient was around 0.011 in Mathieu et al. [155]. Therefore, the difference between results obtained with 2-D and 3-D models for values of h lower than $20 \mu\text{m}$ is lower than the experimental error (see Fig. 4.5). Implants with sand-blasted [257] or laser modified surfaces [199] (see Chapter 5, Table 5.1) have typical arithmetical mean roughness R_a comprised between 0.9 and $5 \mu\text{m}$, which corresponds to values of h between 3 and $16 \mu\text{m}$. Consequently, for standard values of implant roughness, the 2-D modeling of the BII should be sufficient to derive an accurate description of its ultrasonic response.

4.4.3 Physical interpretation of the results in the microscopic case

The results shown in Fig. 4.6a and in Fig. 4.7a show that the roughness does not affect the reflection coefficient r neither in the case of a full-bonded BII (i.e. $W = 0$) nor in the case of an absence of osseointegration (i.e. for high values of W). However, the roughness parameters do influence significantly the values of r in the case of partial osseointegration (see Fig. 4.7a). Figure 4.7a shows that r reaches a maximum value of 0.92 for a value of W comprised between 35 and 45 μm , and then decreases until 0.88, which corresponds to the analytical solution for a planar bone-soft tissue interface. The local maximum of r obtained for W comprised between 35 and 45 μm may be explained by the constructive interference of the echoes of the soft tissue-bone interface with that of the implant-soft tissue interface, leading to similar phenomena compared to the situation described in the next subsection. Moreover, Fig. 4.9a shows the same tendency for the variation of r as a function of W , with a maximal value reached for a value of W that increases when the frequency decreases. Again, the interference of the echoes of the two aforementioned interfaces may explain this variation of r . The maximum value of r is reached for a value W that increases when the frequency decreases because of the increase of the wavelength, leading to different interference conditions.

4.4.4 Physical interpretation of the results in the macroscopic case

Interference between two waves

At 10 MHz, the wavelength $\lambda_P = C_{p,Ti}/f_c$ of the P-wave in the implant is equal to 579 μm , which is of the same order of magnitude compared to typical values of the surface roughness in the macroscopic case. This situation may result in phase cancellation phenomena, as described below. Figure 4.10 illustrates the interaction between an ultrasonic wave ($f_c = 10$ MHz) and the BII and shows different snapshots obtained at different times in the macroscopic case. The color scale codes the vertical displacement as a function of the position. The parameters of the BII in Fig. 4.10a (respectively Fig. 4.10b) are $h = 360$ μm (respectively $h = 1$ mm), $L = 900$ μm and $W/h = 1$. In the case of Fig. 4.10a, two wave fronts indicated by arrows and corresponding to the reflection of the ultrasonic wave on the top and on the bottom of the surface may be distinguished, which is particularly clear in the snapshots at $t = 1.45$ μs of Fig. 4.10a. The presence of these two wave fronts may be explained by the reflection of the wave on the top and bottom regions of the surface, which corresponds to a surface locally perpendicular to the direction of propagation, leading to constructive interference. The interference of the echoes of the top and bottom part of the surface is illustrated more quantitatively in Fig. 4.11a, which shows the envelopes of the signals reflected by the BII ($h = 360$ μm , $L = 900$ μm , $W = 0$). Two echoes can be distinguished in Fig. 4.11a and are separated by 0.12 μs , which corresponds to a distance of 697 μm in the implant. It approximately corresponds to two times the distance between the top and the bottom regions of the surface ($2h = 720$ μm), thus validating the interference of the two echoes originating from the bottom and to top regions of the surface.

Figures 4.11a, 4.11b1 and 4.11b2 show the variation of the envelop of the echo of the interface when h decreases, which leads to an increase of the amplitude of the total echo.

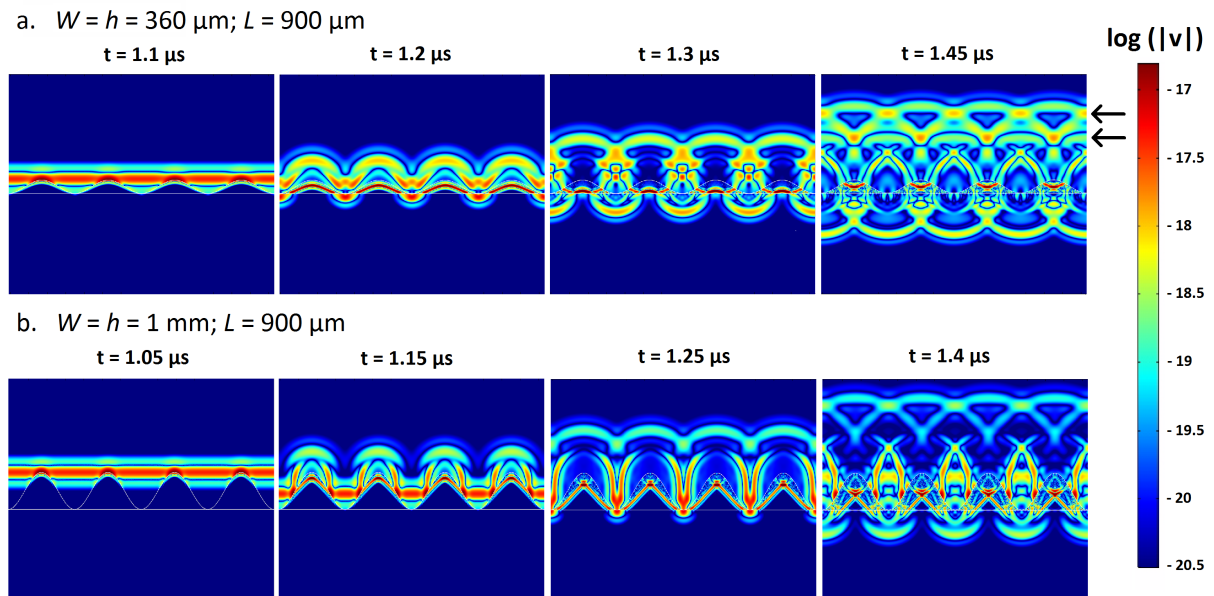


Figure 4.10 – Images corresponding to the spatial variation of the logarithm of the absolute value of the velocity in the y direction at different times in the macroscopic case. The computations are performed for $f_c = 10$ MHz with (a) $h = 360 \mu\text{m}$ and $L = 900 \mu\text{m}$ and (b) $h = 1$ mm and $L = 900 \mu\text{m}$. For $t = 1.45 \mu\text{s}$ (a), two arrows indicate the wave fronts corresponding to the reflection of the ultrasonic wave on the top and on the bottom of the surface.

This increase of the echo amplitude can be explained by a constructive interference of the echoes of the top and bottom regions of the BII. These results may explain the decrease of r as a function of h obtained in Fig. 4.6b and in Fig. 4.7b when $L > W$.

Figures 4.11a, 4.11c1 and 4.11c2 show the variation of the envelope of the echo of the interface when W/h increases from 0 to 1. A comparison of Figs. 4.11a and 4.11c1 shows that the main difference between the results obtained with $W/h = 0$ and $W/h = 0.5$ lies in the amplitude of the first echo, which increases when W/h increases. This variation may be explained by the fact that the first echo originates from the top of the BII, which is in contact with bone tissue when $W/h = 0$, leading to a weaker echo than when it is in contact with soft tissues when $W/h = 0.5$. Similarly, a comparison of Figs. 4.11c1 and 4.11c2 shows that the main difference between the results obtained with $W/h = 0.5$ and $W/h = 1$ lies in the amplitude of the second echo, which increases when W/h increases. This variation may be explained by the fact that the second echo originates from the bottom of the BII, which is in contact with bone tissue when $W/h = 0.5$, leading to a weaker echo than when it is in contact with soft tissues when $W/h = 1$. The aforementioned phenomena may explain the results obtained in Figs. 4.7b and 4.9b, which show an increase of r as a function of W as well as a sudden increase of r around the values $W/h = 0$ and $W/h = 1$.

Multiple scattering

Another interesting phenomenon is illustrated in Fig. 4.10b, which shows the variation of the acoustic field for a relatively rough BII ($h = 1$ mm, $L = 900 \mu\text{m}$). As shown in

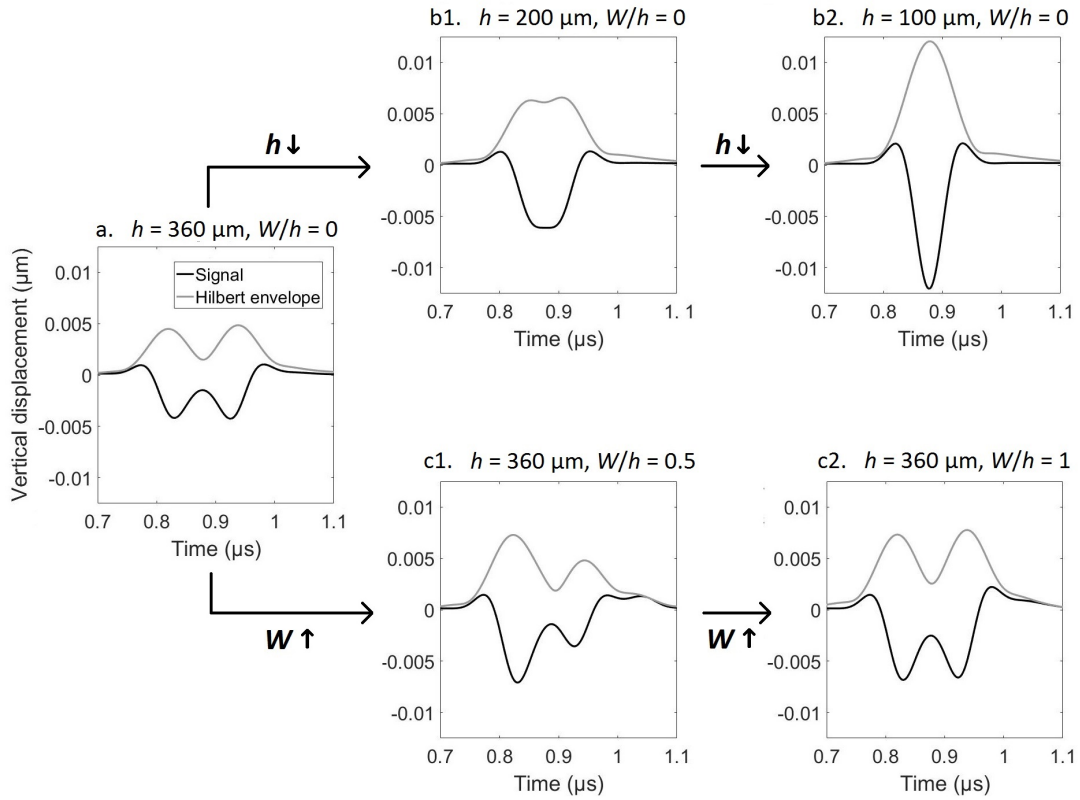


Figure 4.11 – Envelop of the RF signal corresponding to the reflection of a BII with: (a) $h = 360 \mu\text{m}$, $L = 900 \mu\text{m}$, $W = 0$; (b1) $h = 200 \mu\text{m}$, $L = 900 \mu\text{m}$, $W = 0$; (b2) $h = 100 \mu\text{m}$, $L = 900 \mu\text{m}$, $W = 0$; (c1) $h = 360 \mu\text{m}$, $L = 900 \mu\text{m}$, $W/h = 0.5$; (c2) $h = 360 \mu\text{m}$, $L = 900 \mu\text{m}$, $W/h = 1$.

Fig. 4.10b, the angle between the local normal of the interface and the axis y is locally higher than 45° , which leads to reflected waves that may propagate in the x direction. This situation leads to the presence of multiple scattering phenomena that complicate the analysis of the reflected echo.

Multiple scattering phenomena are likely to occur when the two following conditions are fulfilled. First, it is necessary to have $L < h$, which corresponds to a situation where the angle between the local normal of the interface and the axis y goes above the critical value of 45° . Second, another condition given by $k.L > 1$ is also necessary [67], with L considered as the characteristic length of the scatterer. This condition corresponds to a situation where the scatterer size is larger than the wavelength.

The results shown in Fig. 4.6 indicate that multiple scattering phenomena lead to significant variations of the reflection coefficients only when i) $L < h$ and ii) $h \geq 100 \mu\text{m}$, which may be explained by the two aforementioned phenomenological analyses, respectively. Note that $k.L = 1$ corresponds to a value of L equal to $92 \mu\text{m}$, which explains why multiple scattering phenomena do not significantly influence the results for $h < 100 \mu\text{m}$ (which corresponds to the results shown in Fig. 4.6a).

The situation described in Fig. 4.7b corresponds to a value of $k.L = 9.75$. Therefore for $h = 1 \text{ mm}$, which corresponds to $L < h$, multiple scattering phenomena occur at the BII and may explain the complex behavior of r obtained in Fig. 4.7b.

4.4.5 Variations of bone material properties

As shown in Fig. 4.8, r is sensitive to bone properties only when W/h is approximately lower than 0.25, which holds for both the microscopic and the macroscopic cases. For values of W/h higher than 0.25, the reflected wave is weakly affected by variation of bone properties and the reflection coefficient is then mostly affected by changes of W , which may be explained by the lower contact area contact between the bone and the implant. Another interesting feature lies in the fact that r is not sensitive to variation of C_s , which may be due to the fact that ultrasonic propagation occurs perpendicularly to the BII.

4.4.6 Frequency variations

Microscopic roughness

In the microscopic case, the results are shown to depend almost only on $k.W$ and two regimes were evidenced for $k.W < 1$ and for $k.W \geq 1$. While for $k.W \geq 1$, r is shown not to depend on $k.W$, r is shown to first increase and then slightly decrease as a function of $k.W$ when $k.W < 1$. In particular, $k.W < 0.3$ represents the situation for which the ultrasonic response of the BII is the most sensitive to the presence of soft tissue, with an increase of r from 0.55 to 0.9. The results shown in Fig. 4.9a indicate that the slope of the curve representing the variation of r as a function of W increases as a function of f_c , which indicates a higher sensitivity of r to variations of W when f_c increases. This increase of sensitivity of the ultrasound response of the BII to variations of soft tissues thickness when the frequency increases may be explained by the lower value of the wavelength. Moreover, the value of W at which r reaches its maximum value increases as a function of f_c , which can be explained by the same reason.

More generally, the results shown in Fig. 4.9a may help to choose a frequency adapted to the use of ultrasound to characterize the BII. To do so, a simple method is described below, aiming at estimating the minimum soft tissue thickness that can be measured for a given frequency and a given roughness, denoted ST_{min} in what follows. The method assumes a linear variation of r as a function of W (thus for relatively low values of W , which corresponds to the physiological range of interest). The method uses the averaged experimental precision P on the determination of the reflection coefficient, that was found equal to around 0.011 in Mathieu et al. [155], and corresponds to an average error $\epsilon = 3\%$ in the estimation of r . Another parameter used by the method is the slope $S(f_c, h)$ of the variation of r as a function of the soft tissue thickness for the frequency and the roughness considered. ST_{min} is then simply given by:

$$ST_{min}(f_c, h) = \frac{\epsilon \cdot R_0(f_c, h)}{S(f_c, h)} \quad (4.10)$$

where R_0 corresponds to the value of the reflection coefficient for $W = 0$; ST_{min} corresponds to the variation of soft tissue thickness corresponding to a variation of 3% of r . Therefore, ST_{min} can be associated to the resolution of ultrasound to assess the soft tissue thickness. The results are shown in Fig. 4.12 for several values of f_c and h . The resolution ST_{min} decreases as a function of frequency and increases as a function of h . Figure 4.12 shows that the sensitivity of the ultrasonic response of the BII to changes of soft tissue thickness W increases as a function of frequency. However, increasing the frequency above around 10 to 15 MHz leads to higher complexity in terms of electronic

equipment as well as ultrasound transducer manufacturing. Therefore, choosing frequencies around 10-15 MHz (as it was done in previous studies [152, 155, 277, 278, 280]) seems to be a good compromise to obtain an acceptable resolution (around 2-12 μm depending on the implant roughness) at a reasonable price.

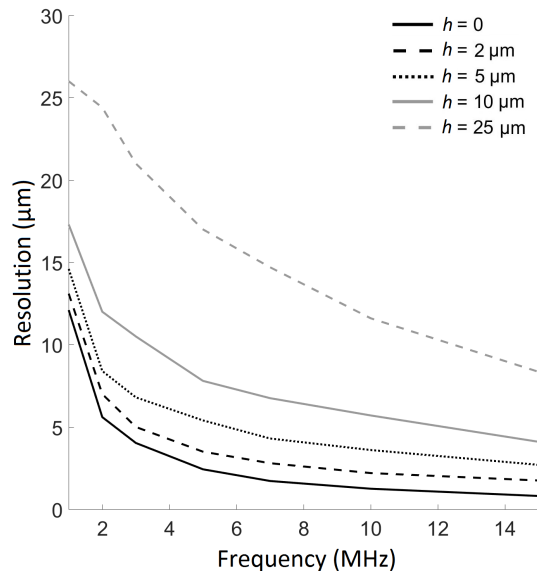


Figure 4.12 – Variation of the sensitivity of ultrasound response of the bone-implant interface to a variation of soft tissue thickness as a function of the frequency f_c and of the roughness amplitude h .

Macroscopic roughness

As shown in Fig. 4.9b, the behavior of the ultrasonic response obtained in the macroscopic case is different than in the microscopic case. For a given value of W/h , the reflection coefficient r decreases as a function of f_c , while the opposite behavior was obtained in the microscopic case. This difference may be explained by the phase cancellation effects described in subsection 4.4.4, which makes the normalization procedure realized above unsuitable for the macroscopic case. For higher frequencies (above around 5 MHz), the echoes of the upper and lower part of the interface can be distinguished. In such situation, increasing the value of W/h above around 0.3 does not lead to a modification of the echo of the top part of the surface, which explains the constant variation of r as a function of W/h . However, for lower frequencies (below around 5 MHz), the situation is different and r increases as a function of W/h .

4.4.7 Sinusoidal approximation of the implant roughness

A sinusoidal function of amplitude h and half-period L is used to describe the implant surface roughness. This sinusoidal description constitutes a strong approximation in the microscopic case and taking into account a real surface is likely to lead to different results, which will be developed in Chapter 5. In particular, phase cancellation phenomena described in subsection 4.4.4 may not occur so clearly if the real surfaces were taken into

account because of the randomness of the roughness. However, this sinusoidal description is quite well adapted to the real configuration in the macroscopic case. Figure 4.13 describes the histological section of a titanium dental implant after 8 weeks of implantation, and illustrates that implant threading could actually be correctly approximated by a sinusoidal function. Moreover, a situation where $W > h$ may not occur throughout the entire implant. However, this situation may occur on relatively large area of the implant. For example, Mathieu et al. [155] and Vayron et al. [276] used coin-shaped implants, which lead to important surface where bone tissue is not in contact with the implant. The situation corresponding to $W > h$ may also occurs at the macroscopic scale, as shown in the bottom of Fig. 4.13, where a large surface of the implants is not in intimate contact with bone tissue.



Figure 4.13 – Image of the histological section of a titanium dental implant after 8 weeks of implantation in a sheep iliac crest. The implant corresponds to the white regions. Mineralized bone tissues correspond to the light red parts of the image and were colored with Van Gieson's stain. The BIC is equal to 45.7%.

4.4.8 Limitations

This study has several limitations. First, microscopic and macroscopic scales were considered separately for the roughness of the implant and both scales have not been combined. Implants used in clinical practice have both macroscopic threading and microscopic surface roughness, resulting in an interaction of the phenomena considered for microscopic and macroscopic scales, which should be considered in future studies. Second, only the direction of propagation from the implant to the bone tissue was taken into account because it corresponds to the experimental situation of interest [155, 280]. Future studies should account for oblique incidences. Third, the variation of the periprosthetic bone geometrical properties is rather simple and modeled by a bone level given by the parameter W . The bone geometry around the implant surface is likely to be much more complex, as shown in Fig. 4.13. Note that *in vivo*, fully bounded interface are not likely to occur since typical values of the BIC is comprised between around

30 and 80% [155, 219, 240, 280]. More generally, cavity and voids may be present in bone tissue, as shown in Fig. 4.13. Fourth, bone materials properties are assumed to be elastic, homogeneous and isotropic, similarly to what was done in some previous studies [91, 153, 281, 282]. However, bone tissue is known to be a strongly dispersive medium [90, 93], which was neglected herein. Moreover, although mature bone tissue is known to be anisotropic [91, 236], the anisotropic behavior of newly formed bone tissue remains unknown [152, 276]. Fifth, adhesion phenomena at the BII [155], which may lead to a non-linear ultrasonic response [25] were not taken into account in the present study. Sixth, only the first reflection of the ultrasonic wave on the BII was considered, similarly to what was done in Mathieu et al. [155], because it constitutes a simple approach to determine the effect of variations of the properties of the BII on its ultrasonic response.

Note that these limitations also apply to the models that will be developed in Chapter 5 and in Chapter 6.

Chapter 5. Tackling real implant surface roughness

Contents

5.1	Introduction	80
5.2	Material and methods	80
5.2.1	Description of the problem	80
5.2.2	Construction of the bone-implant interface	80
5.2.3	Determination of the optimal equivalent sinusoidal profile	82
5.3	Results	83
5.3.1	Influence of roughness on the ultrasonic response	83
5.3.2	Effect of low-pass filtering the surface profile	84
5.3.3	Optimal equivalent sinusoidal profile	87
5.4	Discussion	89
5.4.1	Originality and comparison with literature	89
5.4.2	Influence of the roughness	91
5.4.3	Equivalence of the sinusoidal profile	91

5.1 Introduction

Although the sinusoidal description of the surface profile considered in Chapter 4 may be adapted at the macroscopic scale because it is close to mimicking implant threading, it constitutes a strong approximation in the microscopic case since the surface roughness has random characteristics. The aim of this chapter is to model the interaction between an ultrasonic wave and a rough BII considering actual surface roughness. Another related aim is to determine to what extent actual implant roughness could be replaced by a sinusoidal profile. To do so, a 2-D time domain FEM was used to model the interaction between an ultrasonic wave and the BII, similarly as in Chapter 4.

The work presented in this chapter was published in the *Journal of Acoustical Society of America* [102].

5.2 Material and methods

5.2.1 Description of the problem

Figure 5.1 represents the numerical model considered herein. It is similar to the one employed in Chapter 4, except that actual implant surface profiles are considered. The implant surface profile was defined by the results obtained using profilometry measurements (see subsection 5.2.2), as shown in Fig. 5.1. Such roughness profiles are described as “original” in what follows, by opposition to "sinusoidal" profiles presented in chapter 4. Note that in the case of sinusoidal surface profiles, we have: $h = \pi R_a$ and $L = S_m/2$, where R_a is the arithmetical mean roughness value and S_m is the mean value of the spacing between profile irregularities. The average altitude of the surface roughness was taken as the origin for the y coordinates in all cases.

In this chapter, the center frequency f_c of the ultrasonic pulse applied at the top surface of the implant domain was set equal to 10 MHz as it corresponds to the value used in the QUS device developed to assess dental implant stability and described in Section 2.1. Moreover, the results obtained in Chapter 4 indicate that using a frequency equal to 10 MHz guarantees an acceptable sensitivity of the ultrasound response on changes of the biomechanical properties of the BII (see Fig 4.12). Governing equations, finite element simulation and signal processing were performed identically as in Chapter 4 (see Subsections 4.2.3, 4.2.4 and 4.2.5).

5.2.2 Construction of the bone-implant interface

The implant surface roughness was obtained from twenty-one 5 mm diameter coin-shaped implants similar to the ones employed in Vayron et al. [276] and made of medical grade 5 titanium alloy (Ti-6Al-4V). Twelve implants had their surface modified by laser impacts [72, 249], and nine implants were produced using the EOS supplied Ti-6Al-4V ELE powder and an EOSINT M280 LPBF system (EOS GmbH, Munich, Germany) equipped with a 400 W ytterbium fiber laser. Different levels of surface roughness were obtained by varying the implant orientation in respect to the building platform from 0° (parallel to the platform) to 135°. The roughness profiles of each implant were obtained using a contact profilometer (VEECO Dektak 150) on a 2 mm long line for each sample.

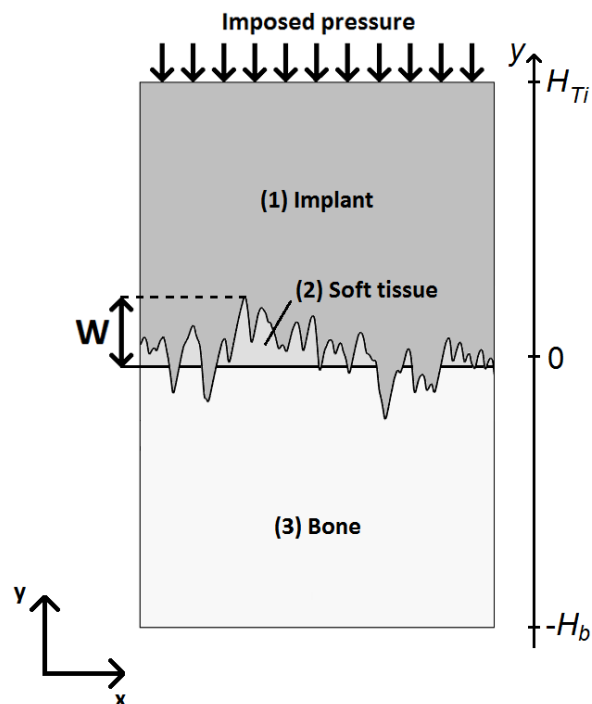


Figure 5.1 – Schematic illustrations of the 2-D model used in numerical simulations for an original roughness profile

The output of each measurement was given by the variation of the surface altitude as a function of the position with a sampling distance of $0.2 \mu\text{m}$. The stylus tip had a radius of $2 \mu\text{m}$ and a force corresponding to 1.00 mg was applied in order to ensure contact between the stylus and the surface at all times.

Different parameters were used to describe the roughness profiles: the average mean roughness R_a , the mean spacing between irregularities S_m , the maximum profile peak height R_p , and the maximum profile valley depth R_v . A fifth parameter s was introduced to describe the degree of similarity of the original profile with a sinusoidal function and was defined as $s = R_p + R_v - \pi \cdot R_a$. A value of $s = 0$ corresponds to a sinusoidal profile, while higher values of s suggest large irregularities in the roughness profile.

Each surface roughness profile was modified in order to determine the sensitivity of the ultrasound response of the interface on the spatial frequency content of the surface profile. To do so, a low-pass Hamming filter was employed with different cut-off lengths L_c comprised between 2.5 and $500 \mu\text{m}$. Note that for the sake of consistency, when comparing the original profile with the filtered ones, the origin for the definition of W always corresponds to the highest position of the original profile.

For each filtered surface profile, the ultrasonic response of the BII was simulated for 13 values of soft tissue thickness W given by: $\{W = W_k = kW_M/12, k \in [0, 12]\}$, where W_M depends on the roughness profile and represents a soft tissue thickness value above which the reflection coefficient r of the BII does not vary. Values of W_M were comprised between 55 and $160 \mu\text{m}$ according to the surface roughness. The range of variation of W was chosen in order to obtain a correct approximation of the ultrasonic response of the BII for various stages of the osseointegration process, including a fully osseointegrated interface ($W = 0$) and a fully debonded interface ($W = W_M$). For each value of W_k , the

value of the simulated reflection coefficient $r_o(k)$ obtained with the original profile was compared with the values of the reflection coefficient $r_f(L_c, k)$ obtained with a filtered profile (with a cut-off length L_c) and the same soft tissue thickness W_k . The maximum difference $D(L_c)$, when varying W between the reflection coefficients obtained with the original profile and the corresponding filtered profile (with a cut-off length equal to L_c), was defined as:

$$D(L_c) = \max_{k \in [0;12]} (|r_o(k) - r_f(L_c, k)|) \quad (5.1)$$

5.2.3 Determination of the optimal equivalent sinusoidal profile

For each profile corresponding to the samples described in Section 5.2.2, an optimization method was developed in order to determine the equivalent sinusoidal profile (with roughness parameters (h_{eq}, L_{eq})) leading to an ultrasonic response that best matches the ones obtained with the original roughness profile. This optimization method is illustrated in Fig. 5.2 and described below.

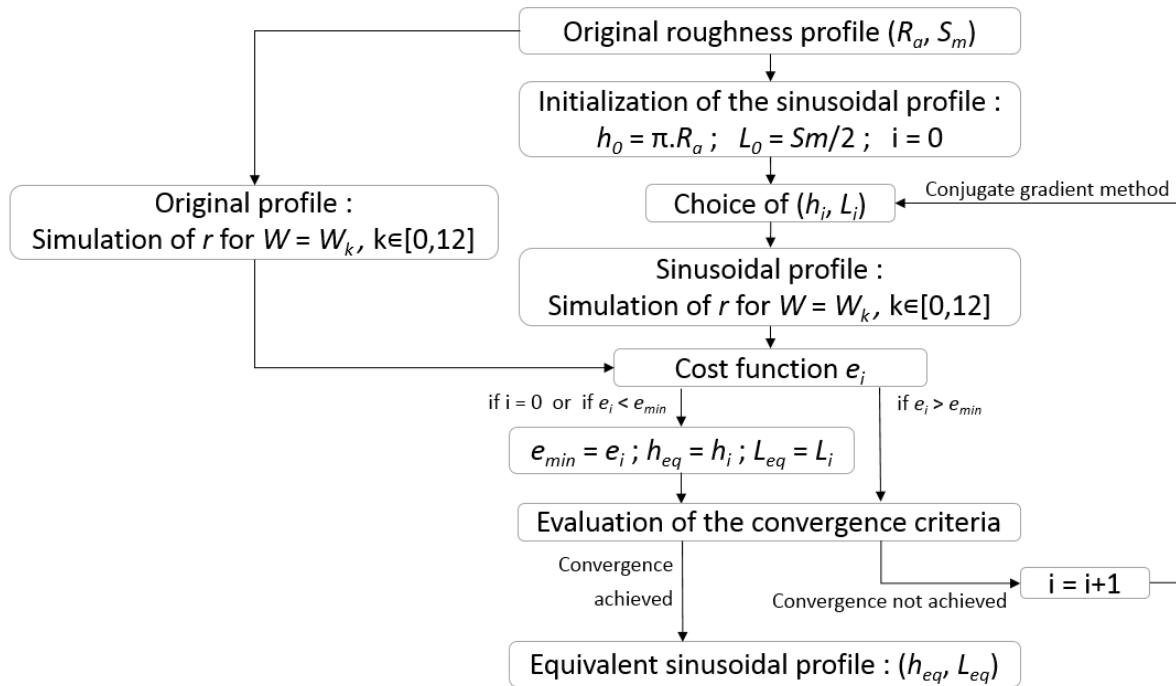


Figure 5.2 – Schematic description of the optimization method aiming at determining the equivalent sinusoidal roughness profile (with parameters h_{eq} , L_{eq}) corresponding to each original roughness profile (with parameters R_a , S_m).

The comparison between the reflection coefficient obtained with the original and the sinusoidal equivalent profiles was realized based on the difference of the reflection coefficients obtained for 13 different values of W defined by: $\{W = W_k = kW_M/12, k \in [0,12]\}$, similarly as what was done in Section 5.2.2. For each original profile, the reflection coefficient $r_o(k)$ was determined for $\{W = W_k, k \in [0,12]\}$. The values of the reflection coefficient $r_o(k)$ obtained with the original profile were compared with the values of the reflection coefficient $r(h, L, k)$ obtained with a sinusoidal profile having for roughness parameters:

(h, L) and with the soft tissue thickness equal to W_k . A cost function $e(h, L)$ was defined in order to assess the difference between the ultrasound response of the original and each sinusoidal profile (with roughness parameters (h, L) following:

$$e(h, L) = \sum_{k=0}^{12} \frac{|r_o(k) - r(h, L, k)|}{13} \quad (5.2)$$

An optimization procedure based on a conjugate gradient method [185] was carried out in order to determine the optimal values of the roughness parameters (h, L) minimizing the cost function e . The algorithm was initiated for $h = \pi R_a$ and $L = S_m/2$ because these parameters correspond to the values that would be obtained if the original profile was sinusoidal. Two convergence criteria that must both be achieved to consider the process as converged were set as:

$$\sqrt{(h_i - h_{i-1})^2 + (L_i - L_{i-1})^2} < 0.02\mu m \quad (5.3)$$

$$|e_i - e_{i-1}| < 10^{-5} \quad (5.4)$$

where i is the number of iterations performed.

5.3 Results

5.3.1 Influence of roughness on the ultrasonic response

Table 5.1 shows the roughness parameters of the 21 original profiles. Implants with laser-modified surfaces have significantly lower roughness amplitude R_a and higher values of S_m compared to 3D-printed implants.

Figure 5.3 shows the rf signals with their envelopes corresponding to the simulated ultrasonic waves recorded at $y = H_{ti} / 2$ and averaged over x for an implant surface with $R_a = 24.2 \mu m$ in the cases of fully-bonded ($W = 0$) and fully debonded ($W = W_M$) interfaces. Note that the results did not significantly vary when the convergence criteria given in Eqs. 5.3-5.4 were decreased, which constitutes a validation of the approach.

Figure 5.4 shows the variation of the reflection coefficient $r_o(k)$ obtained for different roughness profiles as a function of the soft tissue thickness W_k , $k \in [0, 12]$. Figure 5.4a shows the results obtained for the surface profiles corresponding to implants with laser-modified surface, which have a relatively low surface roughness. The results obtained with the different surface profiles are qualitatively similar. The values of r_o first increase as a function of W from 0.54 to a maximum value equal to around 0.92. Then, r_o slightly decreases as a function of W and tends towards 0.88 for all the profiles considered. However, the increase of r_o occurs for smaller values of W when considering surfaces with lower roughness. Similarly, the maximum value of r_o is reached for lower values of W when considering surfaces with lower roughness. The maximum peak height R_p of the surface profile seems to have a higher influence on the variation of r_o than the average roughness amplitude R_a , because the roughness profiles with similar R_p lead to approximately similar ultrasonic responses. Note that the values of the reflection coefficient $r_o(0)$ obtained for $W_0 = 0$ (respectively $r_o(12)$ for $W_{12} = 100 \mu m$) correspond to the analytical values

Table 5.1 – Roughness parameters of the original profiles. The first part of the table corresponds to implants with laser-modified surfaces, and the second part to 3D-printed implants

R_a (μm)	R_p (μm)	R_v (μm)	S_m (μm)	s (μm)
0.898	3.28	2.94	73.9	3.41
1.29	4.74	5.46	67.6	6.14
1.44	4.74	4.24	78.0	4.46
1.52	4.85	5.27	82.5	5.34
2.52	7.40	10.9	95.0	10.4
3.13	10.5	13.3	54.2	14.0
3.92	11.1	14.6	65.1	13.5
4.13	11.5	16.4	77.6	14.9
4.93	17.1	19.5	50.6	21.1
5.77	17.0	18.9	58.1	17.8
5.83	17.9	19.6	56.4	19.3
6.94	20.4	40.0	57.2	38.6
14.0	46.8	40.3	267	43.2
16.8	34.0	51.0	165	32.2
18.1	58.1	33.7	171	34.8
18.2	50.5	51.1	172	44.5
18.4	59.7	44.4	211	46.2
19.0	53.0	45.3	175	38.6
19.7	41.4	58.1	182	37.6
22.8	68.8	48.2	316	45.4
24.2	69.1	50.9	206	44.0

obtained for a planar bone-implant interface (respectively soft tissue-implant interface) and are weakly affected by the profile roughness.

Figure 5.4b shows the results obtained for 3D-printed implants, which correspond to relatively important surface roughness. The reflection coefficient r_o is shown to first increase as a function of W and then to tend towards constant values above approximatively $W = R_v + R_p$ for all the profiles considered. Again, the increase of r_o occurs for lower values of W when considering surface profiles with lower values of R_p . Moreover, the values of r_o obtained for $W_0 = 0$ and for $W_{12} = 200 \mu\text{m}$ increase as a function of R_a , which constitutes a different situation compared to the case of implants with laser-modified surfaces (see Fig. 5.4a) and will be discussed in subsection 5.4.2.

5.3.2 Effect of low-pass filtering the surface profile

Figure 5.5a (respectively 5.5b) shows the different profiles obtained after application of low-pass filters with cut-off lengths L_c between 10 and 125 μm to the original roughness

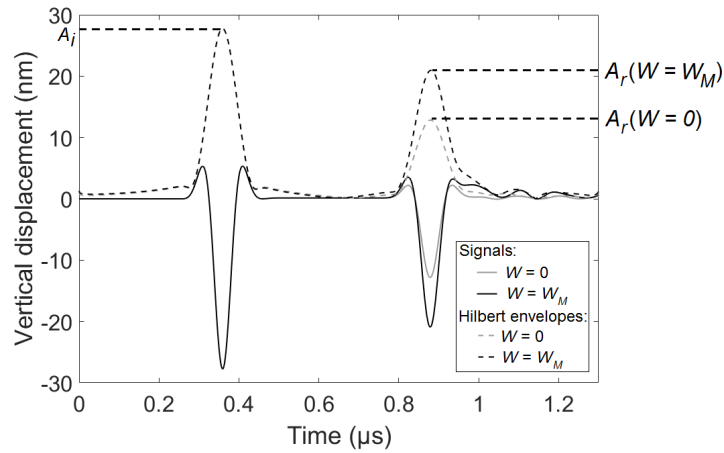


Figure 5.3 – Radiofrequency signals (solid lines) with their envelopes (dashed lines) corresponding to the ultrasonic waves recorded at $\text{textit}H_{ti} / 2$ and averaged over x for an implant surface with $R_a = 24.2 \mu\text{m}$ in the cases of fully-bonded ($W = 0$) and fully debonded ($W = W_M$) interfaces.

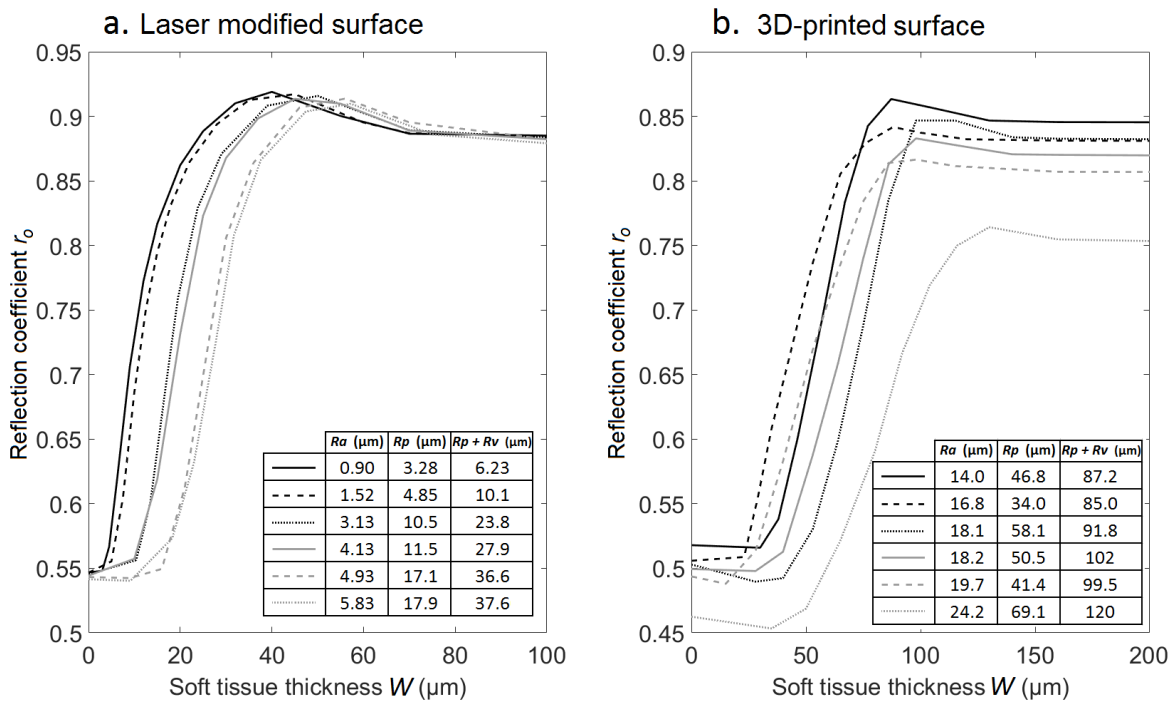


Figure 5.4 – Variation of the reflection coefficient r_o of the bone-implant interface as a function of the soft tissue thickness W for (a) six implants with laser-modified surfaces roughness profiles and (b) six 3D-printed implants roughness profiles.

profile with $R_a = 5.83 \mu\text{m}$ (respectively $R_a = 18.2 \mu\text{m}$). The original profile is also shown. Figure 5.5c (respectively 5.5d) shows the variation of the reflection coefficient r_f as a function of W for the different surface profiles shown in Fig. 5.5a (respectively 5.5b). Figure 5.5c (corresponding to an original profile with $R_a = 5.83 \mu\text{m}$) indicates that the variation of r_f as a function of W is approximately similar for all filtered profiles. Namely, r_f first increases as a function of W from around 0.54 to reach a maximum value equal

to around 0.92. Then, r_f decreases as a function of W and tends towards around 0.88. However, Fig. 5.5d (corresponding to $R_a = 18.2 \mu\text{m}$ for the original profile) indicates that the variation of r_f as a function of W varies according to the filtered profiles. Again, r_f first increases as a function of W , but reaches a maximum value that increases as a function of L_c . Moreover, for a given value of W , r_f is shown to increase as a function of L_c , which may be explained by a progressive decrease of scattering phenomena when the profile is filtered in Fig. 5.5d, whereas the initial roughness was not sufficient to cause scattering effects in the case of the laser modified surface (see Fig. 5.5c).

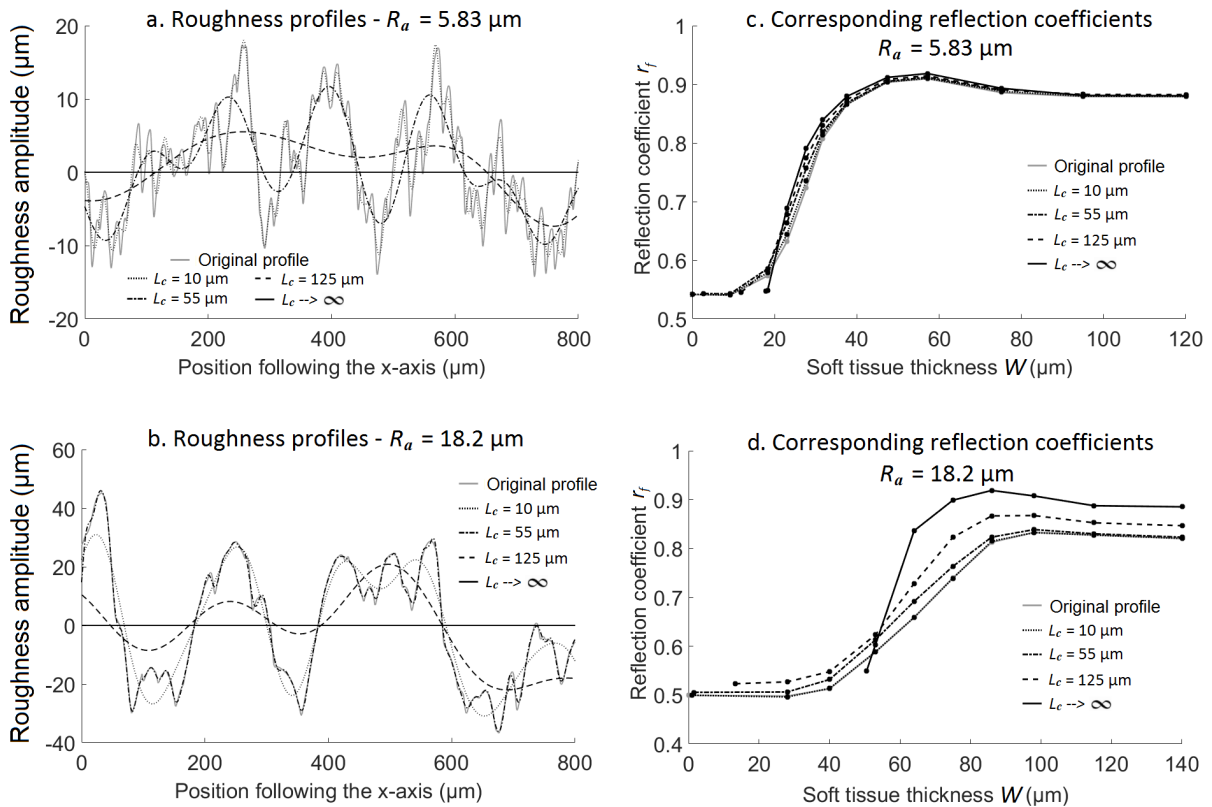


Figure 5.5 – Roughness profiles of an implant surface with (a) $R_a = 5.83 \mu\text{m}$ and (b) $R_a = 18.2 \mu\text{m}$ together with the corresponding profiles filtered with different values of the cut-off lengths L_c . (c) and (d): Variation of the reflection coefficient r_f as a function of the soft tissue thickness W for the corresponding roughness profiles shown in (a) and (b), respectively.

Figure 5.6a shows the variation of the difference D between the reflection coefficient of the filtered profiles and of the corresponding original profiles as a function of L_c . The results are shown for three implants with laser-modified surfaces and three implants with 3D-printed surfaces. For all profiles, D increases as a function of L_c and then reaches a constant value when L_c tends towards infinity. Figure 5.6b shows the variation of the average roughness R_a of the profiles as a function of L_c . For implants with laser-modified surfaces, R_a decreases significantly for low values of L_c and is close to 0 for $L_c > 250 \mu\text{m}$. However, for 3D-printed implants, which had a higher values of R_a and S_m , thus implying more high frequency components, R_a continues to decrease significantly for $L_c > 500 \mu\text{m}$. Consequently, D converges more quickly towards its final value for implants with laser-

modified surfaces compared to 3D-printed implants, as shown in Fig. 5.6a.

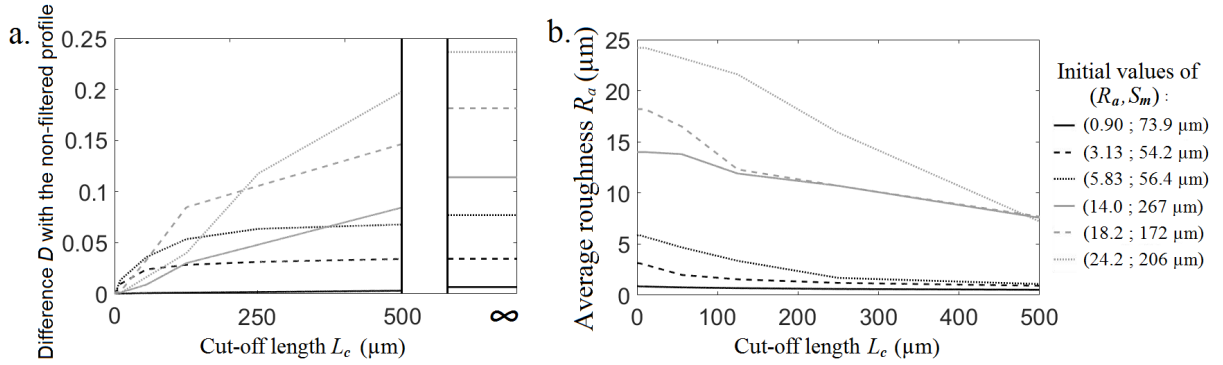


Figure 5.6 – Variation of (a) the difference D between the reflection coefficient of the filtered profiles and of the corresponding original profiles and (b) the average roughness R_a of the filtered profiles as a function of the cut-off length L_c .

5.3.3 Optimal equivalent sinusoidal profile

Figure 5.7 shows three original roughness profiles and their respective equivalent sinusoidal profiles determined using the optimization procedure described in Section 5.2.2.

Figure 5.8 shows the variation of the reflection coefficients r and r_o as a function of W for the same roughness profiles as the ones shown in Fig. 5.7 and for their respective equivalent sinusoidal profiles. The values of r were determined for each value of W for which the cost function e was evaluated (see Eq. 5.2). The results show that the behavior of r is qualitatively the same for the original and for the equivalent sinusoidal profile. However, the minimum value of the cost function is shown to increase as a function of R_a .

Figure 5.9a (respectively 5.9b) shows that h_{eq} increases as a function of R_a (respectively R_p) for all original profiles. Second-order polynomial regressions can approximate the dependence of h_{eq} as a function of both R_a and R_p . However, Spearman's tests indicated a better correlation between h and R_p ($r_S = 0.997$) compared to the correlation between h and R_a ($r_S = 0.970$), which will be discussed in subsection 5.4.3. Moreover, Fig. 5.9a shows that the amplitude h_{eq} of each equivalent sinusoidal profile is always comprised between $\pi \cdot R_a$, which would be the value of h if the original profile was sinusoidal, and $R_p + R_v$, which represents the maximum amplitude of the original profile.

Figure 5.10a (respectively 5.10b) shows that L_{eq} increases as a function of R_a (respectively S_m). For all implants with laser-modified surfaces, L_{eq} stays relatively constant as 83% of the values of L_{eq} are comprised between 54 and 58 μm . For 3D-printed implants, the values of L_{eq} are significantly higher and depend on the roughness of the original profile. Spearman's tests indicate significant correlations between L_{eq} and both R_a ($r_S = 0.843$) and S_m ($r_S = 0.833$), which will be discussed in subsection 5.4.3.

Figure 5.11a (respectively 5.11b) illustrates that the minimum value of the cost function e_{min} increases as a function of R_a (respectively of $s = R_p + R_v - \pi \cdot R_a$). Spearman's tests indicate a significant correlation between L_{eq} and R_a ($r_S = 0.848$) and a stronger one between L_{eq} and s ($r_S = 0.911$), which describes the similarity of the original profile with a sinusoidal variation.

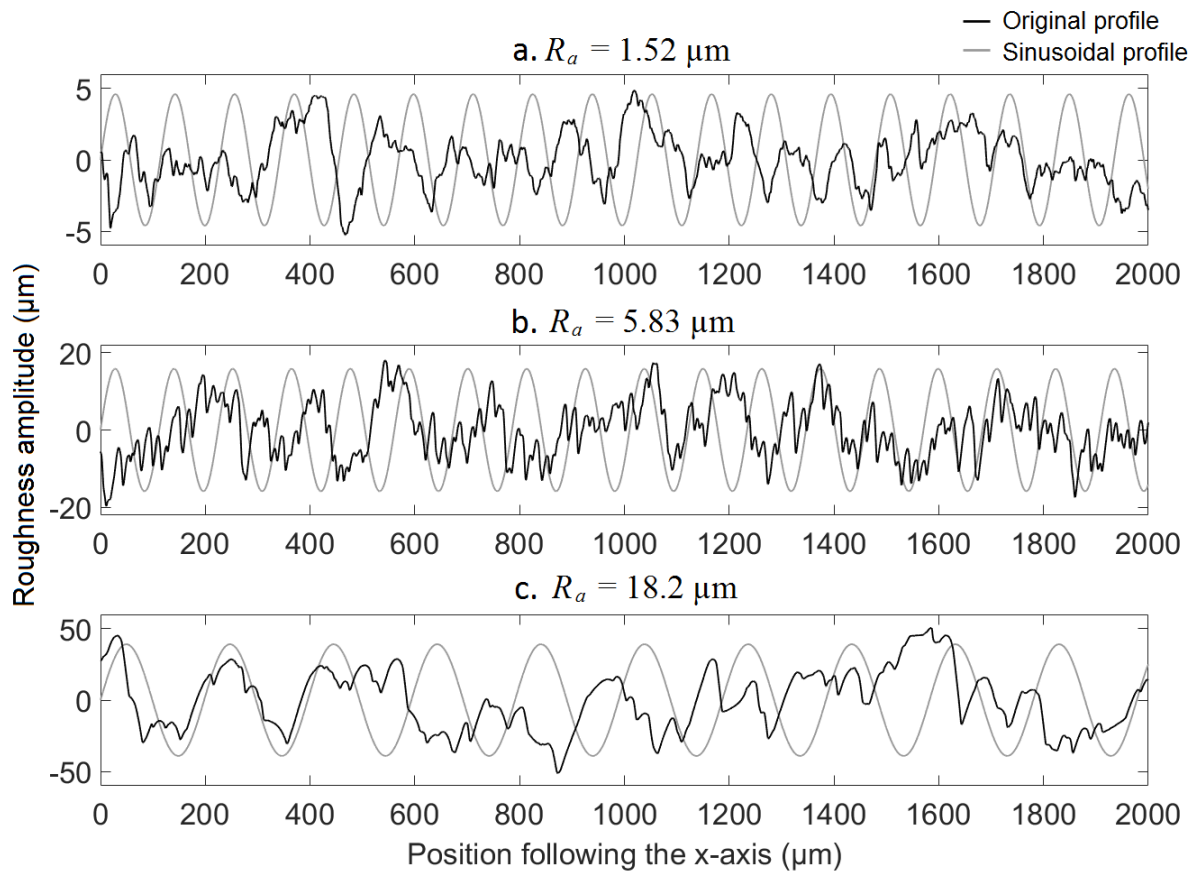


Figure 5.7 – Original roughness profiles of implants (black lines) with (a) $R_a = 1.52 \mu\text{m}$, (b) $R_a = 5.83 \mu\text{m}$, (c) $R_a = 18.2 \mu\text{m}$ and corresponding optimized sinusoidal roughness profiles (grey lines).

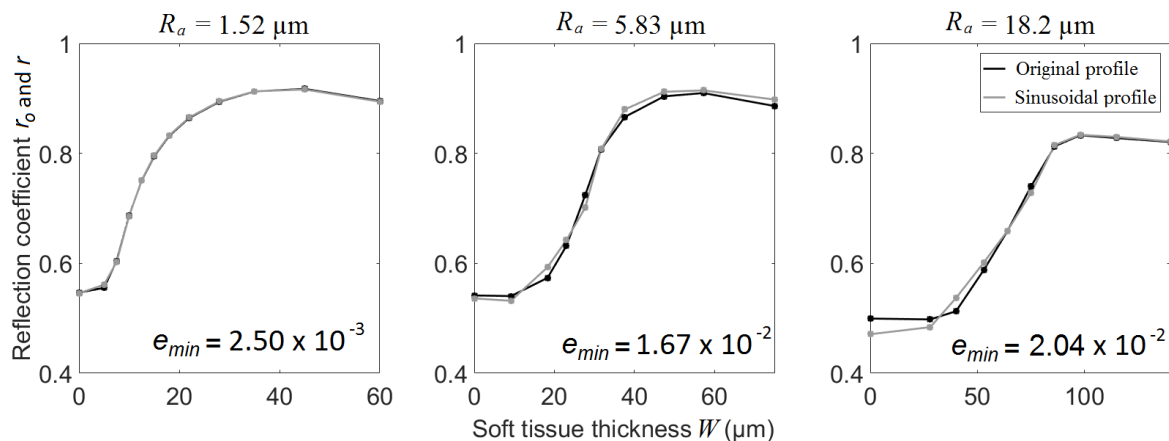


Figure 5.8 – Variation of the reflection coefficient r as function of the soft tissue thickness W for roughness profiles of implants with (a) $R_a = 1.52 \mu\text{m}$, (b) $R_a = 5.83 \mu\text{m}$, (c) $R_a = 18.2 \mu\text{m}$ and for their corresponding optimized sinusoidal roughness profiles.

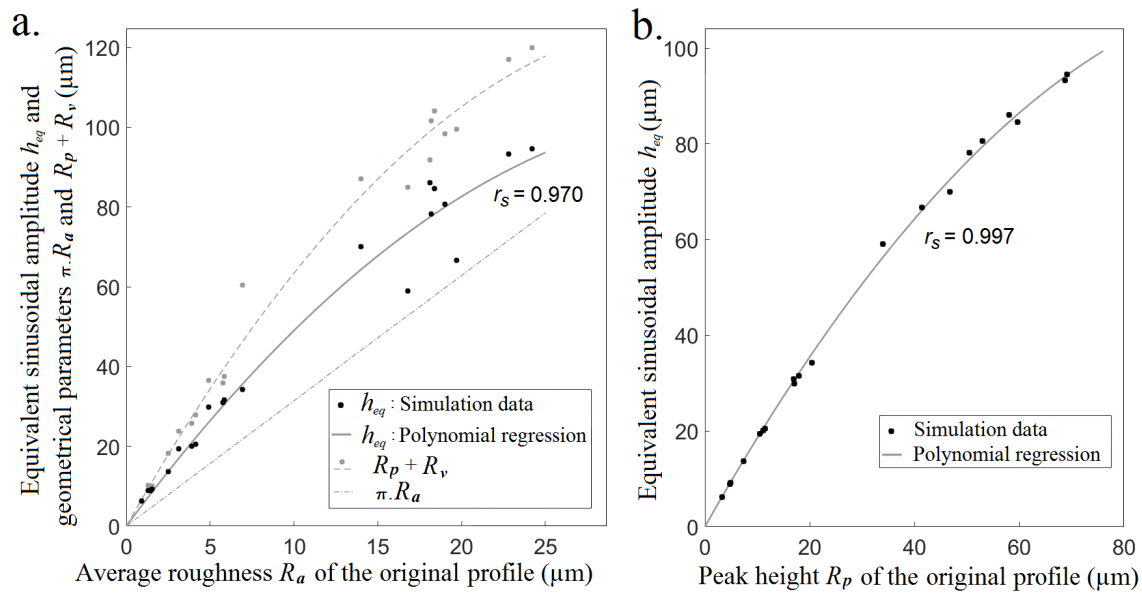


Figure 5.9 – Variation of the optimized sinusoidal roughness amplitude h_{eq} as a function of (a) the average roughness R_a and (b) the maximum peak height R_p of the implant. The solid lines and the equations correspond to the second order polynomial regression analysis of the variation of (a) R_a and (b) R_p . The variation of $\pi \cdot R_a$ and of $R_p + R_v$ as a function of R_a are also represented in Fig. 5.9a.

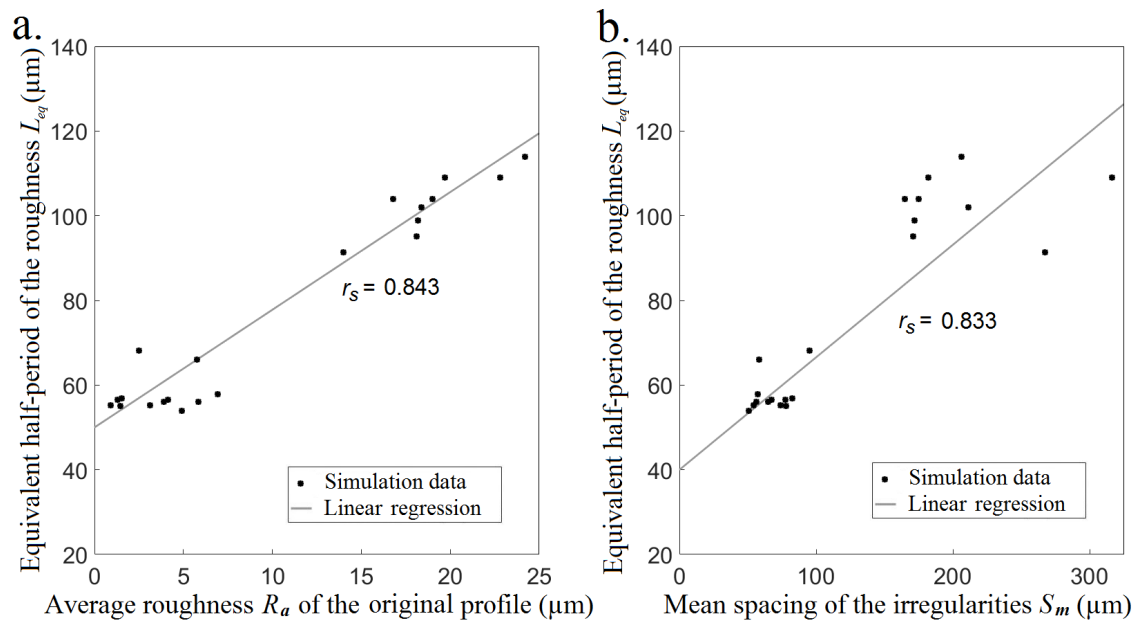


Figure 5.10 – Variation of the optimized half-period of the roughness sinusoid L_{eq} as a function of (a) the average roughness R_a and (b) the mean spacing of irregularities S_m of the implant. The solid lines and the equations correspond to a linear regression analysis.

5.4 Discussion

5.4.1 Originality and comparison with literature

The originality of this study is to consider a realistic description of the BII and to analyze the effect of the different roughness parameters and of osseointegration phenomena

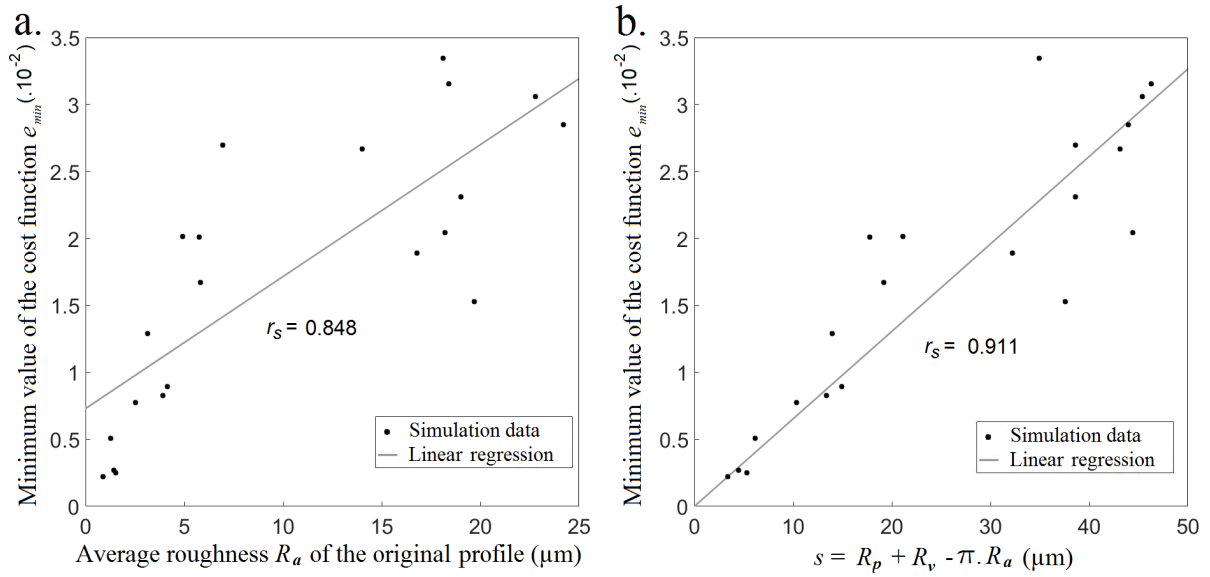


Figure 5.11 – Variation of the minimum value of the cost function e_{min} as a function of (a) the average roughness of the implant R_a and (b) $s = R_p + R_v - \pi \cdot R_a$. The solid lines correspond to a linear regression analysis.

on the ultrasonic response of the BII. The variation of r as a function of W obtained in Chapter 4 in the case of a microscopic roughness (see Fig. 4.8a) is in qualitative agreement with the results of the present chapter (see Fig. 5.4a), which justifies the comparison between both models developed in sections 5.2.3 and 5.3.3. Results are also in qualitative agreement with experimental studies of the literature [155, 280, 283], which were already commented in the previous chapter (see Section 4.4.1). However, quantitative comparison is only possible with Mathieu et al. [155], since it is the only study to measure the surface roughness of implants. Mathieu et al. [155] used implants with an average roughness of $R_a = 1.9 \mu\text{m}$, which is of the same order of magnitude as the implants considered in this study (see Fig 5.4a and Table 5.1). They found a decrease of the apparent reflection coefficient of 7.8% when the BIC increased from 27 to 69%. The model considered herein predicts that an increase of the BIC from 27 to 69% should result in a decrease of r by 7.3% in the case $R_a = 1.52 \mu\text{m}$, and by 10.7%, in the case $R_a = 2.52 \mu\text{m}$, which is relatively close to the experimental results. Moreover, this prediction is more accurate than the one obtained in the previous chapter (see Section 4.4.1).

The averaged experimental precision P on the determination of the reflection coefficient by ultrasonic methods was found equal to $1.1 \cdot 10^{-2}$ [155]. Therefore, considering results presented in Fig. 5.6, the difference between real and filtered profiles would be detected for cut-off lengths between 10 and 60 μm , except for the case of the profile with $R_a = 0.9 \mu\text{m}$. For this last profile, since the roughness is already low, the difference of ultrasonic response with a perfectly smooth implant would not be detectable. Moreover, the minimum value of the cost-function e_{min} corresponding to an averaged difference of r obtained between the original profile and its equivalent sinusoidal profile was comprised between $2.2 \cdot 10^{-3}$ and $3.2 \cdot 10^{-2}$ (see Table II), which is lower or of the same order of magnitude compared to the experimental precision P , and constitutes a validation of the approach developed in section 5.2.3.

5.4.2 Influence of the roughness

The results shown in Fig. 5.4 illustrate that the reflection coefficient of the BII depends on the surface roughness of the implant. In particular, two distinct behaviors may be observed depending whether the implants have a relatively low (implants with laser-modified surfaces, see Fig. 5.4a) or high (3D-printed implants, see Fig. 5.4b) surface roughness. In the cases of a fully-bonded interface ($W = 0$) and of no osseointegration ($W = 100 \mu\text{m}$), Fig. 5.4a shows that r_o is approximately constant for implants with low surface roughness, while for implants with higher surface roughness, r_o decreases as a function of R_a , as shown in Fig. 5.4b. The decrease of r_o as a function of R_a may be explained by scattering effects of the wave on the BII, which increases with the roughness amplitude.

Figure 5.4a shows that for implants with laser-modified surfaces, r_o reaches a local maximum for a value of W comprised between 30 and 60 μm depending on the surface roughness. This result may be explained by constructive interference of the echoes of the soft tissue-bone interface and of the implant-soft tissue interface, as already described in Chapter 4, subsection 4.4.4. When the value of W is sufficiently high so that these interference disappear, r_o finally decreases to reach a final value of around 0.88. To a lesser extent, the effects of these interference may also be observed for 3D-printed implants (see Fig. 5.4b), as r_o also reaches a local maximum. For this latter group of implants, r_o eventually converges for $W \approx R_v + R_p$ towards a value comprised between 0.72 and 0.85 depending on the roughness profile, because when $W > R_v + R_p$, $BIC = 0$ and no bone is in contact with the implant surface.

For all implants, r_o starts to increase for lower values of W when considering lower values of R_p . Figures 5.4a and 5.4b illustrate that the value of soft tissue thickness $W_{r=0.6}$ for which r_o reaches a value of 0.6 increases as a function of R_p . An explanation of this behavior is provided by the geometrical definition of R_p , which induces that R_p is closely related to the value of soft tissue thickness W_{50} corresponding to a BIC value of 50%. Therefore, the BIC value corresponding to a given value of soft tissue thickness W tends to increase as a function of R_p . Since r_o is also an increasing function of the BIC, the aforementioned results explain that $W_{r=0.6}$ is an increasing function of R_p .

5.4.3 Equivalence of the sinusoidal profile

Figure 5.9 shows that the behavior of h_{eq} is more closely related to variations of R_p than to variations of R_a , which may be explained by the interpretation given in Section 5.4.2. R_p is shown to strongly influence the value of soft tissue thickness W at which r_o starts to increase and more generally the behavior of r_o as a function of W . These results explain the important effect of R_p on the value of h_{eq} because r should have the same dependence on W for the original and for the equivalent sinusoidal profiles in order to minimize the cost function e_{min} . Nevertheless, R_a and R_p being interdependent, a significant correlation between h_{eq} and R_a was also obtained in Fig. 5.9a. As shown in Fig. 5.9b, the variation of h_{eq} as a function of R_p can be well approximated by a second order polynomial variation given by:

$$h_{eq} = 1.94R_p - 0.0083R_p^2 \quad (5.5)$$

Equation 5.5 may be used in the future to initialize the optimization process described

in Fig. 5.2 in order to achieve a faster convergence. Moreover, Eq. 5.5 may be explained as follows. Perfectly sinusoidal profiles would lead to the relation: $h_{eq} = 2 R_p$. For low values of R_p , the original profiles also have a low value of s (see Table 5.1), which explains that $h_{eq} \approx 2 R_p$ when R_p tends towards 0. When R_p further increases, the original profiles become more different compared to sinusoidal variations, which explains the second term ($- 0.0083 R_p^2$).

Figure 5.10 shows a significant correlation between L_{eq} and R_a , especially for 3D-printed implants. However, a better correlation would have been expected between L_{eq} and S_m (Fig. 5.10a) than between L_{eq} and R_a (Fig. 5.10b), which is not the case. It may be explained by the fact that S_m strongly depends on local peaks and may therefore not be an accurate indicator of the periodicity of the roughness profiles.

Overall, a good equivalence was obtained between original and sinusoidal profiles, which validates the sinusoidal description of the BII considered in Chapter 4. Therefore, this approach could be used in future numerical models, and in particular in studies considering the macro-geometry of the implant.

Chapter 6. Analytical modeling of the bone-implant interface

Contents

6.1	Introduction	94
6.2	Material and methods	95
6.2.1	Numerical model	95
6.2.2	Analytical model	96
6.2.3	Reflection and transmission coefficients	98
6.3	Results	99
6.3.1	Stiffness K_c due to the bone-implant contact	99
6.3.2	Stiffness K_{st} due to the presence of a soft tissue layer	100
6.3.3	Total stiffness of the interface K	101
6.3.4	Comparison between analytical and numerical reflection and transmission coefficients	101
6.4	Discussion	104
6.4.1	Originality and comparison with the literature	104
6.4.2	Error between analytical and numerical results	105
6.4.3	Contributions of K_c and K_{st}	106
6.4.4	Limitations	106
6.5	Conclusion	106

6.1 Introduction

Chapters 4 and 5 proposed numerical approaches to model the interaction between QUS and the BII. However, analytical modeling could allow to determine the constitutive law of the BII subjected to an ultrasonic wave. This law could then be used to replace the BII conditions in future FEM of bone-implant systems, and therefore simplify numerical models and save computation time.

Analytical models of the interaction between an elastic wave and a rough interface have been developed in the context of non-destructive testing and for geological applications. In particular, Baik and Thompson [16] developed a quasi-static model studying the ultrasonic scattering from imperfect interfaces. Lekesiz et al. [137] assessed the effective spring stiffness of a periodic array of collinear cracks at an interface between two dissimilar materials. The geometric configuration of this model may be of interest to describe a BII, but could not take into account the presence of soft tissues at the interface. Pecorari and Poznic [215] experimentally investigated the effect of a fluid layer confined between two solid rough surfaces on the acoustic non-linear response of an interface, and highlighted that none of the current models from the literature could give an accurate acoustical description of liquid-confining interfaces. More recently, Dwyer-Joyce et al. [61] separately assessed the solid contact stiffness and the fluid stiffness and then added these two contributions in order to describe the ultrasonic propagation near elastohydrodynamic lubricated contacts. However, to the best of our knowledge, such methods have never been applied in the literature to bone-implant systems. The use of spring models to describe a BII has been introduced by Egan and Marsden [63] to describe load transfers at the BII and was more recently considered by [222], but none of these studies investigated the acoustical behavior of the BII.

The aim of the present work is to derive an analytical model describing the interaction between an ultrasonic wave and the BII. To do so, a spring model was considered. Two springs acting in parallel were introduced between the bone and the implant, as illustrated in Figure 6.1. The first spring represents the contribution K_c of the contact between the bone and the implant, while the second spring represents the contribution K_{st} due to the presence of soft tissues at the interface.

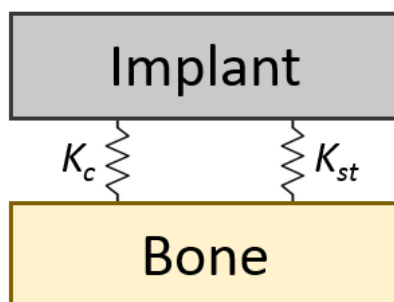


Figure 6.1 – Spring model used to describe the BII. K_c and K_{st} represent the contributions of the contact between the bone and the implant and of soft tissues at the interface, respectively.

The equivalent stiffness K of the BII was determined analytically by separately assessing K_c and K_{st} . Analytical values of the reflection and transmission coefficients were

derived from the stiffness values. Analytical values of the stiffness and of the reflection and transmission coefficients of the BII were compared with numerical results, which were determined using the FEM previously developed in Chapter 4.

The work presented in this chapter was submitted in *Ultrasonics* [107] and was performed in collaboration with Pr. Shiro Biwa from Kyoto University.

6.2 Material and methods

The general strategy used in the present chapter (i) to develop the analytical model and (ii) to compare analytical results with their numerical counterparts is illustrated in Figure 6.2 and will be described in what follows. Note that the superscript *num* refers to numerical results, while the superscript *ana* refers to analytical results.

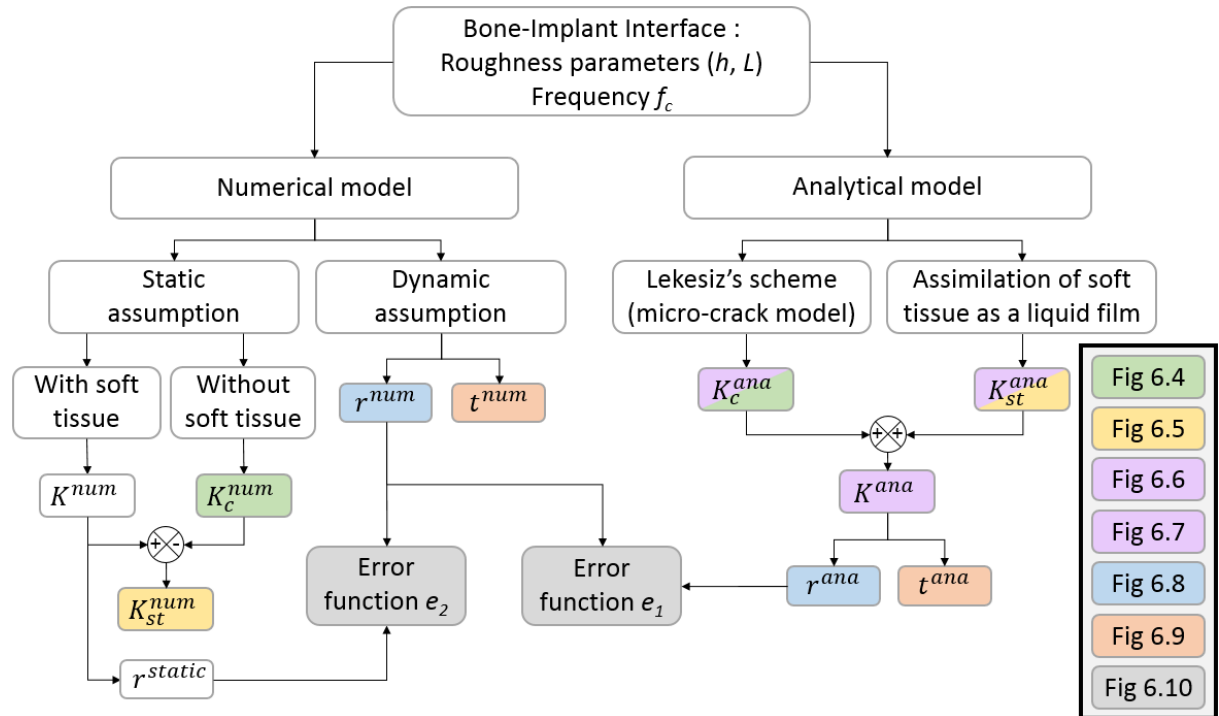


Figure 6.2 – Schematic description of the numerical and analytical models developed to describe the interaction between the BII and an ultrasonic wave. The parameters plotted in Figures 6.4, 6.5, 6.6, 6.7, 6.8, 6.9 and 6.10 are represented in different font colors.

6.2.1 Numerical model

The numerical model considered herein was adapted from the one introduced in Chapter 4 (see Fig. 4.1). Two different studies were performed with this model. First, the values of reflection and transmission coefficients (r^{num}, t^{num}) of the BII were retrieved through a numerical study carried out in the time domain. Second, the equivalent stiffness K^{num} of the BII was estimated through a static study. Both studies considered the same geometry for the BII. Note that r^{num} corresponds to the same parameter as r in

Chapters 4 and 5, but was renamed to ensure the consistency of notations in the present chapter.

The dynamic study was performed identically as in Section 4.2.1, and r^{num} was determined identically as in Section 4.2.5. However, the transmission coefficient t^{num} was also considered in the present chapter. In order to determine t^{num} , the signal representing the displacement along the direction of propagation was averaged along an horizontal line located at $y = -H_b/2$. The obtained signal corresponded to the averaged simulated transmitted signal, noted $s_t(t)$. The module of the Hilbert's transform of $s_t(t)$ was computed, and the maximum amplitude of this envelope was noted A_t . The transmission coefficient in amplitude was determined by:

$$t^{num} = A_t/A_i \quad (6.1)$$

The static study was performed in order to determine the numerical stiffness K^{num} of the model. The approach used herein was similar to the one described in Raffa et al. [222]. The geometry considered was identical as in Fig. 4.1 except for the boundary conditions. A uniform constant tensile stress $\sigma = 1$ MPa was imposed at the top boundary of the implant domain (at $y = H_{ti}$, see Fig. 4.1), and a fixed boundary was imposed at the bottom of the bone domain (at $y = -H_b$). The system of static equations was solved using the finite element software COMSOL Multiphysics, and domains were meshed in the same way as for the dynamic study. The vertical lengthening ΔH of the model due to the tensile stress σ was determined, and was related to the different parameters of the model through the relation:

$$\Delta H = H_{ti} \frac{\sigma}{\lambda_{ti} + 2\mu_{ti}} + H_b \frac{\sigma}{\lambda_b + 2\mu_b} + \frac{\sigma}{K^{num}} \quad (6.2)$$

where (λ_{ti}, μ_{ti}) (respectively (λ_b, μ_b)) are the Lamé parameters of the titanium implant (respectively bone) corresponding to the values of (ρ, C_p, C_s) listed in Table 4.1. Therefore, the stiffness of the interface K^{num} could be numerically assessed through the following expression:

$$K^{num} = \frac{1}{\frac{\Delta L}{\sigma} - \frac{H_{ti}}{\lambda_{ti} + 2\mu_{ti}} - \frac{H_b}{\lambda_b + 2\mu_b}} \quad (6.3)$$

The relative stiffness contributions K_c^{num} due to the contact between the implant and the bone, and K_{st}^{num} due to the presence of the soft tissue layer between the implant and the bone were also determined numerically. In order to assess K_c^{num} , soft tissues were replaced by vacuum for the material (2) of the model (see Fig. 4.1). Simulations were performed similarly as for the estimation of K^{num} , and K_c^{num} was estimated through Eq. 6.3. Note that K_c^{num} could only be estimated for $W < h$ since for $W > h$, there is no more contact between the bone and the implant. Therefore, in this latter case, K_c was considered equal to 0.

Finally, the contribution K_{st}^{num} was assessed through the relation :

$$K_{st}^{num} = K^{num} - K_c^{num} \quad (6.4)$$

6.2.2 Analytical model

An spring model was considered to assess the analytical value of the BII stiffness. First, the stiffness contribution K_c^{ana} due to the contact between implant and bone was

assessed considering the model described in Lekesiz et al. [137]. Second, the stiffness contribution K_{st}^{ana} due to the presence of the soft tissue layer was assessed considering the work of Dwyer-Joyce et al. [61]. Finally, the total stiffness of the interface was defined by:

$$K^{ana} = K_c^{ana} + K_{st}^{ana} \quad (6.5)$$

Stiffness K_c^{ana} due to the bone-implant contact

The analytical expression of the stiffness due to the bone-implant contact K_c^{ana} was obtained from Lekesiz et al. [137]. Assuming that all materials are elastic, Lekesiz et al. [137] provide a closed-form analytical expression for the effective spring stiffness of an infinite array of micro-cracks of length $2a$ spaced at a constant interval $2b$ along the bond line between two dissimilar materials (see Fig. 6.3a), namely the implant and the bone in the present study. To do so, Lekesiz considered the framework of the open crack model [66], and took into account the effect of interactions between cracks. The expression of K_c^{ana} was determined following:

$$K_c^{ana} = \frac{G_{ti}}{b(3 - 4\nu_{ti})} \frac{(1 + \alpha)}{(1 - \beta^2)(1 + 4\epsilon^2)} \frac{\pi}{\ln(\sec(\frac{\pi a}{2b}))} \quad (6.6)$$

where $(\alpha, \beta, \epsilon) = (-0.727, -0.136, -0.0435)$ are Dundurs' parameters [60] depending on the mechanical properties of the bone and of the implant, $\nu_{ti} = 0.3$ is the Poisson's ratio of the titanium implant and $G_{ti} = 42.3$ GPa is the shear modulus of the implant.

Figure 6.3a shows the geometric configuration considered in Lekesiz et al. [137], and figure 6.3b shows the sinusoidal BII considered in the numerical studies. In order to derive an equivalence between both models, the soft tissue regions from the numerical model were assimilated to the interfacial cracks from the model of Lekesiz et al. [137]. This geometric approximation is only valid for $W < h$ since there is no more contact between the bone and the implant when $W > h$. Therefore, in this latter case, K_c^{ana} was considered equal to 0. Note that the validity of this approximation may decrease when the roughness amplitude h increases.

From this approximation, relations between the geometric parameters (a, b) from Lekesiz et al. [137] and (h, L, W) from the numerical model were obtained. First, the period of the sinusoidal roughness $2L$ corresponds to the periodicity of cracks $2b$ (see Fig. 6.3b), so that $b = L$. Second, the length of contact between the bone and soft tissues corresponds to the diameter of the cracks, *i.e.* to $2a$. Based on the sinusoidal expression of the implant roughness, a was defined as:

$$a = L \left(\frac{1}{2} - \frac{\arcsin\left(1 - \frac{2W}{h}\right)}{\pi} \right) \quad (6.7)$$

From the expressions of a and b , it may be noticed that K_c^{ana} depends on the geometrical parameters of the interface only through L and W/h .

Stiffness K_{st}^{ana} due to the presence of a soft tissue layer

Soft tissues have a low S-wave velocity C_s compared to their P-wave velocity C_p (see Table 4.1) and mechanical properties similar to those of liquid, so that they may be assimilated to a thick liquid film present between the bone and the implant. Therefore,

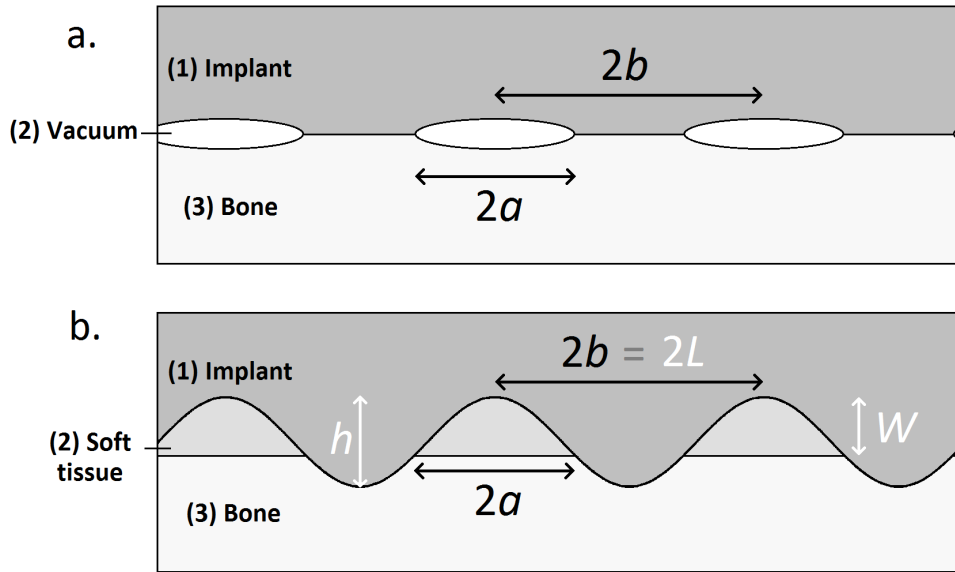


Figure 6.3 – Geometric configurations of the interface considered (a) in Lekesiz et al. [137] and (b) in the present work. Parameters written in white represent the ones that were used in the numerical model (see Fig 4.1) and parameters written in black correspond to the ones used in the work of Lekesiz et al. [137]

the work of Dwyer-Joyce et al. [61] was considered to assess the analytical expression K_{st}^{ana} of the stiffness contribution due to the presence of soft tissues. Dwyer-Joyce et al. [61] studied the stiffness of a lubricated interface by first considering a rough dry interfacial contact and then adding the contribution of the lubricant layer. The following expression was provided:

$$K_{st}^{ana} = \frac{\rho C_p^2}{d} \quad (6.8)$$

where ρ is the density of soft tissues, C_p is the P-wave velocity of soft tissues (see Table 4.1) and d is the gap thickness at the interface. In our case, d corresponds to the mean soft tissue thickness at the interface and was geometrically established through the following expression:

$$d = \begin{cases} \frac{W}{2} + \frac{\sqrt{hW - W^2}}{\pi} - \frac{h}{4} - \frac{\arcsin(1 - \frac{2W}{h})}{\pi} (W - \frac{h}{2}), & \text{if } W \leq h \\ W - \frac{h}{2}, & \text{if } W \geq h \end{cases} \quad (6.9)$$

Note that K_{st} could not be assessed analytically for $W = 0$ because there is no soft tissue at the BII in that configuration ($d = 0$). The total analytical stiffness K^{ana} of the BII was eventually defined following:

$$K^{ana} = K_c^{ana} + K_{st}^{ana} \quad (6.10)$$

6.2.3 Reflection and transmission coefficients

Based on a quasi-static approach in the frequency domain, Tattersall [264] derived the following expressions of the analytical reflection and transmission coefficients (r_f^{ana} , t_f^{ana}) corresponding to the interaction between an ultrasonic wave at an interface:

$$r_f^{ana} = \frac{Z_{ti} - Z_b + i\omega Z_{ti} Z_b / K^{ana}}{Z_{ti} + Z_b + i\omega Z_{ti} Z_b / K^{ana}} \quad (6.11)$$

$$t_f^{ana} = \frac{2Z_{ti}}{Z_{ti} + Z_b + i\omega Z_{ti} Z_b / K^{ana}} \quad (6.12)$$

where Z_{ti} and Z_b correspond to the acoustical impedance of titanium and of bone, respectively.

Since the numerical study was performed in the time domain (see Chapter 4), Eq. 6.11 and 6.12 were transformed into the time domain to determine (r^{ana}, t^{ana}) so that the analytical and numerical results could be compared. To do so, r_f^{ana} (respectively t_f^{ana}) was convoluted by the Laplace transform of the ultrasonic excitation pulse $p(t)$ (see Eq. 4.1). An inverse Laplace transform was then applied to obtain the analytical reflected signal $s_r^{ana}(t)$ (respectively the analytical transmitted signal $s_t^{ana}(t)$). Similarly as for numerical signals (see Sections 4.2.5 and 6.2.1), the moduli of the Hilbert's transform of $s_r^{ana}(t)$ and $s_t^{ana}(t)$ were computed, and the maximum amplitudes of these envelopes were retrieved to assess the analytical reflection coefficient r^{ana} and transmission coefficient t^{ana} .

In order to estimate the difference between the numerical and analytical models, an error function e_1 corresponding to the mean difference between the analytical and numerical reflection coefficients for 4 values of central frequencies f_c and 10 values of W/h was introduced:

$$e_1 = \sum_{i=1}^4 \sum_{j=1}^{10} \frac{|r^{ana}(f_c(i), W/h(j)) - r^{num}(f_c(i), W/h(j))|}{40} \quad (6.13)$$

Note that in Eq. 6.13, r^{ana} and r^{num} were determined in the time domain for input signals of frequency $f_c(i)$ ($i \in [1, 4]$) and considering a ratio of W and h equal to $W/h(j)$ ($j \in [1, 10]$).

Moreover, the reflection coefficient r^{static} derived from the numerical static study was also assessed by introducing the numerical values of K^{num} determined in Section 6.2.1 into Eq. 6.11 instead of K^{ana} , and compared to analytical results in order to validate the model presented here. Similarly as for analytical results, the difference between r^{num} and r^{static} was assessed through the error function e_2 :

$$e_2 = \sum_{i=1}^4 \sum_{j=1}^{10} \frac{|r^{static}(f_c(i), W/h(j)) - r^{num}(f_c(i), W/h(j))|}{40} \quad (6.14)$$

Table 6.1 lists the values of f_c and W/h that were used to estimate e_1 and e_2 . In particular, ratios W/h were considered between 0 and 2 since it represents the main configuration of interest from a physiological point of view [280, 283]. Moreover, values of W/h equal to 0.99 and 1.01 were considered because $W/h = 1$ constitutes a critical situation where bone stops being in contact with the implant.

6.3 Results

6.3.1 Stiffness K_c due to the bone-implant contact

Figure 6.4 presents the variation of the numerical and analytical contact interface stiffness K_c as a function of the ratio of the soft tissue thickness W and of the roughness

Table 6.1 – Values of the geometrical parameters used to estimate the error functions e_1 and e_2 , employed to compare the numerical and analytical results.

	Values considered
Ratio W/h	{0; 0.25; 0.5; 0.75; 0.99; 1.01; 1.25; 1.5; 1.75; 2}
Frequency f_c (MHz)	{2; 5; 10; 15}

amplitude h for $L = 50 \mu\text{m}$. Different values of h were considered for K_c^{num} , while K_c^{ana} was shown to be independent from h for a given value of W/h . K_c decreases as a function of W/h , especially for values of W/h close to 0 and 1. In particular, K_c^{ana} tends towards infinity when W/h tends towards 0, and K_c^{ana} tends towards 0 when W/h tends towards 1. A relatively good agreement is obtained between K_c^{num} and K_c^{ana} . However, the difference between numerical and analytical results increases for higher values of h . Moreover, except for the case $W/h = 0$, K_c^{ana} always remains lower than K_c^{num} .

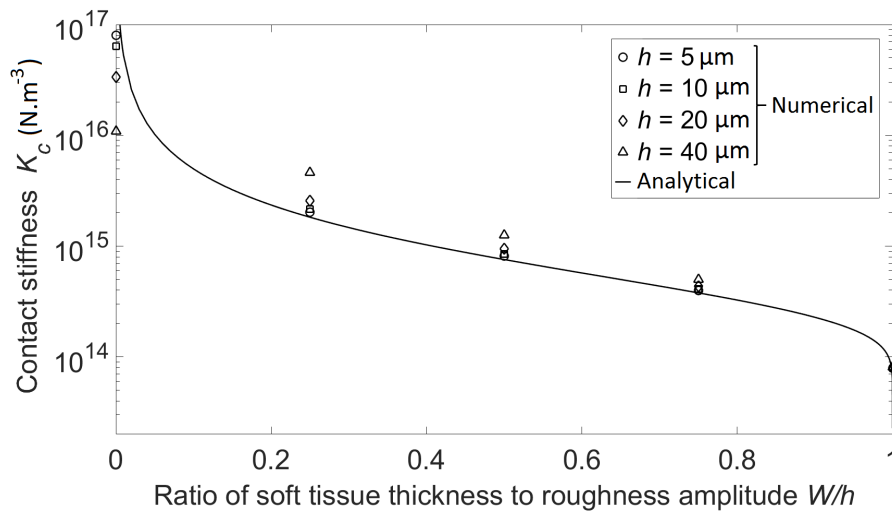


Figure 6.4 – Variation of the contact interface stiffness K_c as a function of the ratio of the soft tissue thickness W and of the roughness amplitude h for $L = 50 \mu\text{m}$. The solid line represents the analytical expression of K_c and punctual values represent values of stiffness obtained through numerical simulation for different values of h .

6.3.2 Stiffness K_{st} due to the presence of a soft tissue layer

Figure 6.5 shows the variation of the analytical and numerical stiffness K_{st} due to the presence of soft tissues as a function of the ratio the soft tissue thickness W and of the roughness amplitude h for $L = 50 \mu\text{m}$ and for different values of h . K_{st} decreases as a function of W/h and as a function of h . A relatively good agreement is obtained between analytical and numerical values when $W/h > 1$. However, for lower values of W/h , K_{st}^{num} is significantly higher than K_{st}^{ana} , especially for high values of h .

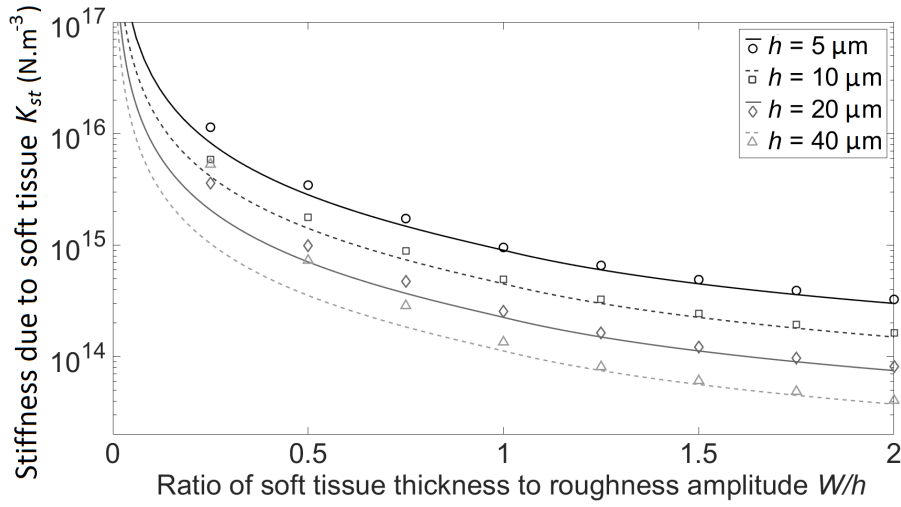


Figure 6.5 – Variation of the interface stiffness due to the presence of a soft tissue layer K_{st} as a function of the ratio of the soft tissue thickness W and of the roughness amplitude h for $L = 50 \mu\text{m}$ and for different values of h . The solid lines represent the analytical expression of K_{st} and punctual values represent values of stiffness obtained through numerical simulation.

6.3.3 Total stiffness of the interface K

Figure 6.6 presents the evolution of K_c^{ana} , K_{st}^{ana} and K^{ana} as a function of the ratio of the soft tissue thickness W and of the roughness amplitude h for $L = 50 \mu\text{m}$ and for different values of h . For low values of h ($h = 5 \mu\text{m}$ and $h = 10 \mu\text{m}$), the contribution of the contact stiffness is low compared to the contribution due to the presence of soft tissues. For $h = 20 \mu\text{m}$, both contributions are in the same order of magnitude. For $h = 40 \mu\text{m}$, the contribution of the contact stiffness becomes higher to the one due to the presence of soft tissues. For all values of h , a step decrease of K is obtained around $W/h = 1$, which corresponds to the point where the bone and the implant stops being in contact, so that K_c suddenly decreases to 0. Moreover, this decrease is more pronounced for higher values of h .

Figure 6.7 presents the evolution of K_c^{ana} , K_{st}^{ana} and K^{ana} as a function of the ratio the soft tissue thickness W and of the roughness amplitude h for $h = 20 \mu\text{m}$ and for different values of L . Figure 6.6 shows that for $L = 50 \mu\text{m}$, K_c and K_{st} are within the same range of values for $h = 20 \mu\text{m}$. For higher values of L ($L = 75 \mu\text{m}$ and $L = 100 \mu\text{m}$), K_c is lower than K_{st} , while for lower values of L ($L = 40 \mu\text{m}$ and $L = 25 \mu\text{m}$), K_c is higher than K_{st} .

6.3.4 Comparison between analytical and numerical reflection and transmission coefficients

Figure 6.8 shows the variation of r^{num} and r^{ana} as a function of W/h for $L = 50 \mu\text{m}$ and for different values of h . Figure 6.9 shows the variation of t^{num} and t^{ana} as a function of the ratio W/h for $L = 50 \mu\text{m}$ and for different values of h . The reflection coefficient increases as a function of W/h and of f_c , while the transmission coefficient decreases as a function of W/h and of f_c .

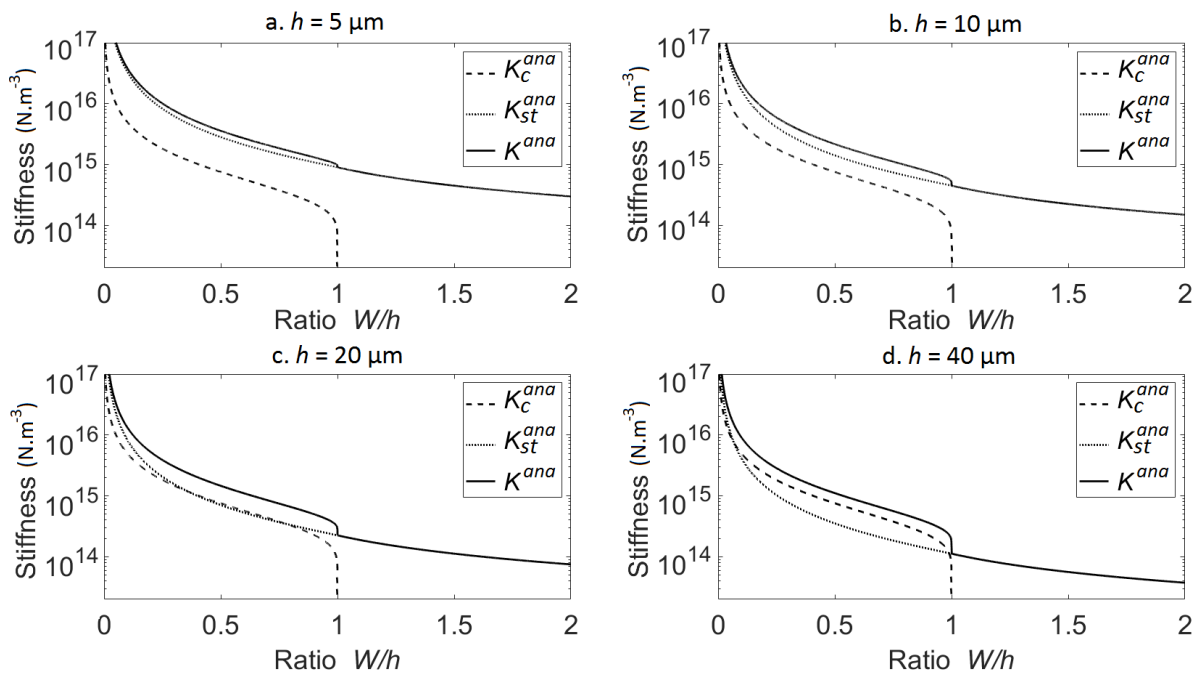


Figure 6.6 – Variation of the analytical total stiffness of the BII K^{ana} and of the stiffness contributions K_c^{ana} and K_{st}^{ana} as a function of the ratio of the soft tissue thickness W and of the roughness amplitude h for $L = 50 \mu\text{m}$ and (a) $h = 5 \mu\text{m}$, (b) $h = 10 \mu\text{m}$, (c) $h = 20 \mu\text{m}$, (d) $h = 40 \mu\text{m}$.

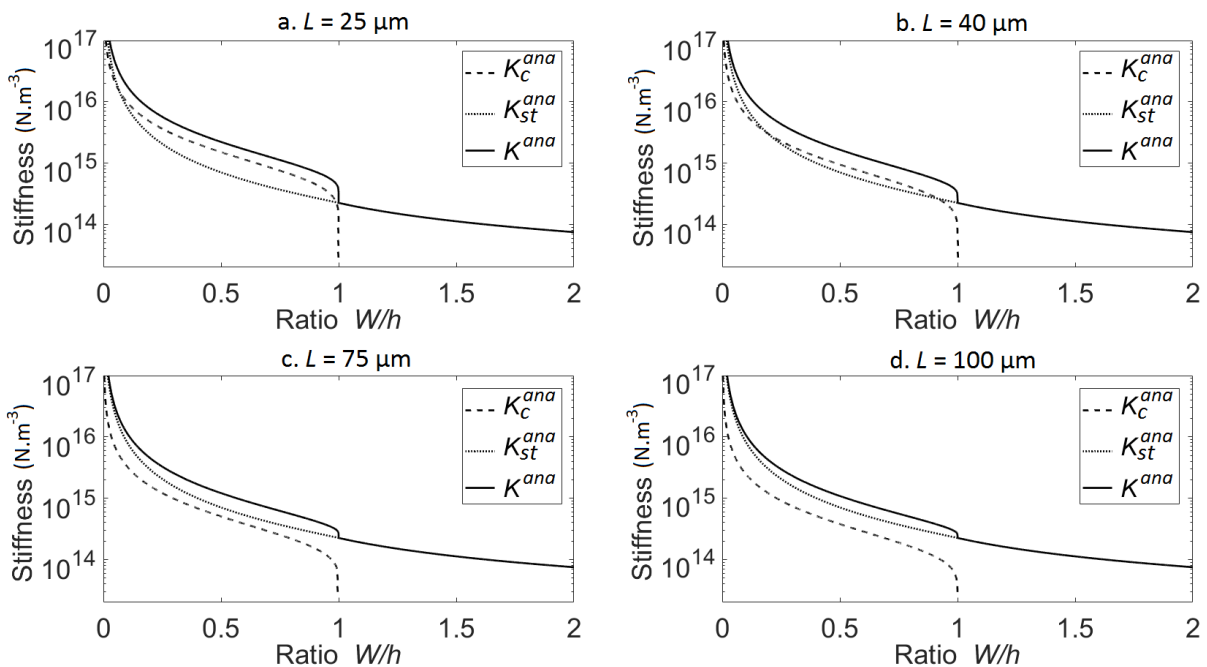


Figure 6.7 – Variation of the analytical total stiffness of the BII K^{ana} and of the stiffness contributions K_c^{ana} and K_{st}^{ana} as a function of the ratio of the soft tissue thickness W and of the roughness amplitude h for $h = 20 \mu\text{m}$ and (a) $L = 25 \mu\text{m}$, (b) $L = 40 \mu\text{m}$, (c) $L = 75 \mu\text{m}$, (d) $L = 100 \mu\text{m}$.

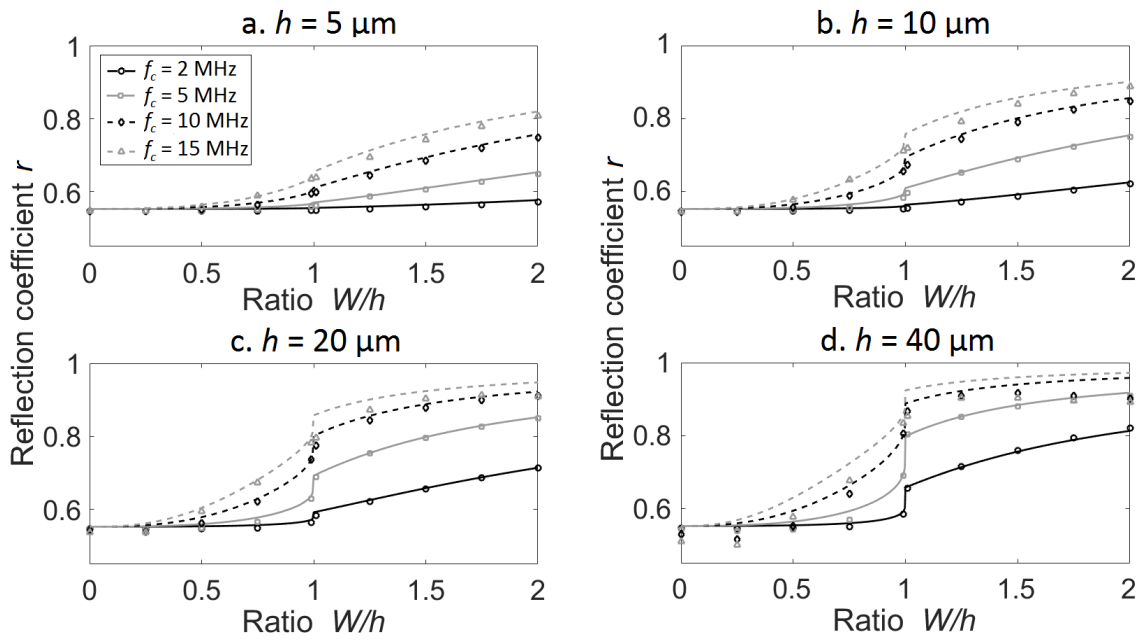


Figure 6.8 – Variation of the reflection coefficient of the BII as a function of the ratio of the soft tissue thickness W and of the roughness amplitude h for $L = 50 \mu\text{m}$, for different frequencies f_c and for (a) $h = 5 \mu\text{m}$, (b) $h = 10 \mu\text{m}$, (c) $h = 20 \mu\text{m}$, (d) $h = 40 \mu\text{m}$. Solid lines represent the analytical values r^{ana} whereas the symbols represent the numerical values r^{num} .

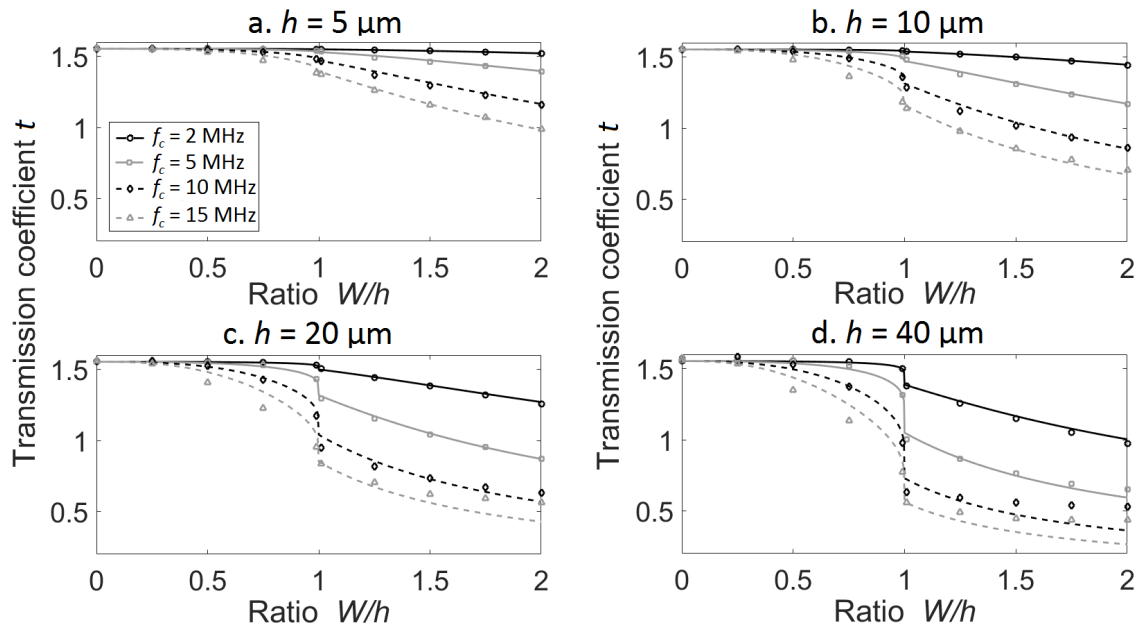


Figure 6.9 – Variation of the transmission coefficient of the BII as a function of the ratio of the soft tissue thickness W and of the roughness amplitude h for $L = 50 \mu\text{m}$, for different frequencies f_c and for (a) $h = 5 \mu\text{m}$, (b) $h = 10 \mu\text{m}$, (c) $h = 20 \mu\text{m}$, (d) $h = 40 \mu\text{m}$. Solid lines represent the analytical values t^{ana} whereas the symbols represent the numerical values t^{num} .

Overall, a good agreement is obtained between analytical and numerical results. In particular, a steep increase (respectively decrease) of the reflection coefficient (respectively transmission coefficient) is observed both analytically and numerically around $W/h = 1$, especially for high roughness and high frequencies. However, when $h.f_c$ is higher than around $200 \text{ MHz} \cdot \mu\text{m}$, significant differences are obtained between analytical and numerical results. In particular, for $h = 40 \mu\text{m}$ and $f_c = 10$ and 15 MHz , (i) for $W/h < 0.25$, the values of r^{num} are significantly lower than values of r^{ana} and (ii) for $W/h > 1.5$, r^{num} (respectively t^{num}) reaches a constant value, while r^{ana} (respectively t^{ana}) still increases (respectively decreases) as a function of W/h .

Figure 6.10 shows the evolution of the error e_1 between analytical and numerical results and of the error e_2 corresponding to the difference between r^{static} and r^{num} as a function of h for $L = 50 \mu\text{m}$. Both error functions increase as a function of h . Furthermore, while considering numerical stiffness values K^{num} leads to lower errors than considering analytical stiffness values K^{ana} , the error difference between the two approaches remains relatively low (around $2.5 \cdot 10^{-3}$). For all the configurations tested, the error between analytical and numerical models remained lower than $2.6 \cdot 10^{-2}$.

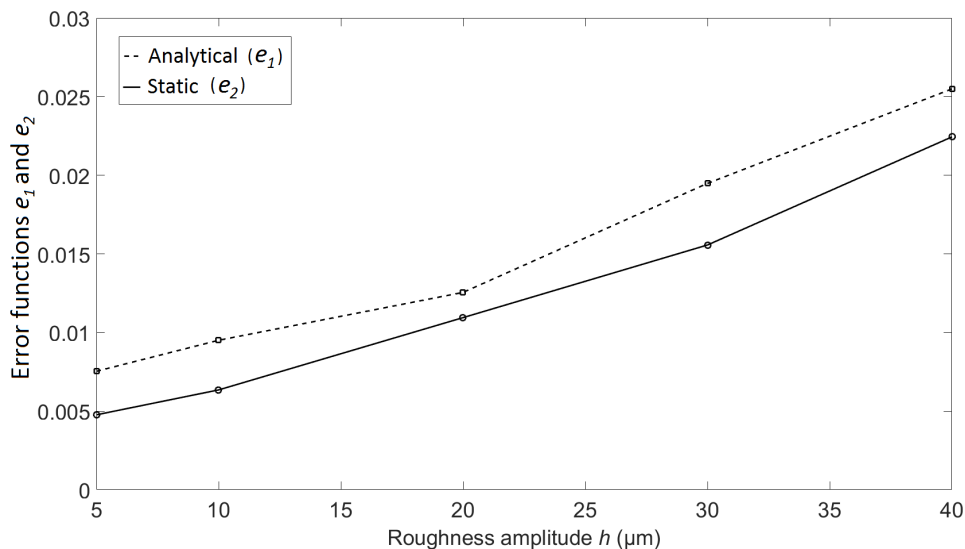


Figure 6.10 – Evolution of the error functions e_1 and e_2 as a function of the the roughness amplitude h for $L = 50 \mu\text{m}$

6.4 Discussion

6.4.1 Originality and comparison with the literature

The originality of this work is to provide an analytical model describing the interaction between an ultrasonic wave and the BII. The proposed model was validated through a comparison with numerical results obtained with FEM studies. Moreover, while most studies in the literature dealing with ultrasonic propagation at rough interfaces were performed in the frequency domain [16, 117, 264, 265], the present study was performed in the time domain, which is closer to configurations of interest.

The numerical model and the sinusoidal description of the BII considered in this chapter were derived from Chapter 4. Given the equivalence between original roughness profiles and sinusoidal profiles established in Chapter 5, the analytical model described herein could be generalized to real implant surface profiles. However, the macroscopic roughness of implants (*e.g.* threading of dental implants) was not considered in the present chapter because it would lead to interference phenomena (see Section 4.4.4), which could not be taken into account with a 2-D analytical model. Note that it is also possible to change the properties of bone tissue in the analytical model (see Eq. 6.11) in order to take into account the evolution of the biomechanical properties of bone, similarly to what was done in Section 4.3.4. In particular, Figure 4.8a shows the relative variation of r^{num} for $h = 5 \mu\text{m}$ and $f_c = 10 \text{ MHz}$ when varying the bone mass density ρ by $\pm 20\%$ compared to its reference value. For a given configuration ($h = 5 \mu\text{m}$; $L = 50 \mu\text{m}$; $W = h/2$ and $f_c = 10 \text{ MHz}$), r^{num} increased from 0.5508 to 0.6215 and r^{ana} increased from 0.5575 to 0.6280 when decreasing ρ from ρ_0 to $80\% \rho_0$. The low difference between r^{num} and r^{ana} when decreasing ρ by 20% further validates the analytical model.

Similarly as in Dwyer-Joyce et al. [61], the present study separately assessed stiffness contributions due to liquid and solid contact in order to determine the equivalent stiffness of a rough interface. In this former study, a lubricant layer was confined at the interface, while soft tissues were considered between the bone and the implant herein. In both studies, the analytical spring model was validated through comparisons with experimental or numerical results. However, lubrication aims at impeding the direct contact of surfaces, so that the contact stiffness contribution always remained lower than the lubricant layer contribution in Dwyer-Joyce et al. [61], which is a different situation compared to the present study. At the beginning of the osseointegration process ($W \geq 0.8 h$), there is a low contact between the bone and the implant, so that K_c is low compared to K_{st} . However, at the end of the osseointegration process ($W = 0$) the bone and the implant are in intimate contact, so that K_c can be higher than K_{st} . Therefore, both K_c and K_{st} can be predominant depending on the configuration of the BII (see Fig. 6.6 and 6.7). Different models of contact stiffness [128, 137] had thus to be considered herein and in Dwyer-Joyce et al. [61]. Moreover, the loss of validity of the analytical formula of K_{st}^{ana} for low values of W (see Fig. 6.5) may be due to the fact that this formula was designed for a configuration with low contact area at the interface ($K_c < K_{st}$).

6.4.2 Error between analytical and numerical results

Figures 6.8 and 6.9 show that analytical reflection and transmission coefficients (r^{ana} , t^{ana}) are in good agreement with numerical results. However, the error e_1 between analytical and numerical models was only estimated based on values of r^{ana} and not of t^{ana} because the reflection coefficient is the parameter of interest when investigating the properties of the BII with QUS (see Section 2.1). In particular, e_1 could be compared with the experimental precision $P = 0.011$ on the estimation of the reflection coefficient assessed in Mathieu et al. [155]. For roughness amplitudes h lower than $20 \mu\text{m}$, the error between analytical and numerical models remains lower to the experimental error (see Fig. 6.10). Consequently, for standard values of implant roughness, the analytical modeling of the BII should be sufficient to derive an accurate description of its ultrasonic response.

Moreover, Figs. 6.4 and 6.5 show that there are some differences between the values of K^{num} and K^{ana} , especially for low values of W and high values of h . However, e_1

and e_2 , which represent the error between r^{num} and r^{ana} and the error between r^{num} and r^{static} , respectively, are within the same order of magnitude. Therefore, the errors between K^{ana} and K^{num} have a relatively weak influence on the estimation of the reflection coefficient. It may be explained as follows. Equation 6.11 shows that the evolution of r^{ana} is especially sensitive to K when it has values around $(Z_{ti} \cdot Z_b \cdot \omega) / (Z_{ti} + Z_b)$, which corresponds to $K = 7.2 \cdot 10^{13}$ at 2 MHz, and $K = 5.4 \cdot 10^{14}$ at 15 MHz. However, errors between K^{ana} and K^{num} are most significant for stiffness values superior to $5 \cdot 10^{14}$, which therefore weakly affect the reflection coefficient. Furthermore, the higher sensitivity of r^{ana} and t^{ana} to values of K around $(Z_{ti} \cdot Z_b \cdot \omega) / (Z_{ti} + Z_b)$ also explains that the errors between the analytical and numerical models are lower for lower frequencies (see Fig. 6.8 and 6.9).

6.4.3 Contributions of K_c and K_{st}

Figures 6.6 and 6.7 show that the contribution of the contact stiffness K_c is predominant compared to the one of soft tissues when the implant roughness is high, *i.e.* for high values of h and for low values of L . It may be due to the fact that a higher implant roughness leads to a higher contact area between the bone and the implant, and therefore to an increase of K_c . Moreover, for higher roughness, a steeper increase (respectively decrease) of r^{ana} and r^{num} (respectively of t^{ana} and t^{num}) is observed around $W = h$. It may be explained as follows. Since K_c is predominant compared to K_{st} for higher roughness, the sudden decrease of K_c when W approaches h has a higher influence on the ultrasonic propagation at the BII in that configuration. Moreover, the steep increase of r around $W = h$ also depends on the frequency since r is especially sensitive to K for a given range of values which depends on the frequency, as described in last section.

6.4.4 Limitations

The 2D approach used for the analytical model is a strong approximation that may not take into account interference phenomena, which are known to occur for high implant roughness (see Chapter 4). In particular, reflection coefficients cannot be lower than 0.55 using the analytical model (which corresponds to $(Z_{ti} - Z_b) / (Z_{ti} + Z_b)$, see Eq. 6.11), while numerical results showed lower reflection coefficients for high roughness (see Eq. 6.11). The error between numerical and analytical results may also be related to the geometrical approximation of the BII by an array of periodic cracks to assess analytical contact stiffness (see Section 6.2.2), which may lose in validity for higher roughness. In particular, it may explain that the difference between K_c^{ana} and K_c^{num} (respectively between K_{st}^{ana} and K_{st}^{num}) increased as a function of h in Fig. 6.4 (respectively in Fig. 6.5). Moreover, limitations listed in Section 4.4.8 are also valid for the present chapter.

6.5 Conclusion

This chapter provides an analytical model of the ultrasonic propagation at the BII. The proposed model allows to replace the rough and multiphasic BII by a simple bi-spring model but still provides a good prediction of the reflected and transmitted coefficient measured from time-domain signals. The use of this analytical model may save computation

costs for future numerical studies, which can be complex due to the multiscale nature of the interaction between an ultrasonic wave and the BII. However, the analytical model was validated considering an ultrasonic wave in normal incidence. Therefore, it should be carefully used when modeling real implant geometries, in which multiple reflections and thus oblique incidence of the ultrasonic wave on the BII should be considered.

More generally, Part III emphasizes the influence of the implant surface roughness as well as of osseointegration phenomena on the interaction between an ultrasonic wave of different frequencies and the BII. Three models of the BII have been proposed, considering original or sinusoidal implant roughness, and using numerical or analytical approaches. An equivalence between the models using original and sinusoidal implant roughness was obtained through an optimization process (see Section 5.2.3), and an equivalence between the numerical and analytical models was obtained through Eqs. 6.6 and 6.8. Table 6.2 summarizes the main parameters of each model. The results lead to a better understanding of the interaction between an ultrasonic wave and the BII, which could help to improve the ultrasound characterization and stimulation techniques.

		Numerical		Analytical (Chapter 6)
		Sinusoidal (Chapter 4)	Original (Chapter 5)	
Ultrasonic wave		Central frequency f_c		
Implant		Titanium mechanical properties (ρ , C_p , C_s)		Impedance $Z_{ti} = \rho C_p$
Bone tissue		Bone mechanical properties (ρ , C_p , C_s)		Impedance $Z_b = \rho C_p$
Bone- implant Interface	Soft tissues	Soft tissues mechanical properties (ρ , C_p , C_s) Soft tissues thickness W		Stiffness due to the soft tissues K_{st}
	Implant roughness	Amplitude h Half-period L	Arithmetical mean roughness R_a Maximum peak height R_p Maximum valley depth R_v Spacing between irregularities S_m Similarity to a sinusoid s	Stiffness due to the partial bone-implant contact K_c

Table 6.2 – Main parameters used in the three models developed in Part III to describe the acoustical behavior of the BII.

Part IV

Applications of ultrasonic methods to dental implant stability estimation

Chapter 7. Experimental and numerical study of the ultrasonic propagation in a dental implant

Contents

7.1	Introduction	112
7.2	Material and Methods	112
7.2.1	Dental implant	112
7.2.2	Ultrasonic device	113
7.2.3	Laser-ultrasonics measurements	114
7.2.4	Numerical modeling and simulation	114
7.3	Results	115
7.3.1	Reproducibility of the measurements	115
7.3.2	Measurements of displacements along the threading	115
7.3.3	Numerical validation	117
7.4	Discussion	119
7.4.1	Propagation of a guided wave in a dental implant	119
7.4.2	Influence of the frequency of the excitation signal	120
7.4.3	Amplitude of displacements and transmitted energy	121
7.4.4	Limitations	121
7.5	Conclusion	122

7.1 Introduction

Part III described the interaction between ultrasound and the BII using a sinusoidal description of the implant roughness. Though a simple model may help to clarify the phenomena occurring during the propagation of an ultrasonic wave at the BII, complex geometries of real implants have to be considered in order to get a more realistic approach. Therefore, the present chapter will consider the ultrasonic propagation in a dental implant.

Understanding the phenomena occurring when an ultrasound wave propagates in a dental implant would be useful for both stimulation and characterization purposes. To do so, numerical simulation of wave propagation in a cylinder mimicking dental implant as well as in a dental implant has already been carried out, using finite difference and finite element modeling, and validated experimentally (see Section 2.1.4). The guided nature of the ultrasonic wave propagating in cylindrical implants has been evidenced [153, 281] but no previous study was able to show whether guided waves could propagate in dental implants.

Moreover, the amount of energy transmitted to the BII is an important parameter for applications corresponding to the ultrasonic characterization and stimulation of the BII (see Chapter 2). Concerning the characterization, the acoustical energy should be sufficiently low so that the tissues around the implant would not be damaged due to excessive micromotion which could be detrimental to osseointegration [261]. Concerning the stimulation, the acoustical energy must be sufficiently high to obtain a significant impact on the implant osseointegration. Note that vibrations generated by a LIPUS device to stimulate bone repair after a fracture have already been quantified using laser interferometric methods [95]. However, no study in the literature focused on the estimation of the displacement induced by an ultrasonic wave at the implant surface.

The goal of the present study is to investigate the interaction between an ultrasonic wave and a dental implant by coupling experimental and numerical approaches. To do so, the amplitude of the displacements generated by an ultrasonic transducer screwed into the dental implant were measured. Laser interferometric techniques were employed, and the data were processed to derive the velocity and the frequency of the first wave propagating along the implant axis. The experimental results were compared to their numerical counterparts.

The work presented in this chapter was published in *Ultrasound in Medicine and Biology* [105].

7.2 Material and Methods

7.2.1 Dental implant

A 10 mm long and 4.1 mm diameter conical dental implant made of grade 5, Ti-Al6-V4 titanium alloy, was used in the present study. The implant was manufactured by Zimmer Biomet (Warsaw, Indiana, USA) under the reference TSVT4B10. The geometrical configuration of the measurements is shown in Fig. 7.1. The implant was slightly polished locally on its extremity and laterally in regions of interest where laser ultrasonic measurements were carried out. Polishing was necessary to obtain a planar surface and therefore maximize specular reflection of the laser interferometer at the implant surface.

Sensitivity to the surface displacement and signal to noise ratio were thereby optimized.

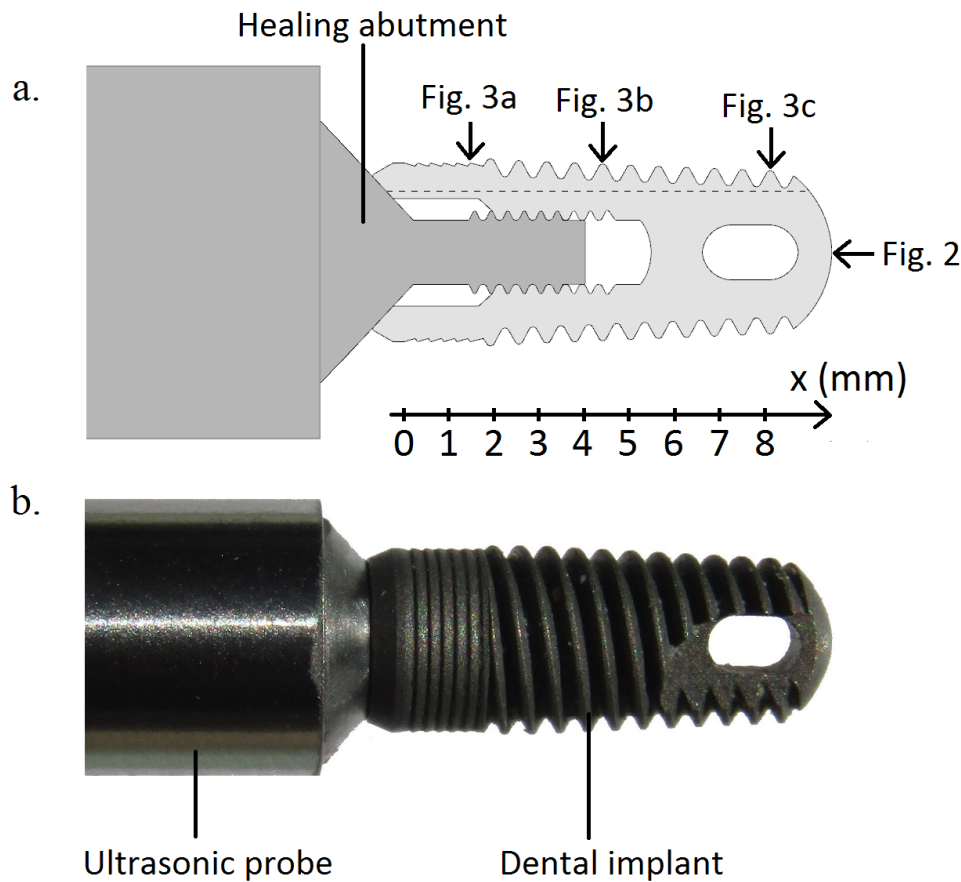


Figure 7.1 – (a) Schematic representation of the experimental setup with an ultrasonic transducer screwed into a dental implant. The x-axis corresponds to the implant axis. Arrows represent the positions corresponding to the results shown in Fig. 7.2 and 7.3. The dotted line represent the positions where radial displacements were numerically assessed to plot dispersion curves. (b) Ultrasonic probe and dental implant used experimentally.

7.2.2 Ultrasonic device

The ultrasonic device was composed of a 5 mm diameter planar ultrasonic mono-element contact transducer (Imasonic, Voray-sur-l'Ognon, France) generating a broadband ultrasonic pulse propagating perpendicularly to its active surface. The probe was used in echographic mode. Its center frequency was equal to 10 MHz, with a frequency bandwidth approximately equal to 6–14 MHz. The probe was rigidly attached to a titanium alloy dental healing abutment with a 5 mm long threaded part, which can be screwed into the implant, similarly to what was done in Vayron et al. [283, 283]. The healing abutment was screwed into the implant with a torque of 3.5 N.cm, which is around 10 times lower than values recommended for implant insertion [121], thus guaranteeing that the measurement is noninvasive. The ultrasonic probe was connected to a pulse generator (Sofranel, model 5052PR) via a standard coaxial cable. The pulse excitation had an amplitude of 100V and a duration of 200 ns.

7.2.3 Laser-ultrasonics measurements

A laser interferometer (B.M.industries, 91029 Evry, France), suited for the detection of ultrasound at the surface of cylinders with millimeter diameter [48, 208], was used in order to evaluate the amplitude of the displacements occurring at the implant surface. The displacements were measured at the extremity of the implant and at different positions along the implant axis. The surface of the implant where the displacements were measured was set perpendicularly to the axis of the beam of the laser interferometer so that the laser signal reflected by the implant could be correctly received by the laser interferometer. The size of the laser beam at the implant surface was about 100 μm . The measurements could not be made at regular spacing intervals because of the imperfect surface conditions of the implant, which did not allow to carry out the measurements for all locations of the implant surface. Therefore, measurements were spaced by around 0.5 mm from each other, but precise positions of measures were adapted so that the laser interferometer correctly received signals reflected by the implant. An oscilloscope was used to capture the signal given by the interferometer. Signals were averaged 500 times for each measurement. A calibration value provided by B.M.industries ($C = 100 \text{ mV/nm}$) allowed to derive the amplitude of the displacements at the surface of the implant and the frequency of the displacements was estimated from these signals. The reproducibility of the measurements was assessed by disassembling the entire set up and reproducing the measurements.

Similarly as in Bossy et al. [27], for all measured signals, the time of flight of the first arriving signal (FAS) was defined as the time for which signals first had an amplitude superior to a threshold equal to 0.5 nm, which is around 2.5 times higher to the magnitude of the noise. A linear interpolation of the variation of the time of flight of the FAS as a function of the position along the implant axis [237] allowed to derive the velocity of the FAS.

Laser-ultrasonics measurements were performed in collaboration with the I2M lab in Talence (University of Bordeaux).

7.2.4 Numerical modeling and simulation

The experimental configuration was reproduced numerically using a 2-D axisymmetric model, corresponding to half of the schematic representation shown in Fig. 7.1a. The approach was detailed in Vayron et al. [281, 282] and is briefly reminded in what follows. All the boundaries of the implant and of the ultrasonic transducer were considered as free. All parts considered in this model were assumed to have homogeneous isotropic mechanical properties and to be composed of Ti-Al6-V4. The mechanical properties of the titanium alloy considered in this study are the same as in Chapter 4 and are listed in Table 4.1.

The ultrasonic attenuation in Ti-Al6-V4 highly depends on the frequency and on the microstructure of titanium alloy. Typical values of bulk viscosity η were found between 1 and 15 Pa.s in the literature [36, 138, 209]. In this study, the same viscosity $\eta = 5 \text{ Pa.s}$ was used for both bulk and shear waves. The components of the stress tensor $\sigma_{i,j}$ in Ti-Al6-V4 are related to the components of the strain tensor $\epsilon_{i,j}$ by the equation:

$$\sigma_{i,j} = 2\mu_{ti}\epsilon_{i,j} + \lambda_{ti}\delta_{i,j}\epsilon_{k,k} + \eta\delta_{i,j}\dot{\epsilon}_{k,k} + 2\eta\dot{\epsilon}_{i,j} \quad (7.1)$$

where $\delta_{i,j}$ is the Kronecker delta, and (λ_{ti}, μ_{ti}) are the Lamé coefficients corresponding

to the mechanical properties of the titanium alloy (C_p , C_s , ρ) listed in Table 4.1.

The acoustical source is modeled by a broadband ultrasonic pulse with a uniform pressure $p(t)$ applied at the top surface of the transducer defined identically as in Chapter 4 (see Eq. 4.1). Different values of f_c were considered throughout this study (1 MHz, 5 MHz and 10 MHz).

All simulations were performed in the time domain using the finite element software COMSOL Multiphysics. Similarly as in Chapters 4 and 5, the implicit direct time integration generalized- α scheme [46] was used to calculate the transient response of the system. Once the solution was obtained, the displacements were determined on the extremity of the implant. To do so, the signal representing the displacement perpendicular to the implant surface was averaged along a vertical line of 150 μm located the closest as possible to the external surface of the implant.

7.3 Results

7.3.1 Reproducibility of the measurements

Figure 7.2 represents the signals measured at the extremity of the implant for three different measurements after the ultrasonic set-up had been screwed and unscrewed from within the implant. The aspect of the signals and the frequency contents are globally identical for all measurements. However, a slight change of up to 25 % in the maximum amplitude of the displacements was observed, which was presumably due to slight changes in the positioning and in the tightening of the implant. Nevertheless, Fig. 7.2 shows the relatively good reproducibility of the measurements in terms of signal pattern.

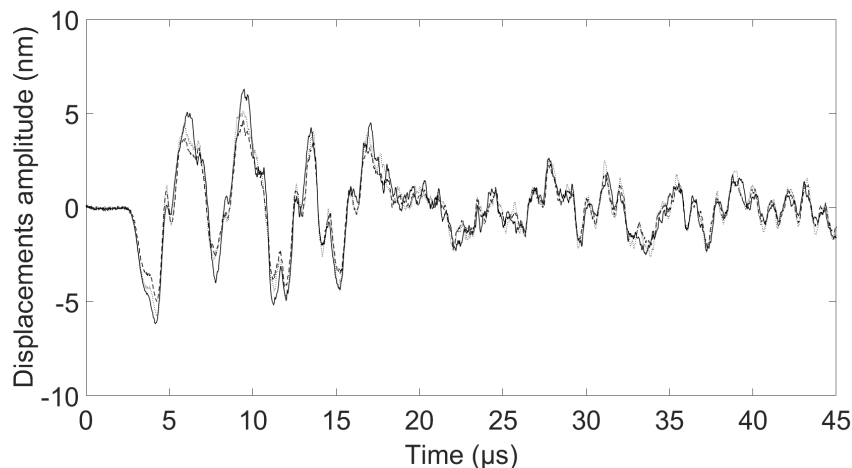


Figure 7.2 – Variation of the displacement measured at the extremity of the implant as a function of time for three measurements performed after screwing and unscrewing the transducer to the implant.

7.3.2 Measurements of displacements along the threading

The magnitude of the noise of the radiofrequency signals was estimated by considering the maximum amplitude of displacements before the time of flight of the FAS (*e.g.* for

time values between 0 and 3 μs in Fig. 7.2). It was about 0.2 nm for each reproduction of the measurement, which is 15 to 60 times lower than the amplitude of the measured signal. Figure 7.3 shows the variation of the measured displacement as a function of time at three different locations along the implant threading. Figure 7.3 shows that for each position, and especially towards the end of the threading (Fig. 7.3c), the most energetic contribution is of relatively low frequency and arrives at a relatively short time, as was also observed at the extremity of the implant (see Fig. 7.2). This low frequency contribution corresponds to the main component of the ultrasonic wave, whereas the contributions issued from multiple reflections of the ultrasonic wave on the implant boundaries are less energetic and arrive later.

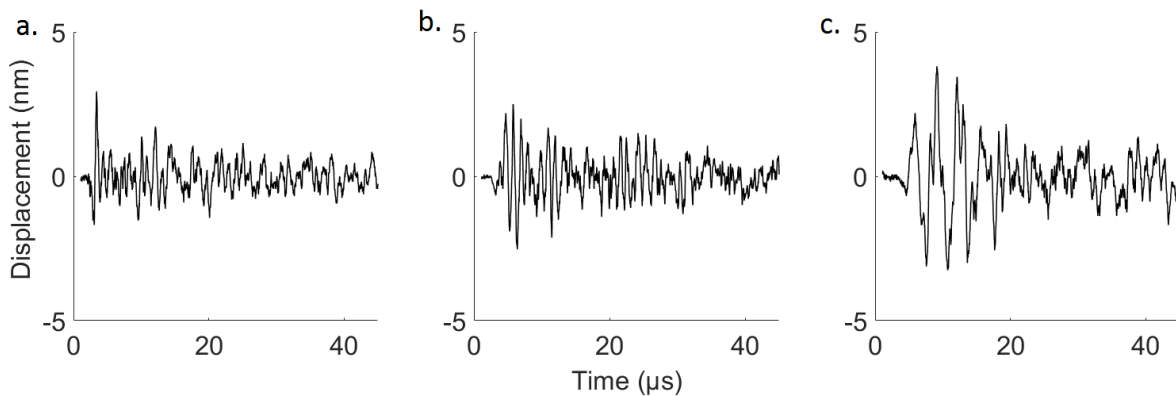


Figure 7.3 – Variation of the displacement at the implant surface measured experimentally as a function of time (a) at the beginning of the threading ($x = 1.5$ mm), (b) at the middle of the threading ($x = 4.35$ mm), and (c) at the end of the threading ($x = 8.3$ mm).

Figure 7.4 represents the frequency spectra associated to the three signals shown in Fig. 7.3. Most components of the spectra are comprised between 0 and 1.5 MHz. For each spectrum, energetic contributions are present around 300 kHz and 900 kHz. For relative low values of x (Fig. 7.4a and 7.4b), an important number of contributions may be distinguished around 300 kHz and 900 kHz, while for higher values of x (Fig. 7.4c), the signal has fewer frequency components.

Figure 7.5a shows the variation of the peak-to-peak amplitude of the displacement as a function of time along the implant axis (corresponding to the x direction), which is comprised between 3.2 nm and 8.9 nm. At the extremity of the implant, the maximum value of the amplitude of displacements is equal to 9.7 nm. Considering a frequency of 300 kHz, which is the main component of the frequency spectra for this position (see Fig. 7.6b), the aforementioned displacement amplitude corresponds to a particle velocity of around $v_m = 18 \text{ mm}\cdot\text{s}^{-1}$. As shown in Fig. 7.5a, the maximum amplitude of the displacement globally decreases during the first 3.5 mm, but then alternates between increasing and decreasing to reach two local maxima around $x = 4.5$ mm and around $x = 7.5$ mm. No repositioning or unscrewing of the implant was realized through the measurements presented on Fig. 7.5a. Therefore, the reproducibility was significantly better than the one obtained in Subsection 7.3.1, with a variation of the displacement amplitude inferior to 10% when reproducing measures for the same position.

Figure 7.5b shows the variation of the time of flight of the FAS as a function of the

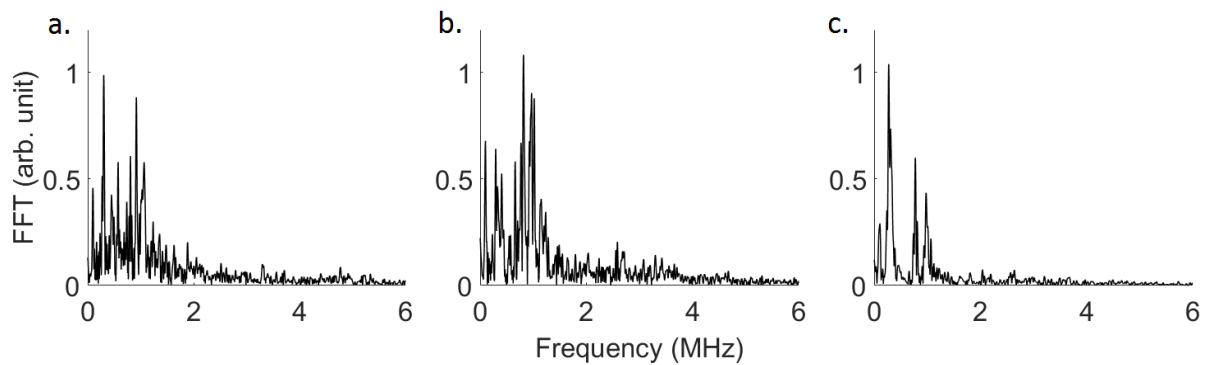


Figure 7.4 – Frequency spectra corresponding to the modulus of the Fast Fourier Transform (FFT) of the signals measured experimentally (a) at the beginning of the threading ($x = 1.5$ mm), (b) at the middle of the threading ($x = 4.35$ mm), and (c) at the end of the threading ($x = 8.3$ mm).

position of the measurement along the x-axis. A linear regression analysis was performed and indicates a wave propagation velocity of around 2110 m.s^{-1} , which corresponds to the FAS velocity [91].

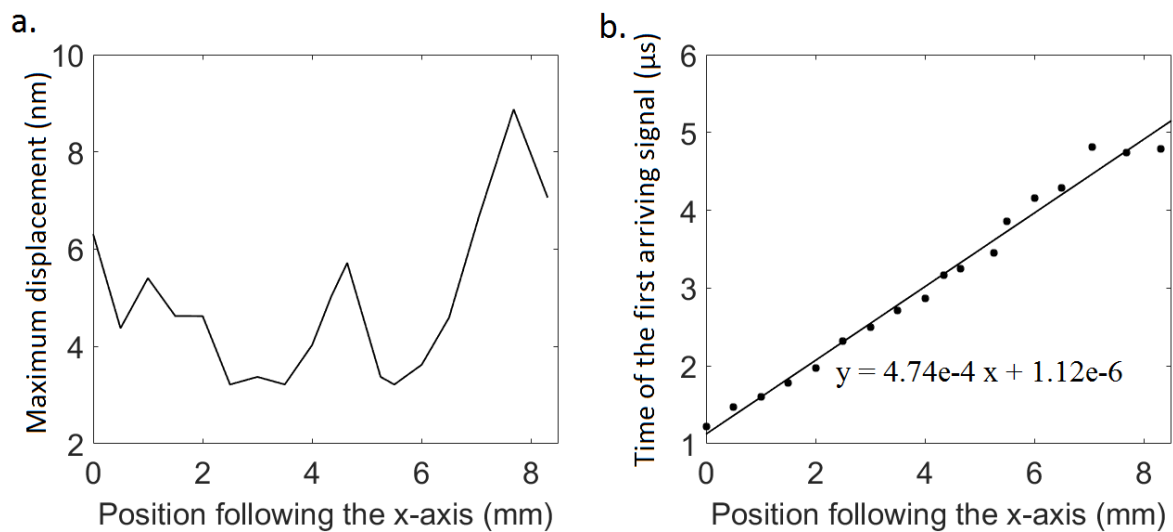


Figure 7.5 – Variation of (a) the peak-to-peak amplitude of the displacement at the implant surface and (b) the time of the first arriving signal (FAS) as a function of the position along the implant axis. The solid line in (b) corresponds to a linear regression analysis leading to a FAS velocity equal to 2110 m^{-1} .

7.3.3 Numerical validation

Figure 7.6 shows the comparison between numerical and experimental results obtained at the implant extremity. The amplitude of the numerical signals was normalized so that it corresponds to the experimental measurements. Figure 7.6b indicates that the frequency components of the experimental and numerical data are lower than the central frequency of the excitation signal ($f_c = 10$ MHz). However, frequency components obtained numer-

ically are higher than for experimental data, and are mostly comprised between 0 and 4 MHz.

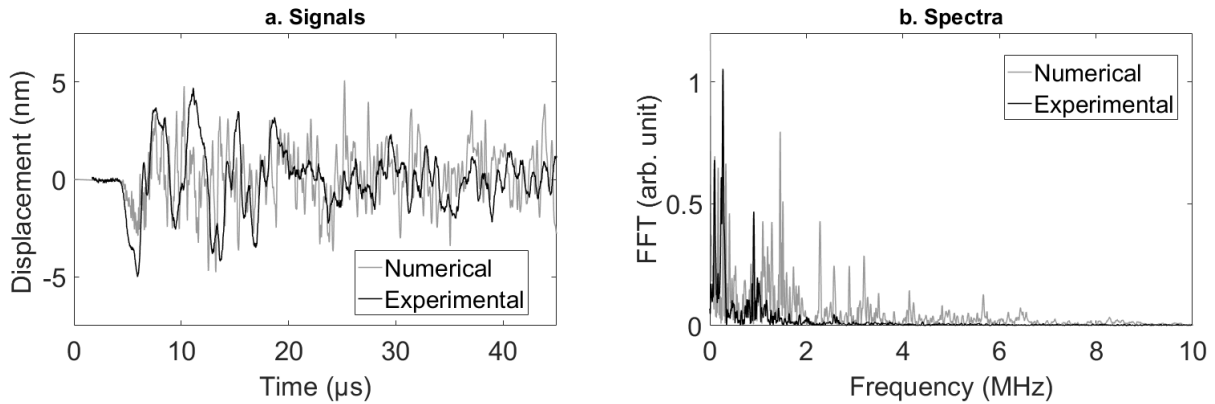


Figure 7.6 – (a) Variation of the displacement measured experimentally (black lines) and simulated numerically (grey lines) for $f_c = 10$ MHz as a function of time at the extremity of the implant. (b) Frequency spectrum associated to each signal.

Figure 7.7 shows the frequency spectra of numerical signals obtained at the extremity of the implant for transducers with different central frequencies f_c equal to 1 MHz, 5 MHz and 10 MHz. Spectra obtained with 5 MHz and 10 MHz transducers are nearly identical, with the main components comprised between 100 kHz and 1.7 MHz, but also a few other components between 1.7 MHz and 3.5 MHz. The spectrum obtained for a 1 MHz transducer is slightly different since it does not contain any frequency component over 1.5 MHz. The results show that the spectrum of the signal weakly depends on the excitation frequency when considering frequencies over 5 MHz.

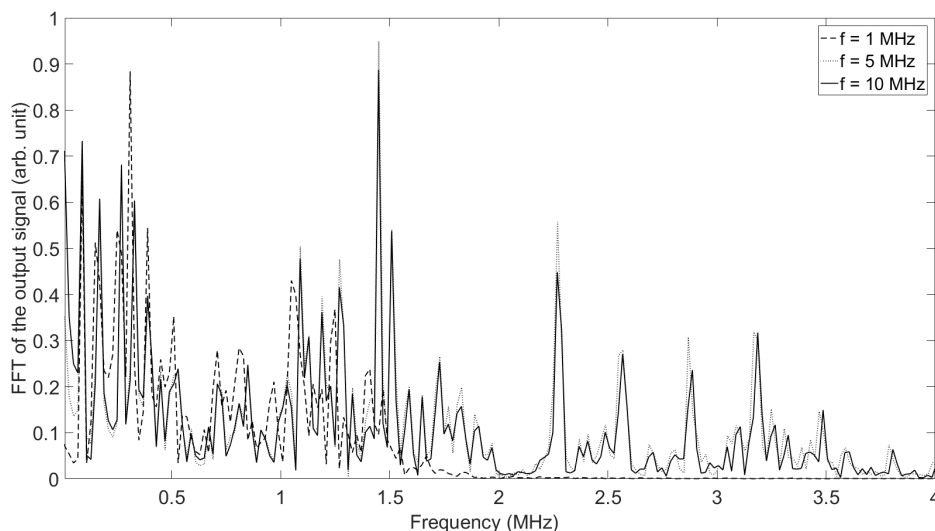


Figure 7.7 – Fast Fourier Transforms (FFT) of the displacement simulated at the extremity of the implants for transducers of central frequencies equal to 1 MHz, 5 MHz and 10 MHz.

7.4 Discussion

The originality of the present study is to propose a combination of experimental and numerical approaches in order to provide further insight on the propagation of an ultrasonic wave in a dental implant. Such investigation is particularly important in the context of ultrasound characterization and stimulation of dental implant osseointegration.

7.4.1 Propagation of a guided wave in a dental implant

Figure 7.4 shows that the frequency spectra corresponding to the displacement measured experimentally are mainly composed of low frequencies (mostly between 300 kHz and 2 MHz) compared to the excitation central frequency (10 MHz). Figure 7.4 also shows that the amplitude of high frequency components tends to decrease along the implant axis. The observation of low-frequency components may result from the attenuation of the ultrasonic wave while propagating along the 1 cm long titanium implant.

Although the frequency range obtained numerically is slightly higher than that obtained experimentally, the numerical results shown in Fig. 7.6b confirm that only low frequencies (between 1 and 3 MHz) are obtained in the implant. The higher frequencies obtained numerically may be explained through different modeling approximations. First, the ultrasonic excitation defined by Eq. 4.1 might not have the exact same characteristics (center frequency, spectral band) as in experiments. Second, the transducer was considered as a perfect planar piston source. Third, the contact between the transducer and the implant was considered as perfect in the simulations. Fourth, the surface roughness of the implant was not considered.

Moreover, Fig. 7.5b indicates that the wave velocity of the FAS is equal to 2110 m.s⁻¹, which is significantly lower than the bulk longitudinal velocity ($C_p = 5810$ m.s⁻¹ in titanium alloys). These two results (slow and low frequency wave propagation) indicate the presence of a dispersive ultrasound wave guided by the implant structure.

In order to understand the value of the wave velocity obtained for the FAS, the dispersion curves of phase velocities were numerically assessed using the numerical model, similarly to what was done in Barshinger and Rose [20] and in Djili and Fouad [56]. Radial displacements were punctually assessed every 10 μm along the dotted line shown in Fig. 7.1a. A double Fourier transform with respect to time and space was then performed to obtain the dispersion curves shown in Fig. 7.8. The maximum amplitudes of the double Fourier transform were obtained for frequencies between 0.7 to 1.3 MHz and phase velocities between 1900 and 2400 m.s⁻¹, which corresponds to frequencies observed experimentally (see Fig. 7.4) and to the experimental speed of the FAS (equal to 2110 m.s⁻¹).

Numerical dispersion curves were also compared to analytical ones obtained using the software Disperse [213] in order to better understand the different modes of propagation of the ultrasonic wave. To do so, the dental implant was approximated by a hollow cylinder made of titanium alloy to obtain a simple model that could be solved analytically by considering the dispersion equation associated to the Disperse software. The values of the internal and external diameters of the cylinder (1.6 and 3.6 mm) were determined based on the implant geometry (see Fig. 7.1). The white lines in Fig. 7.8 represent the analytical dispersion curves corresponding to the first three longitudinal modes propagating in the hollow cylinder. Some similitudes concerning the longitudinal modes L(0,1) and L(0,2)

may be observed for the dispersion curves obtained with the analytical and numerical models. For frequencies higher than 4 MHz, the phase velocity reaches a constant value around 2900 m.s^{-1} in both cases. However, under 4 MHz, many low frequency components were obtained numerically and could not be related to any of the modes determined analytically. The differences between the analytical and numerical models may be due to (i) the approximate geometry considered for the analytical model and (ii) the multiple scattering of the ultrasonic wave occurring numerically due to the complex geometry considered (see Fig. 7.1a). Nevertheless, for a frequency of 700 kHz, the high velocity components (over 6000 m.s^{-1}) found numerically correspond to the vertical asymptote obtained analytically at the same frequency for the mode L(0,2). Finally, the third longitudinal mode L(0,3) and higher longitudinal modes were not observed numerically since they occur for higher frequencies (over 2.5 MHz) than L(0,1) and L(0,2).

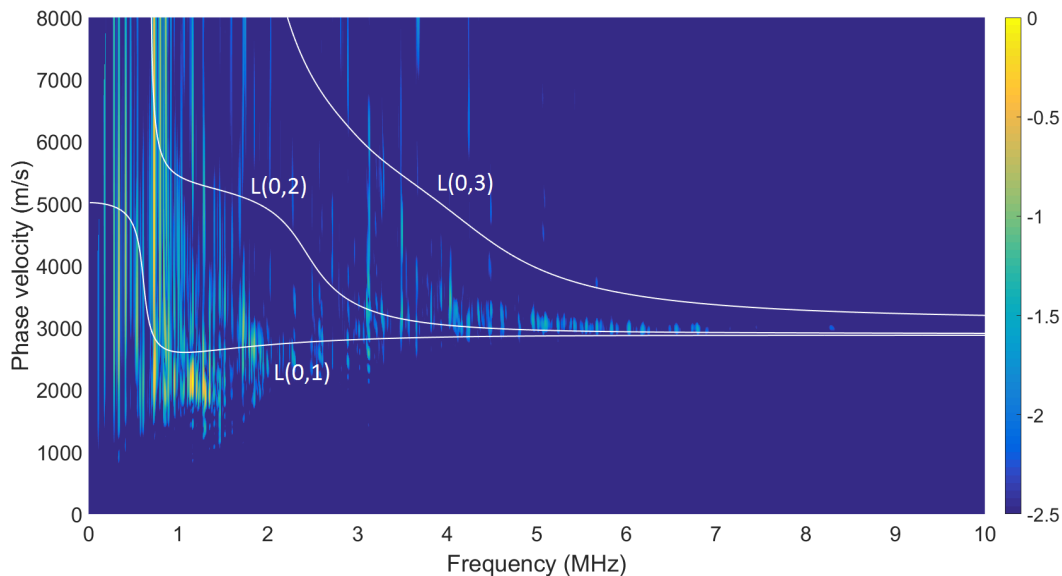


Figure 7.8 – Intensity distribution (dB scale) of the modes propagating in a dental implant in the wavenumber-frequency diagram. The lines correspond to the variation of the phase velocity as a function of the frequency (dispersion curves) of the first three longitudinal modes corresponding to the propagation in a hollow cylinder with an external (respectively internal) diameter of 3.6 mm (respectively 1.6 mm) obtained with the software Disperse [213].

7.4.2 Influence of the frequency of the excitation signal

The results shown in Fig. 7.7 indicate that the frequency components of the ultrasonic response of the implant weakly depend on the central frequency of the excitation signal, as it is expected for a guided wave. This result may affect the choice of the central frequency of the transducer which may be changed between 3 and 10 MHz without affecting significantly wave propagation in the dental implant, as shown in Fig. 7.7. Note that previous studies on the characterization of dental implant stability used a center frequency of 10 MHz (see Section 2.1). Reducing the frequency down to 3 MHz would therefore not significantly modify the ultrasonic propagation and the results obtained with the ultrasonic

set-up. However, further experimental studies are needed to confirm this point.

7.4.3 Amplitude of displacements and transmitted energy

The experimental results show that the amplitude of the displacement reaches local maximum values around $x = 4.7$ mm and around $x = 7.3$ mm (see Fig. 7.5a). These locations correspond to regions of interest where the implant geometry has an internal cavity, at the end of the abutment of the transducer and at the extremity of the implant (see Fig. 7.1). These results may be explained by a concentration of the acoustic energy in regions where the section is lower compared to regions where the cylinder is full. However, the amplitude of the displacement always remains inferior to 10 nm, which is far from the critical level of micromotion (around 50 μm to 150 μm) that may prevent osseointegration [261].

Regulations from the FDA indicate an exposure limit of 720 mW/cm² for diagnostic ultrasound equipment in its legislation from 2017. In our case, the average intensity transmitted by the ultrasonic wave to the implant may be derived from Eq. 7.2 [197]:

$$I = \frac{1}{2} Z_{ti} v_m^2 \quad (7.2)$$

where Z_{ti} is the acoustical impedance of the titanium alloy. Considering the particle velocity v_m measured at the extremity of the implant (see Subsection 7.3.2), the average intensity sent by the ultrasonic transducer is around 460 mW/cm², which therefore respects the FDA requirements.

The excitation signal sent to the transducer is similar to the one used in previous studies using the QUS device developed by my group to assess implant stability (see Section 2.1). Most studies on LIPUS stimulation of implant osseointegration focused on lower intensities, around 30 or 40 mW/cm² (see Table 2.3), but applied during longer duration in the harmonic regime, while the present study was performed in transient mode. Therefore, the amplitude of the displacement measured herein are not representative of displacements generated by LIPUS stimulation. The present study emphasizes that mechanical stimulation induced by ultrasound is highly sensitive to the geometrical configuration and provides order of magnitude of the acoustical energy sent to the BII.

As described above, the geometrical configuration strongly influences the distribution of the acoustical energy at the BII, which in turn significantly influences bone regeneration at the wound site [151]. For example, Harrison et al. [95] investigated nanomotion induced by LIPUS on a fracture site and measured displacements between 0.16 and 0.56 nm with a laser interferometer. It concluded that this precise range of motions promoted an intracellular pathway stimulating bone growth. At the same time, a review of controlled trials indicated that the efficiency of LIPUS on bone regeneration could not be proved [242]. A possible hypothesis is that LIPUS stimulation failures might be explained by ill-adapted choices of LIPUS parameters for the considered configuration, resulting in mechanical effects that may have no impact on bone regeneration.

7.4.4 Limitations

This study has several limitations. First, the implant measured experimentally had been partially polished on one side, which removed a small part of its threading and may

have influenced the results. However, the surface where the implant was polished was around 15% of the implant surface and the geometry was not significantly modified.

Second, the present study only considered the situation where the implant was surrounded by air. The values of displacement of the implant are likely to be lower when considering an implant surrounded by bone or by soft tissues, and the energy transmitted to these media would therefore be lower. Considering implants inserted in bone tissue would be of interest to precisely quantify the intensity transmitted by an ultrasonic wave to the BII. However, the present study provides an upper bound of the acoustic energy applied at the implant surface.

Third, several approximations have been made in the numerical model. In particular, the acoustical source was considered to have a uniform pressure. The geometry of the implant was also approximated, since real threading cannot be thoroughly axisymmetric. A 3D model would therefore depict more precisely the real configuration. Moreover, different values of attenuation coefficient were found in the literature for the titanium alloy, and the one that was chosen in this study may therefore be approximate. Eventually, other types of implant geometry should also be considered and may affect the results.

7.5 Conclusion

This study emphasizes that the propagation of an ultrasonic wave in a titanium dental implant is guided by the implant structure. For characterization purposes, the results indicate that it is not necessary to consider high frequency transducers since ultrasound propagate at frequencies comprised between 300 kHz and 2 MHz in the implant. For stimulation purposes, the results indicate that the intensity transmitted to the BII is highly sensitive to the considered structure.

Chapter 8. Comparison of resonance frequency analysis and quantitative ultrasound methods to assess bone-implant contact

Contents

8.1	Introduction	124
8.2	Material and Methods	124
8.2.1	Animals	124
8.2.2	Surgical procedure	124
8.2.3	Resonance frequency analysis	125
8.2.4	Quantitative ultrasound device	125
8.2.5	Histology	127
8.3	Results	127
8.3.1	Sample analysis and BIC estimation	127
8.3.2	Resonance frequency analysis	128
8.3.3	Ultrasonic measurements	129
8.4	Discussion	131
8.4.1	Originality of the study	131
8.4.2	Evolution of ISQ, UI and BIC values with healing time	131
8.4.3	Correlation between ISQ and BIC values	131
8.4.4	Correlation between UI and BIC values	132
8.4.5	Comparison between RFA and QUS techniques	132
8.4.6	Limitations	133
8.5	Conclusion	133

8.1 Introduction

Chapter 7 described the propagation of an ultrasonic guided wave in a dental implant. The present chapter will now investigate a possible application of ultrasound techniques for dental implantology, which is the assessment of dental implant stability.

The clinical assessment of dental implant stability is a difficult problem [92] because it depends on many parameters such as the geometry and surface properties of the implant, the surgical protocol, and the patient behavior and bone quality (see Subsection 1.3.4). Moreover, there is a lack of standardization of the surgical procedures used in oral implantology, in particular concerning the choice of the duration between implant insertion and loading, which may vary from 0 up to 6 months [223]. Accurate measurements of dental implant stability are therefore of interest since they could improve the surgical strategy by adapting the choice of the healing period in a patient specific manner.

RFA (see Section 1.4.5) and QUS (see Section 2.1) may both be used to assess dental implant stability. Recently, the performance of the two techniques were compared *in vitro* [284] and *in vivo* on sheep [283] (see Section 2.1, Figures 2.3 and 2.9). Both studies showed a better sensitivity of QUS to retrieve information on the properties of the BIL. However, the results obtained with the QUS and RFA devices were not compared to the BIC ratio, which is the gold standard to assess dental implant stability.

The aim of the present study is to evaluate the performance of the RFA and QUS techniques to assess dental implant stability by comparing the results obtained with both methods to those obtained via histological analysis, which leads to an estimation of the BIC ratio. To do so, dental implant inserted in rabbit femur and tibia bone were used. Stability measurements were realized with both techniques (RFA and QUS) at different healing times (0, 4, 8 and 13 weeks), and were then compared to the BIC ratio obtained via histological analysis for each sample.

The work presented in this chapter was submitted in *Clinical Oral Implants Research* [108].

8.2 Material and Methods

8.2.1 Animals

Thirteen 5-month-old New Zealand White male rabbits (Charles River, L'Arbresle, France) with an average weight of 4.360kg were used in the present study. Animals were handled in accordance with the *European guidelines for care and use of laboratory animals*, and the study was approved by the ethics committee of the National Veterinary School of Alfort.

8.2.2 Surgical procedure

The surgical procedure was performed in collaboration with the National Veterinary School of Alfort by the surgeon Dr. Hugues Albin Lomami. Twenty-two identical Ti6Al4V titanium alloy, 10 mm long and 4 mm diameter conical dental implants were used in the present study. The implants were manufactured by Zimmer Biomet under the reference TSVT4B10, similarly as in Chapter 7.

Each dental implant was placed in the femur or tibia of the rabbits as shown in Figure 8.1, similarly to what was done in previous studies [26, 179, 241]. The surgical procedure described in more details by Pearce et al. [214] was reproduced. Briefly, a single skin incision was performed on each rabbit leg around the knee articulation. A conical cavity (10-mm deep and 4.0-mm wide) was created in the medial condyle of each bone in a stepwise fashion, using color-coded 10-mm-length surgical drills (2.3, 2.8, 3.4 mm diameter; Zimmer Biomet). These cavities were thoroughly rinsed with an isotonic saline solution to remove bone fragments prior to the insertion of the titanium implants. Three rabbits were sacrificed at 0, 4 and 8 weeks after initial implant surgery, and four rabbits were sacrificed at 13 weeks after the surgery. The QUS and RFA measurements were realized just before the animal sacrifice. A total number of implants comprised between 1 and 3 was inserted in each rabbit.

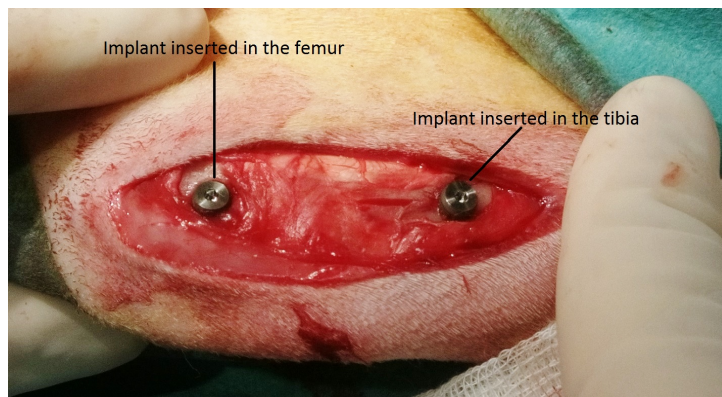


Figure 8.1 – Photography of two dental implants inserted in a rabbit femur and tibia.

8.2.3 Resonance frequency analysis

The RFA response of each implant was measured in ISQ units (on a scale from 1 to 100) using the Ostell device. Figure 8.2 shows the configuration of the measurements, which were realized using a smart peg screwed into the implant, as recommended by the manufacturer. Each measurement was performed in two perpendicular directions denoted 0° and 90° , and was repeated three times in order to assess the reproducibility of the measurements. The values obtained in the 0° direction (respectively in the 90° direction) were denoted $ISQ0$ (respectively $ISQ90$). For each sample $\#i$, the average and standard deviation of the three values of $ISQ0$ (respectively $ISQ90$) were denoted $ISQ0_i^m$ and $ISQ0_i^{std}$ (respectively $ISQ90_i^m$ and $ISQ90_i^{std}$).

8.2.4 Quantitative ultrasound device

The QUS device consists of a planar ultrasonic monoelement transducer (Sonaxis, Besançon, France) which generates a 10 MHz broadband ultrasonic pulse propagating perpendicularly to its active surface. The probe was attached rigidly to a titanium alloy dental healing abutment as it was done in Vayron et al. [283]. The healing abutment is screwed into the implant so that the measurements are not influenced by positioning problems of the probe related to the abutment. The QUS device was screwed into the

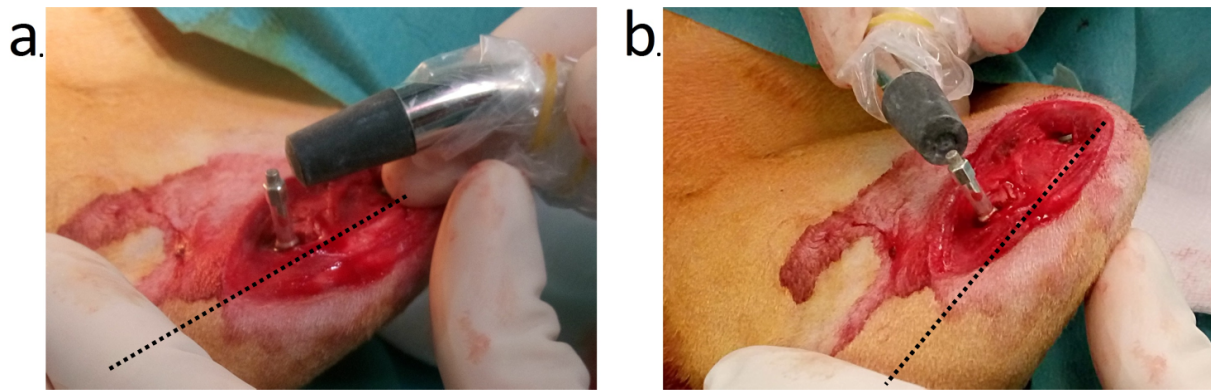


Figure 8.2 – Measurement configuration of the implant stability quotient (ISQ) using the RFA device realized in two perpendicular directions ((a): 0° and (b): 90°). Dotted lines represent the tibia axis.

implant in order to realize the measurement for each implant, as shown in Figure 8.3. The ultrasonic probe was linked to a pulser-receiver via a standard coaxial cable. A transient recorder was used to record the radiofrequency (rf) signal with a sampling frequency equal to 100 MHz.



Figure 8.3 – Measurement configuration of the ultrasonic indicator using the ultrasonic transducer screwed into a dental implant.

For each measurement, the transducer was screwed in the implant with a controlled torque of 3.5 N.cm, which is around 10 times lower than torque values recommended by implant manufacturers for the implant insertion [121]. The ultrasound measurement was made instantaneously. The transducer was then unscrewed and the same measurement was carried three times in order to assess the reproducibility of the measurements.

The same method as in Vayron et al. [283] was used to derive an ultrasonic indicator UI , which was shown to be related to implant stability. The envelope $S(t)$ of the radiofrequency signal $s(t)$ was first determined. Then, an indicator I that estimates the average amplitude of the signal between 20 and 120 μ s was defined following:

$$I = \sum_{i=2,000}^{12,000} S(iT_0) \quad (8.1)$$

where $T_0 = 0.01 \mu\text{s}$ corresponds to the sampling period. The lower bound of the time window was chosen equal to $20 \mu\text{s}$ to not consider first values of the RF signals, which are approximately constant due to a saturation of the signals. The upper bound of the time window was chosen equal to $120 \mu\text{s}$ to get a good compromise between a sufficient duration to obtain relevant information and the requirement of a sufficient signal to noise ratio for all RF signals. In order to obtain values that (i) are comprised between 1 and 100, similarly to the ISQ and (ii) increase when bone quantity and quality increase around the implant, the ultrasonic indicator UI was defined by:

$$UI = 100 - 10 * I \quad (8.2)$$

For each sample $\#i$, the average and standard deviation of the three values of UI were denoted UI_i^m and UI_i^{std} .

8.2.5 Histology

After the RFA and QUS measurements were realized, the animals were sacrificed and the samples were prepared for histological analysis. A procedure described in detail by Soffer et al. [254] and Chevallier et al. [44] for nondecalcified histology was used. Histological images were analyzed by classical microscopy in order to evaluate the percentage of the implant surface in intimate contact with mineralized bone tissue, which was assessed manually. Two histological sections (see Fig. 4.13) were studied for each sample, so that two histological measurements of the BIC could be realized. For each sample $\#i$, the average and standard deviation of the two BIC ratio were denoted BIC_i^m and BIC_i^{std} .

8.3 Results

8.3.1 Sample analysis and BIC estimation

Table 8.1 shows the average value of BIC_i^m and BIC_i^{std} obtained for all samples corresponding to the same healing duration and to all data pooled. The mean value of BIC_i^{std} corresponds to the average reproducibility of the BIC measurements. Table 8.1 also shows the standard deviation of BIC_i^m obtained for all samples corresponding to the same healing duration and to all data pooled, which corresponds to the interspecimen variability. ANOVA test of the results obtained with all 22 implants showed a significant effect of healing time on the BIC ratio (p-value = 5.8×10^{-5}), with BIC values first increasing as a function of healing time and then decreasing for healing times between 8 and 13 weeks. However, an important interindividual variability was also observed for samples with a healing time of 13 weeks. The mean measurement error was comprised between 2.62 and 5.84 for the various values of healing durations.

Table 8.1 – Average value, mean measurement error and interindividual variability obtained for the BIC, *ISQ0*, *ISQ90* and *UI* values for each healing duration and for all data pooled.

Healing time (weeks)		0	4	8	13	All data
Number of implants		6	5	5	6	22
BIC	Mean value of BIC_i^m	18.61	45.53	58.50	49.51	42.22
	Mean value of BIC_i^{std} (measurement error)	3.32	5.84	3.87	2.62	3.68
	Standard deviation of BIC_i^m (interindividual variability)	12.56	5.57	4.94	15.14	18.52
<i>ISQ0</i>	Mean value of $ISQ0_i^m$	63.00	75.52	73.88	70.67	70.41
	Mean value of $ISQ0_i^{std}$ (measurement error)	1.18	0.23	1.67	1.95	1.29
	Standard deviation of $ISQ0_i^m$ (interindividual variability)	9.15	3.82	3.55	1.63	7.11
<i>ISQ90</i>	Mean value of $ISQ90_i^m$	71.38	84.08	77.40	74.00	76.35
	Mean value of $ISQ90_i^{std}$ (measurement error)	0.75	1.82	2.73	3.08	2.08
	Standard deviation of $ISQ90_i^m$ (interindividual variability)	12.39	3.86	6.31	7.61	9.16
<i>UI</i>	Mean value of UI_i^m	66.01	74.53	80.42	82.47	75.71
	Mean value of UI_i^{std} (measurement error)	0.73	0.54	0.47	0.31	0.51
	Standard deviation of UI_i^m (interindividual variability)	11.18	4.41	2.79	1.63	9.00

8.3.2 Resonance frequency analysis

Table 8.1 shows the same parameters corresponding to *ISQ0* and *ISQ90* as the ones shown for the BIC in the last subsection. An ANOVA test of the 22 implants demonstrated a significant effect of healing time on *ISQ0* (p-value = 6.0×10^{-3}), but no significant effect of healing time on *ISQ90* (p-value = 0.11). Both *ISQ0* and *ISQ90* first increase as a function of healing time, but then decrease for healing times superior to 4 weeks. The interindividual reproducibility of *ISQ0* decreases as a function of healing time, suggesting that a similar value of *ISQ0* is reached for all samples once healing is achieved. However, no global trend was observed in the evolution of this same parameter for *ISQ90*.

Figure 8.4 shows the relation between i) *ISQ0* and *ISQ90* and ii) the BIC measured with histology. A significant correlation was obtained between *ISQ0* and the BIC, while no correlation was obtained between *ISQ90* and the BIC. The vertical error bars correspond to the standard deviation obtained for the three measurements of the ISQ ($ISQ0_i^{std}$ and $ISQ90_i^{std}$) and indicate the reproducibility of each measurements. The horizontal error bars correspond to the standard deviation obtained for the two measurements of the

BIC (BIC_i^{std}).

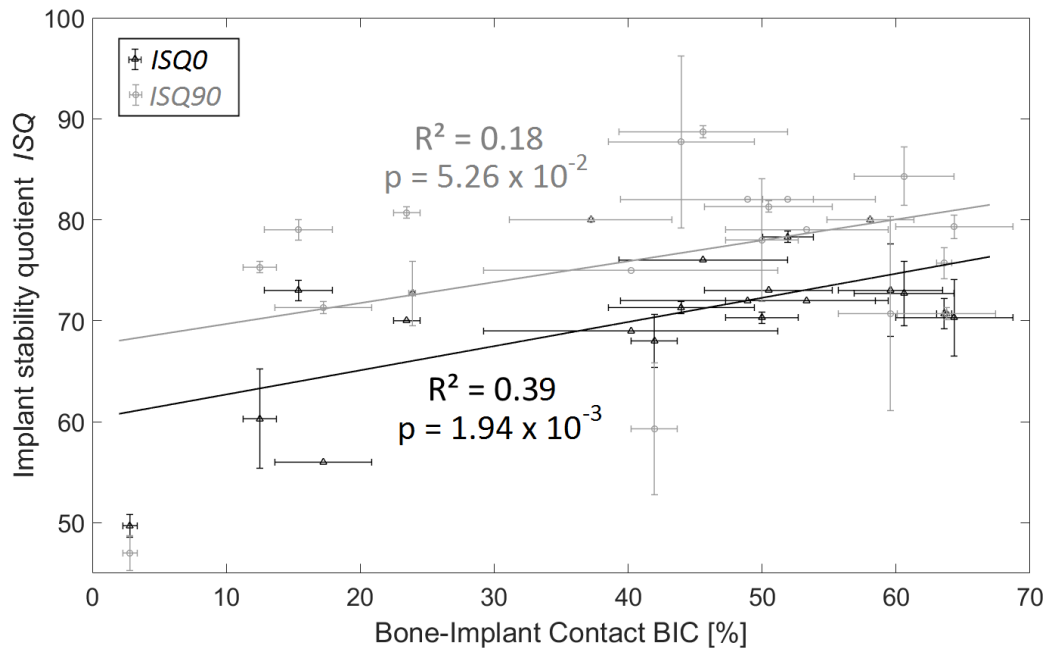


Figure 8.4 – Relationship obtained between the ISQ measured in the directions 0° (black points) and 90° (grey points) and the BIC. The solid lines correspond to a linear regression analysis. The error bars denote the reproducibility of the measurements. The determination coefficients are indicated.

8.3.3 Ultrasonic measurements

Table 8.1 shows the same parameters corresponding to UI as the one shown for the BIC in subsection 8.3.1. An ANOVA test of the 22 implants demonstrated a significant effect of healing time on UI (p -value = 1.65×10^{-3}), UI increasing as a function of healing time for all data. However, this increase becomes relatively weak between 8 and 13 weeks. Moreover, the interindividual variability of UI significantly decreases as a function of healing time, suggesting that a similar value of UI is reached for all samples once healing is achieved.

Figure 8.5 shows the relation between the UI and the BIC measured via histology. The vertical error bars correspond to the standard deviation obtained for the three measurements of the UI (UI_i^{std}) and indicate the reproducibility of each measurements. The horizontal error bars correspond to the standard deviation obtained for the two measurements of the BIC (BIC_i^{std}). A significant correlation was obtained between UI and the BIC.

Figure 8.6 shows the relationship between i) $ISQ0$ and $ISQ90$ and ii) the UI . A significant correlation was obtained between $ISQ0$ and UI , whereas no correlation was obtained between $ISQ90$ and UI .

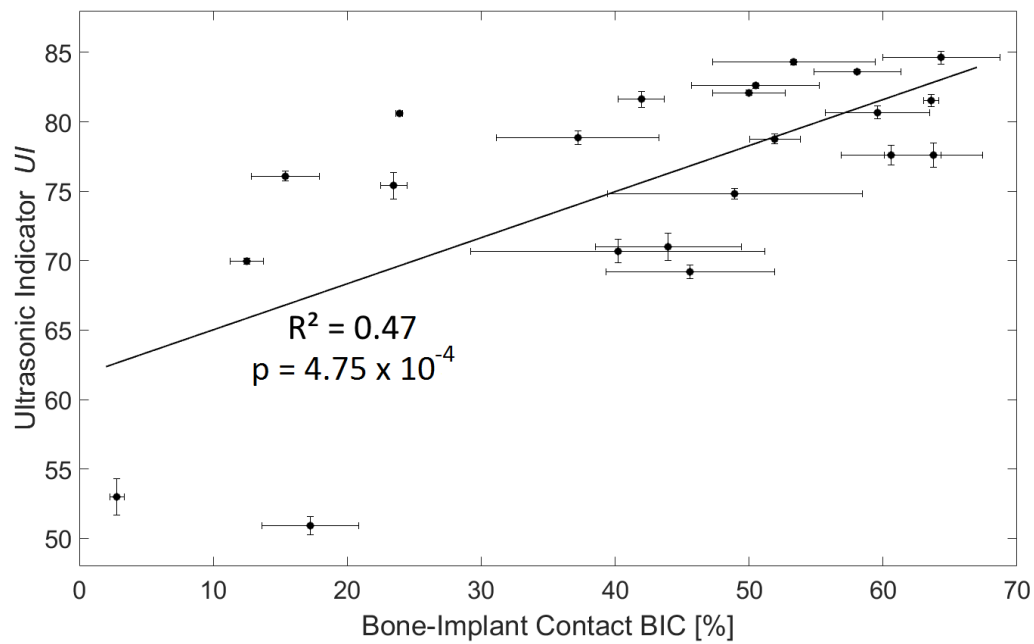


Figure 8.5 – Relationship obtained between *UI* and the BIC. The solid lines correspond to a linear regression analysis. The error bars denote the reproducibility of the measurements. The determination coefficient is indicated.

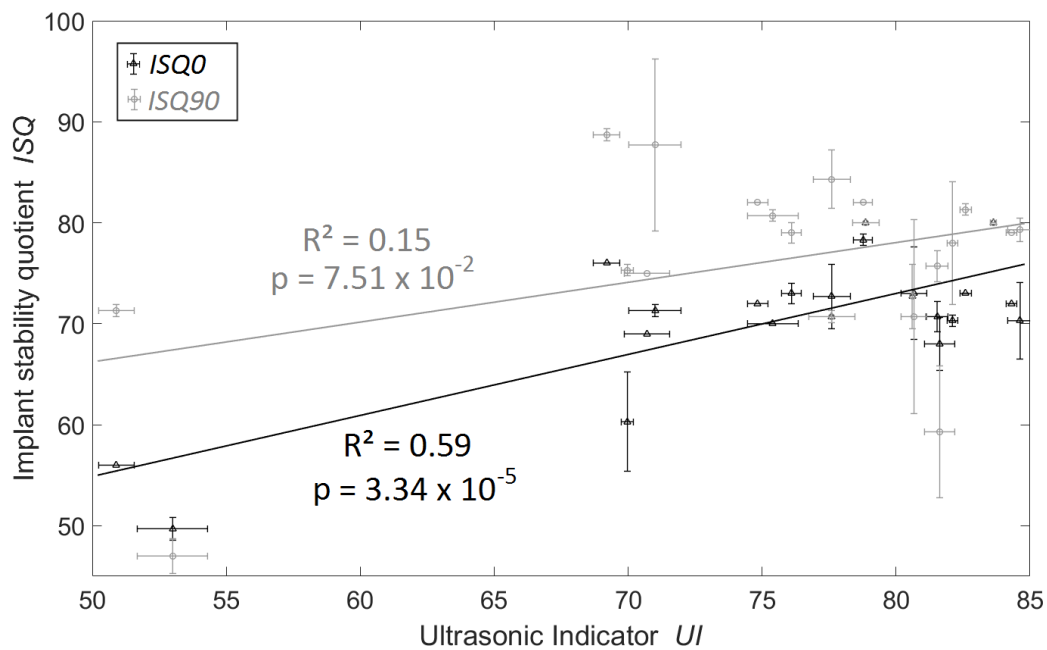


Figure 8.6 – Variation of i) the ISQ measured in the directions 0° (black points) and 90° (grey points) and ii) the *UI*. The solid lines correspond to a linear regression analysis. The error bars denote the reproducibility of the measurements. The determination coefficients are indicated.

8.4 Discussion

8.4.1 Originality of the study

The originality of the present study is to compare ISQ, *UI* and BIC values obtained for the same samples, which provides further insight regarding the development of the QUS device dedicated to dental implant stability measurement (see Section 2.1). Previously, the relationship between the *UI* and BIC values was investigated for a lower number of samples compared to the present study (13 in Vayron et al. [280]; 22 herein). However, the QUS device was different since the ultrasonic probe was manually positioned on the implant abutment screw, leading to reproducibility issues, whereas a controlled insertion torque is introduced in the present study. Moreover, the relationship between the ISQ and BIC values have also been previously investigated [3, 4, 51, 113, 130, 178, 196, 240] (see subsection 8.4.3) but none of these studies considered QUS measurements.

8.4.2 Evolution of ISQ, UI and BIC values with healing time

While a consistent increase of BIC values was obtained for lower values of healing time (0-8 weeks), BIC values obtained for higher healing duration (8-13 weeks) tend to decrease (see Table 8.1) and have an important variability depending on the implant considered. A similar behavior was obtained in previous studies realized with Labrador dogs [3] and on sheep [283] (see Fig. 2.9). It may be explained as follows. During implant surgery, cavity drilling triggers wound healing events and thus promotes remodeling around the implant. However, the lack of mechanical stimulation applied to the implant is likely to lead to bone resorption at the BII [142, 216], which explains possible bone loss for healing times higher than 8 weeks. This variation of the BIC as a function of healing time may explain the variation of *UI* values. *UI* first increases significantly (0-8 weeks), and then tends to reach a constant value (8-13 weeks) with a relatively low values of interindividual variability (see Table 8.1), which is in agreement with results obtained in Vayron et al. [283]. However, the variation of ISQ values as a function of healing time is more difficult to relate to BIC variations since *ISQ0* decreases for healing times over 4 weeks, and ANOVA tests indicated that similarly as in Vayron et al. [283], no correlation with healing time could be established for *ISQ90*.

Maximal measurement errors on BIC values were observed after 4 weeks of healing (see Table 8.1). It may be explained as follows. In the early period after implant insertion, bone resorption primarily occurs around the implant. However, after around 3 to 4 weeks of healing, bone formation highly increases and becomes predominant over bone resorption [159, 255]. Therefore, after 4 weeks of healing, there is a high heterogeneity in the amount of bone in contact with the implant, which leads to a high value of BIC_i^{std} .

8.4.3 Correlation between ISQ and BIC values

Figures 8.4 and 8.5 show that *ISQ0* and *UI* are correlated to BIC values, whereas no correlation between *ISQ90* and BIC was obtained. The results shown in Fig. 8.6 are in agreement with those shown in Fig. 8.5 since *ISQ0* and *UI* are significantly correlated, whereas no correlation was obtained between *ISQ90* and *UI*. These results highlight that ISQ values highly depend on the direction of the measurements, which is in agreement

with results from Pattijn et al. [211]. Moreover, the correlation obtained between ISQ and BIC measurement in the present study was relatively weak. Note that there is also controversy in the literature regarding the dependence of BIC and ISQ, since some studies conclude with a significant correlation between ISQ and BIC [4, 196, 240] with p-values varying between 0.016 and 0.024, while other studies showed there was no correlation between the two aforementioned parameters [3, 51, 113, 130, 178].

8.4.4 Correlation between UI and BIC values

The correlation found between *UI* and BIC values is in good agreement with results obtained in a previous *in vivo* study [280], where a determination coefficient of $R^2 = 0.45$ was found for the correlation between BIC and the *UI* (see Fig. 2.8). Vayron et al. [280] showed that the indicator *UI* increased during healing, which is consistent with the present results since the BIC also increases during healing time [158, 247]. Moreover, as discussed in Subsection 4.4.1, *in silico* [281, 282] and *in vitro* [278, 284] studies also showed that the *UI* increased when bone quantity around the implant increases, which may be explained as follows. When the BIC is low, the implant surface is mostly in contact with fibrous tissues, which leads to a stronger gap of mechanical properties at the implant surface than for higher BIC, which corresponds to a situation where the implant is mostly in contact with bone tissue. Consequently, as suggested by the results from Part III, the transmission coefficient at the BII is lower for lower values of the BIC and acoustic energy leakage out of the implant is therefore lower. As a result, the acoustic energy recorded at the upper surface of the implant is lower when there is more bone in contact with the implant, and the *UI* thus increases. However, the correlation between the BIC and the *UI* found herein is only moderate ($R^2 = 0.47$), which may be explained by experimental errors on the BIC estimation (see Table 8.1). Furthermore, the BIC is an indicator of bone quantity and not of bone quality, which also influences QUS measures since the *UI* was shown to increase while (i) trabecular density increases and (ii) cortical thickness increases [282, 284] (see Fig. 2.3). Note that Figure 4.8 in Chapter 4 also suggested that *UI* depends on bone quality.

8.4.5 Comparison between RFA and QUS techniques

Previous studies showed that the QUS technique is more sensitive to variations of *in vitro* implant stability [284] and to healing time [283] compared to the RFA techniques (see Section 2.1), which is in agreement with the present study. Besides a better correlation of the *UI* with BIC values compared to ISQ, ultrasonic measurements were also more reproducible than ISQ measurements, with a mean standard deviation on *UI* values equal to 0.51 while the mean standard deviation on ISQ values was equal to 1.69 (see Table 8.1 and Fig. 8.4 and 8.5). The better sensitivity of QUS compared to RFA to variations of the BIC can be explained physically. The ISQ is related to the resonance frequency of the bone-implant system, which depends on properties of the entire host bone that vibrates when excited mechanically [227]. However, as shown in Chapter 4 (see Fig. 4.9a), the ultrasonic response of the BII is sensitive to properties of tissue located at a distance W lower than around $0.3/k$ from the implant surface, where k is the wavenumber of the ultrasonic wave in titanium. Since Chapter 7 evidenced the propagation of guided waves with frequency components around 1 MHz (see Fig 7.4) in TSVT4B10 dental implants,

QUS measurements are sensitive to properties of tissues located at a distance lower than around 250 μm from the implant surface, which corresponds to the region of interest where osseointegration phenomena are known to occur [110, 155]. Therefore, QUS are likely to be more sensitive to the properties of the BII and to osseointegration phenomena.

8.4.6 Limitations

The present study has several limitations. First, only one type of implant was considered and the comparison between RFA and QUS techniques should be done with other implant types. Second, uncertainties on the estimation of BIC values was high because (i) only two BIC measurements could be realized for each implant and (ii) BIC measurements were realized on 2D histological sections, and can therefore only approximate actual BIC values on the entirety of the 3D implant. Third, the relatively low number of rabbits in this study is a limitation and more animals should be considered in the future. Fourth, the only parameter representing the progress of osseointegration considered herein was the BIC, which is not representative of the evolution of bone quality during healing.

8.5 Conclusion

The present study allows to assess the performances of RFA and QUS techniques to assess dental implant stability by comparing the results obtained on the same samples with both methods to BIC ratio measurements. A better correlation between the BIC and the UI was found compared to the ISQ, which was shown to be dependent on the direction of measurements. Moreover, the errors realized on the UI were 3.3 times lower to the ones realized on the ISQ. These results may be explained by the reproducibility and by the principle of measurements of both methods. Future works should now focus on the development of an ultrasonic device that could be used in clinical practice in the future to estimate dental implant primary and secondary stability. In particular, clinical studies could help to define a target value for the UI above which an implant is considered to be stable enough to be loaded.

Conclusion

This work focuses on the development of ultrasonic techniques in order to assess implant stability. QUS methods are promising tools in order to retrieve information on the evolution of the biomechanical properties of the BII, which is the main determinant for the success of osseointegration. Moreover, another interesting application of ultrasonic techniques to the BII is the stimulation of osseointegration by LIPUS. Therefore, understanding the phenomena occurring when an ultrasonic wave propagates in an implant would be useful for both stimulation and characterization purposes.

In previous studies, the effects of healing time on the ultrasonic response of the BII have been studied. However, the sensitivity of the QUS response of the BII to loading conditions is still unknown. Part II showed that (i) the reflection coefficient at the BII significantly decreases when compression stresses are applied to the BII and that (ii) the acoustic propagation at the BII is strongly correlated to the mechanical behavior of periprosthetic bone tissue. The influence of compressive stresses on the ultrasonic response of the BII is particularly significant until a plateau stress corresponding to bone fracture is reached, and may be explained by an increase of the BIC when trabecular bone is compressed onto the implant, as well as by changes of the bone global structure. These results highlight two points: first, the stress distribution around the implant, which is known to be heterogeneous due to their complex geometry, is a significant parameter influencing the ultrasonic propagation at the BII and has to be considered when using QUS to investigate implant stability. Second, the sensitivity of QUS to compressive stresses confirms the potential of QUS to estimate implant primary stability, which is highly dependent on the stress distribution around the implant.

While *in vitro* and *in vivo* studies are necessary to validate the performance of QUS methods, it is difficult to accurately control the parameters influencing the interaction between an ultrasonic wave and the rough BII using experimental approaches. Therefore, numerical and analytical models of the ultrasonic propagation at the BII were developed in part III. In particular, the effects of the implant roughness was investigated at two different scales, denoted as microscopic and macroscopic. Considering a sinusoidal implant roughness model was shown to be a good approximation to describe the interaction between an ultrasonic wave and an osseointegrating BII for both scales because (i) for the microscopic scale, an equivalence between sinusoidal roughness profiles and real im-

Conclusion

plants surface roughness profiles measured by profilometry was obtained and (ii) for the macroscopic scale, a sinusoidal profile is an accurate description of the implant roughness, especially regarding dental implant thread designs. Moreover, a 2-D model was considered in order to decrease associated calculation costs because for standard implant roughness, 2-D results were similar to the ones obtained with a 3-D model. For microscopic roughness, an analytical expression of the equivalent stiffness of the interface was obtained and the relative contributions of (i) the contact between the bone and the implant and (ii) the presence of soft tissues at the interface were assessed. Based on these results, the reflection and transmission coefficients at the BII could be determined analytically and were in good agreement with numerical results. Both analytical and numerical models show that for microscopic roughness, the reflection coefficient at the BII increases from around 0.55 until 0.9 when the product $k.W$ of the wave number by the soft tissue thickness increases from 0 to around 0.3. Moreover, at a frequency of 10 MHz, the reflection coefficient significantly depends on the properties of bone tissue located at a distance comprised between 1 and 25 μm from the implant surface. Therefore, the QUS response of the BII was shown to be sensitive to osseointegration processes, especially when using high frequencies. At the macroscopic scale, the ultrasonic propagation is highly dependent on the implant roughness, which may be explained by phase cancellation and multiple scattering effects for high roughness parameters.

Modeling approaches were developed using a simple implant geometry, with roughness profiles mostly described as sinusoidal. Though a simple model is useful to better understand the propagation of an ultrasonic wave at the BII, complex geometries of real implants have to be considered to get a more realistic approach. Therefore, the specific case of dental implants was investigated in part IV. A first study combining *in vitro* and numerical approaches examined how the propagation of ultrasound in dental implants is affected by their complex geometry. An ultrasonic transducer was screwed into a dental implant, and was excited in transient regime at 10 MHz. Laser-ultrasonic techniques were employed to measure the amplitude of the displacements at the implant surface, which varied between 3.2 nm and 8.9 nm along the implant axis. The results evidenced the propagation of a guided wave mode along the implant axis. The velocity of the first arriving signal was equal to 2110 $\text{m}\cdot\text{s}^{-1}$, with frequency components around 1 MHz, in agreement with numerical results. Two main conclusions may be derived from this work. First, for characterization purposes on dental implants, it is not necessary to consider high frequency transducers since ultrasound propagate at frequencies comprised between 300 kHz and 2 MHz in the implant. Second, for stimulation purposes, LIPUS parameters should be adequately correlated to the considered configuration since it may influence the amount of energy transmitted to the BII. A second study investigated the concrete performance of QUS to assess dental implant stability using an *in vivo* approach. To do so, a rabbit model was considered and results were compared to values of BIC and of ISQ obtained through histological analysis and through RFA, respectively. The values of the ultrasonic indicator UI were found to be better correlated (i) to BIC values and (ii) to healing time compared to ISQ values, which were shown to depend on the direction of measurements. Errors on the UI were 3.3 times lower to the errors on the ISQ. Therefore, this study showed that QUS provides a better estimation of dental implant stability compared to RFA and confirmed that it could be a useful tool to assess implant stability.

The studies described in the present document further validate the potential of QUS methods to characterize implant stability, and provide a better understanding of the parameters influencing the interaction between an ultrasonic wave and the BII. Different perspectives may be derived from this work. First, the numerical model presented in Part III could be used to study the effects of other parameters. In particular, considering oblique incidence of the ultrasonic wave could be of interest in order to better take into account the propagation of shear waves at the BII. Considering 3D surface profiles of real implants could also be interesting for future works since it represents a configuration closer to real ones. Another interesting perspective would be to solve the inverse problem in order to be able to determine the BII characteristics corresponding to a given reflection coefficient. Second, the present work mostly focused on the characterization of the BII with QUS. However, the stimulation of implant osseointegration with LIPUS still has to be more extensively studied. In particular, *in vivo* studies would be required in order to optimize the parameters of LIPUS enhancing osseointegration. As highlighted by results from Chapter 7, these optimal parameters are likely to depend on the considered configuration. Finally, results presented here are to be confirmed by clinical studies in the future. As described in Chapter 2, a QUS device has already been developed in order to assess dental implant stability and it has been validated *in vitro*, *in vivo* and *in silico*. However, clinical studies are needed to define a target value for the ultrasonic indicator above which an implant is considered to be stable enough to be loaded. Moreover, it would confirm the performance of QUS to assess implant stability.

Bibliography

- [1] E. A. Abdulhameed, H. Enezei, M. Omar, A. Komori, Y. Sugita, F. Hegazy, A. Sam-sudin, H. Maeda, and M. Alam. The effect of low intensity pulsed ultrasound therapy on osseointegration and marginal bone loss around dental implants. *J Hard Tissue Biol*, 26:323–330, 2017.
- [2] I. Abrahamsson, T. Berglundh, E. Linder, N. P. Lang, and J. Lindhe. Early bone formation adjacent to rough and turned endosseous implant surfaces. an experimen-tal study in the dog. *Clin Oral Implants Res*, 15(4):381–92, 2004.
- [3] I. Abrahamsson, E. Linder, and N. P. Lang. Implant stability in relation to osseoin-tegration: an experimental study in the labrador dog. *Clin Oral Implants Res*, 20(3):313–8, 2009.
- [4] Y. Acil, J. Sievers, A. Gulses, M. Ayna, J. Wiltfang, and H. Terheyden. Correlation between resonance frequency, insertion torque and bone-implant contact in self-cutting threaded implants. *Odontology*, 105(3):347–353, 2017.
- [5] I. Al Haffar, F. Padilla, R. Nefussi, S. Kolta, J. M. Foucart, and P. Laugier. Exper-imental evaluation of bone quality measuring speed of sound in cadaver mandibles. *Oral Surg Oral Med Oral Pathol Oral Radiol Endod*, 102(6):782–91, 2006.
- [6] T. Albrektsson and C. Johansson. Osteoinduction, osteoconduction and osseointe-gration. *Eur Spine J*, 10 Suppl 2:S96–101, 2001.
- [7] T. Albrektsson, P. I. Branemark, H. A. Hansson, and J. Lindstrom. Osseointegrated titanium implants. requirements for ensuring a long-lasting, direct bone-to-implant anchorage in man. *Acta Orthop Scand*, 52(2):155–70, 1981.
- [8] T. Albrektsson, G. Zarb, P. Worthington, and A. R. Eriksson. The long-term efficacy of currently used dental implants: a review and proposed criteria of success. *Int J Oral Maxillofac Implants*, 1(1):11–25, 1986.
- [9] T. Albrektsson, E. Dahl, L. Enbom, S. Engevall, B. Engquist, A. R. Eriksson, G. Feldmann, N. Freiberg, P. O. Glantz, O. Kjellman, and et al. Osseointegrated oral implants. a swedish multicenter study of 8139 consecutively inserted nobelpharma implants. *J Periodontol*, 59(5):287–96, 1988.

Bibliography

- [10] American Academy of Implant Dentistry. What are dental implants?, 2018. URL <https://www.aaid-implant.org/dental-implants/what-are-dental-implants/>.
- [11] C. Aparicio, P. Perales, and B. Rangert. Tilted implants as an alternative to maxillary sinus grafting: a clinical, radiologic, and periotest study. *Clin Implant Dent Relat Res*, 3(1):39–49, 2001.
- [12] C. Aparicio, N. P. Lang, and B. Rangert. Validity and clinical significance of biomechanical testing of implant/bone interface. *Clin Oral Implants Res*, 17 Suppl 2:2–7, 2006.
- [13] P. Aspenberg, S. Goodman, S. Toksvig-Larsen, L. Ryd, and T. Albrektsson. Intermittent micromotion inhibits bone ingrowth. titanium implants in rabbits. *Acta Orthop Scand*, 63(2):141–5, 1992.
- [14] M. Atsumi, S. H. Park, and H. L. Wang. Methods used to assess implant stability: current status. *Int J Oral Maxillofac Implants*, 22(5):743–54, 2007.
- [15] W. Aunmeungtong, P. Khongkhunthian, and P. Rungsiyakull. Stress and strain distribution in three different mini dental implant designs using in implant retained overdenture: a finite element analysis study. *ORAL & implantology*, 9(4):202–212, 2016.
- [16] J.-M. Baik and R. B. Thompson. Ultrasonic scattering from imperfect interfaces: A quasi-static model. *Journal of Nondestructive Evaluation*, 4(3):177–196, 1984.
- [17] S. F. Balshi, F. D. Allen, G. J. Wolfinger, and T. J. Balshi. A resonance frequency analysis assessment of maxillary and mandibular immediately loaded implants. *Int J Oral Maxillofac Implants*, 20(4):584–594, 2005.
- [18] R. M. Barewal, T. W. Oates, N. Meredith, and D. L. Cochran. Resonance frequency measurement of implant stability in vivo on implants with a sandblasted and acid-etched surface. *Int J Oral Maxillofac Implants*, 18(5):641–651, 2003.
- [19] C. Baron, C. Guivier-Curien, V.-H. Nguyen, and S. Naili. Bone repair and ultrasound stimulation: An insight into the interaction of lipus with the bone callus through a multiscale computational study. *The Journal of the Acoustical Society of America*, 142(4):2600–2600, 2017.
- [20] J. N. Barshinger and J. L. Rose. Guided wave propagation in an elastic hollow cylinder coated with a viscoelastic material. *IEEE Transactions on Ultrasonics, Ferroelectrics, and Frequency Control*, 51(11):1547–1556, Nov 2004.
- [21] A. P. Berkhoff, P. M. van den Berg, and J. M. Thijssen. Iterative calculation of reflected and transmitted acoustic waves at a rough interface. *IEEE Transactions on Ultrasonics, Ferroelectrics, and Frequency Control*, 42(4):663–671, 1995.
- [22] A. P. Berkhoff, P. M. van den Berg, and J. M. Thijssen. Ultrasound wave propagation through rough interfaces: Iterative methods. *The Journal of the Acoustical Society of America*, 99(3):1306–1314, 1996.

-
- [23] V. Bhaskar, H. L. Chan, M. MacEachern, and O. D. Kripfgans. Updates on ultrasound research in implant dentistry: a systematic review of potential clinical indications. *Dentomaxillofac Radiol*, 47(6):20180076, 2018.
- [24] M. Bischof, R. Nedir, S. Szmukler-Moncler, J. P. Bernard, and J. Samson. Implant stability measurement of delayed and immediately loaded implants during healing. *Clin Oral Implants Res*, 15(5):529–539, Oct 2004.
- [25] S. Biwa, S. Nakajima, and N. Ohno. On the acoustic nonlinearity of solid-solid contact with pressure-dependent interface stiffness. *Journal of Applied Mechanics*, 71(4):508–515, 2004.
- [26] O. G. Bodelón, C. Clemente, M. A. Alobera, S. Aguado-Henche, M. L. Escudero, and M. C. G. Alonso. Osseointegration of ti6al4v dental implants modified by thermal oxidation in osteoporotic rabbits. *International journal of implant dentistry*, 2(1):18–18, 2016.
- [27] E. Bossy, M. Talmant, and P. Laugier. Effect of bone cortical thickness on velocity measurements using ultrasonic axial transmission: A 2d simulation study. *The Journal of the Acoustical Society of America*, 112:297–307, 07 2002.
- [28] U. Bragger. Use of radiographs in evaluating success, stability and failure in implant dentistry. *Periodontol 2000*, 17:77–88, 1998.
- [29] P.-I. Branemark. Osseointegration and its experimental background. *Journal of Prosthetic Dentistry*, 50(3):399–410, 1983.
- [30] P. I. Branemark, B. O. Hansson, R. Adell, U. Breine, J. Lindstrom, O. Hallen, and A. Ohman. Osseointegrated implants in the treatment of the edentulous jaw. experience from a 10-year period. *Scand J Plast Reconstr Surg Suppl*, 16:1–132, 1977.
- [31] J. B. Brunski. Avoid pitfalls of overloading and micromotion of intraosseous implants. *Dent Implantol Update*, 4(10):77–81, 1993.
- [32] J. B. Brunski. In vivo bone response to biomechanical loading at the bone/dental-implant interface. *Adv Dent Res*, 13:99–119, 1999.
- [33] D. Buser, S. Ingimarsson, K. Dula, A. Lussi, H. P. Hirt, and U. C. Belser. Long-term stability of osseointegrated implants in augmented bone: a 5-year prospective study in partially edentulous patients. *Int J Periodontics Restorative Dent*, 22(2):109–17, 2002.
- [34] H. U. Cameron, R. M. Pilliar, and I. Macnab. The effect of movement on the bonding of porous metal to bone. *Journal of Biomedical Materials Research*, 7(4):301–311, 1973.
- [35] L. Capek, A. Simunek, R. Slezak, and L. Dzan. Influence of the orientation of the Osstell transducer during measurement of dental implant stability using resonance frequency analysis: a numerical approach. *Med Eng Phys*, 31(7):764–769, Sep 2009.

Bibliography

- [36] H. Carreon, M. Carreon, and A. Dueñas. Assessment of precipitates of aged ti-6al-4v alloy by ultrasonic attenuation. *Philosophical Magazine*, 97(1):58–68, 2017.
- [37] D. Carter and W. Hayes. Bone compressive strength: the influence of density and strain rate. *Science*, 194(4270):1174–1176, 1976.
- [38] D. R. Carter and G. S. Beaupré. *Skeletal Function and Form: Mechanobiology of Skeletal Development, Aging, and Regeneration*. Cambridge University Press, 2000.
- [39] D. R. Carter, G. H. Schwab, and D. M. Spengler. Tensile fracture of cancellous bone. *Acta Orthop Scand*, 51(5):733–41, 1980.
- [40] H. Caulier, I. Naert, W. Kalk, and J. A. Jansen. The relationship of some histologic parameters, radiographic evaluations, and Periotest measurements of oral implants: an experimental animal study. *Int J Oral Maxillofac Implants*, 12(3):380–386, 1997.
- [41] H.-L. Chan, H.-L. Wang, J. B. Fowlkes, W. V. Giannobile, and O. D. Kripfgans. Non-ionizing real-time ultrasonography in implant and oral surgery: A feasibility study. *Clinical Oral Implants Research*, 28(3):341–347, 2017.
- [42] W. H.-S. Chang, J.-S. Sun, S.-P. Chang, and J. C. Lin. Study of thermal effects of ultrasound stimulation on fracture healing. *Bioelectromagnetics*, 23(4):256–263, 2002.
- [43] P. Chavassieux and P. J. Meunier. Histomorphometric approach of bone loss in men. *Calcif Tissue Int*, 69(4):209–13, 2001.
- [44] N. Chevallier, F. Anagnostou, S. Zilber, G. Bodivit, S. Maurin, A. Barrault, P. Bierling, P. Hernigou, P. Layrolle, and H. Rouard. Osteoblastic differentiation of human mesenchymal stem cells with platelet lysate. *Biomaterials*, 31(2):270–8, 2010.
- [45] A. Chopra, A. A. Mhapuskar, S. Marathe, S. U. Nisa, S. Thopte, and R. Saddiwal. Evaluation of osseointegration in implants using digital orthopantomogram and cone beam computed tomography. *J Contemp Dent Pract*, 17(11):953–957, 2016.
- [46] J. Chung and G. M. Hulbert. A Time Integration Algorithm for Structural Dynamics With Improved Numerical Dissipation: The Generalized- α Method. *Journal of Applied Mechanics*, 60(2):371–375, 06 1993.
- [47] L. Claes and B. Willie. The enhancement of bone regeneration by ultrasound. *Prog Biophys Mol Biol*, 93(1-3):384–98, 2007.
- [48] D. Clorenec and D. Royer. Investigation of surface acoustic wave propagation on a sphere using laser ultrasonics. *Applied Physics Letters*, 85:2435–2437, 09 2004.
- [49] D. M. Cooper, C. E. Kawalilak, K. Harrison, B. D. Johnston, and J. D. Johnston. Cortical bone porosity: What is it, why is it important, and how can we detect it? *Curr Osteoporos Rep*, 14(5):187–98, 2016.
- [50] S. Cowin. *Bone Mechanics Handbook, Second Edition*. Taylor & Francis, 2001. ISBN 9780849391170.

-
- [51] M. Dagher, N. Mokbel, G. Jabbour, and N. Naaman. Resonance frequency analysis, insertion torque, and bone to implant contact of 4 implant surfaces: comparison and correlation study in sheep. *Implant Dent*, 23(6):672–678, Dec 2014.
- [52] J. E. Davies. Understanding peri-implant endosseous healing. *J Dent Educ*, 67(8):932–49, 2003.
- [53] M. S. de Almeida, C. D. Maciel, and J. C. Pereira. Proposal for an ultrasonic tool to monitor the osseointegration of dental implants. *Sensors (Basel)*, 7(7):1224–37., Jul 2007.
- [54] H. Denissen, R. Eijssink-Smeets, A. van Lingen, and R. van Waas. Assessing mineral density in small trephined jawbone biopsy specimens. *Clin Oral Implants Res*, 10(4):320–5, 1999.
- [55] R. Dimitriou and G. Babis. Biomaterial osseointegration enhancement with bio-physical stimulation. *J Musculoskelet Neuronal Interact*, 7:257–263, 2007.
- [56] S. Djili and B. Fouad. Propagation of guided waves in a hollow circular cylinder application to non destructive testing. *The European Physical Journal Conferences*, 6, 06 2010.
- [57] A. Dorogoy, D. Rittel, K. Shemtov-Yona, and R. Korabi. Modeling dental implant insertion. *J Mech Behav Biomed Mater*, 68:42–50, 2017.
- [58] A. Dorogoy, G. Haïat, K. Shemtov-Yona, and D. Rittel. Modeling ultrasonic wave propagation in a dental implant - bone system. *Journal of the Mechanical Behavior of Biomedical Materials*, 103:103547, 2020.
- [59] L. R. Duarte. The stimulation of bone growth by ultrasound. *Archives of orthopaedic and traumatic surgery*, 101(3):153–159, 1983.
- [60] J. Dundurs. Effect of elastic constants on stress in a composite under plane deformation. *Journal of Composite Materials*, 1(3):310–322, 1967.
- [61] R. Dwyer-Joyce, T. Reddyhoff, and J. Zhu. Ultrasonic measurement for film thickness and solid contact in elastohydrodynamic lubrication. *Journal of Tribology*, 133, 07 2011.
- [62] M. Dyson and J. Suckling. Stimulation of tissue repair by ultrasound: a survey of the mechanisms involved. *Physiotherapy*, 64(4):105–108, April 1978.
- [63] J. M. Egan and D. C. Marsden. A spring network model for the analysis of load transfer and tissue reactions in intra-medullary fixation. *Clin Biomech (Bristol, Avon)*, 16(1):71–9, 2001.
- [64] P. Eickholz and E. Hausmann. Accuracy of radiographic assessment of interproximal bone loss in intrabony defects using linear measurements. *Eur J Oral Sci*, 108(1):70–3, 2000.

Bibliography

- [65] K. Endo, S. Yamada, M. Todoh, M. Takahata, N. Iwasaki, and S. Tadano. Structural strength of cancellous specimens from bovine femur under cyclic compression. *PeerJ*, 4:e1562, 2016.
- [66] A. H. England. A Crack Between Dissimilar Media. *Journal of Applied Mechanics*, 32(2):400–402, 06 1965.
- [67] D. Ensminger and L. J. Bond. *Ultrasonics: Fundamentals, Technologies, and Applications, Third Edition*. CRC Press, 2011.
- [68] I. Ericsson, K. Randow, K. Nilner, and A. Peterson. Early functional loading of branemark dental implants: 5-year clinical follow-up study. *Clin Implant Dent Relat Res*, 2(2):70–7, 2000.
- [69] R. A. Eriksson and R. Adell. Temperatures during drilling for the placement of implants using the osseointegration technique. *J Oral Maxillofac Surg*, 44(1):4–7, 1986.
- [70] S. Ersanli, C. Karabuda, F. Beck, and B. Leblebicioglu. Resonance frequency analysis of one-stage dental implant stability during the osseointegration period. *J Periodontol*, 76(7):1066–71, 2005.
- [71] M. Esposito, J. M. Hirsch, U. Lekholm, and P. Thomsen. Biological factors contributing to failures of osseointegrated oral implants. (i). success criteria and epidemiology. *Eur J Oral Sci*, 106(1):527–51, 1998.
- [72] R. S. Faeda, H. S. Tavares, R. Sartori, A. C. Guastaldi, and J. Marcantonio, E. Evaluation of titanium implants with surface modification by laser beam. biomechanical study in rabbit tibias. *Braz Oral Res*, 23(2):137–43, 2009.
- [73] J. T. Fokkema. Reflection and transmission of elastic waves by the spatially periodic interface between two solids (theory of the integral-equation method). *Wave Motion*, 2(4):375–393, 1980.
- [74] J. T. Fokkema. Reflection and transmission of elastic waves by the spatially periodic interface between two solids (numerical results for the sinusoidal interface). *Wave Motion*, 3(1):33–48, 1981.
- [75] M. Franchi, B. Bacchelli, G. Giavaresi, V. De Pasquale, D. Martini, M. Fini, R. Giardino, and A. Ruggeri. Influence of different implant surfaces on peri-implant osteogenesis: Histomorphometric analysis in sheep. *Journal of Periodontology*, 78(5):879–888, 2007.
- [76] N. L. Frederiksen. Diagnostic imaging in dental implantology. *Oral Surg Oral Med Oral Pathol Oral Radiol Endod*, 80(5):540–54, 1995.
- [77] B. Friberg, L. Sennerby, J. Roos, P. Johansson, C. G. Strid, and U. Lekholm. Evaluation of bone density using cutting resistance measurements and microradiography: an in vitro study in pig ribs. *Clin Oral Implants Res*, 6(3):164–71, 1995.

-
- [78] B. Friberg, L. Sennerby, K. Grondahl, C. Bergstrom, T. Back, and U. Lekholm. On cutting torque measurements during implant placement: a 3-year clinical prospective study. *Clin Implant Dent Relat Res*, 1(2):75–83, 1999.
- [79] B. Friberg, S. Jisander, G. Widmark, A. Lundgren, C. J. Ivanoff, L. Sennerby, and C. Thoren. One-year prospective three-center study comparing the outcome of a "soft bone implant" (prototype mk iv) and the standard branemark implant. *Clin Implant Dent Relat Res*, 5(2):71–7, 2003.
- [80] H. M. Frost. Bone's mechanostat: a 2003 update. *Anat Rec A Discov Mol Cell Evol Biol*, 275(2):1081–101, 2003.
- [81] K. Ganzorig, S. Kuroda, Y. Maeda, K. Mansjur, M. Sato, K. Nagata, and E. Tanaka. Low-intensity pulsed ultrasound enhances bone formation around miniscrew implants. *Arch Oral Biol*, 60(6):902–10, 2015.
- [82] R. Gapski, H. L. Wang, P. Mascarenhas, and N. P. Lang. Critical review of immediate implant loading. *Clin Oral Implants Res*, 14(5):515–27, 2003.
- [83] H. García-Roncero, J. Caballé-Serrano, J. Cano-Batalla, J. Cabratosa-Termes, and O. Figueras-Álvarez. In-vitro development of a temporal abutment screw to protect osseointegration in immediate loaded implants. *J Adv Prosthodont*, 7(2):160–165, 2015.
- [84] J.-P. Geng, K. B. C. Tan, and G.-R. Liu. Application of finite element analysis in implant dentistry: A review of the literature. *Journal of Prosthetic Dentistry*, 85(6):585–598, 2001.
- [85] L. J. Gibson. The mechanical behaviour of cancellous bone. *Journal of Biomechanics*, 18(5):317–328, 1985.
- [86] A. Gill and F. G. Shellock. Assessment of mri issues at 3-tesla for metallic surgical implants: findings applied to 61 additional skin closure staples and vessel ligation clips. *J Cardiovasc Magn Reson*, 14:3, 2012.
- [87] S. A. Goldstein. The mechanical properties of trabecular bone: dependence on anatomic location and function. *J Biomech*, 20(11-12):1055–61, 1987.
- [88] M. B. Gorbet and M. V. Sefton. Biomaterial-associated thrombosis: roles of coagulation factors, complement, platelets and leukocytes. *Biomaterials*, 25(26):5681–703, 2004.
- [89] T. S. Gross, J. L. Edwards, K. J. Mcleod, and C. T. Rubin. Strain gradients correlate with sites of periosteal bone formation. *Journal of bone and mineral research : the official journal of the American Society for Bone and Mineral Research*, 12 6:982–8, 1997.
- [90] G. Haiat, F. Padilla, F. Peyrin, and P. Laugier. Fast wave propagation in trabecular bone: numerical study of the influence of porosity and structural anisotropy. *Journal of the Acoustical Society of America*, 123(3):1694–1705, 2008.

Bibliography

- [91] G. Haiat, S. Naili, Q. Grimal, M. Talmant, C. Desceliers, and C. Soize. Influence of a gradient of material properties on ultrasonic wave propagation in cortical bone: Application to axial transmission. *The Journal of the Acoustical Society of America*, 125(6):4043–4052, 2009.
- [92] G. Haiat, H.-L. Wang, and J. Brunski. Effects of biomechanical properties of the bone–implant interface on dental implant stability: From in silico approaches to the patient’s mouth. *Annual Review of Biomedical Engineering*, 16(1):187–213, 2014.
- [93] G. Haiat and S. Naili. Independent scattering model and velocity dispersion in trabecular bone: comparison with a multiple scattering model. *Biomechanics and Modeling in Mechanobiology*, 10(1):95–108, 2011.
- [94] G. Haiat, F. Padilla, F. Peyrin, and P. Laugier. Variation of ultrasonic parameters with microstructure and material properties of trabecular bone: A 3d model simulation. *J Bone Miner Res*, 22:665–674, 2007.
- [95] A. Harrison, S. Lin, N. Pounder, and Y. Mikuni-Takagaki. Mode & mechanism of low intensity pulsed ultrasound (lipus) in fracture repair. *Ultrasonics*, 70:45–52, 2016.
- [96] S. Hecht, W. H. Adams, J. Narak, and W. B. Thomas. Magnetic resonance imaging susceptibility artifacts due to metallic foreign bodies. *Vet Radiol Ultrasound*, 52(4): 409–14, 2011.
- [97] J. Heckman, J. Ryaby, J. McCabe, J. Frey, and R. Kilcoyne. Acceleration of tibial fracture-healing by non-invasive, low-intensity pulsed ultrasound. *J Bone Joint Surg Am*, 76:26–34, 1994.
- [98] A. L. Heller and R. L. Heller. Clinical evaluations of a porous-surfaced endosseous implant system. *J Oral Implantol*, 22(3-4):240–6, 1996.
- [99] C. Henselmann. *Chassin’s operative strategy in general surgery : An expositive atlas (Fourth edition)*. New York: Springer, 2014.
- [100] K. Horiuchi, H. Uchida, K. Yamamoto, and M. Sugimura. Immediate loading of branemark system implants following placement in edentulous patients: a clinical report. *Int J Oral Maxillofac Implants*, 15(6):824–30, 2000.
- [101] Y. Hériveaux, V. H. Nguyen, and G. Haiat. Reflection of an ultrasonic wave on the bone-implant interface: A numerical study of the effect of the multiscale roughness. *J Acoust Soc Am*, 144(1):488–499, 2018.
- [102] Y. Hériveaux, V. H. Nguyen, V. Brailovski, C. Gorny, and G. Haiat. Reflection of an ultrasonic wave on the bone-implant interface: effect of the roughness parameters. *J Acoust Soc Am*, 145(6):3370–3381, 2019.
- [103] Y. Hériveaux, V.-H. Nguyen, D. Geiger, and G. Haiat. Elastography of the bone-implant interface. *Scientific Reports*, 9(1):14163, 2019.

-
- [104] Y. Hériveaux, G. Haiät, and V.-H. Nguyen. Reflection of an ultrasonic wave on the bone-implant interface: Comparison of two-dimensional and three-dimensional numerical models. *The Journal of the Acoustical Society of America*, 147(1):EL32–EL36, 2020.
- [105] Y. Hériveaux, B. Audoin, C. Biateau, V.-H. Nguyen, and G. Haiät. Ultrasonic propagation in a dental implant. *Ultrasound Med Biol*, in press.
- [106] Y. Hériveaux, V. H. Nguyen, R. Vayron, and G. Haiat. Ultrasonic evaluation of dental implant stability. In A. Chan and O. Kripfgans, editors, *Dental Ultrasound*. Springer, in press.
- [107] Y. Hériveaux, V.-H. Nguyen, S. Biwa, and G. Haiät. Analytical modeling of the interaction of an ultrasonic wave with a rough bone-implant interface. *Ultrasonics*, submitted.
- [108] Y. Hériveaux, R. Vayron, M. Fraulob, H. Albin Lomami, C. Lenormand, and G. Haiät. Assessment of dental implant stability using resonance frequency analysis and quantitative ultrasound methods. *Clinical Oral Implants Research*, submitted.
- [109] S.-K. Hsu, W.-T. Huang, B.-S. Liu, S.-M. Li, H.-T. Chen, and C.-J. Chang. Effects of near-field ultrasound stimulation on new bone formation and osseointegration of dental titanium implants in vitro and in vivo. *Ultrasound in Med. & Bio.*, 37(3):403–416, 2011.
- [110] S. Huja, T. R Katona, D. Burr, L. P Garetto, and W. Roberts. Microdamage adjacent to endosseous implants. *Bone*, 25:217–22, 1999.
- [111] M. A. Huwiler, B. E. Pjetursson, D. D. Bosshardt, G. E. Salvi, and N. P. Lang. Resonance frequency analysis in relation to jawbone characteristics and during early healing of implant installation. *Clin Oral Implants Res*, 18(3):275–280, Jun 2007.
- [112] T. Irinakis and C. Wiebe. Initial torque stability of a new bone condensing dental implant. a cohort study of 140 consecutively placed implants. *J Oral Implantol*, 35(6):277–82, 2009.
- [113] Y. Ito, D. Sato, S. Yoneda, D. Ito, H. Kondo, and S. Kasugai. Relevance of resonance frequency analysis to evaluate dental implant stability: simulation and histomorphometrical animal experiments. *Clin Oral Implants Res*, 19(1):9–14, 2008.
- [114] C. J. Ivanoff, G. Widmark, C. Johansson, and A. Wennerberg. Histologic evaluation of bone response to oxidized and turned titanium micro-implants in human jawbone. *Int J Oral Maxillofac Implants*, 18(3):341–8, 2003.
- [115] T. Iwai, Y. Harada, K. Imura, S. Iwabuchi, J. Murai, K. Hiramatsu, A. Myoui, H. Yoshikawa, and N. Tsumaki. Low-intensity pulsed ultrasound increases bone ingrowth into porous hydroxyapatite ceramic. *J Bone Miner Metab*, 25(6):392–9, 2007.

Bibliography

- [116] K. Jayaraj and A. Pius. 15 - biocompatible coatings for metallic biomaterials. In P. Balakrishnan, S. M. S, and S. Thomas, editors, *Fundamental Biomaterials: Metals*, Woodhead Publishing Series in Biomaterials, pages 323 – 354. Woodhead Publishing, 2018. ISBN 978-0-08-102205-4.
- [117] K.-Y. Jhang. Nonlinear ultrasonic techniques for nondestructive assessment of micro damage in material: A review. *International Journal of Precision Engineering and Manufacturing*, 10(1):123–135, Jan 2009.
- [118] M. John Y. Chai BDS, M. Jason Yamada DDS, and I.-C. Pang BDS. In vitro consistency of the periostest instrument. *Journal of Prosthodontics*, 2:9 – 12, 03 1993.
- [119] K. S. Jones. Assays on the influence of biomaterials on allogeneic rejection in tissue engineering. *Tissue Engineering Part B: Reviews*, 14(4):407–417, 2008.
- [120] S. Kanagaraja, I. Lundstrom, H. Nygren, and P. Tengvall. Platelet binding and protein adsorption to titanium and gold after short time exposure to heparinized plasma and whole blood. *Biomaterials*, 17(23):2225–32, 1996.
- [121] A. Kanawati, M. W. Richards, J. J. Becker, and N. E. Monaco. Measurement of clinicians’ ability to hand torque dental implant components. *J Oral Implantol*, 35 (4):185–8, 2009.
- [122] D.-Y. Kang, M. Kim, S.-J. Lee, I.-W. Cho, H.-S. Shin, J. Caballé-Serrano, and J.-C. Park. Early implant failure: a retrospective analysis of contributing factors. *J Periodontal Implant Sci*, 49(5):287–298, 2019.
- [123] J. Kenkre and J. Bassett. The bone remodelling cycle. *Annals of Clinical Biochemistry*, 55(3):308–327, 2018. PMID: 29368538.
- [124] S. N. Khan, M. Ramachandran, S. Senthil Kumar, V. Krishnan, and R. Sundaram. Osseointegration and more—a review of literature. *Indian Journal of Dentistry*, 3 (2):72–76, 2012.
- [125] R. Korabi, K. Shemtov Yona, and D. Rittel. On stress/strain shielding and the material stiffness paradigm for dental implants. *Clinical implant dentistry and related research*, 19, 06 2017.
- [126] G. Koubi, P. Colon, J. C. Franquin, A. Hartmann, G. Richard, M. O. Faure, and G. Lambert. Clinical evaluation of the performance and safety of a new dentine substitute, biodentine, in the restoration of posterior teeth - a prospective study. *Clin Oral Investig*, 17(1):243–9, 2013.
- [127] S. Koubi, H. Elmerini, G. Koubi, H. Tassery, and J. Camps. Quantitative evaluation by glucose diffusion of microleakage in aged calcium silicate-based open-sandwich restorations. *International Journal of Dentistry*, 2012, 2012.
- [128] J. Królikowski, J. Szczepek, and Z. Witczak. Ultrasonic investigation of contact between solids under high hydrostatic pressure. *Ultrasonics*, 27(1):45 – 49, 1989.

-
- [129] V. V. Kumar, K. Sagheb, M. O. Klein, B. Al-Nawas, P. H. Kann, and P. W. Kammerer. Relation between bone quality values from ultrasound transmission velocity and implant stability parameters—an ex vivo study. *Clin Oral Implants Res*, 23(8):975–80, 2012.
- [130] A. T. Kunnekel, K. C. Nair, E. M. Naidu, and G. Sivagami. Validation of resonance frequency analysis by comparing implant stability quotient values with histomorphometric data. *J Oral Implantol*, 37(3):301–8, 2011.
- [131] P. R. Kuzyk and E. H. Schemitsch. The basic science of peri-implant bone healing. *Indian J Orthop*, 45(2):108–15, 2011.
- [132] S. Laporte, F. David, V. Bousson, and S. Pattofatto. Dynamic behavior and microstructural properties of cancellous bone. *arXiv e-prints*, 2009.
- [133] Larousse encyclopedia. Coupe d’un os. URL https://www.larousse.fr/encyclopedie/images/Coupe_dun_os/1001990.
- [134] S. Le Cann, A. Galland, B. Rosa, T. Le Corroller, M. Pithioux, J.-N. Argenson, P. Chabrand, and S. Parratte. Does surface roughness influence the primary stability of acetabular cups? a numerical and experimental biomechanical evaluation. *Medical engineering & physics*, 36, 07 2014.
- [135] L. Le Guehennec, A. Soueidan, P. Layrolle, and Y. Amouriq. Surface treatments of titanium dental implants for rapid osseointegration. *Dent Mater*, 23(7):844–54, 2007.
- [136] R. Leighton, J. T. Watson, P. Giannoudis, C. Papakostidis, A. Harrison, and R. G. Steen. Healing of fracture nonunions treated with low-intensity pulsed ultrasound (lipus): A systematic review and meta-analysis. *Injury*, 48(7):1339 – 1347, 2017.
- [137] H. Lekesiz, N. Katsube, S. I. Rokhlin, and R. R. Seghi. Effective spring stiffness for a planar periodic array of collinear cracks at an interface between two dissimilar isotropic materials. *Mech Mater*, 43(2):87–98, 2011.
- [138] A. Li, R. Roberts, F. J. Margetan, and R. B. Thompson. Study of the effect of microstructure on ultrasonic signal attenuation. *AIP Conference Proceedings*, 557 (1):1322–1329, 2001.
- [139] D. Li, S. J. Ferguson, T. Beutler, D. L. Cochran, C. Sittig, H. P. Hirt, and D. Buser. Biomechanical comparison of the sandblasted and acid-etched and the machined and acid-etched titanium surface for dental implants. *J Biomed Mater Res*, 60(2): 325–32, 2002.
- [140] G.-Y. Li and Y. Cao. Mechanics of ultrasound elastography. *Proceedings. Mathematical, physical, and engineering sciences*, 473(2199):20160841–20160841, 2017. 28413350[pmid] PMC5378248[pmcid] rspa20160841[PII].
- [141] L. Li, Z. Zhu, C. Huang, and W. Chen. Ultrasound: a potential technique to improve osseointegration of dental implants. *Medical hypotheses*, 71 4:568–71, 2008.

Bibliography

- [142] Z. Li, R. Muller, and D. Ruffoni. Bone remodeling and mechanobiology around implants: Insights from small animal imaging. *J Orthop Res*, 36(2):584–593, 2018.
- [143] T. Lieuwen. Explicit results for wave scattering and transmission through a rough fluid–fluid interface. *Applied Acoustics*, 63(9):1031–1050, 2002.
- [144] F. Lin, C. Lin, C. Lu, H. Liu, and C. Wang. The effects of ultrasonic stimulation on dp-bioglass bone substitute. *Med Eng Phys*, 17:20–26, 1995.
- [145] N. Lioubavina-Hack, N. P. Lang, and T. Karring. Significance of primary stability for osseointegration of dental implants. *Clin Oral Implants Res*, 17(3):244–50, 2006.
- [146] Q. Liu, X. Liu, B. Liu, K. Hu, X. Zhou, and Y. Ding. The effect of low-intensity pulsed ultrasound on the osseointegration of titanium dental implants. *Br J Oral Maxillofac Surg*, 50(3):244–50, 2012.
- [147] G. Luo, A. M. Sadegh, H. Alexander, W. Jaffe, D. Scott, and S. C. Cowin. The effect of surface roughness on the stress adaptation of trabecular architecture around a cylindrical implant. *J Biomech*, 32(3):275–84, 1999.
- [148] G. Maintz. [animal experiments in the study of the effect of ultrasonic waves on bone regeneration]. *Strahlentherapie*, 82(4):631–8, 1950.
- [149] K. N. Malizos, M. Hantes, V. Protopappas, and A. A. Papachristos. Low-intensity pulsed ultrasound for bone healing: an overview. *Injury*, 37 Suppl 1:S56–62, 2006.
- [150] M.-E. Marquis, E. Lord, E. Bergeron, O. Drevelle, H. Park, F. Cabana, H. Senta, and N. Fauchoux. Bone cells-biomaterials interactions. *Frontiers in Bioscience*, 14:1023–1067, 01 2009.
- [151] L. Massari, F. Benazzo, F. Falez, D. Perugia, L. Pietrogrande, S. Setti, R. Osti, E. Vaienti, C. Ruosi, and R. Cadossi. Biophysical stimulation of bone and cartilage: state of the art and future perspectives. *International Orthopaedics*, 43(3):539–551, Mar 2019.
- [152] V. Mathieu, F. Anagnostou, E. Soffer, and G. Haiat. Ultrasonic evaluation of dental implant biomechanical stability: An in vitro study. *Ultrasound in Medicine & Biology*, 37(2):262–270, 2011.
- [153] V. Mathieu, F. Anagnostou, E. Soffer, and G. Haiat. Numerical simulation of ultrasonic wave propagation for the evaluation of dental implant biomechanical stability. *J. Acoust. Soc. Am.*, 129(6):4062–72, 2011.
- [154] V. Mathieu, K. Fukui, M. Matsukawa, M. Kawabe, R. Vayron, E. Soffer, F. Anagnostou, and G. Haiat. Micro-brillouin scattering measurements in mature and newly formed bone tissue surrounding an implant. *J Biomech Eng*, 133(2):021006, 2011.
- [155] V. Mathieu, R. Vayron, E. Soffer, F. Anagnostou, and G. Haiat. Influence of healing time on the ultrasonic response of the bone-implant interface. *Ultrasound Med Biol*, 38(4):611–8, 2012.

-
- [156] V. Mathieu, A. Michel, C. H. Flouzat Lachaniette, A. Poignard, P. Hernigou, J. Alain, and G. Haiat. Variation of the impact duration during the in vitro insertion of acetabular cup implants. *Med Eng Phys*, 35(11):1558–63, 2013.
- [157] V. Mathieu, R. Vayron, G. Richard, G. Lambert, S. Naili, J. P. Meningaud, and G. Haiat. Biomechanical determinants of the stability of dental implants: influence of the bone-implant interface properties. *J Biomech*, 47(1):3–13, 2014.
- [158] H. Matsumoto, M. Ochi, Y. Abiko, Y. Hirose, T. Kaku, and K. Sakaguchi. Pulsed electromagnetic fields promote bone formation around dental implants inserted into the femur of rabbits. *Clin Oral Implants Res*, 11(4):354–60, 2000.
- [159] J. McCullough and P. Klokkevold. The effect of implant macro-thread design on implant stability in the early post-operative period: A randomized, controlled pilot study. *Clinical Oral Implants Research*, 28, October 2017.
- [160] T. J. McKee, G. Perlman, M. Morris, and S. V. Komarova. Extracellular matrix composition of connective tissues: a systematic review and meta-analysis. *Scientific Reports*, 9(1):10542, 2019.
- [161] Medizintechnik Gulden. Periotest - dental measuring instrument for implantology and high quality dentistry. URL <https://pdf.medicalexpo.com/pdf/medizintechnik-gulden/periotest-m/72414-136058.html>.
- [162] N. Meredith. Assessment of implant stability as a prognostic determinant. *Int J Prosthodont*, 11(5):491–501, 1998.
- [163] N. Meredith, K. Book, B. Friberg, T. Jemt, and L. Sennerby. Resonance frequency measurements of implant stability in vivo. A cross-sectional and longitudinal study of resonance frequency measurements on implants in the edentulous and partially dentate maxilla. *Clin Oral Implants Res*, 8(3):226–233, Jun 1997.
- [164] N. Meredith, F. Shagaldi, D. Alleyne, L. Sennerby, and P. Cawley. The application of resonance frequency measurements to study the stability of titanium implants during healing in the rabbit tibia. *Clin Oral Implants Res*, 8(3):234–43, 1997.
- [165] N. Meredith, B. Friberg, L. Sennerby, and C. Aparicio. Relationship between contact time measurements and p_{tv} values when using the periotest to measure implant stability. *Int J Prosthodont*, 11(3):269–75, 1998.
- [166] J. Merheb, N. Van Assche, W. Coucke, R. Jacobs, I. Naert, and M. Quirynen. Relationship between cortical bone thickness or computerized tomography-derived bone density values and implant stability. *Clin Oral Implants Res*, 21(6):612–7, 2010.
- [167] R. Mericske-Stern, D. Milani, E. Mericske, and A. Olah. Periotest measurements and osseointegration of mandibular ITI implants supporting overdentures. A one-year longitudinal study. *Clin Oral Implants Res*, 6(2):73–82, Jun 1995.
- [168] F. Mesa, R. Muñoz, B. Noguero, J. d. D. Luna, P. Galindo, and F. O’Valle. Multivariate study of factors influencing primary dental implant stability. *Clinical Oral Implants Research*, 19(2):196–200, 2008.

Bibliography

- [169] U. Meyer, H. P. Wiesmann, T. Fillies, and U. Joos. Early tissue reaction at the interface of immediately loaded dental implants. *Int J Oral Maxillofac Implants*, 18(4):489–99, 2003.
- [170] U. Meyer, U. Joos, J. Mythili, T. Stamm, A. Hohoff, T. Fillies, U. Stratmann, and H. P. Wiesmann. Ultrastructural characterization of the implant/bone interface of immediately loaded dental implants. *Biomaterials*, 25(10):1959–67, 2004.
- [171] A. Michel, R. Bosc, R. Vayron, and G. Haiat. In vitro evaluation of the acetabular cup primary stability by impact analysis. *Journal of Biomechanical Engineering*, 137(3):031011–031011–6, 2015.
- [172] A. Michel, R. Bosc, J. P. Meningaud, P. Hernigou, and G. Haiat. Assessing the acetabular cup implant primary stability by impact analyses: A cadaveric study. *PLoS One*, 11(11):e0166778, 2016.
- [173] A. Michel, R. Bosc, F. Sailhan, R. Vayron, and G. Haiat. Ex vivo estimation of cementless acetabular cup stability using an impact hammer. *Medical Engineering & Physics*, 38(2):80 – 86, 2016.
- [174] C. E. Misch, Z. Qu, and M. W. Bidez. Mechanical properties of trabecular bone in the human mandible: implications for dental implant treatment planning and surgical placement. *J Oral Maxillofac Surg*, 57(6):700–6; discussion 706–8, 1999.
- [175] K. Miura, M. Motoyoshi, M. Inaba, H. Iwai, Y. Karasawa, and N. Shimizu. A preliminary study of the effects of low-intensity pulsed ultrasound exposure on the stability of orthodontic miniscrews in growing rats. *Eur J Orthod*, 36(4):419–24, 2014.
- [176] I. Miyamoto, Y. Tsuboi, E. Wada, H. Suwa, and T. Iizuka. Influence of cortical bone thickness and implant length on implant stability at the time of surgery—clinical, prospective, biomechanical, and imaging study. *Bone*, 37(6):776 – 780, 2005.
- [177] A. Moerman, A. A. Zadpoor, A. Oostlander, M. Schoeman, P. Rahnamay Moshtagh, B. Pouran, and E. Valstar. Structural and mechanical characterisation of the peri-prosthetic tissue surrounding loosened hip prostheses. an explorative study. *J Mech Behav Biomed Mater*, 62:456–467, 2016.
- [178] A. Monje, A. Insua, F. Monje, F. Munoz, G. E. Salvi, D. Buser, and V. Chappuis. Diagnostic accuracy of the implant stability quotient in monitoring progressive peri-implant bone loss: An experimental study in dogs. *Clin Oral Implants Res*, 29(10):1016–1024, 2018.
- [179] H. Mori, M. Manabe, Y. Kurachi, and M. Nagumo. Osseointegration of dental implants in rabbit bone with low mineral density. *Journal of Oral and Maxillofacial Surgery*, 55(4):351–361, 1997.
- [180] J. Mu Jung and C. Sang Kim. Analysis of stress distribution around total hip stems custom-designed for the standardized asian femur configuration. *Biotechnology, biotechnological equipment*, 28(3):525–532, 2014.

-
- [181] R. Mundi, S. Petis, R. Kaloty, V. Shetty, and M. Bhandari. Low-intensity pulsed ultrasound: Fracture healing. *Indian journal of orthopaedics*, 43:132–40, 04 2009.
- [182] P. B. Nagy. Ultrasonic classification of imperfect interfaces. *Journal of Nondestructive Evaluation*, 11(3):127–139, 1992.
- [183] S. Naili, M.-B. Vu, Q. Grimal, M. Talmant, C. Desceliers, C. Soize, and G. Haïat. Influence of viscoelastic and viscous absorption on ultrasonic wave propagation in cortical bone: Application to axial transmission. *The Journal of the Acoustical Society of America*, 127(4):2622–2634, 2010.
- [184] Y. Nakanishi, P.-L. Wang, M. Ochi, K. Nakanishi, and H. Matsubara. Low-intensity pulsed ultrasound stimulation significantly enhances the promotion of bone formation around dental implants. *Journal of Hard Tissue Biology*, 20(2):139–146, 2011.
- [185] J. L. Nazareth. Conjugate gradient method. *Wiley Interdisciplinary Reviews: Computational Statistics*, 1(3):348–353, 2009.
- [186] R. Nedir, M. Bischof, J. M. Briaux, S. Beyer, S. Szmukler-Moncler, and J. P. Bernard. A 7-year life table analysis from a prospective study on ITI implants with special emphasis on the use of short implants. Results from a private practice. *Clin Oral Implants Res*, 15(2):150–157, Apr 2004.
- [187] C. A. Neldam and E. M. Pinholt. State of the art of short dental implants: A systematic review of the literature. *Clinical Implant Dentistry and Related Research*, 14(4):622–632, 2012.
- [188] C. A. Neldam and E. M. Pinholt. Synchrotron μ -ct imaging of bone, titanium implants and bone substitutes – a systematic review of the literature. *Journal of Cranio-Maxillofacial Surgery*, 42(6):801 – 805, 2014.
- [189] C. A. Neldam, T. Lauridsen, A. Rack, T. T. Lefolii, N. R. Jørgensen, R. Feidenhans'l, and E. M. Pinholt. Application of high resolution synchrotron micro-ct radiation in dental implant osseointegration. *Journal of Cranio-Maxillofacial Surgery*, 43(5):682 – 687, 2015.
- [190] C. A. Neldam, J. Sporning, A. Rack, T. Lauridsen, E.-M. Hauge, H. L. Jørgensen, N. R. Jørgensen, R. Feidenhansl, and E. M. Pinholt. Synchrotron radiation μ ct and histology evaluation of bone-to-implant contact. *Journal of Cranio-Maxillofacial Surgery*, 45(9):1448 – 1457, 2017.
- [191] S. K. Nemli, M. B. Güngör, C. Aydın, H. Yılmaz, B. T. Bal, and Y. K. Arıcı. Clinical and radiographic evaluation of new dental implant system: Results of a 3-year prospective study. *Journal of Dental Sciences*, 11(1):29 – 34, 2016.
- [192] I. Nenadic, M. Urban, J. Greenleaf, J.-L. Gennisson, M. Bernal, and M. Tanter. Ultrasound elastography for biomedical applications and medicine. *Ultrasound Elastography for Biomedical Applications and Medicine*, 10 2018.
- [193] V.-H. Nguyen, S. Naili, and V. Sansalone. A closed-form solution for in vitro transient ultrasonic wave propagation in cancellous bone. *Mechanics Research Communications*, 37(4):377–383, 2010.

Bibliography

- [194] M. Niinomi and M. Nakai. Titanium-based biomaterials for preventing stress shielding between implant devices and bone. *International Journal of Biomaterials*, 2011: 10, 2011.
- [195] C. F. Njeh, D. Hans, C. Wu, E. Kantorovich, M. Sister, T. Fuerst, and H. K. Genant. An in vitro investigation of the dependence on sample thickness of the speed of sound along the specimen. *Medical Engineering & Physics*, 21(9):651–659, 1999.
- [196] E. Nkenke, M. Hahn, K. Weinzierl, M. Radespiel-Troger, F. W. Neukam, and K. Engelke. Implant stability and histomorphometry: a correlation study in human cadavers using stepped cylinder implants. *Clin Oral Implants Res*, 14(5):601–9, 2003.
- [197] M. P. Norton and D. G. Karczub. *Fundamentals of Noise and Vibration Analysis for Engineers*. Cambridge University Press, 2 edition, 2003.
- [198] O. E. Ogle. Implant surface material, design, and osseointegration. *Dent Clin North Am*, 59(2):505–20, 2015.
- [199] G. Orsini, B. Assenza, A. Scarano, M. Piattelli, and A. Piattelli. Surface analysis of machined versus sandblasted and acid-etched titanium implants. *Int J Oral Maxillofac Implants*, 15(6):779–84, 2000.
- [200] M. Oskarsson, M. Otsuki, M. Welander, and I. Abrahamsson. Peri-implant tissue healing at implants with different designs and placement protocols: An experimental study in dogs. *Clin Oral Implants Res*, 29(8):873–880, 2018.
- [201] Z. Ossi, W. Abdou, R. L. Reuben, and R. J. Ibbetson. In vitro assessment of bone-implant interface using an acoustic emission transmission test. *Proc Inst Mech Eng H*, 226(1):63–9, 2012.
- [202] Z. Ossi, W. Abdou, R. L. Reuben, and R. J. Ibbetson. Transmission of acoustic emission in bones, implants and dental materials. *Proc Inst Mech Eng H*, 227(11): 1237–45, 2013.
- [203] Osstell. The objective way to measure implant stability. URL https://www.orthosmiledental.com/m/upload/con_tech_img6.jpg.
- [204] P. O. Ostman, M. Hellman, I. Wendelhag, and L. Sennerby. Resonance frequency analysis measurements of implants at placement surgery. *Int J Prosthodont*, 19(1): 77–83; discussion 84, 2006.
- [205] D. O’Sullivan, L. Sennerby, and N. Meredith. Measurements comparing the initial stability of five designs of dental implants: a human cadaver study. *Clin Implant Dent Relat Res*, 2(2):85–92, 2000.
- [206] D. O’Sullivan, L. Sennerby, D. Jagger, and N. Meredith. A comparison of two methods of enhancing implant primary stability. *Clin Implant Dent Relat Res*, 6(1):48–57, 2004.

-
- [207] F. Padilla, R. Puts, L. Vico, and K. Raum. Stimulation of bone repair with ultrasound: A review of the possible mechanic effects. *Ultrasonics*, 54(5):1125–1145, 2014.
- [208] Y. Pan, L. Li, C. Rossignol, B. AuXdoin, and N. Chigarev. Acoustic waves generated by a laser line pulse in a hollow cylinder. *Ultrasonics*, 44 Suppl 1:e843–7, 2006.
- [209] P. D. Panetta and R. B. Thompson. Ultrasonic attenuation in duplex titanium alloys. In D. O. Thompson and D. E. Chimenti, editors, *Review of Progress in Quantitative Nondestructive Evaluation: Volume 18A–18B*, pages 1717–1724. Springer US, Boston, MA, 1999. ISBN 978-1-4615-4791-4.
- [210] V. Pattijn, C. Van Lierde, G. Van der Perre, I. Naert, and J. Vander Sloten. The resonance frequencies and mode shapes of dental implants: Rigid body behaviour versus bending behaviour. a numerical approach. *Journal of Biomechanics*, 39(5):939–947, 2006.
- [211] V. Pattijn, S. V. N. Jaecques, E. De Smet, L. Muraru, C. Van Lierde, G. Van der Perre, I. Naert, and J. Vander Sloten. Resonance frequency analysis of implants in the guinea pig model: Influence of boundary conditions and orientation of the transducer. *Medical Engineering & Physics*, 29(2):182–190, 2007.
- [212] A. Paul and M. Campillo. Diffraction and conversion of elastic waves at a corrugated interface. *Geophysics*, 53(11):1415–1424, 1988.
- [213] B. Pavlakovic, M. Lowe, D. Alleyne, and P. Cawley. *Disperse: A General Purpose Program for Creating Dispersion Curves*, pages 185–192. Springer US, Boston, MA, 1997.
- [214] A. I. Pearce, R. G. Richards, S. Milz, E. Schneider, and S. G. Pearce. Animal models for implant biomaterial research in bone: a review. *Eur Cell Mater*, 13:1–10, 2007.
- [215] C. Pecorari and M. Poznic. On the linear and nonlinear acoustic properties of dry and water-confining elasto-plastic interfaces. *Proceedings of the Royal Society A: Mathematical, Physical and Engineering Sciences*, 462(2067):769–788, 2006.
- [216] W. Pietrzak. *Musculoskeletal Tissue Regeneration: Biological Materials and Methods*. Springer, 01 2008. ISBN 978-1-58829-909-3.
- [217] R. M. Pilliar, J. M. Lee, and C. Maniopoulos. Observations on the effect of movement on bone ingrowth into porous-surfaced implants. *Clin Orthop Relat Res*, 208:108–13, 1986.
- [218] E. M. Pinholt. Brånemark and iti dental implants in the human bone-grafted maxilla: a comparative evaluation. *Clinical Oral Implants Research*, 14(5):584–592, 2003.
- [219] A. E. F. Pontes, F. S. Ribeiro, G. Iezzi, J. R. Pires, E. P. Zuza, A. Piattelli, and E. Marcantonio Junior. Bone-implant contact around crestal and subcrestal dental implants submitted to immediate and conventional loading. *The Scientific World Journal*, 2014:606947, 2014.

Bibliography

- [220] D. A. Puleo and A. Nanci. Understanding and controlling the bone-implant interface. *Biomaterials*, 20(23-24):2311–21, 1999.
- [221] A. Rabel, S. G. Kohler, and A. M. Schmidt-Westhausen. Clinical study on the primary stability of two dental implant systems with resonance frequency analysis. *Clin Oral Investig*, 11(3):257–65, 2007.
- [222] M. L. Raffa, V.-H. Nguyen, and G. Haiat. Micromechanical modeling of the contact stiffness of an osseointegrated bone-implant interface. *BioMedical Engineering OnLine*, 18(1):114, Dec 2019. ISSN 1475-925X.
- [223] S. Raghavendra, M. C. Wood, and T. D. Taylor. Early wound healing around endosseous implants: a review of the literature. *Int J Oral Maxillofac Implants*, 20(3):425–31, 2005.
- [224] L. Rasmusson, N. Meredith, I. H. Cho, and L. Sennerby. The influence of simultaneous versus delayed placement on the stability of titanium implants in onlay bone grafts. A histologic and biomechanic study in the rabbit. *Int J Oral Maxillofac Surg*, 28(3):224–231, Jun 1999.
- [225] N. M. Rawool, B. B. Goldberg, F. Forsberg, A. A. Winder, and E. Hume. Power doppler assessment of vascular changes during fracture treatment with low-intensity ultrasound. *Journal of Ultrasound in Medicine*, 22(2):145–153, 2003.
- [226] D. Rittel, K. Shemtov-Yona, and R. Korabi. Engineering dental implants. *Current Oral Health Reports*, 4(3):239–247, Sep 2017.
- [227] D. Rittel, A. Dorogoy, G. Haiat, and K. Shemtov-Yona. Resonant frequency analysis of dental implants. *Med Eng Phys*, 66:65–74, 04 2019.
- [228] J. Rivière, G. Renaud, S. Hauptert, M. Talmant, P. Laugier, and P. A. Johnson. Nonlinear acoustic resonances to probe a threaded interface. *Journal of Applied Physics*, 107(12):124901, 2010.
- [229] J. Rivière, S. Hauptert, P. Laugier, and P. A. Johnson. Nonlinear ultrasound: Potential of the cross-correlation method for osseointegration monitoring. *The Journal of the Acoustical Society of America*, 132(3):EL202–EL207, 2012.
- [230] J. Rivière, S. Hauptert, P. Laugier, T. J. Ulrich, P.-Y. L. Bas, and P. A. Johnson. Time reversed elastic nonlinearity diagnostic applied to mock osseointegration monitoring applying two experimental models. *The Journal of the Acoustical Society of America*, 131(3):1922–1927, 2012.
- [231] W. E. Roberts, K. E. Simmons, L. P. Garetto, and R. A. DeCastro. Bone physiology and metabolism in dental implantology: risk factors for osteoporosis and other metabolic bone diseases. *Implant Dent*, 1(1):11–21, 1992.
- [232] G. Y. Rochefort, S. Pallu, and C. L. Benhamou. Osteocyte: the unrecognized side of bone tissue. *Osteoporos Int*, 21(9):1457–69, 2010.

-
- [233] C. L. Romano, D. Romano, and N. Logoluso. Low-intensity pulsed ultrasound for the treatment of bone delayed union or nonunion: A review. *Ultrasound in Medicine & Biology*, 35(4):529 – 536, 2009.
- [234] G. E. Romanos. Bone quality and the immediate loading of implants-critical aspects based on literature, research, and clinical experience. *Implant Dent*, 18(3):203–9, 2009.
- [235] D. Ruppert, O. LA Harrysson, D. Marcellin-Little, S. Bollenbecker, and P. Weinhöhl. Osteogenic benefits of low-intensity pulsed ultrasound and vibration in a rodent osseointegration model. *Journal of musculoskeletal & neuronal interactions*, 19:150–158, 06 2019.
- [236] V. Sansalone, V. Bousson, S. Naili, C. Bergot, F. Peyrin, J. D. Laredo, and G. Haiat. Anatomical distribution of the degree of mineralization of bone tissue in human femoral neck: Impact on biomechanical properties. *Bone*, 50(4):876–884, 2012.
- [237] M. Sasso, M. Talmant, G. Haiat, S. Naili, and P. Laugier. Analysis of the most energetic late arrival in axially transmitted signals in cortical bone. *IEEE transactions on ultrasonics, ferroelectrics, and frequency control*, 56:2463–70, 11 2009.
- [238] R. C. Savadi, J. Agarwal, R. S. Agarwal, and V. Rangarajan. Influence of implant surface topography and loading condition on stress distribution in bone around implants: A comparative 3d fea. *Journal of Indian Prosthodontic Society*, 11(4): 221–231, 2011.
- [239] I. Scala, G. Rosi, V.-H. Nguyen, R. Vayron, G. Haiat, S. Seuret, S. Jaffard, and S. Naili. Ultrasonic characterization and multiscale analysis for the evaluation of dental implant stability: A sensitivity study. *Biomedical Signal Processing and Control*, 42:37–44, 2018.
- [240] A. Scarano, M. Degidi, G. Iezzi, G. Petrone, and A. Piattelli. Correlation between implant stability quotient and bone-implant contact: a retrospective histological and histomorphometrical study of seven titanium implants retrieved from humans. *Clin Implant Dent Relat Res*, 8(4):218–22, 2006.
- [241] A. Scarano, A. Piattelli, A. Quaranta, and F. Lorusso. Bone response to two dental implants with different sandblasted/acid-etched implant surfaces: A histological and histomorphometrical study in rabbits. *BioMed Research International*, 2017:8, 2017.
- [242] S. Schandelmaier, A. Kaushal, L. Lytvyn, D. Heels-Ansdell, R. A. C. Siemieniuk, T. Agoritsas, G. H. Guyatt, P. O. Vandvik, R. Couban, B. Mollon, and J. W. Busse. Low intensity pulsed ultrasound for bone healing: systematic review of randomized controlled trials. *BMJ*, 356, 2017.
- [243] W. Schulte, B. d’Hoedt, D. Lukas, L. Muhlbradt, F. Scholz, J. Bretsch, D. Frey, H. Gudat, M. König, M. Markl, and et al. [periost—a new measurement process for periodontal function]. *Zahnärztl Mitt*, 73(11):1229–30, 1233–6, 1239–40, 1983.

Bibliography

- [244] L. Sennerby, P. Thomsen, and L. E. Ericson. Early tissue response to titanium implants inserted in rabbit cortical bone. *Journal of Materials Science: Materials in Medicine*, 4(3):240–250, May 1993.
- [245] L. Sennerby, P. Thomsen, and L. E. Ericson. Early tissue response to titanium implants inserted in rabbit cortical bone. *Journal of Materials Science: Materials in Medicine*, 4(5):494–502, Sep 1993.
- [246] V. Sáenz de Viteri and E. Fuentes. Titanium and titanium alloys as biomaterials. *Tribology - Fundamentals and Advancements*, pages 154–181, 05 2013.
- [247] W. J. Seong, U. K. Kim, J. Q. Swift, J. S. Hodges, and C. C. Ko. Correlations between physical properties of jawbone and dental implant initial stability. *J Prosthet Dent*, 101(5):306–18, 2009.
- [248] G. Serra, L. S. Morais, C. N. Elias, M. A. Meyers, L. Andrade, C. Muller, and M. Muller. Sequential bone healing of immediately loaded mini-implants. *Am J Orthod Dentofacial Orthop*, 134(1):44–52, 2008.
- [249] F. A. Shah, M. L. Johansson, O. Omar, H. Simonsson, A. Palmquist, and P. Thomsen. Laser-modified surface enhances osseointegration and biomechanical anchorage of commercially pure titanium implants for bone-anchored hearing systems. *PLOS ONE*, 11(6):e0157504, 2016.
- [250] M. Shalabi, J. Wolke, V. Cuijpers, and J. A. Jansen. Evaluation of bone response to titanium-coated polymethyl methacrylate resin (pmma) implants by x-ray tomography. *J Mater Sci Mater Med*, 18:2033–9, 2007.
- [251] K. Shemtov-Yona and D. Rittel. An overview of the mechanical integrity of dental implants. *BioMed Research International*, 2015:11, 2015.
- [252] K. Shemtov-Yona, D. Rittel, and A. Dorogoy. Mechanical assessment of grit blasting surface treatments of dental implants. *J Mech Behav Biomed Mater*, 39:375–90, 2014.
- [253] R. M. S. Sigrist, J. Liau, A. E. Kaffas, M. C. Chammas, and J. K. Willmann. Ultrasound elastography: Review of techniques and clinical applications. *Theranostics*, 7(5):1303–1329, 2017.
- [254] E. Soffer, J. P. Ouhayoun, A. Meunier, and F. Anagnostou. Effects of autologous platelet lysates on ceramic particle resorption and new bone formation in critical size defects: The role of anatomical sites. *J Biomed Mater Res B Appl Biomater*, 79:86–94, 2006.
- [255] D. Soto-Peñaloza, M. Caneva, J. Viña-Almunia, J. J. Martín-de Llano, D. Peñarrocha-Oltra, and M. Peñarrocha-Diago. Bone-healing pattern on the surface of titanium implants at cortical and marrow compartments in two topographic sites: an experimental study in rabbits. *Materials (Basel)*, 12(1), 2018.
- [256] B. S. Sotto-Maior, E. P. Rocha, E. O. de Almeida, A. C. Freitas-Junior, R. B. Anchieta, and A. A. Del Bel Cury. Influence of high insertion torque on implant placement: an anisotropic bone stress analysis. *Braz Dent J*, 21(6):508–14, 2010.

-
- [257] G. Strnad and N. Chirila. Corrosion rate of sand blasted and acid etched ti6al4v for dental implants. *Procedia Technology*, 19(Supplement C):909–915, 2015.
- [258] D. Y. Sullivan, R. L. Sherwood, T. A. Collins, and P. H. Krogh. The reverse-torque test: a clinical report. *Int J Oral Maxillofac Implants*, 11(2):179–85, 1996.
- [259] N. Sumitomo, K. Noritake, T. Hattori, K. Morikawa, S. Niwa, K. Sato, and M. Niinomi. Experiment study on fracture fixation with low rigidity titanium alloy. *Journal of Materials Science: Materials in Medicine*, 19(4):1581–1586, Apr 2008.
- [260] V. Swami, V. Vijayaraghavan, and V. Swami. Current trends to measure implant stability. *J Indian Prosthodont Soc*, 16(2):124–30, 2016.
- [261] S. Szmukler-Moncler, H. Salama, Y. Reingewirtz, and J. H. Dubruille. Timing of loading and effect of micromotion on bone-dental implant interface: review of experimental literature. *J Biomed Mater Res*, 43(2):192–203, 1998.
- [262] M. Tanzer, E. Harvey, A. Kay, P. Morton, and J. Bobyn. Effect of noninvasive low-intensity ultrasound on bone growth into porous-coated implants. *J Orthop Res*, 14:901–906, 1996.
- [263] M. Tanzer, S. Kantor, and J. Bobyn. Enhancement of bone growth into porous intramedullary implants using non-invasive low intensity ultrasound. *J Orthop Res*, 19:195–199, 2001.
- [264] H. G. Tattersall. The ultrasonic pulse-echo technique as applied to adhesion testing. *Journal of Physics D: Applied Physics*, 6(7):819–832, may 1973.
- [265] D. O. Thompson and D. E. Chimenti. *Review of Progress in Quantitative Non-destructive Evaluation: Volume 30A*. American Institute of Physics; 2011 edition, 2011. ISBN 0735408882.
- [266] A. Tijou, G. Rosi, P. Hernigou, C. H. Flouzat-Lachaniette, and G. Haiat. Ex vivo evaluation of cementless acetabular cup stability using impact analyses with a hammer instrumented with strain sensors. *Sensors (Basel)*, 18(1), 2017.
- [267] A. Tijou, G. Rosi, R. Vayron, H. A. Lomami, P. Hernigou, C.-H. Flouzat-Lachaniette, and G. Haiat. Monitoring cementless femoral stem insertion by impact analyses: An in vitro study. *Journal of the Mechanical Behavior of Biomedical Materials*, 88:102–108, 2018.
- [268] J. Tricio, P. Laohapand, D. van Steenberghe, M. Quirynen, and I. Naert. Mechanical state assessment of the implant-bone continuum: a better understanding of the Periotest method. *Int J Oral Maxillofac Implants*, 10(1):43–49, 1995.
- [269] P. Trisi and W. Rao. Bone classification: clinical-histomorphometric comparison. *Clin Oral Implants Res*, 10(1):1–7, 1999.
- [270] M. Ueda, M. Matsuki, M. Jacobsson, and A. Tjellstrom. Relationship between insertion torque and removal torque analyzed in fresh temporal bone. *Int J Oral Maxillofac Implants*, 6(4):442–7, 1991.

Bibliography

- [271] Y. Ustun, O. Erdogan, M. Kurkcu, T. Akova, and A. Damlar. Effects of low-intensity pulsed ultrasound on dental implant osseointegration: A preliminary report. *European Journal of Dentistry*, 2:254–262, 2008.
- [272] P. Valderrama, T. W. Oates, A. A. Jones, J. Simpson, J. D. Schoolfield, and D. L. Cochran. Evaluation of two different resonance frequency devices to detect implant stability: a clinical trial. *J Periodontol*, 78(2):262–72, 2007.
- [273] D. E. Van Scotter and C. J. Wilson. The periotest method for determining implant success. *J Oral Implantol*, 17(4):410–3, 1991.
- [274] D. van Steenberghe, J. Tricio, I. Naert, and M. Nys. Damping characteristics of bone-to-implant interfaces. A clinical study with the Periotest device. *Clin Oral Implants Res*, 6(1):31–39, Mar 1995.
- [275] R. Vayron, E. Barthel, V. Mathieu, E. Soffer, F. Anagnostou, and G. Haiat. Variation of biomechanical properties of newly formed bone tissue determined by nanoindentation as a function of healing time. *Computer Methods in Biomechanics and Biomedical Engineering*, 14(sup1):139–140, 2011.
- [276] R. Vayron, E. Barthel, V. Mathieu, E. Soffer, F. Anagnostou, and G. Haiat. Nanoindentation measurements of biomechanical properties in mature and newly formed bone tissue surrounding an implant. *Journal of Biomechanical Engineering*, 134(2):021007–021007–6, 2012.
- [277] R. Vayron, P. Karasinski, V. Mathieu, A. Michel, D. Loriot, G. Richard, G. Lambert, and G. Haiat. Variation of the ultrasonic response of a dental implant embedded in tricalcium silicate-based cement under cyclic loading. *Journal of Biomechanics*, 46(6):1162–1168, 2013.
- [278] R. Vayron, V. Mathieu, A. Michel, and G. Haiat. Assessment of in vitro dental implant primary stability using an ultrasonic method. *Ultrasound in Medicine & Biology*, 40(12):2885–2894, 2014.
- [279] R. Vayron, M. Matsukawa, R. Tsubota, V. Mathieu, E. Barthel, and G. Haiat. Evolution of bone biomechanical properties at the micrometer scale around titanium implant as a function of healing time. *Physics in medicine and biology*, 59:1389–1406, 2014.
- [280] R. Vayron, E. Soffer, F. Anagnostou, and G. Haiat. Ultrasonic evaluation of dental implant osseointegration. *Journal of Biomechanics*, 47(14):3562–3568, 2014.
- [281] R. Vayron, V.-H. Nguyen, R. Bosc, S. Naili, and G. Haiat. Finite element simulation of ultrasonic wave propagation in a dental implant for biomechanical stability assessment. *Biomech Model Mechanobiol*, 14(5):1021–32, 2015.
- [282] R. Vayron, V.-H. Nguyen, R. Bosc, S. Naili, and G. Haiat. Assessment of the biomechanical stability of a dental implant with quantitative ultrasound: A three-dimensional finite element study. *The Journal of the Acoustical Society of America*, 139(2):773–780, 2016.

- [283] R. Vayron, V.-H. Nguyen, B. Lecuelle, H. Albini Lomami, J.-P. Meningaud, R. Bosc, and G. Haiat. Comparison of resonance frequency analysis and of quantitative ultrasound to assess dental implant osseointegration. *Sensors (Basel, Switzerland)*, 18(5):1397, 2018.
- [284] R. Vayron, V. H. Nguyen, B. Lecuelle, and G. Haiat. Evaluation of dental implant stability in bone phantoms: Comparison between a quantitative ultrasound technique and resonance frequency analysis. *Clin Implant Dent Relat Res*, 2018.
- [285] M. Veltri, P. Balleri, and M. Ferrari. Influence of transducer orientation on Osstell stability measurements of osseointegrated implants. *Clin Implant Dent Relat Res*, 9(1):60–64, Mar 2007.
- [286] M. Veltri, R. Valenti, E. Ceccarelli, P. Balleri, R. Nuti, and M. Ferrari. The speed of sound correlates with implant insertion torque in rabbit bone: an in vitro experiment. *Clin Oral Implants Res*, 21(7):751–5, 2010.
- [287] S. K. Venkatesh and R. L. Ehman. *Magnetic Resonance Elastography*. Springer-Verlag New York, 2014.
- [288] M. T. Vestermark, J. E. Bechtold, P. Swider, and K. Søballe. Mechanical interface conditions affect morphology and cellular activity of sclerotic bone rims forming around experimental loaded implants. *Journal of Orthopaedic Research*, 22(3):647 – 652, 2004.
- [289] H. G. Welgus, J. J. Jeffrey, A. Z. Eisen, W. T. Roswit, and G. P. Stricklin. Human skin fibroblast collagenase: Interaction with substrate and inhibitor. *Collagen and Related Research*, 5(2):167 – 179, 1985.
- [290] J. Wolff. *The Law of Bone Remodeling*. Springer, 1892.
- [291] C. C. Wyatt and M. J. Pharoah. Imaging techniques and image interpretation for dental implant treatment. *Int J Prosthodont*, 11(5):442–52, 1998.
- [292] M. Özcan and C. Hämmerle. Titanium as a reconstruction and implant material in dentistry: Advantages and pitfalls. *Materials*, 5(9):1528–1545, 2012.
- [293] H. Zhou, Y. Hou, Z. Zhu, W. Xiao, Q. Xu, L. Li, X. Li, and W. Chen. Effects of low-intensity pulsed ultrasound on implant osseointegration in ovariectomized rats. *Journal of Ultrasound in Medicine*, 35(4):747–754, 2016.
- [294] H. Zitter and J. Plenk, H. The electrochemical behavior of metallic implant materials as an indicator of their biocompatibility. *J Biomed Mater Res*, 21(7):881–96, 1987.
- [295] P. K. Zysset, X. Edward Guo, C. Edward Hoffer, K. E. Moore, and S. A. Goldstein. Elastic modulus and hardness of cortical and trabecular bone lamellae measured by nanoindentation in the human femur. *Journal of Biomechanics*, 32(10):1005–1012, 1999.

Personal publications and presentations

Peer-reviewed publications

1. Hériveaux Y., Nguyen V-H., and Haïat G., "Reflection of an ultrasonic wave on the bone-implant interface: A numerical study of the effect of the multiscale roughness.", *Journal of the Acoustical Society of America*, 144(1): 488-499 (2018).
2. Hériveaux Y., Nguyen V-H., Brailovski V., Gorny C., and Haïat G., "Reflection of an ultrasonic wave on the bone-implant interface: Effect of the roughness parameters", *Journal of the Acoustical Society of America*, 145(6): 3370-3381 (2019).
3. Hériveaux Y., Nguyen V-H., Geiger D., and Haïat G., "Elastography of the bone-implant interface", *Scientific Reports*, 9(1): 14163 (2019).
4. Hériveaux Y., Haïat G. and Nguyen V-H., "Reflection of an ultrasonic wave on the bone-implant interface: Comparison of two-dimensional and three-dimensional numerical models", *Journal of the Acoustical Society of America - Express Letters*, 147(1): EL32-EL36 (2020).
5. Hériveaux Y., Audoin B., Biateau C., Nguyen V-H., and Haïat G., "Ultrasonic propagation in a dental implant", *Ultrasound in Medicine and Biology*, (in press).
6. Hériveaux Y., Vayron R., Fraulob M., Albin Lomami H., Lenormand C., and Haïat G., "Assessment of dental implant stability using resonance frequency analysis and quantitative ultrasound methods ", *Clinical Oral Implants Research*, (submitted).
7. Hériveaux Y., Nguyen V-H., Biwa, S., and Haïat G., "Analytical modeling of the interaction of an ultrasonic wave with a rough bone-implant interface", *Ultrasonics*, (submitted).

Book chapters

1. Hériveaux Y., Nguyen V-H., Vayron R., and Haïat G., "Ultrasonic evaluation of dental implant stability", in *Dental Ultrasound*, Ed. Albert Chan and Oliver Kripfgans, Springer. (in press).

International congress presentations

1. Hériveaux Y., Nguyen V-H., and Haïat G., "Reflection of an ultrasonic wave from the bone-implant interface: a numerical study", *8th World congress of Biomechanics*, 8th-12th July 2018, Dublin, Ireland. Poster presentation.
2. Hériveaux Y., Nguyen V-H., and Haïat G., "Reflection of an ultrasonic wave from the bone-implant interface: a numerical study on the effect of roughness", *176th Meeting Acoustical Society of America*, 5th-9th November 2018, Victoria BC, Canada. Oral presentation.
3. Hériveaux Y., Nguyen V-H., and Haïat G., "Numerical study on the reflection of an ultrasonic wave from a rough bone-implant interface", *8th International Symposium on Ultrasonic Characterization of Bone*, 24th-26th June 2019, Fréjus, France. Oral presentation.
4. Hériveaux Y., Nguyen V-H., and Haïat G., "Effect of roughness parameters on the reflection of an ultrasonic wave from the bone-implant interface", *25th Congress of the European Society of Biomechanics*, 7th-10th July 2019, Vienna, Austria. Oral presentation.
5. Hériveaux Y., Audoin B., Biateau C., Nguyen V-H., and Haïat G., "Ultrasonic guided wave propagation in a dental implant", *178th Meeting Acoustical Society of America*, 2nd-6th December 2019, San Diego, United-States. Oral presentation.
6. Hériveaux Y., Nguyen V-H., Geiger D., and Haïat G., "Influence of compressive stresses on the ultrasonic response of the bone-implant interface", *178th Meeting Acoustical Society of America*, 2nd-6th December 2019, San Diego, United-States. Oral presentation.

Seminars and other oral presentations

1. Hériveaux Y., "Ultrasonic characterization of the bone-implant interface", 24th September 2019, Acoustics and Vibration Lab, Hanyang University, Seoul.
2. Hériveaux Y., "Ultrasonic characterization of the bone-implant interface", 23rd October 2019, Department of Electrical Engineering, Faculty of Science and Engineering, Doshisha University, Kyoto.
3. Hériveaux Y., "Ultrasonic characterization of the bone-implant interface", 29th October 2019, Department of Aeronautics and Astronautics, Graduate School of Engineering, Kyoto University (Katsura), Kyoto.
4. Hériveaux Y., "Influence of stress on the ultrasonic response of the bone-implant interface", 8th November 2019, PhD students day, Laboratoire Modélisation et Simulation Multi-Echelle, Université Paris-Est Marne-La-Vallée (UPEM).

Résumé substantiel

Ce travail porte sur le développement de techniques ultrasonores afin de caractériser l'évolution des propriétés biomécaniques des tissus environnant l'implant au cours du processus d'ostéointégration. Bien que les implants en titane sont aujourd'hui utilisés de façon routinière pour des opérations dentaires, orthopédiques ou maxillo-faciales, le risque d'échec subsiste. De plus, ces échecs sont souvent difficiles à appréhender, notamment du fait de la complexité du tissu osseux.

La majorité des échecs survenant en implantologie sont liés au manque de standardisation des procédures chirurgicales. En effet, de nombreux chirurgiens utilisent encore des méthodes empiriques afin d'estimer la stabilité des implants. Il est donc nécessaire de développer des méthodes quantitatives. Pour ce faire, l'utilisation d'ultrasons quantitatifs a récemment été proposée. Du fait de leur caractère non-invasif, non-irradiant et de leur faible coût, les ultrasons quantitatifs semblent être une solution prometteuse afin d'évaluer les propriétés biomécaniques de l'interface os-implant (IOI), dont l'évolution est fortement corrélée au succès du processus d'ostéointégration. De plus, plusieurs études ont mis en évidence la possibilité de stimuler la repousse osseuse en utilisant des ultrasons pulsés de faible intensité (LIPUS), ce qui constitue une autre application potentielle des techniques ultrasonores à l'IOI. Pour autant, la propagation d'une onde ultrasonore à l'IOI est encore mal comprise. De ce fait, clarifier les phénomènes survenant au cours de la propagation ultrasonore au niveau de l'IOI permettrait d'améliorer ces techniques ultrasonores. C'est l'objectif principal de ce travail.

La partie I de ce document vise à rappeler le contexte général de l'étude, notamment en présentant les caractéristiques biomécaniques des tissus osseux ainsi que certaines propriétés mécaniques et géométriques des implants osseux en alliage de titane. Les notions de stabilité primaire et secondaire ainsi que l'ostéointégration sont également définies, et les différents paramètres impliqués dans ces processus sont exposés. Les différentes techniques permettant d'évaluer la stabilité implantaire, ainsi que leurs avantages et inconvénients sont brièvement présentées. En particulier, une revue détaillée des études de la littérature traitant de la caractérisation de l'IOI par ultrasons quantitatifs ainsi que de la stimulation du processus d'ostéointégration par LIPUS est fournie dans le chapitre 2.

Cependant, ces précédentes études se sont majoritairement focalisées sur les effets du temps de cicatrisation sur la réponse ultrasonore de l'IOI. La sensibilité des ultrasons quantitatifs aux contraintes présentes à l'IOI n'a encore jamais été étudiée. Dans la partie II, il a été démontré (i) que le coefficient de réflexion à l'IOI décroît significativement en fonction des contraintes de compression appliquées au niveau de l'IOI, et (ii) que la propagation ultrasonore à l'IOI est fortement corrélée au comportement mécanique du tissu osseux. Cette influence des contraintes sur la réponse ultrasonore de l'IOI est particulièrement importante jusqu'à ce qu'une contrainte seuil correspondant à la fracture de l'os soit atteinte. Ceci peut être expliqué par une augmentation du contact entre l'os et l'implant lorsque le réseau trabéculaire de l'os est comprimé sur l'implant, ainsi que par un changement global de la structure de l'os. Deux conclusions peuvent être tirées de ces résultats. D'une part, la distribution des contraintes autour des implants, souvent hétérogène du fait de leur géométrie complexe, est un paramètre influençant la propagation ultrasonore à l'IOI dont il faut donc tenir compte lors de l'utilisation d'ultrasons quantitatifs pour évaluer la stabilité implantaire. D'autre part, la sensibilité des ultrasons quantitatifs aux contraintes à l'IOI confirment leur potentiel afin d'estimer la stabilité primaire d'un implant, laquelle est fortement corrélée à la distribution de contraintes autour de l'implant.

Si les approches expérimentales sont nécessaires afin de mieux appréhender les techniques d'ultrasons quantitatifs, celles-ci ne permettent toutefois pas un contrôle précis des paramètres influençant l'interaction entre une onde ultrasonore et l'IOI. Pour cette raison, des modèles numérique par éléments finis et analytique de la propagation ultrasonore ont été développés dans la partie III. En particulier, les effets de la rugosité de l'implant ont été étudiés à deux différentes échelles, que l'on notera par la suite « macroscopique » et « microscopique ». Le chapitre 5 a permis de montrer qu'il était possible d'approximer la rugosité de l'implant par un profil sinusoïdal puisque (i) cela permet de décrire de façon satisfaisante la rugosité réelle de nombreux implants à l'échelle macroscopique, comme par exemple le filetage d'implants dentaires, et (ii) à l'échelle microscopique, une équivalence entre la réponse ultrasonore de l'IOI pour des profils de rugosité sinusoïdaux et mesurés par profilométrie sur implants réels a été démontrée. Toutefois, l'influence des différents paramètres de rugosité associés aux profils de rugosité d'implants réels a également été étudiée. Le processus d'ostéointégration a été simulé en diminuant progressivement l'épaisseur W d'une couche de tissus mous située entre l'os et l'implant, dont la présence modélise les tissus non minéralisés au niveau de l'IOI lorsque l'implant n'est pas parfaitement ostéointégré. Les simulations ont été réalisées à la fois sur des modèles 2-D et 3-D. Cependant, puisque les résultats obtenus sur ces deux modèles sont très similaires, seul le modèle 2-D a été utilisé pour réaliser les différentes études paramétriques de ce travail afin de diminuer les coûts de calcul associés aux simulations.

Pour les rugosités microscopiques, une expression analytique de la rigidité équivalente de l'IOI a pu être déterminée en distinguant les contributions respectives (i) du contact entre l'os et l'implant, et (ii) de la présence de tissus mous au niveau de l'interface. A partir de ces résultats, les coefficients de réflexion et de transmission de l'IOI ont pu être estimés analytiquement, ceux-ci étant en accord avec les coefficients obtenus numériquement. Les modèles numérique et analytique ont permis de mettre en évidence qu'à l'échelle microscopique, le coefficient de réflexion de l'IOI augmente d'une valeur initiale d'environ 0.55 jusqu'à une valeur finale d'environ 0.9 lorsque le produit $k.W$ du nombre d'onde par l'épaisseur des tissus mous augmente de 0 jusqu'à environ 0.3. De plus, le coefficient de réflexion dépend fortement des propriétés des tissus osseux à une distance inférieure à 25 μm de la surface de l'implant. Ceci permet donc de mettre en avant la sensibilité des ultrasons quantitatifs au processus d'ostéointégration de l'IOI, en particulier lorsque des hautes fréquences sont utilisées. A l'échelle macroscopique, la propagation ultrasonore est fortement dépendante de la rugosité de l'implant du fait de phénomènes d'interférences tels que le déphasage de l'onde ultrasonore ou la diffusion multiple à l'IOI. Ceux-ci devront donc être pris en compte lors de l'analyse de la réponse ultrasonore de l'IOI.

Dans la partie III, la modélisation de l'IOI a donc été effectuée en considérant une géométrie simple pour l'implant, avec une rugosité modélisée comme sinusoidale. Bien que l'utilisation d'un modèle simple permet de mieux comprendre les phénomènes mis en jeu lors de la propagation ultrasonore à l'IOI, il est également nécessaire de considérer des géométries plus complexes afin de tenir compte des caractéristiques réelles des implants utilisés en clinique. C'est pourquoi le cas spécifique des implants dentaires a été étudié dans la partie IV. Une première étude combinant des approches expérimentales et numériques a permis de démontrer que la propagation ultrasonore dans un implant dentaire était fortement impactée par sa géométrie. Pour cela, un transducteur ultrasonore a été vissé sur un implant dentaire puis excité à une fréquence centrale de 10 MHz. Des techniques d'ultrasons-laser ont ensuite été employées pour mesurer l'amplitude des déplacements générés par l'onde ultrasonore le long de l'axe de l'implant, comprise entre 3.2 nm et 8.9 nm selon la position de la mesure. De plus, l'analyse des signaux mesurés a permis de mettre en évidence la propagation d'une onde guidée le long de l'axe de l'implant. En effet, le premier signal se propage dans l'implant à une vitesse d'environ 2110 m.s^{-1} , soit une vitesse beaucoup plus faible que celle des ondes longitudinales dans le titane, qui est d'environ 5800 m.s^{-1} . Les composantes fréquentielles principales du signal sont de plus comprises entre 300 kHz et 2 MHz, soit des fréquences beaucoup plus faibles que celle d'excitation (10 MHz). Ces résultats ont par la suite été confirmés par la simulation numérique. Deux conclusions découlent principalement de cette étude. D'une part, il n'est pas nécessaire d'utiliser des transducteurs à haute fréquence pour caractériser la stabilité d'implants dentaires comme cela a pu être fait dans la littérature, puisque l'onde ultrasonore se propagera dans tous les cas à des fréquences proches de 1 MHz. D'autre part, l'intensité transmise à l'IOI dépend fortement de la structure de l'implant dentaire, si bien que si l'on souhaite stimuler l'ostéointégration d'implants par l'émission de LIPUS, il est nécessaire de choisir des caractéristiques d'ondes ultrasonores en adéquation avec la configuration considérée.

Une seconde étude a également été réalisée afin d'évaluer les performances des ultrasons quantitatifs pour estimer la stabilité implantaire à partir d'une étude *in vivo* sur lapins. Les résultats des mesures ultrasonores ont notamment été comparées aux valeurs de contact os-implant (BIC) obtenues par histologie ainsi qu'à celles de l'indicateur ISQ, obtenues par une méthode d'analyse de la fréquence de résonance de l'implant (RFA) actuellement utilisée en clinique. Les valeurs de l'indicateur ultrasonore *UI* sont mieux corrélées à la fois aux valeurs de BIC et au temps de cicatrisation que celles de l'ISQ, lesquelles dépendent fortement de la manière dont les mesures ont été effectuées. De plus, les erreurs sur l'*UI* sont 3.3 fois plus faibles que celles sur l'ISQ. En conclusion, l'étude a démontré une meilleure performance des ultrasons quantitatifs afin d'estimer la stabilité d'implants dentaires par rapport à la technique RFA, ce qui confirme le potentiel des méthodes ultrasonores pour caractériser le processus d'ostéointégration.

En conclusion, les travaux décrits dans ce document ont permis de valider l'utilisation d'ultrasons quantitatifs afin de caractériser la stabilité implantaire, ainsi que de fournir de nouveaux éléments pour mieux comprendre les paramètres influençant la propagation d'une onde ultrasonore à l'IOI. Plusieurs études futures pourront découler de ce travail. Notamment, le modèle numérique proposé en partie III pourra être utilisé pour étudier l'influence d'autres paramètres, comme par exemple l'angle d'incidence de l'onde ultrasonore. Tenir compte de l'incidence oblique des ultrasons permettrait entre autres de mieux comprendre la propagation des ondes de cisaillement à l'IOI. Il pourrait également être intéressant d'introduire des profils de rugosité d'implants réels dans un modèle numérique 3-D afin de s'approcher davantage des configurations réelles. De plus, la résolution du problème inverse, laquelle permettrait de remonter aux caractéristiques précises de l'IOI correspondant à un coefficient de réflexion donné, est actuellement en cours d'étude.

Par ailleurs, les travaux présentés dans ce document se concentrent principalement sur l'utilisation de techniques ultrasonores pour caractériser l'IOI. Cependant, la stimulation ultrasonore du processus d'ostéointégration, également mentionnée, devra être étudiée de façon plus poussée par la suite. En particulier, il serait intéressant de réaliser des études *in vivo* afin d'optimiser les paramètres des ondes LIPUS permettant de promouvoir l'ostéointégration. Comme mis en avant dans le chapitre 7, ces paramètres optimaux devront notamment être adaptés à la configuration considérée.

Enfin, l'utilisation d'ultrasons quantitatifs pour caractériser l'IOI doit encore être validée par des études cliniques. Comme détaillé dans le chapitre 2, un dispositif a déjà été développé pour estimer la stabilité d'implants dentaires, et a été validé par des études numériques, *in vitro* et *in vivo*. Toutefois, les études cliniques seront nécessaires afin de définir une valeur cible pour l'indicateur ultrasonore *UI* au-dessus de laquelle l'implant pourra être considéré comme suffisamment stable pour être chargé. De plus, ces études permettront de confirmer la fonctionnalité et les performances du dispositif d'ultrasons quantitatifs.

Résumé

Titre: Caractérisation ultrasonore de l'interface os-implant.

Malgré le caractère routinier des interventions chirurgicales en implantologie, les risques d'échecs subsistent et peuvent être lourds de conséquences. L'issue clinique est directement liée au processus d'ostéointégration, qui correspond à la repousse osseuse au contact direct de l'implant. Ce travail porte sur le développement de techniques ultrasonores afin de caractériser les propriétés biomécaniques de l'interface os-implant (IOI), qui déterminent le succès de l'ostéointégration.

Une première étude *in vitro* a permis d'estimer la sensibilité des ultrasons quantitatifs aux contraintes de compression générées au niveau de l'IOI. Pour cela, des échantillons d'os trabéculaire bovin ont été comprimés sur des implants cylindriques et la réponse ultrasonore de l'IOI a été mesurée au cours de la compression. Une diminution significative du coefficient de réflexion de l'IOI en fonction des contraintes a été obtenue jusqu'à ce qu'une contrainte seuil correspondant à la fracture de l'os soit atteinte.

Dans un deuxième temps, la propagation ultrasonore à l'IOI a été modélisée et simulée d'abord numériquement puis analytiquement, ce qui a permis de distinguer l'effet de différents paramètres sur la réponse ultrasonore de l'IOI. En particulier, l'influence de la rugosité de l'implant a été étudiée à des échelles microscopique et macroscopique. Une diminution significative du coefficient de réflexion de l'IOI a été démontrée lorsque (i) l'ostéointégration de l'IOI augmente, (ii) la rugosité de l'implant diminue, (iii) la fréquence centrale des ultrasons diminue et (iv) la masse volumique de l'os augmente. De plus, des phénomènes d'interférence ont été mis en évidence à l'échelle macroscopique.

Enfin, le potentiel des ultrasons quantitatifs pour déterminer la stabilité d'implants dentaires a été évalué. La propagation ultrasonore dans un implant dentaire a été étudiée par des méthodes d'interférométrie-laser. L'analyse spectrale ainsi que du temps d'arrivée des premiers signaux a permis de démontrer la propagation d'une onde guidée le long de l'implant, ce qui a été confirmé numériquement. De plus, une étude *in vivo* sur lapins a permis de comparer les performances des ultrasons quantitatifs avec celles de l'analyse de la fréquence de résonance (RFA) afin d'estimer la stabilité d'implants dentaires. Une meilleure sensibilité aux changements de qualité et de quantité de l'os survenant durant l'ostéointégration a été obtenue avec les ultrasons quantitatifs.

Grâce au couplage de méthodes numériques et expérimentales, ces travaux ont permis de mieux comprendre la propagation des ondes ultrasonores à l'IOI, ainsi que de valider les performances d'un dispositif médical visant à évaluer la stabilité d'implants dentaires.

Mots-clés: Ultrasons quantitatifs, Interface os-implant, Stabilité implantaire, Implant dentaire, Ostéointégration, Simulation numérique, Onde guidée.

Abstract

Title: Ultrasonic characterization of the bone-implant interface.

While surgical interventions involving the use of endosseous implants are now routinely performed, failures still occur and may have dramatic consequences. The clinical outcome depends on osseointegration processes, which correspond to the growth of bone in intimate contact with the implant. This work focuses on the development of quantitative ultrasound (QUS) techniques for the characterization of the biomechanical properties of the bone-implant interface (BII), which are the main determinant for the success of osseointegration.

First, an *in vitro* approach is carried out to assess the sensitivity of the QUS response of the BII to loading conditions. Trabecular bovine bone samples are compressed onto coin-shaped implants and the ultrasonic response of the BII is measured during compression. A significant decrease of the reflection coefficient of the BII as a function of the stress is obtained until a plateau is reached, corresponding to bone fracture.

Second, finite element modeling and simulations are performed in order to distinguish the effects of different parameters on the ultrasonic response of the BII. In particular, the impact of the implant surface roughness is investigated at the microscopic and macroscopic scales. An analytical model of the ultrasonic propagation at the BII is also proposed. The reflection coefficient of the BII is shown to significantly decrease when (i) the BII is better osseointegrated, (ii) the roughness amplitude decreases, (iii) the central frequency of ultrasound decreases and (iv) bone mass density increases. Moreover, interference phenomena are evidenced at the macroscopic scale.

Third, *in silico*, *in vitro* and *in vivo* studies are combined to investigate the use of QUS methods to estimate dental implant stability. Ultrasound propagation inside a dental implant is examined using laser-interferometric techniques. First arriving signal and spectral analyses evidence the propagation of a guided wave mode along the implant axis, which is confirmed by numerical simulation. An *in vivo* study is performed to compare the performances of QUS and of resonance frequency analysis to estimate dental implant stability in a rabbit model. The QUS results were shown to have a better sensitivity to changes of bone quantity and quality during the osseointegration processes.

By coupling experimental and numerical approaches, this work provides new insights to better understand the propagation of ultrasonic waves at the BII. Moreover, it proves the performances of a future medical device that could assess dental implant stability.

Keywords: Quantitative ultrasound, Bone-implant interface, Implant stability, Dental implant, Osseointegration, Numerical simulation, Guided wave.